



The  
University  
Of  
Sheffield.

## Access to Electronic Thesis

Author: Mark Pipe  
Thesis title: Limits on spin-dependent WIMP-proton cross-sections using the DRIFT-IIId directional dark matter detector  
Qualification: PhD

**This electronic thesis is protected by the Copyright, Designs and Patents Act 1988. No reproduction is permitted without consent of the author. It is also protected by the Creative Commons Licence allowing Attributions-Non-commercial-No derivatives.**

If this electronic thesis has been edited by the author it will be indicated as such on the title page and in the text.

UNIVERSITY OF SHEFFIELD

**Limits on spin-dependent WIMP-proton  
cross-sections using the DRIFT-II  
directional dark matter detector**

by

Mark Pipe

A thesis submitted in partial fulfillment for the  
degree of Doctor of Philosophy

in the  
Faculty of Science  
Department of Physics and Astronomy

December 2011



UNIVERSITY OF SHEFFIELD

# *Abstract*

Faculty of Science  
Department of Physics and Astronomy

Doctor of Philosophy

by Mark Pipe

The nature of dark matter remains one of the biggest questions in physics today. Weakly Interacting Massive Particles (WIMPs) are a particularly well motivated candidate for the missing matter that makes up 85% of the mass of the Universe. The most promising method for an unambiguous proof of the existence of WIMPs is via detection of the predicted directional anisotropy.

The DRIFT detector at the Boulby Underground Laboratory in the UK is the world's first large scale directionally sensitive dark matter detector. This thesis presents work focussing on the ability of DRIFT to be competitive with non-directional detectors in exploring new spin-dependent WIMP interaction phase-space. Experimental efforts towards this are discussed, including the first calibration measurements of spin-dependent target gases in DRIFT, and development and implementation of an automated gas mixing system required for spin-dependent gas mixture operation.

This thesis presents the first long-term study of backgrounds in DRIFT in which current limiting backgrounds are identified and studied, providing information crucial to future background reduction strategies. Developments of the WIMP analysis procedure are presented that result in an improved sensitivity to WIMP-mimicking neutron-induced nuclear recoils by a factor of 2.4. Data from the first runs with spin-dependent sensitive CS<sub>2</sub>-CF<sub>4</sub> gas mixtures are presented with improved analysis methods. This thesis presents the first blind analysis results from a directionally sensitive dark matter detector with upper limits on the SD WIMP-proton interaction cross-section with a minimum of 0.93 pb for a 100 GeV WIMP.

## *Acknowledgements*

Firstly I would like to thank my supervisor Dr. Ed Daw for giving me the opportunity to undertake this PhD. Dr. Daw has shown continued faith in me, ever since my undergraduate project with him, which has led me to where I am now. His encouragement and guidance throughout this process have been invaluable. Thanks must also go to Professor Neil Spooner, for his guidance throughout. His advice has been essential in keeping me on track along the way, for which I am grateful. Financial support for this work was provided by STFC, for which I am also grateful.

I am grateful to all in the DRIFT collaboration for making my PhD an enjoyable and enlightening experience. I would like to pay particular thanks to Dr. Sean Paling, who taught me everything there is to know about the DRIFT detector and whose expertise and enthusiasm in all things underground have been a source of inspiration. The days underground at the Boulby Mine followed by evenings in Whitby will be missed. Particular thanks are also due to Professor Daniel Snowden-Ifft for his assistance throughout this PhD and for teaching me much about experimental physics during my trips to Occidental College, Los Angeles.

Thanks are due to all those in the department who have offered me assistance throughout this research. Particular thanks to Dr. Matthew Robinson, whose computing wizardry, has rescued me from many headaches and Dr. Susan Cartwright who has aided me greatly in my understanding of cosmology.

I would like to thank my various housemates throughout my time at Sheffield, for making these truly enjoyable years. Sheffield and the friends I have here will be sorely missed. I must also mention The Sex Panthers, the questionably named six-a-side team I have had the pleasure of playing for, for the past few years. Thursday nights have long been a highlight of the week, despite the occasional double-figure defeats.

I must also express my sincere gratitude to Suzanne, whose relentless encouragement and belief has been an invaluable aid to me. She has endured much in the past six months and I have relied heavily on the daily chats and regular texts of encouragement for retaining my sanity. I am grateful to have her in my life and, on completion of this research, am looking forward to nothing more than spending more time with her.

I gratefully acknowledge my brother Andrew and sister Claire, who, between telling me to ‘hurry up and get a proper job’, have always shown me a huge amount of support and encouragement. Finally and foremost, I thank my parents, who have given me unlimited love and support, and to whom I owe everything.

# Author's contributions

Working as part of the DRIFT collaboration, much of the work in this thesis was only possible in collaboration with other members of the group. Here the personal contributions of the author are highlighted by chapter.

**Chapter 3.** The identification of previously unknown MWPC signal effects in DRIFT was the authors work, as was the identification of a means of continuous in situ measurements of drift velocity, and the analysis procedure developed to achieve it.

**Chapter 4.** The first calibration measurements of gas mixtures in DRIFT were performed by the author in collaboration with Occidental College. The design, building and programming of the new gas mixing system, was led by the author. The long term monitoring of the system after installation at the Boulby Underground Laboratory is also the work of the author.

**Chapter 5.** The analysis for  $^{55}\text{Fe}$  energy calibration on a per-channel basis was developed by the author. The author led operation of the underground DRIFT-IIId detector for a period of  $\sim 1$  year, including the period in which data for this chapter was collected. The WIMP analysis presented is based on existing DRIFT analysis code, which was re-structured and optimised by the author. The extensive improvements to the existing cuts and parameterisation procedure leading to a factor 2.4 increase in sensitivity was the author's own work.

**Chapter 6.** The identification of four dominating background sub-populations through careful cut selection was the authors work. The long-term study of backgrounds in DRIFT was performed for the first time by the author. The author was heavily involved in the described background reduction operations including acid etching of detector components and commissioning of improved cathode design.

**Chapter 7.** All simulated DRIFT data was provided by Professor Daniel Snowden-Ifft. Independent verification of simulated neutron data was performed by the author, and techniques of correcting simulated data developed by the author. Blind analysis of DRIFT data producing an upper limit on the SD WIMP-proton interaction cross-section was performed by the author.



# Contents

<b>Abstract</b>	<b>iii</b>
<b>Acknowledgements</b>	<b>iv</b>
<b>Author's contributions</b>	<b>v</b>
<b>List of Figures</b>	<b>xi</b>
<b>List of Tables</b>	<b>xv</b>
<b>1 An introduction to dark matter</b>	<b>1</b>
1.1 Evidence for dark matter in the Universe . . . . .	1
1.1.1 The composition of the Universe . . . . .	1
1.1.2 Cosmic background radiation . . . . .	2
1.1.3 Light element abundances . . . . .	4
1.1.4 Large-scale structure formation . . . . .	7
1.2 Evidence for dark matter in galaxies and galaxy clusters . . . . .	9
1.2.1 Virially bound systems . . . . .	9
1.2.2 Galaxy rotation curves . . . . .	10
1.2.3 Gravitational lensing . . . . .	11
1.3 Dark matter particles . . . . .	14
1.3.1 WIMPs . . . . .	14
1.3.2 WIMP halo characteristics . . . . .	15
1.4 WIMP dark matter searches . . . . .	18
1.4.1 Search for WIMPs by indirect detection . . . . .	18
1.4.2 Search for WIMPs by direct detection . . . . .	20
1.4.3 Galactic signals . . . . .	21
<b>2 Direct detection of WIMPs</b>	<b>25</b>
2.1 Theory of WIMP detection . . . . .	25
2.1.1 WIMP scattering kinematics . . . . .	26
2.1.2 Total event rate of WIMP scattering . . . . .	29
2.1.3 Differential event rate . . . . .	30
2.1.4 Correcting for realistic WIMP velocities . . . . .	30

2.1.5	Nuclear form factor corrections . . . . .	33
2.1.6	WIMP-nucleon cross-sections . . . . .	35
2.1.7	Event rate spectra . . . . .	38
2.2	Detector backgrounds . . . . .	40
2.2.1	Electron recoils . . . . .	40
2.2.2	Nuclear recoils . . . . .	41
2.3	Directional dark matter detection . . . . .	42
2.4	Existing directional dark matter detection experiments . . . . .	46
2.4.1	NEWAGE . . . . .	46
2.4.2	DMTPC . . . . .	47
2.4.3	MIMAC . . . . .	48
<b>3</b>	<b>The DRIFT directional dark matter detector</b>	<b>51</b>
3.1	The DRIFT detector concept . . . . .	51
3.1.1	The time projection chamber . . . . .	51
3.1.2	TPC for dark matter detection . . . . .	52
3.1.3	Negative ion drift gas choice . . . . .	53
3.2	The DRIFT-II detector . . . . .	54
3.2.1	Boulby Underground Laboratory . . . . .	54
3.2.2	Detector hardware design . . . . .	55
3.2.3	Detector readout electronics . . . . .	58
3.2.4	The DRIFT-II event file . . . . .	62
3.3	Track production and readout in DRIFT . . . . .	64
3.3.1	Track production . . . . .	64
3.3.2	Track drifting and diffusion . . . . .	66
3.3.3	Charge multiplication . . . . .	69
3.4	Response of MWPCs to spark-like events . . . . .	70
3.4.1	Identifying spark-like events . . . . .	71
3.4.2	Qualitative analysis of spark-like events . . . . .	72
3.4.3	Consequences for DRIFT . . . . .	75
3.5	In situ measurements of gas mobility . . . . .	76
3.5.1	Drift time measurements . . . . .	76
3.5.2	Drift time results . . . . .	77
3.5.3	Comparison with existing measurements, and conclusions . . . . .	78
<b>4</b>	<b>Development of spin-dependent <math>\text{CF}_4</math> target for DRIFT-II</b>	<b>81</b>
4.1	Spin-dependent WIMPs . . . . .	81
4.1.1	Spin-dependent vs spin-independent . . . . .	81
4.1.2	Spin-dependent sensitive target . . . . .	83
4.1.3	Properties of $\text{CS}_2$ - $\text{CF}_4$ mixtures . . . . .	84
4.2	Gas mixture tests in DRIFT-IIc . . . . .	88
4.2.1	$^{55}\text{Fe}$ calibrations . . . . .	88
4.2.2	Neutron calibrations . . . . .	89
4.3	Gas mixing system design and construction . . . . .	91
4.3.1	Hardware design . . . . .	91
4.3.2	Electronics design . . . . .	94
4.3.3	Software design . . . . .	97

4.4	Gas mixing system underground on DRIFT-IIId . . . . .	103
4.4.1	Stability and monitoring . . . . .	103
4.4.2	Conclusions . . . . .	107
<b>5</b>	<b>DRIFT-II data analysis</b> . . . . .	<b>109</b>
5.1	Waveform preprocessing . . . . .	109
5.1.1	High frequency noise removal . . . . .	109
5.1.2	Low frequency noise removal . . . . .	111
5.2	$^{55}\text{Fe}$ energy calibration . . . . .	112
5.2.1	$^{55}\text{Fe}$ interactions in $\text{CS}_2$ and $\text{CS}_2\text{-CF}_4$ mixtures . . . . .	112
5.2.2	Analysis, smoothing and thresholds . . . . .	114
5.2.3	Stability of $^{55}\text{Fe}$ analysis configuration . . . . .	120
5.2.4	Energy calibration on a per-channel basis . . . . .	123
5.2.5	Long term stability . . . . .	124
5.2.6	Tuning shaping amplifier gains . . . . .	126
5.3	WIMP analysis . . . . .	127
5.3.1	Parameterisation of hits . . . . .	128
5.3.2	Rebound hits . . . . .	130
5.3.3	Stage 1 cuts . . . . .	130
5.3.4	Parameterisation of events . . . . .	131
5.3.5	Stage 2 cuts . . . . .	134
5.4	Final stage cuts . . . . .	135
5.4.1	NIPs Ratio cuts . . . . .	136
5.4.2	RMST vs. NIPs plots . . . . .	142
5.4.3	Pulse shape cuts . . . . .	143
5.4.4	Additional pulse shape cuts and signal region . . . . .	147
5.5	Conclusion . . . . .	148
<b>6</b>	<b>Long-term study of backgrounds in DRIFT-IIId</b> . . . . .	<b>151</b>
6.1	Background events in DRIFT-IIId . . . . .	151
6.1.1	Alpha-like background events . . . . .	152
6.1.2	Alpha events as a diagnostic for DRIFT . . . . .	152
6.1.3	Recoil-like background events . . . . .	155
6.1.4	Radon progeny recoils in DRIFT . . . . .	156
6.1.5	DRIFT-II detector operations . . . . .	158
6.2	Characterising recoil-like backgrounds . . . . .	159
6.2.1	Identification of background recoil-like populations . . . . .	159
6.2.2	Quantifying backgrounds . . . . .	163
6.3	Long term background studies . . . . .	165
6.3.1	Population 3 recoil-like events . . . . .	165
6.3.2	Alpha-tagged recoil events . . . . .	167
6.3.3	Population 2 recoil events . . . . .	169
6.3.4	1MWPC alpha events . . . . .	171
6.3.5	GPCC events . . . . .	172
6.3.6	Further discussion of RMST effects in recoil-like events . . . . .	173
6.4	Conclusions . . . . .	177

---

<b>7</b>	<b>Dark matter results</b>	<b>179</b>
7.1	The DRIFT-IIId event simulator . . . . .	179
7.1.1	The DRIFT-IIId detector simulation . . . . .	179
7.1.2	Simulated vs. experimental neutron data . . . . .	180
7.1.3	Grid signals and the anode sum line . . . . .	182
7.1.4	Corrections to other simulated data parameters . . . . .	186
7.1.5	Simulated vs. experimental data in the RMST vs. NIPs plane . . . . .	189
7.2	A non-blind limit on the spin-dependent WIMP-proton cross-section . . . . .	190
7.2.1	DRIFT-IIId detection efficiency for 100 GeV WIMPs . . . . .	191
7.2.2	Spin-dependent WIMP-proton limit plot . . . . .	192
7.3	A first blind search for WIMP-proton interactions in DRIFT-IIId . . . . .	195
7.3.1	Setting parameters for the blind WIMP search . . . . .	196
7.3.2	Defining acceptance box for blind thin film cathode data . . . . .	198
7.3.3	Opening the box . . . . .	205
7.3.4	Spin-dependent WIMP-proton limit plot from a blind analysis . . . . .	207
7.4	Conclusions . . . . .	208
<b>8</b>	<b>Conclusions</b>	<b>209</b>
<b>A</b>	<b>Background reduction operations</b>	<b>213</b>
A.1	Cathode etching . . . . .	213
A.2	MWPC etching . . . . .	214
A.3	Thin film cathode . . . . .	215
<b>B</b>	<b>Dataset run details</b>	<b>217</b>
	<b>Bibliography</b>	<b>219</b>

# List of Figures

1.1	Power spectrum and E-mode polarisation of the CMB . . . . .	4
1.2	Baryon density constraints from Big Bang Nucleosynthesis . . . . .	7
1.3	Dark matter density images from the Millennium-II Simulation . . . . .	8
1.4	Decomposition of the NGC3198 spiral galaxy. . . . .	11
1.5	Image of strong gravitational lensing . . . . .	12
1.6	Images of the Bullet cluster . . . . .	14
1.7	Motion of Earth through the WIMP halo . . . . .	17
1.8	Measurements of cosmic positron abundance . . . . .	19
1.9	Current upper bounds on WIMP-nucleon interaction cross-sections . . . . .	21
2.1	Elastic scattering of WIMP with target nucleus . . . . .	26
2.2	WIMP passing through detector volume . . . . .	29
2.3	Probability density of recoil energy . . . . .	31
2.4	Nuclear form factors for SI WIMP-nucleus interactions . . . . .	35
2.5	Nuclear form factors for SD WIMP-nucleus interactions . . . . .	36
2.6	Theoretical differential event rate spectrum for various SI targets. . . . .	39
2.7	Theoretical differential event rate spectra for SD WIMPs. . . . .	39
2.8	Estimated directional anisotropy of WIMP signal . . . . .	43
2.9	Expected directional anisotropy . . . . .	43
2.10	Exposure to reject isotropy vs. energy threshold for a DRIFT-like detector	45
2.11	NEWAGE $\mu$ -PIC readout plane . . . . .	47
2.12	DMTPC 10-litre detector . . . . .	48
2.13	Prototype MIMAC detector . . . . .	49
2.14	Images of the bulk micromegas readout of the MIMAC detector . . . . .	50
3.1	Schematic of a generic time projection chamber . . . . .	52
3.2	The DRIFT-IIId detector . . . . .	55
3.3	Depths of underground laboratories . . . . .	56
3.4	Photos of the DRIFT-IIId vacuum vessel and neutron shielding housing. . . . .	58
3.5	Schematic diagram of the standard gas flow system . . . . .	59
3.6	Wire grouping schematic . . . . .	60
3.7	Pulse preamplification figure . . . . .	60
3.8	Pulse shaping electronics. . . . .	61
3.9	A typical DRIFT-II event file . . . . .	63
3.10	Quenching factors of C and S recoils . . . . .	65
3.11	Simulated ranges in 40 Torr CS <sub>2</sub> . . . . .	66
3.12	Simulated $dE/dx$ for alpha particle and S nucleus in CS <sub>2</sub> . . . . .	67
3.13	Drift lines . . . . .	69

3.14	Electric field equipotentials and field lines within an MWPC . . . . .	70
3.15	Evolution of charge in the vicinity of the anode wire. . . . .	70
3.16	Comparison of a spark-like event compared to a typical nuclear recoil event	71
3.17	Grid and anode lines of a typical spark-like event . . . . .	73
3.18	Comparison of the direct hit to the average induced signal . . . . .	74
3.19	Separation of anode and grid pulses in spark-like events in 40 Torr CS <sub>2</sub> . .	77
3.20	$\Delta t$ measurements plotted as a function of time . . . . .	79
4.1	Spin-independent WIMP-nucleon cross-section as a function of WIMP mass	82
4.2	Current limits on spin-dependent WIMP-proton scattering cross-sections .	83
4.3	Gas gains in CS <sub>2</sub> -CF <sub>4</sub> mixtures . . . . .	86
4.4	Nuclear recoil quenching factors for recoils in CS <sub>2</sub> -CF <sub>4</sub> mixtures. . . . .	87
4.5	Track range as a function of recoil energy in CS <sub>2</sub> -CF <sub>4</sub> gas mixtures . . . .	87
4.6	<sup>55</sup> Fe gain calibration in DRIFT-IIc . . . . .	89
4.7	Schematic of neutron run geometry . . . . .	90
4.8	Schematic diagram of the CS <sub>2</sub> -CF <sub>4</sub> gas mixing system . . . . .	93
4.9	Scale diagram of gas mixing panel . . . . .	94
4.10	Representative circuit diagram for the gas mixing system control . . . . .	96
4.11	Schematic of PCB for control of gas mixing system . . . . .	97
4.12	Gas mixing . . . . .	99
4.13	Comparison of old gas flow control to new . . . . .	101
4.14	Screenshots of the GasMix GUI . . . . .	102
4.15	Gas mixing panel installed on DRIFT-IIId . . . . .	103
4.16	Mixing and supply chamber pressures over a 24 hour period . . . . .	104
4.17	Mixing and supply cylinder pressures with dwindling CS <sub>2</sub> supply . . . . .	105
4.18	Ratio of CS <sub>2</sub> to CF <sub>4</sub> added to the mixture in each cycle . . . . .	106
4.19	Histogram of CS <sub>2</sub> to CF <sub>4</sub> fill ratios . . . . .	106
4.20	<sup>55</sup> Fe gain plots in DRIFT-IIId . . . . .	108
4.21	Mean pulse area produced by <sup>55</sup> Fe events over time . . . . .	108
5.1	Effects of 55 kHz noise removal . . . . .	110
5.2	Power spectrum of grid sum line . . . . .	111
5.3	Grid sum line before and after 50 Hz noise removal . . . . .	112
5.4	Interaction between 5.9 keV x-ray and sulphur atom. . . . .	114
5.5	<sup>55</sup> Fe spectra at different analysis thresholds . . . . .	116
5.6	A typical <sup>55</sup> Fe event file before and after boxcar smoothing . . . . .	117
5.7	Effects of boxcar smoothing . . . . .	119
5.8	Boxcar smoothing effects on measured <sup>55</sup> Fe peak area . . . . .	121
5.9	Savitzky-Golay smoothing effects on measured <sup>55</sup> Fe peak area . . . . .	122
5.10	<sup>55</sup> Fe calibration spectra before tuning of the shaping amplifiers. . . . .	123
5.11	Gains of individual anode lines over time. . . . .	125
5.12	<sup>55</sup> Fe calibration spectra after tuning of the shaping amplifiers. . . . .	126
5.13	<sup>55</sup> Fe spectrum of left MWPC showing improved energy resolution . . . . .	127
5.14	Event with rebound hits and event removed by stage 1 cuts . . . . .	132
5.15	Events removed by stage 1 and stage 3 cuts . . . . .	133
5.16	Events cut by stage 2 and final stage cuts . . . . .	135
5.17	<i>anodeSumNips</i> to <i>gridSumNips</i> ratio for neutron and WIMP-search runs .	137

5.18	Two events cut by the <i>anodeSumNips</i> to <i>gridSumNips</i> ratio cut . . . . .	138
5.19	Anode track nips vs. anode sum nips . . . . .	140
5.20	Two events cut by the <i>anodeNips</i> to <i>anodeSumNips</i> ratio cut . . . . .	141
5.21	Events in <i>anodeTrackRMST</i> vs. <i>anodeTrackNips</i> before pulse shape cuts . . . . .	143
5.22	Comparison of background event to neutron event . . . . .	144
5.23	Ratio of <i>anodeTrackSigma</i> to <i>anodeTrackRmst</i> . . . . .	145
5.24	Frequency plot of <i>gridPhRatio</i> . . . . .	146
5.25	<i>anodeTrackRMST</i> vs. <i>anodeTrackNips</i> plot before cuts . . . . .	147
5.26	Events in <i>anodeTrackRMST</i> vs. <i>anodeTrackNips</i> plane after all cuts . . . . .	148
6.1	Event file for a typical alpha event. . . . .	153
6.2	A typical GPCC event . . . . .	154
6.3	Tagged RPR example . . . . .	155
6.4	Typical recoil-like event from a neutron calibration run . . . . .	156
6.5	RPR schematic . . . . .	157
6.6	Radon decay chains . . . . .	158
6.7	Comparison of WIMP-search data to neutron data with reduced cuts . . . . .	161
6.8	WIMP analysis of $^{55}\text{Fe}$ calibration data . . . . .	162
6.9	Gaussian fits to recoil-like events . . . . .	164
6.10	Mean event rate of population 3 recoil events . . . . .	166
6.11	Mean RMST of population 3 recoil events . . . . .	167
6.12	Mean RMST of alpha-tagged recoil events . . . . .	168
6.13	Mean event rate of alpha-tagged recoil events . . . . .	169
6.14	Mean event rate of population 2 recoil-like events . . . . .	170
6.15	Mean event rate of 1MWPC alpha events . . . . .	172
6.16	Mean event rate of GPCC events . . . . .	173
6.17	Mean RMST of population 2 recoil events . . . . .	175
6.18	Gas change and cathode cleaning effect on the backgrounds . . . . .	176
7.1	Real vs. simulated data for <i>anodeSumNIPs/gridSumNIPs</i> . . . . .	183
7.2	Real vs. simulated data for <i>anodeNIPs/anodeEventNips</i> . . . . .	184
7.3	Comparison of real and simulated nuclear recoil event file . . . . .	186
7.4	Real vs. simulated data for anode pulse shape parameters . . . . .	188
7.5	Comparison of real and simulated data in the RMST vs. RMST plane . . . . .	189
7.6	Comparison of real and simulated data . . . . .	190
7.7	Simulated fluorine recoils from 100 GeV WIMPs . . . . .	192
7.8	SD WIMP-proton limit plot from wire cathode data . . . . .	195
7.9	Non-blind thin film cathode WIMP-search data in RMST vs. NIPs plane . . . . .	197
7.10	Alpha-tagged recoils in RMST vs. NIPs plane . . . . .	198
7.11	Low NIPs background . . . . .	199
7.12	Comparison of recoil events to alpha-tagged recoil events. . . . .	201
7.13	Signal region set from mean of alpha-tagged recoil population. . . . .	201
7.14	Illustrations of double-recoil and low energy alpha events . . . . .	202
7.15	Comparison of recoil events to double-recoil events. . . . .	204
7.16	Thin film cathode signal region with various event types. . . . .	205
7.17	Opening up the blind dataset . . . . .	206
7.18	Candidate WIMP interaction from blind WIMP-search data . . . . .	207

---

7.19 Upper limits on SD WIMP-proton cross-sections . . . . .	208
A.1 Photograph taken during the cathode cleaning operation . . . . .	214

# List of Tables

1.1	Cosmological parameters from the WMAP experiment . . . . .	5
2.1	Assumed WIMP halo parameters . . . . .	26
2.2	Table of existing low pressure gaseous TPC experiments for directional dark matter searches . . . . .	50
3.1	Descriptions of datasets . . . . .	76
3.2	$\Delta t$ and reduced mobility measurements . . . . .	78
3.3	Reduced mobility calculations from single wire proportional counter . . . . .	79
4.1	SD enhancement factors . . . . .	84
4.2	W-value and reduced mobility measurements of CS <sub>2</sub> -CF <sub>4</sub> gas mixtures. . . . .	85
4.3	Nuclear recoil event rates . . . . .	91
4.4	Measurement of $\Delta z$ component of neutron induced nuclear recoils in CS <sub>2</sub> -CF <sub>4</sub> gas mixtures . . . . .	91
4.5	Logic truth table for TTL control of mass flow controllers . . . . .	95
5.1	Gas parameters for <sup>55</sup> Fe interactions . . . . .	113
5.2	Effect of cuts on event rates . . . . .	149
7.1	Simulated WIMP statistics . . . . .	193
B.1	Descriptions of datasets used for long-term study of backgrounds . . . . .	218



# Chapter 1

## An introduction to dark matter

Over the past eight decades, evidence has accumulated to suggest that a large fraction of the Universe is unaccounted for by ordinary baryonic matter. The latest results determine the composition of the Universe, with extraordinary precision, to be 72.8% dark energy, 22.6% dark matter and only 4.6% baryonic matter [1].

In this chapter, key evidence for the existence of non-baryonic matter is presented. This evidence is derived from two classes of observations. In Section 1.1, evidence is presented for the existence of dark matter in the Universe from observations of the cosmic background radiation and from measurements of the relative abundance of the light elements. In Section 1.2, evidence is presented for the existence of dark matter locally, from observations of single galaxies and galaxy clusters. In Section 1.3 weakly interacting massive particles are introduced as a single class of non-baryonic dark matter that can explain this great variety of observations. Finally, in Section 1.4, the characteristics of the dark matter halo and a number of experiments attempting to verify the existence of dark matter on Earth are discussed

### 1.1 Evidence for dark matter in the Universe

#### 1.1.1 The composition of the Universe

A new understanding of the Universe emerged in the 1920s with the prediction [2, 3] and experimental observation [4] that the Universe is expanding. Hubble's observations provided the first evidence that led to the wide-spread acceptance of the *Big Bang theory*. The Big Bang theory, now a fundamental part of the Standard Model of cosmology, proposes that the Universe began as a hot dense singularity that expanded rapidly, and has been expanding ever since.

During the 1990s experimental evidence showed that the rate of expansion of the Universe is increasing, in conflict with the universally attractive force of gravity that is dominant at local scales [5]. Recent models explain this observation with a Universe that is dominated by an energy of unknown composition, but with the property of negative pressure, thus tending to increase the rate of expansion of the Universe [6].

The composition of the Universe today is often described in terms of the *density parameter*  $\Omega_{\text{tot}}$ . If the Universe has no large-scale curvature, as is strongly implied by recent measurements [1], then  $\Omega_{\text{tot}} = 1$  and  $\Omega_{\text{tot}}$  is dominated by components of mass  $\Omega_m$  and dark energy  $\Omega_\Lambda$

$$\Omega_{\text{tot}} = \Omega_m + \Omega_\Lambda. \quad (1.1)$$

Furthermore, the mass component can be separated into components of baryonic matter  $\Omega_b$  and dark matter  $\Omega_{\text{DM}}$

$$\Omega_m = \Omega_b + \Omega_{\text{DM}}. \quad (1.2)$$

This section discusses estimates of the  $\Omega_m$  and  $\Omega_b$  values that lead to the conclusion that the Universe is dominated by non-baryonic dark matter.

### 1.1.2 Cosmic background radiation

After the formation of light elements in the early universe (Section 1.1.3) the Universe continues to expand and cool, with radiation tightly coupled to matter and unable to escape due to Thomson scattering with free electrons. At an age of  $\sim 380,000$  years the temperature is  $\sim 3000$  K — cool enough for electrons and protons to join to form hydrogen atoms in the process of *recombination*. The Universe thus becomes transparent to radiation and the previously coupled photons escape, travelling virtually unimpeded through space. This relic radiation remains today, though, through the continuing expansion of the Universe, at a reduced temperature of  $\sim 3$  K. This corresponds, for thermal black body radiation, to a spectrum that is largely in the microwave region, leading to this background radiation being named the *Cosmic Microwave Background* (CMB).

The existence of relic radiation from the Big Bang was first predicted in 1948 by Alpher et al. [7]. In 1965, Penzias and Wilson were trying to determine the source of an unexplained background in their 20-foot horn-reflector antenna that was at  $3.5 \pm 1.0$  K and was “isotropic, unpolarised and free from seasonal variations” [8]. Coincidentally, around that time Dicke, Wilkinson, Peebles and Roll were devising an experiment to attempt to measure the CMB. When they heard about the result from Penzias and Wilson it was realised that they were detecting the CMB [9]. The black body radiation of the CMB was later measured to great precision by the COBE satellite borne FIRAS experiment,

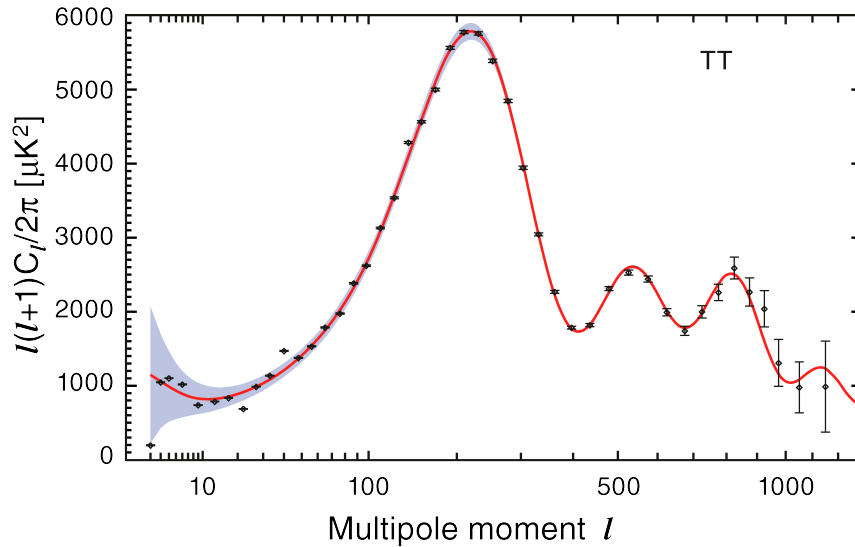
which measured the CMB to be isotropic to a level of  $10^{-5}$  with a temperature of  $2.726 \pm 0.010$  K [10].

Despite this high level of isotropy the CMB is predicted to contain small anisotropies from density perturbations that existed at the time of decoupling of radiation from matter. The CMB measured today therefore contains an image of the mass density of the Universe at a time of  $\sim 380,000$  years after the Big Bang. The COBE satellite was the first experiment to detect the predicted CMB anisotropies in 1992 [11]. In 2001 the Wilkinson Anisotropy Probe (WMAP) was launched and operated for over 9 years observing the CMB anisotropy to extremely high resolution.

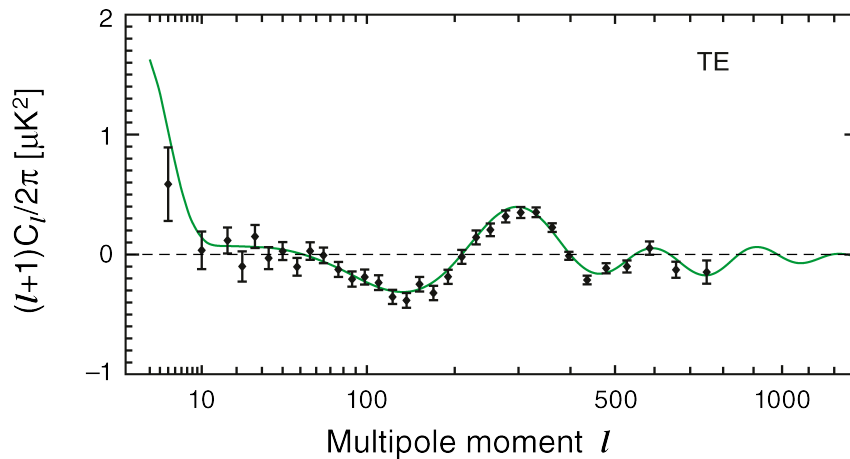
Figure 1.1(a) shows the temperature power spectrum of the CMB background, in terms of angular separation, revealing the spatial structure of the anisotropies. The most dramatic feature of the plot — the large peaks, with the largest at around  $l = 200$ , corresponding to an angular size of about  $1^\circ$  — are *Doppler peaks* caused by *baryonic acoustic oscillation* (BAO) in the early Universe. BAO occurred in the early Universe driven by competition between the repulsive pressure of radiation and the attractive gravitational force of matter. The oscillations caused density perturbations that were ‘frozen-in’ at the time of decoupling resulting in temperature anisotropies with a certain regularity in the CMB. The Doppler peaks therefore contain information on the composition of the Universe, and fitting models of the early Universe to the measured power spectrum provides precise estimates of the matter content of the Universe. The position of the first Doppler peak determines  $\Omega_m = 0.266 \pm 0.029$  and the ratio of the amplitudes of the second-to-first Doppler peaks determines the baryonic density parameter  $\Omega_b = 0.0449 \pm 0.0028$  [1].

The primordial photons are also polarised by the anisotropic Thomson scattering process. While matter and radiation are coupled, the photons continually meet free electrons and no net polarisation is produced. However, at the photon’s last scattering at the time of decoupling, the induced polarisation remains and the subsequently free-streaming photon possesses a quadrupole moment. Figure 1.1(b) shows the measured polarisation of the CMB where the fit to the data provides confirmation of the validity of the models used in determining the cosmological parameters.

Table 1.1 shows a selection of the cosmological parameters that have been determined from measurements of the CMB by the WMAP experiment [1]. These measurements show that the Universe consists of  $73.4 \pm 2.9\%$  dark energy and  $26.6 \pm 2.9\%$  matter, of which only  $4.5 \pm 0.3\%$  is baryonic matter. This discrepancy between total matter and baryonic matter lead to the conclusion that  $\sim 21.5\%$  of the Universe must be in the form of non-baryonic dark matter.



(a) Temperature power spectrum of the cosmic microwave background.



(b) E-mode polarisation of the cosmic microwave background.

FIGURE 1.1: Power spectrum and E-mode polarisation of the CMB from the seven-year WMAP observations. The multipole moment on the x-axis is the Fourier series counterpart to the angular size  $\theta$  where  $l = 0, 1, 2$  are the monopole, dipole, quadrupole etc. and  $l = 100$  corresponds to an angular separation of  $\sim 1^\circ$ . Plots from Jarosik et al. [1].

### 1.1.3 Light element abundances

At approximately three minutes after the Big Bang, the Universe had cooled enough to form stable protons and neutrons, and the Universe was a hot, dense mass of photons, neutrinos, and free neutrons, protons and electrons. Thermodynamical arguments can be used to determine that in this state the proton-to-neutron ratio is  $p/n \approx 7$  [12].

Parameter	Value	Description
$h$	$0.710 \pm 0.025$	Reduced Hubble parameter
$t_0$	$13.75 \pm 0.13$	Age of the Universe in Gyr
$\Omega_b$	$0.0449 \pm 0.0028$	Baryonic matter density parameter
$\Omega_m$	$0.266 \pm 0.029$	Total matter density parameter
$\Omega_\Lambda$	$0.734 \pm 0.029$	Dark energy density

TABLE 1.1: Values from the seven-year WMAP observations [1].

At this time the process of *Big Bang Nucleosynthesis* (BBN) — the formation of light atomic nuclei from protons and neutrons in the early Universe — began.

The BBN period was brief, lasting around 17 minutes until it became too cool for nuclear fusion to continue. During this period protons and neutrons fused to form the stable nuclei of  $^2\text{H}$ ,  $^3\text{He}$ ,  $^4\text{He}$ ,  $^6\text{Li}$  and  $^7\text{Li}$ . The extreme stability of the  $^4\text{He}$  nucleus resulted in essentially all fusion leading to  $^4\text{He}$ , with further fusion rare. Thus essentially all neutrons fused to form  $^4\text{He}$  and, from the initial proton abundance of  $p/n \approx 7$ , the primordial mass fraction of  $^4\text{He}$  is estimated as  $Y_p \approx 0.25$ . The processes that occur during BBN are well understood and the theory also predicts the formation of small amounts of  $^2\text{H}$  ( $\sim 10^{-5}$ ),  $^3\text{He}$  ( $\sim 10^{-5}$ ) and  $^7\text{Li}$  ( $\sim 10^{-10}$ ) during the BBN period.

Assuming the neutron lifetime and the number of neutrino species are well determined [13, 14], the relative abundances of the light elements produced during BBN are determined largely by a single free parameter — the baryon-to-photon ratio

$$\eta = \frac{\text{number density of baryons}}{\text{number density of photons}}. \quad (1.3)$$

For example, a smaller value of  $\eta$  (more radiation in the early Universe), delays the process of fusion such that more neutrons will have decayed to protons before nucleosynthesis begins, resulting in a reduced  $^4\text{He}$  abundance at the end of the BBN period. A lower baryon density also results in fewer  $^2\text{H}$  collisions so that fusion is less complete leading to a higher relative abundance of  $^2\text{H}$ . Similar effects on  $^3\text{He}$  and  $^7\text{Li}$  exist and are well understood. Figure 1.2 shows the predicted abundances of the light elements formed during BBN as a function of  $\eta$ .

At the end of the BBN process, approximately 20 minutes after the Big Bang, the Universe is too cool for nuclear fusion to occur and these elemental abundances are fixed. From this time to the present day only the decay of radioactive products of BBN and the production/destruction of light elements in stars have the potential to change these abundances. Therefore, estimates of the primordial abundances of the light elements based on measurements of their abundances today allow estimates of  $\eta$ .

The baryon-to-photon ratio is in turn related to the baryon density parameter by

$$\Omega_b h^2 \approx 3.65 \times 10^7 \eta \quad (1.4)$$

where  $h$  is the dimensionless reduced Hubble parameter

$$h = \frac{H_0}{100 \text{ km s}^{-1} \text{ Mpc}^{-1}}. \quad (1.5)$$

The  ${}^4\text{He}$  abundance has been determined from measurements of the  ${}^4\text{He}/\text{H}$  ratio in regions of hot ionised gas in galaxies. Currently the best measurement comes from a survey of 45 low-metallicity H II regions giving a primordial  ${}^4\text{He}$  abundance of  $Y_p = 0.249 \pm 0.009$  [15]. This estimate, and the  $\eta$  value implied by it, are shown in the top section of Figure 1.2.

The  ${}^2\text{H}$  (deuterium) abundance, also measured experimentally, is of particular interest because there is no known process of producing it in significant quantities outside of the Big Bang. Systematic errors on projections from present day measurements to primordial values are, therefore, small. Presently the best measurements of  ${}^2\text{H}$  abundances are obtained from measurements of the Lyman alpha forest. Pettini et al. determine a value of  $\log(D/H)_p = -4.55 \pm 0.03$ . This estimate, and the  $\eta$  value implied by it, are shown in the middle section of Figure 1.2.

The combined estimates of the primordial  ${}^2\text{H}$  and  ${}^4\text{He}$  abundances result in a predicted baryon density of

$$0.038 \leq \Omega_b \leq 0.047 \text{ (95\% CL)}. \quad (1.6)$$

Shown in the bottom section of Figure 1.2 is the current estimate of the primordial  ${}^7\text{Li}/\text{H}$  abundance, inferred from observations of metal-poor stars. It can be seen that this leads to an estimate of the baryon density parameter that is incompatible with those obtained from  ${}^2\text{H}$  and  ${}^4\text{He}$  abundances, and with the CMB measurements [16]. This discrepancy may be due to systematic errors in observations, or due to uncertainties in the chemical evolution and stellar astrophysics used to extrapolate from present day to primordial abundances.

Despite the lithium discrepancy, the concordance between the  ${}^2\text{H}$  and  ${}^4\text{He}$  abundance predictions from BBN, and the independent predictions from the CMB measurements, which rely on entirely different physical processes, is quite remarkable. Combined, these theories are extremely convincing evidence that baryonic matter makes up only a small fraction of the Universe, implying the existence of vast quantities of dark matter in the Universe.

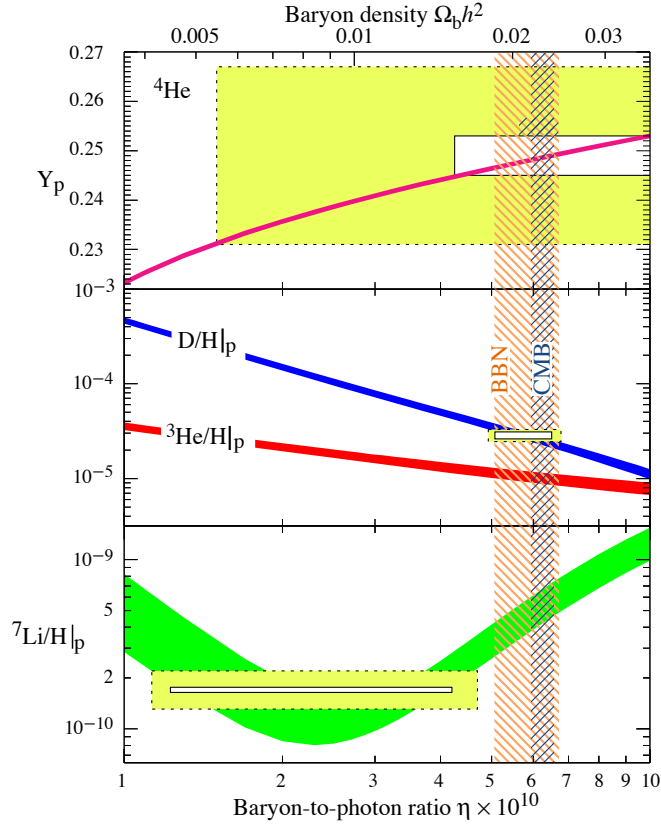


FIGURE 1.2: Solid bands show the 95% C.L. range of the abundances of  ${}^4\text{He}$ , D,  ${}^3\text{He}$  and  ${}^7\text{Li}$  as predicted by Standard Model BBN. The white and yellow boxes show primordial abundances consistent with observation with  $\pm 2\sigma$  statistical errors and  $\pm 2\sigma$  statistical *and* systematic errors respectively. The two vertical bands indicate the  $\eta$  values predicted by BBN and the CMB, each at 95% C.L. This figure shows that the BBN predictions of relative abundances are in agreement with experimental data and that the inferred  $\Omega_b$  value is in agreement with that from CMB measurements. Image from Nakamaru et al. [13].

#### 1.1.4 Large-scale structure formation

The early Universe was hot, dense, and very nearly homogeneous. The Universe today, however, has structure — dense matter clusters separated by large voids — on the scales of galaxies, clusters of galaxies and galaxy filaments.

Structure formation cosmology is the study of how the structure that is observed today could have formed from initial homogeneity. It is believed that structure began with quantum density fluctuations in the very early Universe that got expanded during inflation. These small density fluctuations then seeded structure in a ‘bottom-up’ fashion with small structures forming first and then combining to form larger structures [17]. Although the initial linear growth of density perturbations can be calculated analytically, the following build-up of structure is highly non-linear and models require direct numerical simulation [18].

The Millennium Simulation Project have performed large-scale, high resolution structure formation simulations to determine the growth of structure in galaxies. The Millennium Simulation models the Universe as  $\sim 10^{10}$  particles, of mass  $\sim 10^9 M_\odot$  in a cube of side 2 billion light-years [19], whereas the Millennium-II Simulation is at a higher resolution with  $\sim 10^{10}$  particles of mass  $\sim 10^7 M_\odot$  in a cube of side 400 million light-years [20]. The simulations have successfully modelled the formation of structure from an almost homogeneous and isotropic universe at the time of decoupling to a universe containing structure consistent with that which is observed in the Universe today. Successful structure formation models, however, require a universe that is dominated by non-interacting, non-relativistic dark matter — a baryonic universe does not produce structure consistent with observations. The simulations therefore provide further independent evidence that the Universe is dominated by dark matter.

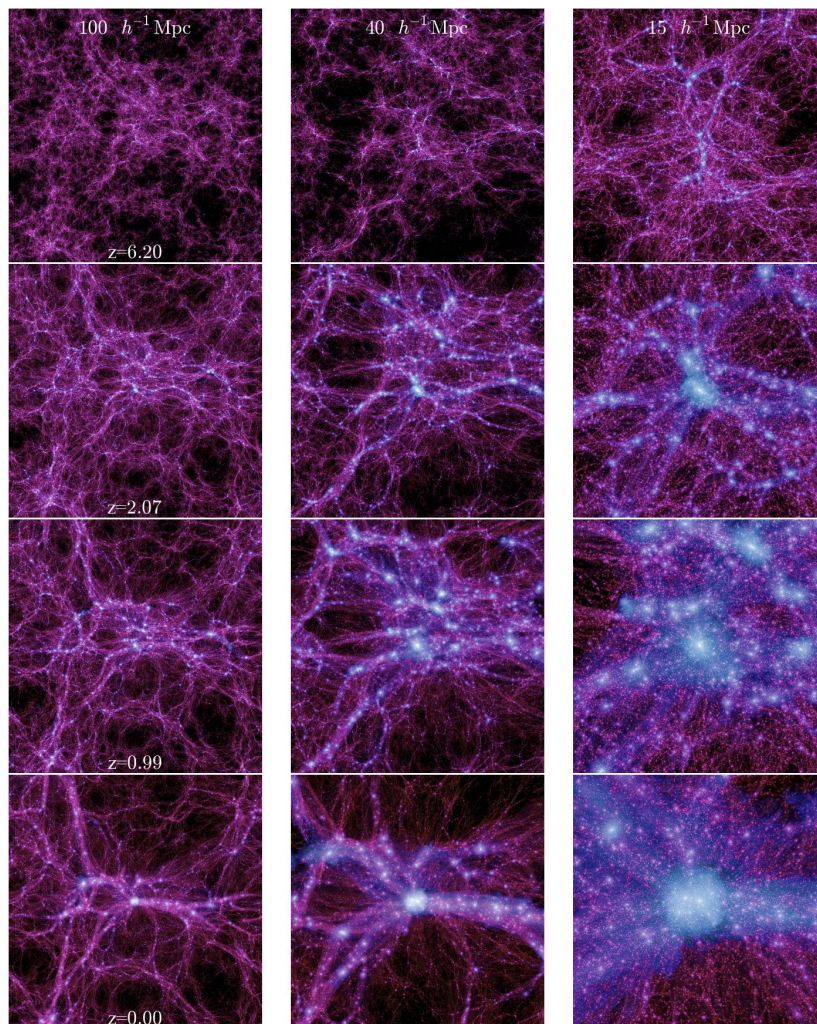


FIGURE 1.3: Time evolution of a dark matter halo in the Millennium-II Simulation. The halo is shown with increasing scales (from left to right: 100, 40, and  $15 h^{-1} \text{Mpc}$ ) and with increasing time (from top to bottom:  $z=6.2$ , 2.07, 0.99, and 0). Image from Boylan-Kolchin et al. [20].

## 1.2 Evidence for dark matter in galaxies and galaxy clusters

### 1.2.1 Virially bound systems

In 1933 Fritz Zwicky, of the California Institute of Technology, used redshift measurements to determine the individual velocities of 8 galaxies in the Coma Cluster, a nearby cluster of over 1,000 galaxies at a mean distance of  $\sim 100$  Mpc from Earth [21, 22]. He measured large differences in the velocities, with a velocity dispersion of  $\sigma = 1019 \pm 360 \text{ km s}^{-1}$  (in agreement with the more recent measurement of  $1082 \text{ km s}^{-1}$ , determined from the redshifts of 465 cluster members [23]).

Zwicky realised that if the Coma Cluster is assumed to be a mechanically stationary state, with its mass uniformly distributed within it, then the virial theorem can be applied to the velocity measurements to determine the total mass of the galaxy cluster. For a statistically steady, spherical, self-gravitating system, the virial theorem states that

$$E_{\text{KE}} = -\frac{1}{2}E_{\text{PE}}. \quad (1.7)$$

For a galaxy cluster of radius  $R$ , containing  $N$  galaxies of average mass  $m$ , with a mean velocity  $\sqrt{\langle v^2 \rangle}$  the total kinetic energy  $E_{\text{KE}}$  is approximated by

$$E_{\text{KE}} = \frac{1}{2}M\langle v^2 \rangle, \quad (1.8)$$

where  $M = Nm$ , and the total gravitational potential energy  $E_{\text{PE}}$  by [22]

$$E_{\text{PE}} = -\frac{3}{5}\frac{GM^2}{R}. \quad (1.9)$$

Equation 1.7 therefore provides an estimate for the total mass of the cluster  $M$  as

$$M = \frac{5R\langle v^2 \rangle}{3G}. \quad (1.10)$$

Zwicky used this equation to determine the *dynamic mass* of the Coma Cluster to be

$$M \approx 4.5 \times 10^{13} M_{\odot}. \quad (1.11)$$

Zwicky also deduced the mass of the Coma cluster by the light emitted from the galaxy cluster. He determined that the cluster contained  $\sim 1000$  galaxies, each with an average luminosity of about  $8.5 \times 10^7$  times the luminosity of the Sun. Assuming a mass-to-light ratio equal to that in the local solar neighbourhood,  $\gamma = 3$ , the *luminous mass* was

calculated as [24]

$$M \approx 2.6 \times 10^{11} M_{\odot}. \quad (1.12)$$

Zwicky was troubled by the large discrepancy, over two orders of magnitude, between the dynamic mass and the luminous mass of the Coma Cluster. Writing in 1933, he commented that “If this would be confirmed we would get the surprising result that dark matter is present in much greater amount than luminous matter”. This work by Zwicky is widely considered as the first evidence for the existence of missing matter.

Recent advances in astronomy techniques, such as x-ray telescopes that reveal clouds of hot gas by their x-ray emissions, and infra-red telescopes revealing dust clouds, have led to a significant revision of Zwicky’s result, but with the same problem that the majority of the mass in the Coma cluster is unaccounted for by visible matter. Current estimates determine the composition of the cluster to be 85% dark matter, 13% hot intracluster medium and 2% stars [25]. The virial techniques first used by Zwicky have also been applied to many other galaxy clusters, in each case revealing a dynamic mass that is many times greater than the luminous mass [26].

## 1.2.2 Galaxy rotation curves

Zwicky’s claims of *missing matter* in the Coma Cluster went largely unnoticed until the 1970s, when measurements of the rotation of spiral galaxies provided further, more convincing, evidence for missing matter in individual galaxies.

Spiral galaxies are stable, gravitationally bound systems. Their visible mass consists primarily of stars, gas and dust that orbit the Galactic Centre in almost circular orbits. If an object, such as a star or gas cloud, is at a distance  $r$  from the Galactic Centre with a circular orbit of velocity  $v$  encircling a mass  $M(r)$ . In order for the system to be stable (and hence in existence today) the centripetal acceleration of this object  $v^2/r$  must equal the inward force of gravity  $GM(r)/r^2$ . This gives Kepler’s law

$$v = \sqrt{\frac{GM(r)}{r}}. \quad (1.13)$$

A *galaxy rotation curve* is a plot of the orbital velocities of objects, in the disc of a spiral galaxy as a function of their distance from the Galactic Centre. From Equation 1.13, such a plot is expected to fall as  $1/\sqrt{r}$ . Galaxy rotation curves of the Andromeda galaxy measured by Rubin and Ford in 1970 [27], and by Roberts and Whitehurst in 1975 [28], however, showed a rotation curve with no sign of the expected Keplerian drop-off. The orbital velocity instead was measured to be approximately constant from  $\sim 5$  kpc to

beyond the visible mass of the galaxy at  $\sim 30$  kpc. A more recent measurement of the rotation curve of the NGC3198 spiral galaxy in the constellation Ursa Major is shown in Figure 1.4. The dashed line labelled ‘disk’ shows the expected rotation curve from the luminous matter, while the solid line shows the fit of the measured velocities. The simplest conclusion from this data is that there is a large, diffuse halo of unseen mass that encompasses, and extends beyond, the visible disc of the galaxy. The dark matter halo required to give the observed orbital velocities is given by the dotted line labelled ‘dark halo’ in Figure 1.4.

Rotation curves have been produced for many spiral galaxies, of various types, all with the same conclusion — that the rotation curves do not follow the  $v \propto 1/\sqrt{r}$  relationship that would be expected if their mass was dominated by luminous matter, but instead remain approximately flat to large  $r$ , implying the existence of large quantities of unseen matter [29, 30].

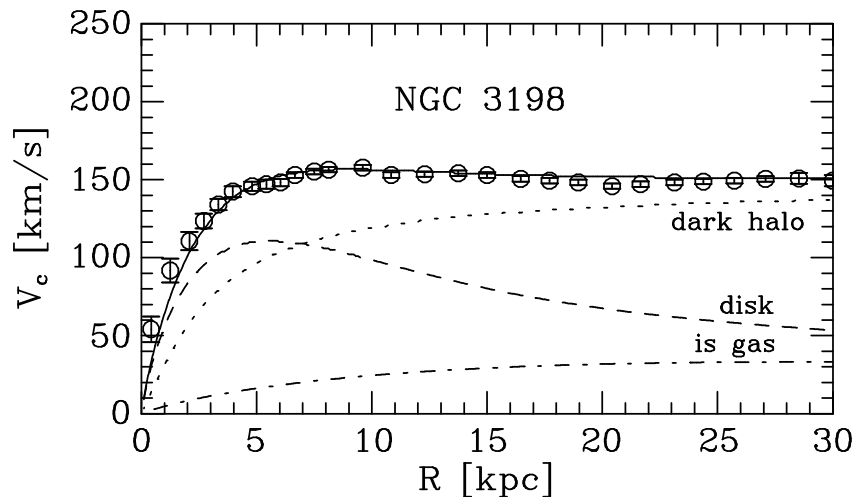


FIGURE 1.4: Decomposition of the NGC3198 spiral galaxy. The dashed line labelled ‘disk’ shows the rotation curve expected from the visible matter of the galaxy. The dotted line labelled ‘dark halo’ is the required effect of dark matter in order for the curve of the visible matter to match the observed rotation curve shown by the data points and fitted solid line. Plot from Fuchs [29].

### 1.2.3 Gravitational lensing

A consequence of Einstein’s general relativity is that energy density (matter) causes curvature of spacetime, so that the path of a photon of light can be altered by a gravitational field [31]. A result of this is that large celestial bodies can act as a *gravitational lens*, affecting the path of photons in its vicinity. This effect can be used to determine the mass of a *lensing object* providing a *source object* (a radiation emitting object such

as a planet, star, galaxy, hot gas cloud or quasar) exists beyond it. The effects that a gravitational lens can have on the observed image of a source object range from subtle changes in apparent brightness to large distortions, magnification and duplication of the image. The extent of the effects depend on the relative position of the source, lens and observer, and on the mass and shape of the lens. Gravitational lensing is particularly useful for the probing of dark matter because the lensing effects are independent of the type of radiation of the source object and independent of the composition of the lens object.

**Strong lensing** — Strong gravitational lensing occurs in systems with massive gravitational lenses and good alignment between the source object and the lens. Strong lensing can cause dramatic effects to the image of the source object such as multiple images, arcs and ring-like image deformations called *Einstein rings* [32]. Figure 1.5 shows an image of the Abell 1689 galaxy cluster in which strong lensing effects can be seen. The SLACS collaboration use data from the Sloan Digital Sky Survey (SDSS) to identify strong lensing candidates. Strong lensing techniques are then applied to data from the Hubble Space Telescope ACS for these candidates. A survey of 15 galaxies revealed in each case gravitational fields consistent with the visible disc being at the centre of an approximately spherical, isothermal dark matter halo [33].

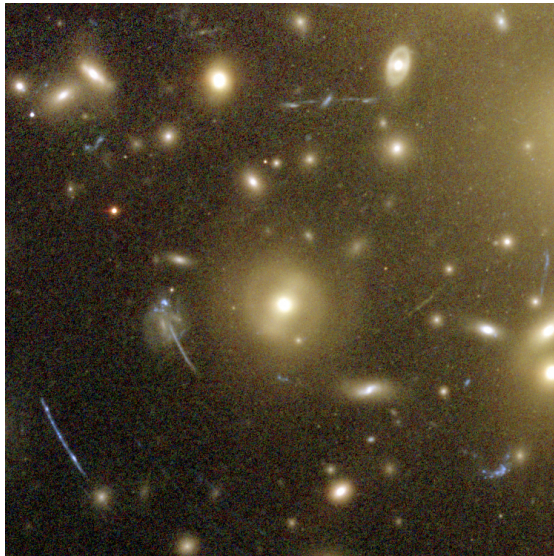


FIGURE 1.5: Image of strong gravitational lensing from the Abell 1689 galaxy cluster showing large distortions and Einstein rings. Image from the Hubble Space Telescope website [34].

**Weak lensing and the Bullet cluster** — Weak lensing techniques are used when the lensing object is less massive, causing less drastic distortion of the source object in the form of magnification and shear. Weak lensing involves a statistical estimate of ellipticities in background galaxies caused by lensing effects. The Sloan Lens ACS

(SLACS) Survey used weak lensing techniques in a survey of 22 galaxies and determined an average mass density profile that is consistent with the existence of an isothermal dark matter halo (i.e.,  $\rho \propto r^{-2}$ ) that extends to a distance of over  $300h^{-1}$  kpc, ( $\sim 100$  effective radii) [35]. This extends by an order of magnitude the galaxy rotation measurements from visible matter discussed in Section 1.2.2, adding further evidence for the existence of a dark matter halo that extends way beyond the visible matter of the galaxy.

The first direct, model independent proof of the existence of dark matter was claimed in 2006 from observations using weak lensing techniques of 1E 0657-558, a merger of two galaxy clusters more commonly known as the *Bullet Cluster*. Clowe et al. created a map of the total mass/energy distribution of the colliding galaxy clusters by applying weak gravitational lensing techniques to a wide range of optical images from ground based telescopes and the Advanced Camera for Surveys (ACS) on the Hubble Space Telescope [36]. The distribution of mass is shown by the green contour lines of Figure 1.6(a). It can be seen that these lines roughly trace the distribution of the visible galaxies, which themselves contribute only  $\sim 2\%$  of the mass of the system [37]. The x-ray emission spectra of the Bullet Cluster was also mapped using data from the Chandra X-ray Observatory. Since the hot, x-ray emitting intracluster medium (ICM) accounts for  $>90\%$  of the baryonic mass of the clusters, this provides a map of the baryonic matter distribution of the cluster system.

The composite image of Figure 1.6(b) shows a clear separation between the total mass of the system, indicated by the green contour lines, and the baryonic mass indicated by the coloured cloud. The observation is explained by the hypothesis that the two galaxy clusters are in the process of colliding. As the galaxy clusters collide and pass through each other the x-ray emitting ICM of each cluster collides and interacts strongly. The ICM heats up and is slowed down by the drag force, the effect of which is visible in the bow shock structure of the x-ray images in Figure 1.6(b). The collisionless dark matter on the other hand (the majority of the total mass of the structure) along with the optically visible parts of the galaxy (the stars, of negligible mass) travel through unaffected. The validity of this hypothesis has been confirmed by simulations [38].

The Bullet cluster observation is further compelling evidence for the existence of dark matter in galaxy clusters. More recently examples of this phenomenon have been observed at other colliding galaxy cluster sites including MACS J0025.4-1222 [39] and Cl 0024+17 [40] in which the collision is occurring along the line of sight of an observer on Earth.

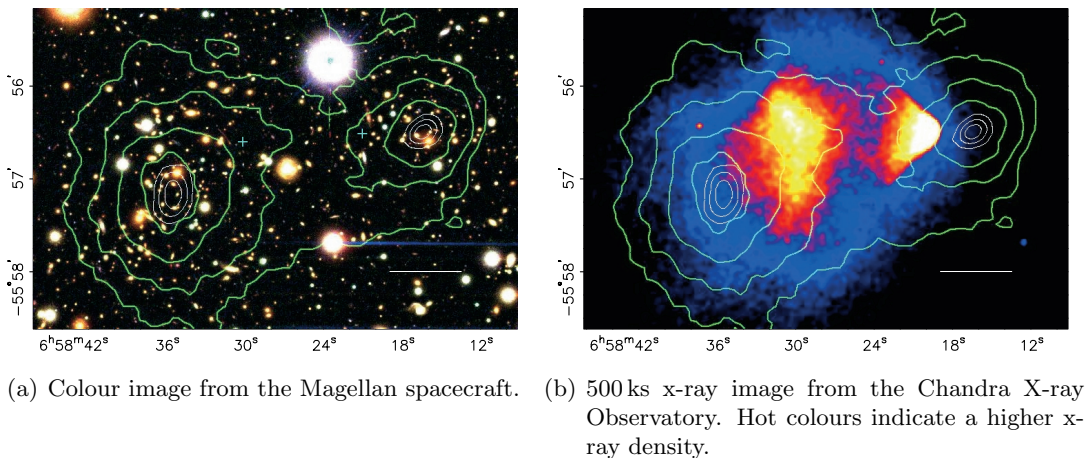


FIGURE 1.6: Images of the Bullet cluster. Green lines are mass contours from weak lensing analysis. White bar indicates 200 kpc at the distance of the cluster. Images from Clowe et al. [36].

### 1.3 Dark matter particles

One highly motivated explanation to the observations of the previous sections is the existence of non-baryonic cold dark matter (CDM) particles. Candidate particles must be cold, i.e. non-relativistic at the time of decoupling, so as not to smooth out small-scale structure formation in the early Universe and dark, i.e. not electromagnetically interacting, explaining why it has not yet been detected. In addition any particle must have been produced in sufficient quantity in the early Universe, and must be stable enough that it is still in existence today.

There are no particles within the Standard Model of particle physics that satisfy all of these criteria, and the exact nature of the CDM remains one of the biggest questions in physics today. A review of dark matter candidates can be found at e.g. [41, 42]. For the remainder of this thesis, however, the focus will be on the highly motivated hypothesis that dark matter consists of a class of particles known as *weakly interactive massive particles*, or WIMPs.

#### 1.3.1 WIMPs

To account for the observed cosmological density of  $\Omega_m \approx 0.3$ , WIMPs are required to have interaction strengths on the scale of the electroweak interaction [43]. Since they are weakly interacting, the WIMP mass is determined by the mass scale of the weak interaction, i.e. the Z boson of mass  $\sim 90 \text{ GeV } c^{-2}$ . WIMPs are therefore assumed to have a rest mass on the order of 10 to 1000  $\text{GeV } c^{-2}$ .

Although there is no particle within the Standard Model with the required properties, there are a wide range of extensions to the Standard Model that produce WIMP-like particles. These include the Lightest Supersymmetric Particle (LSP) in Supersymmetry (SUSY) models [43], the Lightest Kaluza-Klein Particle (LKP) in Universal extra dimension (UED) models [44], or the lightest T-odd particle (LTP) in Little Higgs models [45, 46]. SUSY is currently a favoured extension to the Standard Model, which predicts the existence of a WIMP-like particle in the form of a Majorana fermion that is a superposition of the SUSY partners of the electroweak gauge bosons (gauginos) and Higgs particles (Higgsinos).

If WIMPs are to exist with sufficient abundance to account for the missing matter they must have some non-zero coupling to ordinary baryonic matter [43]. Elastic scattering of WIMPs with atomic nuclei is therefore a potential means of direct detection of WIMPs on Earth. WIMP-WIMP annihilations are also theoretically expected to offer a means of indirect detection through detection of annihilation products. Methods of direct and indirect WIMP detection will be discussed in Section 1.4.

### 1.3.2 WIMP halo characteristics

The simplest models that can account for the galaxy rotation curve observations, and are compatible with structure formation simulations, suggest that WIMPs exist in the form of an approximately spherical, isothermal halo, with the visible matter of the galaxy concentrated in a disc at the centre. This section discusses the kinematics of the WIMP halo.

**WIMP velocity distribution** — There is little experimental data on the velocity distribution of WIMPs in the local halo. The simplest models use the assumption that WIMPs are trapped in the potential well of the Milky Way and have had time to reach thermal equilibrium but, due to the almost collisionless nature of the WIMPs, do not form a disk as seen in the visible matter of a galaxy. Instead the WIMPs form an approximate spherically symmetric halo that is modelled as a collisionless *Boltzmann gas* with WIMPs throughout the halo exhibiting a velocity distribution given by the Maxwell-Boltzmann distribution. This can be expressed as

$$f(v) = \frac{4\pi v^2}{(2\pi/3)^{3/2} v_{\text{rms}}^3} e^{-\frac{3v^2}{2v_{\text{rms}}^2}} \quad (1.14)$$

where  $v_{\text{rms}}$  is the *velocity dispersion*, related to the local circular speed  $v_0$  ( $\sim 230 \text{ km s}^{-1}$ ) by  $v_{\text{rms}} = \sqrt{3/2} v_0$ .

The velocity distribution must be truncated at the galactic escape velocity, as WIMPs with velocities above this would have escaped the gravitation of the galaxy. There are large uncertainties in the galactic escape velocity with estimates ranging from around  $v_{\text{esc}} = 450$  to  $650 \text{ km s}^{-1}$  [47, 48]. The value of  $v_{\text{esc}} = 600 \text{ km s}^{-1}$  is commonly used by dark matter detection experiments and will be assumed throughout this thesis.

**Target velocity relative to the WIMP halo** — On average the WIMP halo is stationary, with no co-rotation about the Galactic Centre. The mean WIMP velocity relative to the target is therefore determined by the motion of the target on Earth through the WIMP halo. This motion is dominated by the galactic rotation but, as shown in Figure 1.7, consists of four components. The velocity of Earth  $v_E$ , relative to the WIMP halo, can be expressed in galactic coordinates as

$$\vec{v}_E = \vec{u}_r + \vec{u}_S + \vec{u}_E, \quad (1.15)$$

where  $\vec{u}_r$  is the velocity of the Local Standard of Rest (LSR)

$$\vec{u}_r = (0, 230, 0) \text{ km s}^{-1}, \quad (1.16)$$

$\vec{u}_S$  is the motion of the Sun relative to the LSR

$$\vec{u}_S = (9, 12, 7) \text{ km s}^{-1}, \quad (1.17)$$

and  $\vec{u}_E$  is Earth's orbital velocity relative to the Sun, given by [49]

$$\vec{u}_E = \langle u_E \rangle [1 - e \sin \lambda - \lambda_o] (\cos \beta_x \sin (\lambda - \lambda_x), \quad (1.18)$$

$$\cos \beta_y \sin (\lambda - \lambda_y), \quad (1.19)$$

$$\cos \beta_z \sin (\lambda - \lambda_z)) \text{ km s}^{-1}. \quad (1.20)$$

where  $\beta$  and  $\lambda$  are the ecliptic latitudes and longitudes respectively of the  $x$ ,  $y$ , and  $z$  axis in galactic coordinates and  $\langle u_E \rangle = 29.79 \text{ km s}^{-1}$  is the mean orbital velocity of Earth. A practical approximation of  $v_E$  is [49]

$$v_E = 244 + 15 \sin (2\pi y) \text{ km s}^{-1} \quad (1.21)$$

where  $y$  is the elapsed time from 2 March in years.

In addition to this, as shown in Figure 1.7, the spinning of the Earth of its axis results in the direction of the WIMP wind varying significantly over the course of a day. For a detector positioned optimally at a latitude of  $45^\circ$  the WIMP wind direction oscillates

over  $90^\circ$ , from e.g. passing from left to right across the detector at midday, to passing from top to bottom through the detector at midnight.

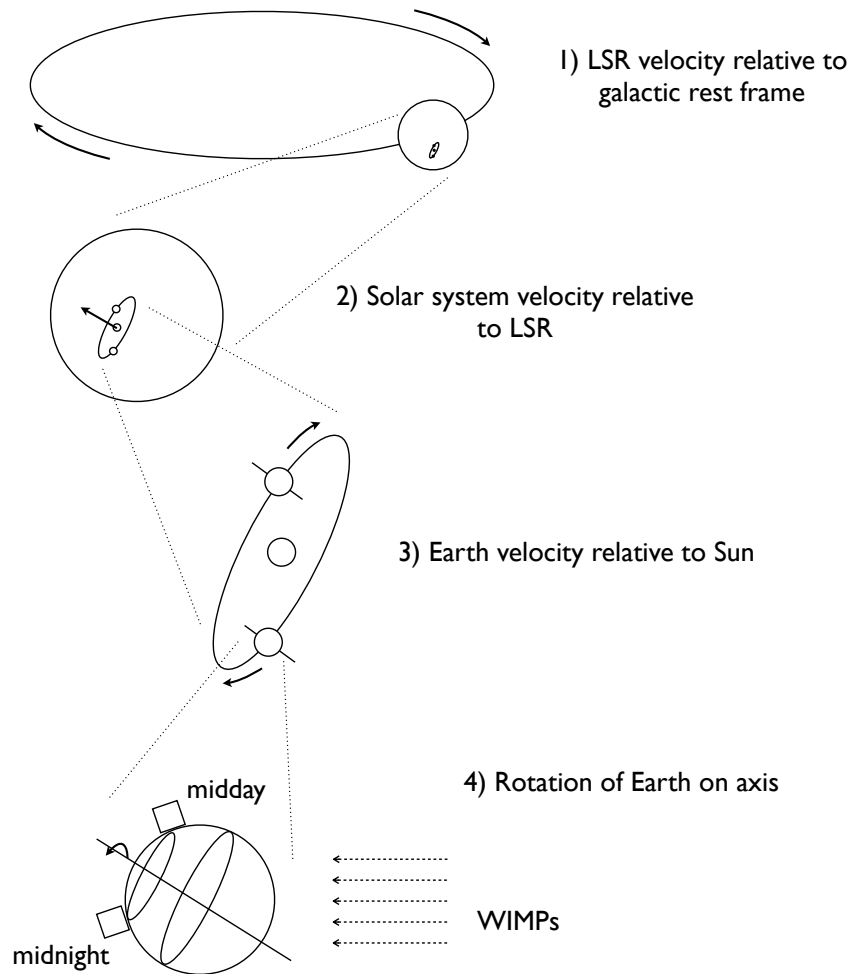


FIGURE 1.7: Components determining the speed and direction of the ‘WIMP wind’. 1) The orbit of the LSR about the Galactic Centre. 2) The ‘peculiar motion’ of our solar system relative to the LSR. 3) The orbit of the Earth about the Sun. 4) The spinning of Earth on its axis.

**WIMP density distribution** — The local density of WIMPs is an essential parameter for the detection of WIMPs. The simplest model of the WIMP density distribution that fits the observed data is an isothermal distribution given by

$$\rho(r) \propto \frac{1}{r^2}. \quad (1.22)$$

This produces the required flat rotation curves at moderate radii but has a singularity at the core and produces a diverging total mass. The following model produces a more realistic mass distribution by forcing a core of constant density within a small core radius

of  $r_0$

$$\rho(r) = \frac{\rho_0}{1 + \left(\frac{r}{r_0}\right)^2}. \quad (1.23)$$

The local WIMP density  $\rho_0$  is one of the most important parameters in determining the expected event rate. When a simplistic isothermal sphere is assumed estimates for  $\rho_0$  are in the range  $0.2$  to  $0.4 \text{ GeV c}^{-2} \text{ cm}^{-3}$  [49]. However, more recent observations suggest that the halo is not spherically symmetric but is flattened. This leads to predictions for  $\rho_0$  with large inconsistencies but generally higher values in the range of  $0.2$  to  $0.7 \text{ GeV c}^{-2} \text{ cm}^{-3}$  [50]. For consistency with previous and competing experimental results, however,  $\rho_0 = 0.3 \text{ GeV c}^{-2} \text{ cm}^{-3}$  has become the assumed density of choice for dark matter detection experiments, and will be the assumed value in this thesis.

## 1.4 WIMP dark matter searches

### 1.4.1 Search for WIMPs by indirect detection

The majority of WIMP candidates are Majorana particles such that WIMP-WIMP annihilations resulting in detectable Standard Model particles are predicted [43]. These WIMP annihilation products may result in detectable signals on Earth, offering a means of indirect detection of dark matter WIMPs. Some potential signals and experimental results are discussed here.

**Neutrinos from the Sun** — Halo WIMPs may, as they pass through the Sun, interact with protons and helium nuclei causing the WIMPs to lose energy and become captured by the Sun. As a result, thermalised WIMPs may accumulate in the Sun. At a sufficient WIMP density, WIMP annihilation may form a number of Standard Model particles such as quarks and leptons, or, if the WIMPs are heavy enough, gauge and Higgs bosons and top quarks. Most of these decay products will be absorbed by the Sun but some could produce energetic neutrinos detectable on Earth. Neutrino energies would be broadly distributed about  $\frac{1}{3}m_\chi$  to  $\frac{1}{2}m_\chi$ , i.e. 10s to 100s of GeV, making them separable from solar neutrinos with energies in the MeV range. The Super-Kamiokande (Super-K) neutrino observation experiment has searched for such WIMP-WIMP annihilation products from the Sun, as well as from the centre of the Earth and the Galactic Centre, and found no excess above expected atmospheric levels [51].

**Cosmic rays from WIMP annihilation in the halo** — Annihilation of WIMPs in the dark matter halo may form products that result in anomalous cosmic rays detectable on Earth. Although the propagation of cosmic rays in the galaxy is not well understood, leading to difficulty in separation of WIMP-WIMP annihilation cosmic rays

from standard background sources, the known cosmic ray positron background is predicted to decrease slowly with increasing energies. The Payload for Antimatter/Matter Exploration and Light-nuclei Astrophysics (PAMELA) experiment, however, has recently detected a significant increase in the positron fraction in the 1.5 to 100 GeV region as shown in Figure 1.8 [52]. The result suggests an unknown source which could be attributed to positrons produced in WIMP-WIMP annihilations either directly or via hadronisation followed by decay of charged pions. In addition the Advanced Thin Ionization Calorimeter (ATIC) instrument [53], the FERMI Large Area Telescope [54] and High Energy Stereoscopic System experiment (HESS) [55] have all detected significant excesses in electron flux compared to predicted background in the energy region of 100 GeV to 1000 GeV energy.

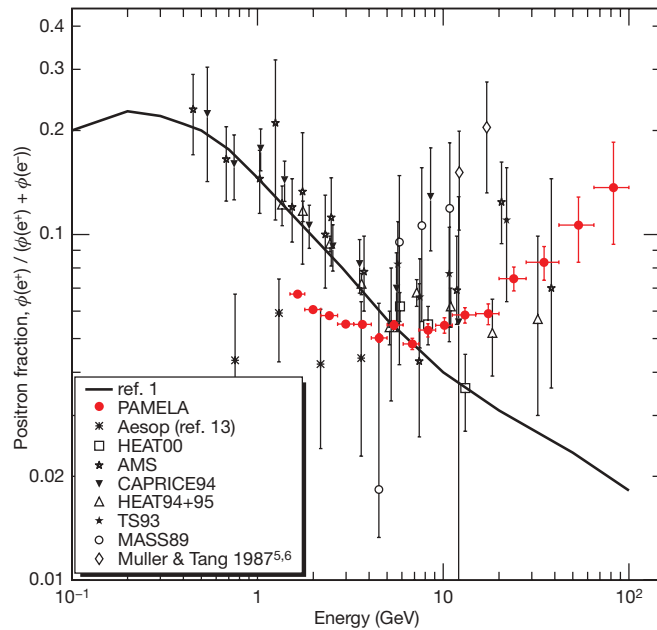


FIGURE 1.8: Measurements of cosmic positron abundance from the PAMELA collaboration showing excess positrons at high energy. Plot from Adriani et al. [52].

There presently remains significant discrepancies between these results such that no clear dark matter candidate can be predicted. In addition, the dark matter required to account for the PAMELA and ATIC results require interaction rates orders of magnitude larger than those currently predicted for WIMPs [56]. Though these may be hints to the existence of dark matter in the galaxy, the results demonstrate the difficulties caused by the poorly understood cosmic ray backgrounds, and highlight the need for less ambiguous direct detection experiments.

### 1.4.2 Search for WIMPs by direct detection

Although WIMPs do not interact electromagnetically or by the strong nuclear force, they are predicted to elastically scatter off atomic nuclei, resulting in potentially detectable nuclear recoils (Section 2.1). The expected nuclear recoil energy spectrum, however, decreases exponentially with energy, and has no characteristic features (Section 2.1.7). In addition, ambient neutrons and gamma-rays produce interactions with energies in the regions expected from WIMP-induced nuclear recoils, and typically with rates many orders of magnitude higher. The biggest challenge in direct dark matter detection is the reduction and discrimination of background events from the potential WIMP-induced nuclear recoil signal.

Backgrounds for dark matter detectors exist in two main forms: gamma-rays, that cause electron recoils, and neutrons that cause nuclear recoils. As will be discussed further in Section 2.2, electron recoils are generally far more numerous, but can be rejected using discrimination techniques, whereas neutron backgrounds produce events identical to the expected WIMP-induced nuclear recoils, and therefore must be eliminated from the detector. Having minimised detector backgrounds and estimated the rate of remaining WIMP-mimicking backgrounds, experiments are operated in a controlled state for a period of time. Any events detected above the expected background are candidates for WIMP-induced nuclear recoils. If no WIMP signal is seen, limits can be placed on allowed WIMP masses and cross-sections based on the fact that they have failed to cause detectable interactions in the experiment.

There are various target materials in use in direct dark matter detection experiments. Some of the leading dark matter search experiments use a target of liquid noble gas. These include ZEPLIN-III [57] and XENON100 [58], which search for WIMP-induced nuclear recoils in liquid xenon. Similarly sensitive experiments such as CDMS-II [59] and EDELWEISS-II [60] look for WIMP-induced nuclear recoils in semiconductor crystals at mK temperatures. Figure 1.9 shows the upper bounds on the WIMP-nucleon interaction cross-sections that have been determined by null results from these experiments.

Recently the CRESST-II collaboration, operating a cryogenic direct detection experiment with a target of  $\text{CaWO}_4$  crystals, published results of an exposure in which 67 events were detected with a background prediction of a maximum of 38 events [63]. A  $4\sigma$  discrepancy is claimed, that could be explained by nuclear recoils from low mass WIMPs as illustrated in Figure 1.9. CDMS-II and EDELWEISS-II also detect events above their predicted background rate. The CDMS-II experiment, detected 2 events with an expected background of  $0.9 \pm 0.2$  events [59] and the EDELWEISS-II experiment, predicted less than 3 events, with energies above 20 keV, but detected 5 [60].

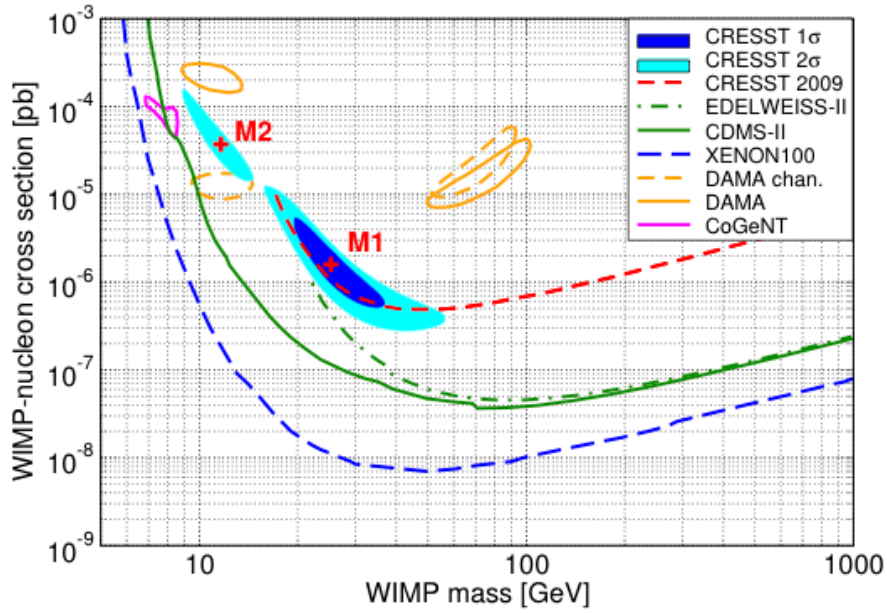


FIGURE 1.9: Limit plot showing current upper bounds on WIMP-nucleon interaction cross-sections. Exclusion limits from EDELWEISS-II [60] (green dot-dashed), CDMS-II [59] (green solid) and XENON100 [58] (blue dashed). Also shown are 90% C.L. regions favoured by CoGeNT [61], DAMA [62] and CRESST-II [63]. Plot from Angloher et al. [63].

In these cases the excess signal is assumed to be unaccounted for background events and null detection limits are presented. Positive dark matter detections have also been claimed by the DAMA and CoGeNT collaborations. The predicted WIMP masses and cross-sections of these experiments, discussed further in Section 1.4.3, are shown in Figure 1.9.

Despite detecting events characteristic of the predicted WIMP-induced nuclear recoils, each collaboration is cautious to claim a dark matter detection due to the difficulty in excluding all terrestrial sources of background in the detectors. The uncertainty in such results presents a strong argument for a dark matter detection method that allows discrimination between recoils from terrestrial sources and recoils from WIMPs by showing that the nuclear recoils are of galactic origin.

### 1.4.3 Galactic signals

As described in Section 1.3.2 the mean velocity of WIMPs as seen by an Earth bound detector depends on the motion of the Earth through the WIMP halo. The Earth can therefore be thought of as being subject to a ‘WIMP wind’ with a velocity that is determined by the path of the Earth through the halo.

**Annual modulation** — As shown in Figure 1.7, the Earth’s orbit of the Sun adds a component to the WIMP wind velocity that will vary with a period of one year. From Equation 1.21 it is seen that the result is a sinusoidal velocity modulation with an amplitude of  $\sim 6\%$ , a period of 1 year and a maximum on around 2 June. Assuming an isothermal, spherically symmetric WIMP halo, this modulation in WIMP velocity results in an expected WIMP detection rate that exhibits a sinusoidal modulation of around  $\sim 3\%$  with a period of one year [47].

The DAMA/NaI, and subsequent DAMA/LIBRA experiment, which use high radiopurity NaI(Tl) scintillators, differs from the the previously mentioned detectors in that it does not attempt to discriminate between electron recoils and nuclear recoils. Instead the collaboration focus on minimising all backgrounds and controlling systematics. The group then searches for the predicted small modulation on top of an overall large event rate. The DAMA collaboration claim a positive result with an  $8.9\sigma$  confidence limit, having detected, over a combined exposure period of  $\sim 13$  years, an annual modulation in the event rate that is consistent with predictions. The event rate modulation is sinusoidal, with a period of one year peaking on  $\sim 2$  June with a modulation amplitude of  $< 7\%$  of the total event rate [62]. In addition the modulation is only present in low  $E$  interactions, and only in ‘single-hit events’ characteristic of WIMP interactions.

More recently the CoGeNT collaboration, from 15 months of data operating a germanium dark matter detector, has similarly claimed detection of an annual modulation signature that could be due to WIMP interactions [61]. The data can be compatible with the DAMA result with some non-standard WIMP assumptions [64].

Despite the significance of the dark matter discovery claimed by DAMA, the community remains sceptic. The reasons are twofold. Firstly, for the majority of favoured dark matter models, the results are in direct contradiction with many other dark matter experiments (as shown in Figure 1.9). There are however some more exotic dark matter models that allow compatibility between the DAMA detection and the null results of other experiments [65]. In addition, although this annual modulation is consistent with the predicted modulation in the WIMP event rate, there exist many terrestrial backgrounds that exhibit seasonal variation with the potential to mimic this signature. The difficulty in ruling out unknown sources of background highlights the need for a yet more definitive signature, which cannot be mimicked by a terrestrial source.

**Directional signal** — As described in Section 1.3.2, the direction of the WIMP wind in the laboratory frame is determined by the motion of the Earth through the WIMP halo, with a strong oscillation — of up to  $\sim 90^\circ$  over the course of a sidereal day, for an optimally located experiment — due to the spinning of Earth on its axis.

The directionality of WIMP-induced nuclear recoils, biased in the direction of the WIMP wind, potentially produces a unique signal that shows unambiguously that detected nuclear recoils are of galactic origin. The powerful discrimination of the directional signal is such that, in principal, a positive WIMP detection would be possible with as few as tens of WIMP-induced nuclear recoils [66]. Detectors sensitive to the direction of the low energy nuclear recoils expected from WIMP-nucleus interactions also have the potential to perform ‘WIMP astronomy’ studying the local dark matter density and the kinematics of WIMPs in the galactic halo.

The DRIFT-II detector, the subject of this thesis, is the first, and one of only a handful of experiments around the world, pioneering the design of directionally sensitive WIMP detectors, that could offer comprehensive proof for the existence of WIMPs in the galaxy [67]. The DRIFT-II detector, along with other directional dark matter detectors, will be discussed in the following chapter.



## Chapter 2

# Direct detection of WIMPs

In order for WIMPs to account for the observed cosmological mass density, WIMPs must have some small, non-zero coupling to baryonic matter [43]. WIMP-nucleus scattering is predicted to produce nuclear recoils that are, in principal, detectable. An unambiguous detection of these WIMP interactions requires a detector capable of detecting recoil energies of the order of 1 to 100 keV. In addition background sources of similar recoils must be understood so that they can be either eliminated, or removed from the data with efficient cuts.

In Section 2.1 characteristics of WIMP-induced nuclear recoils are discussed through simple kinematic arguments. These calculations lead to a theoretical estimate of the expected nuclear recoil energy spectra in typical WIMP detector target materials. In Section 2.2 backgrounds common to all direct dark matter detection experiments are discussed. In Section 2.3 concepts of directional dark matter detection are introduced, before, in Section 2.4, the technologies currently being developed for directional reconstruction of low-energy nuclear recoils are discussed.

### 2.1 Theory of WIMP detection

This section derives an equation for the expected nuclear recoil spectrum in a dark matter detector. This is done in a number of stages. In § 2.1.1 Classical kinematics are used to derive the range of recoil energies expected from WIMP-nucleus interactions. In § 2.1.2 a strongly simplified dark matter detection model is used to estimate the total rate of scatters expected for WIMPs of a fixed velocity. In § 2.1.3 the *differential event rate* is calculated, expressing the total event rate as a sum of differential event rates over all allowed recoil energies. In § 2.1.4 corrections are made to the differential rate

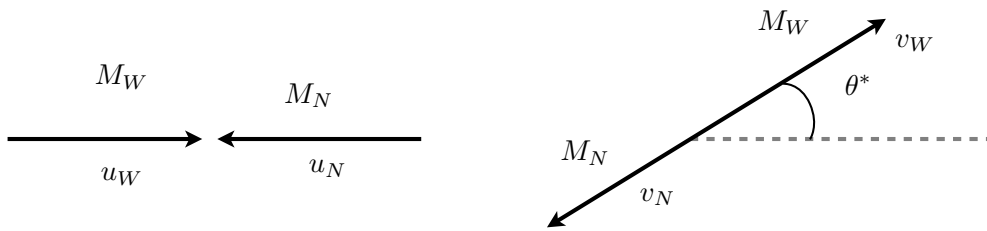
to account for the velocity distribution of WIMPs and in § 2.1.5 further corrections are made with the inclusion of nuclear form factors. In § 2.1.6 the WIMP-nucleus interaction cross-sections are discussed and finally, in § 2.1.7 these calculations are used to estimate the expected differential event rate spectrum in typical dark matter detector targets.

Parameter	Value	Description
$\rho_0$	$0.3 \text{ GeV c}^{-2} \text{ cm}^{-3}$	Local WIMP density (assuming isothermal sphere)
$v_E$	$244 \text{ km s}^{-1}$	Mean velocity of Earth relative to the WIMP halo
$v_0$	$230 \text{ km s}^{-1}$	Most probable WIMP velocity
$v_{\text{rms}}$	$282 \text{ km s}^{-1}$	WIMP velocity dispersion = $v_{\text{rms}} = \sqrt{\frac{3}{2}}v_0$
$\langle v \rangle$	$260 \text{ km s}^{-1}$	WIMP mean velocity $\langle v \rangle = \frac{2}{\sqrt{\pi}}v_0$
$v_{\text{esc}}$	$600 \text{ km s}^{-1}$	WIMP escape velocity

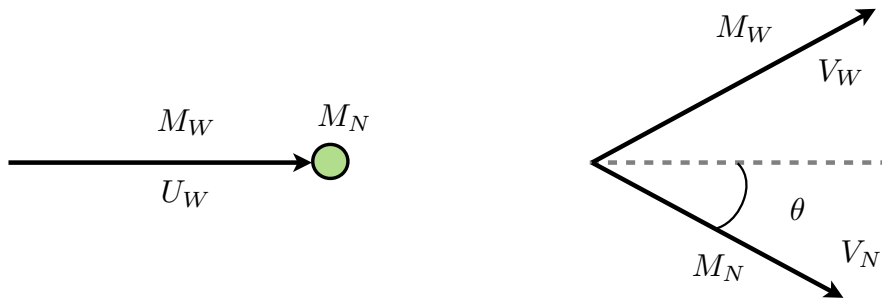
TABLE 2.1: Assumed WIMP halo parameters. From Lewin and Smith [49].

### 2.1.1 WIMP scattering kinematics

As WIMP velocities are highly non-relativistic the kinetic energy transferred from the WIMP to the target nucleus in the elastic scattering interaction can be determined using classical kinematics. Figure 2.1(a) shows a WIMP-nucleus interaction in the centre of mass (COM) frame.



(a) Before (left) and after (right) the collision in the centre of mass frame.



(b) Before (left) and after (right) the collision in the laboratory frame.

FIGURE 2.1: Elastic scattering of WIMP with target nucleus.

The initial velocity of the target nucleus in the COM frame can be expressed as

$$u_N = \frac{M_W}{M_N} u_W \quad (2.1)$$

where  $u_W$  is the initial velocity of the WIMP in the COM frame and  $M_W$  and  $M_N$  are the rest masses of the WIMP and neutron respectively. The initial total kinetic energy in the COM frame is given by

$$E_{\text{COM}}^i = \frac{1}{2} M_W u_W^2 + \frac{1}{2} M_N u_N^2. \quad (2.2)$$

The initial velocity of the WIMP in the COM frame can therefore be expressed as

$$u_W^2 = \frac{2E_{\text{COM}}^i}{M_W \left(1 + \frac{M_W}{M_N}\right)}. \quad (2.3)$$

Since it is an elastic collision,  $E_{\text{COM}}^f = E_{\text{COM}}^i = E_{\text{COM}}$ , so that

$$u_W^2 = v_W^2 = \frac{2E_{\text{COM}}}{M_W \left(1 + \frac{M_W}{M_N}\right)}. \quad (2.4)$$

Equation 2.4 implies  $|u_W| = |v_W|$  and  $|u_N| = |v_N|$ , i.e., for an elastic collision in the COM frame the speeds of the particles do not change, only their direction.

Since the velocities are highly non-relativistic, to transfer from the COM frame to the target rest frame, shown in Figure 2.1(b), it is sufficient to add  $u_N = \frac{M_W}{M_N} u_W$  to the  $x$ -components of each velocity. The velocities in the lab frame can therefore be expressed as

$$\vec{U}_W = u_W \left(1 + \frac{M_W}{M_N}, 0\right), \quad (2.5)$$

$$\vec{V}_W = u_W \left(\cos \theta^* + \frac{M_W}{M_N}, \sin \theta^*\right), \quad (2.6)$$

and

$$\vec{V}_N = u_W \frac{M_W}{M_N} (1 - \cos \theta^*, -\sin \theta^*). \quad (2.7)$$

In the lab frame the kinetic energy transferred to the recoiling target nucleus from the WIMP-nucleus scatter  $E_r$  can, therefore, be expressed as

$$E_r = \frac{1}{2} M_N V_N^2 = \frac{1}{2} M_N u_W^2 \left(\frac{M_W}{M_N}\right)^2 \left((1 - \cos \theta^*)^2 + \sin^2 \theta^*\right). \quad (2.8)$$

Using the reduced mass of the WIMP-nucleus system  $\mu_{WN}$ , defined as

$$\mu_{WN} = \frac{M_N M_W}{M_N + M_W}, \quad (2.9)$$

Equation 2.5 gives

$$M_W^2 u_W^2 = \mu_{WN}^2 U_W^2. \quad (2.10)$$

Substituting this into Equation 2.8 results in

$$\begin{aligned} E_r &= \frac{\mu_{WN}^2 U_W^2}{2M_N} (1 - 2 \cos \theta^* + \cos^2 \theta^* + \sin^2 \theta^*) \\ &= \frac{\mu_{WN}^2 U_W^2}{M_N} (1 - \cos \theta^*) \end{aligned} \quad (2.11)$$

where, as shown in Figure 2.1(a),  $\theta^*$  is the scattering angle in the COM frame. To express the recoil energy in terms of the scattering angle in the lab frame  $\theta$ , the WIMP velocity in the lab frame, Equation 2.6, gives

$$\tan \theta = \frac{\sin \theta^*}{1 - \cos \theta^*} \quad (2.12)$$

or

$$\tan^2 \theta = \frac{\sin^2 \theta^*}{(1 - \cos \theta^*)^2} = \frac{1 - \cos^2 \theta^*}{(1 - \cos \theta^*)^2} = \frac{1 + \cos \theta^*}{1 - \cos \theta^*}. \quad (2.13)$$

Using the identity  $\tan^2 \theta = \sec^2 \theta - 1$ , this gives

$$\sec^2 \theta = \frac{1 + \cos \theta^* + 1 - \cos \theta^*}{1 - \cos \theta^*} = \frac{2}{1 - \cos \theta^*}, \quad (2.14)$$

or

$$\cos^2 \theta = \frac{1}{2}(1 - \cos \theta^*). \quad (2.15)$$

Substituting this into Equation ?? leads to an expression for the kinetic energy of the recoiling nucleus

$$E_r = \frac{2\mu_{WN}^2 U_W^2}{M_N} \cos^2 \theta. \quad (2.16)$$

Thus the kinetic energy of the recoiling nucleus is dependent on the scattering angle, with a minimum energy transferred when there is a glancing blow and the nucleus recoils at a right angle ( $\theta = 90^\circ$ ) and a maximum energy transferred in a head-on collision ( $\theta^* = 0^\circ$  or  $180^\circ$ ) resulting in a recoil energy of

$$E_{max} = \frac{2\mu_{WN}^2 U_W^2}{M_N}. \quad (2.17)$$

Assuming recoils are uniformly distributed in  $\cos\theta^*$  (and hence in  $\cos^2\theta$ ), and using  $\langle\cos^2\theta\rangle = \frac{1}{2}$ , the mean energy transferred in a collision is given by

$$\langle E \rangle = \frac{\mu_{WN}^2 U_W^2}{M_N}. \quad (2.18)$$

For a WIMP of mass  $100 \text{ GeV c}^{-2}$  and a velocity of  $220 \text{ km s}^{-1}$ , colliding with a sulphur nucleus (from the typical  $\text{CS}_2$  target in DRIFT) of mass  $32 \text{ GeV c}^{-2}$ , this equates to a mean recoil energy of  $\sim 10 \text{ keV}$ .

### 2.1.2 Total event rate of WIMP scattering

Figure 2.2 illustrates a dark matter detector of mass 1 kg containing  $N$  target nuclei in a volume of  $L^3$ . A single WIMP of velocity  $v$  and a WIMP-nucleus interaction cross-section of  $\sigma_{WN}$  effectively interacts with all target nuclei in a volume of  $v\sigma_{WN}$ , each second. With a target density of  $N/L^3$  this gives an interaction rate of  $N \times \sigma_{WN}v/L^3$  per second. For a WIMP number density of  $n_0$  there are  $L^3 n_0$  WIMPs passing through the detector at any one time giving a total WIMP-nucleus interaction rate of

$$R = \sigma_{WN}vNn_0. \quad (2.19)$$

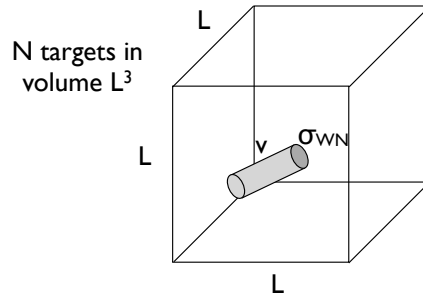


FIGURE 2.2: A WIMP of cross-section  $\sigma_{WN}$  and velocity  $v$ , passing through a detector of  $N$  targets in a volume  $L^3$  produces an interaction rate of  $N \times \sigma_{WN}v/L^3$  per WIMP per second.

The number of target nuclei in the 1 kg detector is given by

$$N = \frac{1000}{A} \times N_A \quad (2.20)$$

where  $A$  is the atomic number and  $N_A$  is Avogadro's constant ( $6.02 \times 10^{23}$ ). Expressing the number density of dark matter particles as

$$n_0 = \frac{\rho_o}{M_W}, \quad (2.21)$$

where  $\rho_o$  is halo density and  $M_W$  is the WIMP mass, gives the total rate of WIMP-nucleus interactions for a 1 kg detector, assuming WIMPs of fixed velocity  $v$ , of

$$R = \frac{10^3 \sigma_{WN} v N_A \rho_0}{A M_W}. \quad (2.22)$$

### 2.1.3 Differential event rate

The total recoil rate  $R$  can be considered as a sum of the separate contributions from recoils in energy ranges from zero to the maximum possible recoil energy  $E_{max}$ . The *differential rate* is the rate of interactions in an energy range  $E_r$  to  $E_r + dE_r$  and is given by the total rate  $R$  multiplied by the probability of the interaction producing a recoil in that energy range

$$\frac{dR}{dE_r} = R \cdot p(E_r). \quad (2.23)$$

Assuming that the scattering angles are isotropic in  $\cos \theta^*$ , Equation 2.16 implies that the recoil energies are uniform in the range  $E_{min}$  to  $E_{max}$ . Since all probabilities must sum to unity, Equation 2.17 implies that, as illustrated in Figure 2.3,

$$p(E_r) = \frac{M_N}{2\mu_{WN}^2 v^2} \quad (2.24)$$

for all energies up to  $E_{max}$ . The differential rate is thus given, using Equation 2.22 and Equation 2.24, by

$$\frac{dR}{dE_r} = \frac{10^3 \sigma_{WN} N_A \rho_0 M_N}{2A M_W \mu_{WN}^2 v}. \quad (2.25)$$

### 2.1.4 Correcting for realistic WIMP velocities

Equation 2.25 gives a prediction of the nuclear recoil energy spectrum expected in a detector assuming all WIMPs have the same fixed velocity  $v$ . A more realistic scenario is that WIMPs instead have a range of velocities from  $v_{min}$  to  $v_{max}$  with some velocity distribution  $f(v)$ . In this case the following substitution is made:

$$\frac{1}{v} \rightarrow \int_{v_{min}}^{v_{max}} \frac{f(v) dv}{v}. \quad (2.26)$$

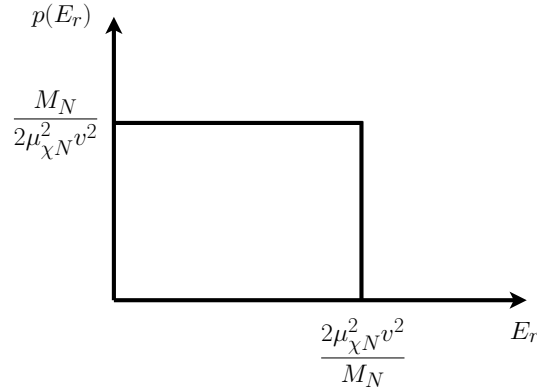


FIGURE 2.3: Probability density of nuclear recoil energy.

As discussed in Section 1.3.2 the velocity distribution of the halo WIMPs is given by the Maxwell-Boltzmann distribution

$$f(v) = \frac{4\pi v^2}{(2\pi/3)^{3/2} v_{\text{rms}}^3} e^{-\frac{3v^2}{2v_{\text{rms}}^2}} \quad (2.27)$$

where  $v_{\text{rms}}$  is the *velocity dispersion*, related to the most probable WIMP velocity  $v_0$  ( $\sim 230 \text{ km s}^{-1}$ ) by  $v_{\text{rms}} = \sqrt{3/2}v_0$ . Equation 2.26 therefore becomes

$$\int_{v_{\text{min}}}^{v_{\text{max}}} \frac{f(v)}{v} dv = \frac{4\pi v_0^2}{v_0^3 \pi^{3/2}} \int_{v_{\text{min}}}^{v_{\text{max}}} v e^{-\frac{v^2}{v_0^2}} dv \quad (2.28)$$

$$= \frac{2}{v_0 \sqrt{\pi}} \left[ e^{(-v^2/v_0^2)} \right]_{v_{\text{max}}}^{v_{\text{min}}}. \quad (2.29)$$

The parameter  $v_{\text{min}}$  is the minimum WIMP velocity capable of producing a recoil of energy  $E_r$ . From Equation 2.17, this is given by

$$v_{\text{min}} = \sqrt{\frac{E_r M_N}{2\mu_{WN}^2}}. \quad (2.30)$$

The maximum WIMP velocity  $v_{\text{max}}$  is determined by the escape velocity of WIMPs  $v_{\text{max}} = v_{\text{esc}}$ . For simplicity the escape velocity is often assumed to be infinite giving the substitution

$$\frac{1}{v} \rightarrow \frac{2}{v_0 \sqrt{\pi}} e^{-\frac{E_r M_N}{2\mu_{WN}^2 v_0^2}} \quad (2.31)$$

so that Equation 2.25 becomes

$$\frac{dR}{dE_r} = \frac{10^3 \sigma_{WN} N_A \rho_0 M_N}{2 A M_W \mu_{WN}^2} \frac{2}{v_0 \sqrt{\pi}} e^{-\frac{E_r M_N}{2\mu_{WN}^2 v_0^2}}. \quad (2.32)$$

The mean velocity of WIMPs in the Maxwellian halo is  $\langle v \rangle = (2/\sqrt{\pi})v_0$ . Defining  $R_0$  as the total event rate for the strongly simplified model in which all WIMPs have a fixed velocity of  $v = \langle v \rangle = (2/\sqrt{\pi})v_0$ , Equation 2.22 gives

$$R_0 = \frac{2 \times 10^3 \sigma_{WN} N_A v_0 \rho_0}{\sqrt{\pi} A M_W} \quad (2.33)$$

and Equation 2.32 can be expressed as

$$\frac{dR}{dE_r} = R_0 \frac{M_N}{2\mu_{WN}^2} \frac{1}{v_0^2} e^{-\frac{E_r M_N}{2\mu_{WN}^2 v_0^2}}. \quad (2.34)$$

Defining  $E_0$  as the kinetic energy of a WIMP with a velocity of  $v_0$

$$E_0 = \frac{1}{2} M_W v_0^2 \quad (2.35)$$

and defining a kinematic factor  $r$  as

$$r = \frac{4\mu^2}{M_N M_W} \quad (2.36)$$

allows Equation 2.32 to be expressed as

$$\frac{dR(0, \infty)}{dE_r} = \frac{R_0}{E_0 r} e^{-E_r/E_0 r}. \quad (2.37)$$

Equation 2.37 is the differential rate for a 1 kg detector in an isothermal WIMP halo, with the assumptions that the Earth is stationary in the galactic standard of rest (GSR) frame ( $v_E = 0$ ) and that the galactic escape velocity is infinite ( $v_{\text{esc}} = \infty$ ).

A more realistic expression is obtained when the velocity of the Earth with respect to the GSR  $v_E$  is taken into account. The differential event rate spectrum is then expressed as [49]

$$\frac{dR(v_E, \infty)}{dE_r} = \frac{R_0}{E_0 r} \frac{\sqrt{\pi}}{4} \frac{v_0}{v_E} \left[ \text{erf} \left( \frac{v_{\text{min}} + v_E}{v_0} \right) - \text{erf} \left( \frac{v_{\text{min}} - v_E}{v_0} \right) \right] \quad (2.38)$$

where erf is the error function defined by

$$\text{erf}(x) = \frac{2}{\sqrt{\pi}} \int_0^x e^{-t^2} dt. \quad (2.39)$$

This expression can be made yet more realistic by correcting for the finite galactic escape velocity  $v_{\text{esc}}$ , resulting in the differential event rate of [49]

$$\frac{dR(v_E, v_{\text{esc}})}{dE_r} = \frac{k_0}{k_1} \left[ \frac{dR(v_E, \infty)}{dE_r} - \frac{R_0}{E_0 r} e^{-(v_{\text{esc}}/v_0)^2} \right] \quad (2.40)$$

where  $k_0/k_1$  is a normalisation constant that is defined by

$$\frac{k_0}{k_1} = \left[ \text{erf} \left( \frac{v_{\text{esc}}}{v_0} \right) - \frac{2}{\sqrt{\pi}} \frac{v_{\text{esc}}}{v_0} e^{-(v_{\text{esc}}/v_0)^2} \right]^{-1}. \quad (2.41)$$

Using the halo model assumptions summarised in Table 2.1 with measured particle physics properties of the target materials there remains only two unknowns in Equation 2.40 — the WIMP mass  $M_W$ , and the WIMP-nucleus cross-section  $\sigma_{WN}$ . Comparison of event rates measured by experiment to the differential event rate spectra predicted by Equation 2.40 therefore enables constraints to be placed on allowed WIMP mass and WIMP-nucleus interaction cross-sections.

### 2.1.5 Nuclear form factor corrections

The equations quoted so far have been derived in the *zero momentum transfer* limit. That is, under the assumption that the momentum gained by the recoiling nucleus  $q$  is small

$$q = \sqrt{2M_N E_r} \approx 0. \quad (2.42)$$

This assumption, however, is only reasonable when the de Broglie wavelength associated with  $q$  ( $\lambda = h/q$ , where  $h$  is Planck's constant) is much larger than the nuclear radius. In this case the WIMP effectively interacts with the nucleus as a whole and the spatial distribution of nuclear spin within the nucleus can be neglected. Thus the hard sphere classical scattering assumptions that have been made are acceptable. The mean recoil energy derived in Section 2.1.1 for a WIMP of mass  $100 \text{ GeV c}^{-2}$  and a sulfur target nucleus of mass  $32 \text{ GeV c}^{-2}$  result in a momentum transfer of  $\sim 70 \text{ fm}$ . This is relatively large compared to the  $\sim 3 \text{ fm}$  effective nuclear radius of the sulfur [68], so the zero momentum transfer limit provides a reasonable approximation.

With increasing  $q$ , however, the effects of nuclear spin structure are significant and act to reduce the effective cross-section. This has the effect of adding a  $q$ , and therefore  $E_r$ , dependence to the WIMP-nucleus interaction cross-section, which is accounted for by a *nuclear form factor*. The nuclear form factor is the Fourier transform of the assumed density function of the nucleus and is expressed as a function of the dimensionless quantity  $qr_n/\hbar$ , where  $r_n$  is the effective radius of the nucleus.

The form factor reduces the WIMP-nucleus interaction cross-section by a factor of  $F^2(qr_n)$  so that the non-zero momentum transfer cross-section is expressed as [49]

$$\sigma_{WN}(qr_n) = F^2(qr_n)\sigma_{WN} \quad (2.43)$$

where  $\sigma_{WN}$  is the previously defined cross-section assuming zero momentum transfer.

The appropriate form factor depends on the nature of the WIMP-nucleus interaction. WIMPs generally couple to nuclei via either scalar, *spin-independent* (SI) interactions, where the WIMP couples to the mass of the nucleus through the exchange of Higgs bosons, and/or via axial-vector, *spin-dependent* (SD) interactions, where the WIMP couples to the spin of the nucleus through Z boson exchange.

**Spin-independent** — For spin-independent (SI) interactions the nuclear charge density can be approximated by a solid sphere (approximating an interaction with the entire nucleus) with a correction for a ‘soft-edge’ where the charge density of the nucleus falls to zero over a finite skin thickness. The form factor, derived from the Fourier transform of this density distribution, is estimated by the expression [69]

$$F(qr_n) = \frac{3j_1(qr_n)}{qr_n} e^{-(qs)^2/2} \quad (2.44)$$

where  $r_n$  is the effective nuclear radius approximated by  $r_n \approx 1.14A^{1/3}$  fm,  $s \approx 0.9$  fm is the surface thickness and  $j_1$  is the second spherical Bessel function

$$j_1(x) = \frac{\sin x}{x^2} - \frac{\cos x}{x}. \quad (2.45)$$

The SI form factors for the target elements in the DRIFT detector, as well as some other typical spin-independent target materials, are plotted in Figure 2.4. At low energies the limit of low energy classical theorem (zero momentum transfer) is approached and the form factor tends to 1.

**Spin-dependent** — For spin-dependent interactions a thin shell charge density distribution can be assumed, approximating an interaction with a single unpaired nucleon in the outer shell. This is known as the *single particle* approximation. The *odd-group* model is a more detailed approximation that instead takes into account the WIMP coupling to all nucleons of the same type as the unpaired nucleon [70]. A commonly used estimate of the form factor for SD interactions, derived from the Fourier transform of the odd-group approximation, is given by

$$F(qr_n) = \begin{cases} j_0(qr_n) & (qr_n < 2.55, qr_n > 4.5) \\ \sqrt{0.047} & (2.55 \leq qr_n \leq 4.5) \end{cases} \quad (2.46)$$

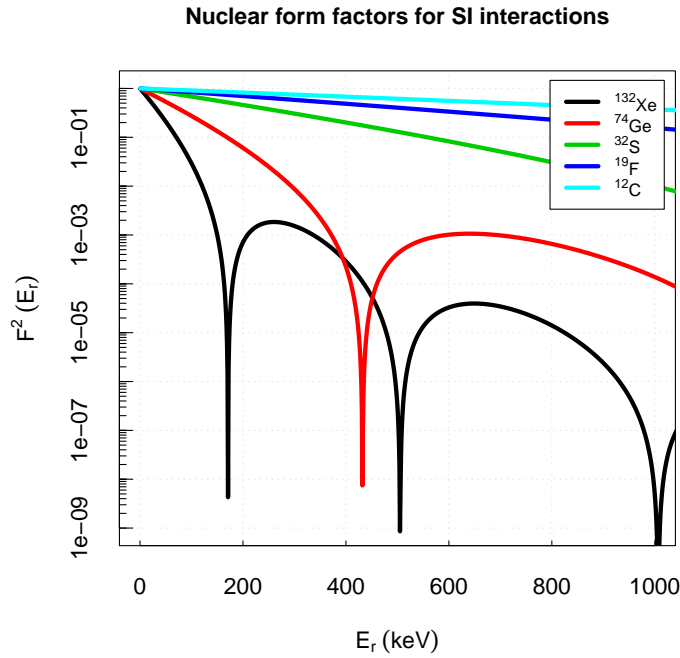


FIGURE 2.4: Estimates of nuclear form factor as a function of recoil energy for SI WIMP-nucleus interactions. Elements plotted are typical SI detector target materials.

where the effective nuclear radius is approximated by  $r_n \approx 1.0A^{1/3}$  fm and  $j_0$  is the first spherical Bessel function

$$j_0(x) = \frac{\sin x}{x}. \quad (2.47)$$

Using this approximation the form factors of some elements used in spin-dependent detectors are plotted in Figure 2.5, as a function of energy.

### 2.1.6 WIMP-nucleon cross-sections

The WIMP-nucleus cross-section can be expressed as [43]

$$\sigma_{WN} = 4G_F^2 \mu_{WN}^2 C_N \quad (2.48)$$

where  $\mu_{WN}$  is the reduced mass of the WIMP-nucleus system, defined in Equation 2.9, and  $C_N$  is the dimensionless *enhancement factor*, which contains particle physics model information.  $G_F^2$  is the *Fermi coupling constant*, defined by

$$\frac{G_F}{(\hbar c)^3} = \frac{\sqrt{2}g^2}{8m_W^2} \approx 1.16 \times 10^{-5} \text{ GeV}^{-2} \quad (2.49)$$

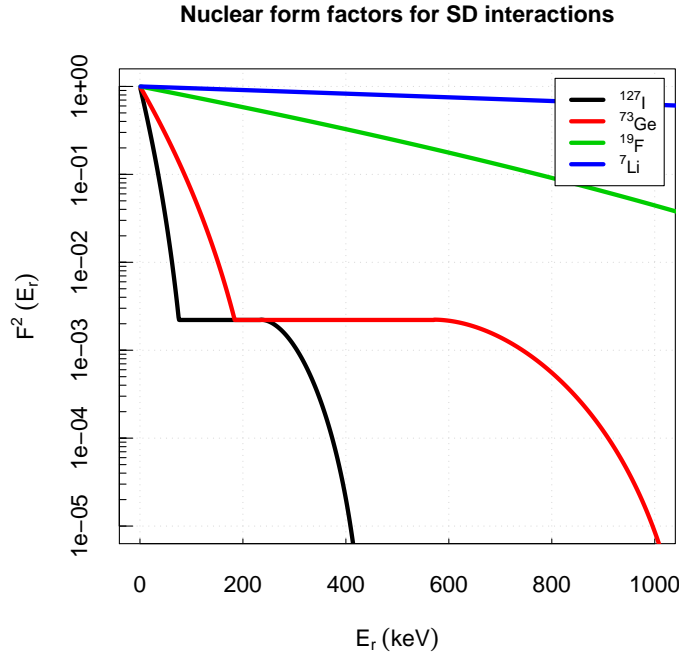


FIGURE 2.5: Estimates of nuclear form factor as a function of recoil energy for SD WIMP-proton interactions. Elements plotted are typical SD WIMP-proton detector target materials.

where  $m_W$  is the mass of the W boson,  $g$  is the coupling constant of the weak interaction and  $\hbar$  is the reduced Planck constant.

In order to compare results from detectors of different target materials, and also to allow comparison to theoretical models, it is convenient to express experimentally determined constraints on WIMP-nucleus cross-sections ( $\sigma_{WN}$ ) in terms of the cross-section for a WIMP interaction with a single free neutron ( $\sigma_{Wn}$ ) or proton ( $\sigma_{Wp}$ ). From Equation 2.48

$$\frac{\sigma_{WN}}{\mu_{WN}^2 C_N} = \frac{\sigma_{Wp}}{\mu_{Wp}^2 C_p} = \frac{\sigma_{Wn}}{\mu_{Wn}^2 C_n} \quad (2.50)$$

where  $C_p$  and  $C_n$  are the enhancement factors and  $\mu_{Wp}$  and  $\mu_{Wn}$  are the reduced masses for the proton and neutron respectively. The enhancement factor  $C_N$  contains components from both the SI and SD couplings

$$C_N = C_N^{SI} + C_N^{SD}. \quad (2.51)$$

**Spin-independent** — The SI interaction enhancement factor can be expressed as [71]

$$C_N^{SI} = \frac{1}{\pi G_F^2} [Zf_p + (A - Z)f_n]^2 \quad (2.52)$$

where  $A$  is the mass number and  $Z$  is the atomic number of the target. The parameters  $f_p$  and  $f_n$  are the WIMP-proton and WIMP-neutron couplings respectively. In most models WIMPs are Majorana particles so  $f_p \approx f_n$  and from Equation 2.52

$$\frac{C_N^{SI}}{C_p^{SI}} \approx \frac{C_N^{SI}}{C_n^{SI}} \approx A^2. \quad (2.53)$$

From Equation 2.50 the SI WIMP-nucleus cross-section can then be defined in terms of the cross-section for a single proton

$$\sigma_{Wp}^{SI} = \sigma_{WN}^{SI} \frac{\mu_{Wp}^2}{\mu_{WN}^2} \frac{1}{A^2}. \quad (2.54)$$

**Spin-dependent** — In the SD case the enhancement factor can be expressed as [71]

$$C_N^{SD} = \frac{8}{\pi} (a_p \langle S_p \rangle + a_n \langle S_n \rangle)^2 \frac{J+1}{J} \quad (2.55)$$

where  $J$  is the total spin of the nucleus,  $\langle S_p \rangle$  and  $\langle S_n \rangle$  are the expectation values of the proton and neutron spin respectively and  $a_p$  and  $a_n$  are the WIMP-proton and WIMP-neutron SD couplings respectively.

Lacking a detailed model of the interference between the WIMP-proton and WIMP-neutron scattering amplitudes in the spin-dependent case, the interference between WIMP-proton and WIMP-neutron collisions is neglected (acknowledging that in some theories this interference may significantly reduce the cross section). The enhancement factor can then be written in terms of neutron only and proton only components as [72]

$$C_N^{SD(p)} = \frac{8}{\pi} (a_p \langle S_p \rangle)^2 \frac{J+1}{J} \quad (2.56)$$

and

$$C_N^{SD(n)} = \frac{8}{\pi} (a_n \langle S_n \rangle)^2 \frac{J+1}{J}, \quad (2.57)$$

with the total nucleus enhancement factor expressed as

$$C_N^{SD} = \left( \sqrt{C_N^{SD(p)}} \pm \sqrt{C_N^{SD(n)}} \right)^2. \quad (2.58)$$

The SD WIMP-nucleon cross-section can then be defined in terms of pure proton coupling

$$\sigma_{Wp}^{SD} = \sigma_{WN}^{SD} \frac{\mu_{Wp}^2}{\mu_{WN}^2} \frac{C_p^{SD}}{C_N^{SD(p)}}, \quad (2.59)$$

and pure neutron coupling

$$\sigma_{Wn}^{SD} = \sigma_{WN}^{SD} \frac{\mu_{Wn}^2}{\mu_{WN}^2} \frac{C_n^{SD}}{C_N^{SD(n)}} \quad (2.60)$$

where, using  $J = 0.5$  and  $\langle S_p \rangle^2 = \langle S_n \rangle^2 = 0.5$  for a free proton or neutron,

$$\frac{C_N^{SD(p)}}{C_p^{SD}} = \frac{4}{3} \langle S_p \rangle^2 \frac{J+1}{J} \quad (2.61)$$

and

$$\frac{C_N^{SD(n)}}{C_n^{SD}} = \frac{4}{3} \langle S_n \rangle^2 \frac{J+1}{J}. \quad (2.62)$$

### 2.1.7 Event rate spectra

Combining Equation 2.40 with the form factors in the previous section gives the total differential event rate for an idealised dark matter detector of a single element

$$\frac{dR}{dE_r} = \frac{dR(v_E, v_{\text{esc}})}{dE_r} \cdot F^2(E_r). \quad (2.63)$$

Figure 2.6 and Figure 2.7 show theoretical differential event rate spectra for a number of commonly used target materials in SI and SD sensitive dark matter detectors respectively.

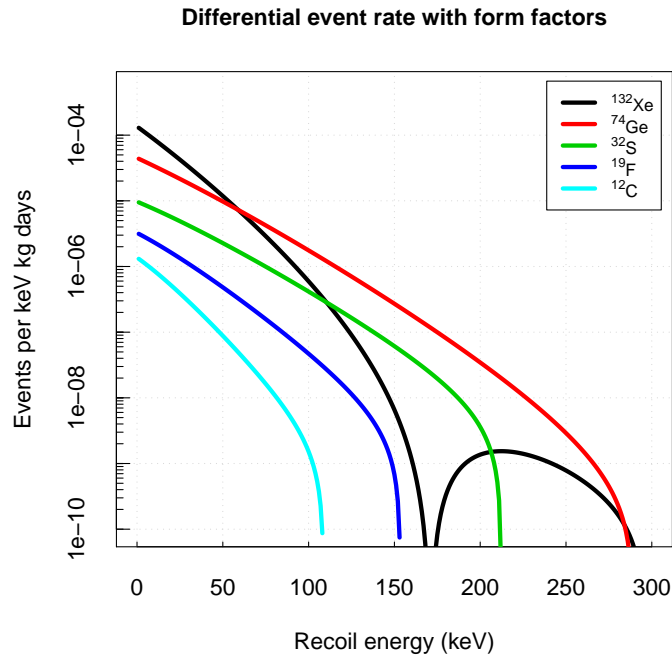


FIGURE 2.6: Theoretical differential event rate spectra assuming SI WIMPs of mass 100 GeV and a WIMP-nucleon interaction cross-section of  $7 \times 10^{-9}$  pb. Assumed halo parameters listed in Table 2.1.

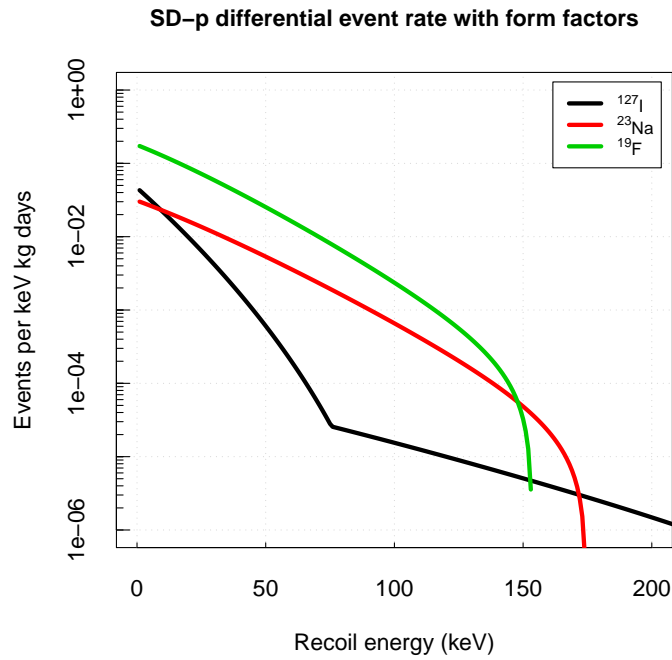


FIGURE 2.7: Theoretical differential event rate spectra assuming SD WIMPs of mass 100 GeV and a WIMP-proton interaction cross-section of  $4 \times 10^{-2}$  pb. Assumed halo parameters listed in Table 2.1.

## 2.2 Detector backgrounds

Expected WIMP-nucleon interaction rates are low, with typical rates less than  $\sim 1$  event per kg of detector mass per year. In addition the energy transferred to the recoiling nucleus is low, on the order of 1 to 100 keV. This section discusses naturally occurring backgrounds that produce events in this energy range, typically with rates many orders of magnitude above the expected WIMP event rate. Techniques to reduce these backgrounds are considered.

### 2.2.1 Electron recoils

Gamma radiation is a potential source of electron recoils in the target volume, which may mimic the WIMP signal. Minimising gamma-ray interactions in the detector target volume firstly requires that the detector itself is not an inherent source of gamma radiation. Detector construction materials are typically analysed for radiopurity in low background germanium detectors before being selected. Construction and maintenance of detectors are also performed under clean room conditions to minimise radioactive contaminants being introduced to detector surfaces. In addition, gamma-rays from external sources must be prevented from entering the target volume. This is achieved by surrounding the detector in materials of high atomic mass, typically layers of copper and/or lead shielding, which, must also have a high level of radiopurity.

Despite efforts to minimise gamma-ray backgrounds, electron recoil event rates typically remain orders of magnitude higher than the predicted rate of WIMP-induced nuclear recoils. However, electron recoils produced by gamma-ray interactions deposit energy with characteristic differences, when compared to the nuclear recoils expected from WIMP interactions. Discrimination techniques can therefore be used to distinguish electron recoils from, potentially WIMP-induced, nuclear recoils.

Discrimination techniques take advantage of the fact that particle interactions deposit energy in the target in the form of heat, ionisation and excitation. In electron recoils the total energy is distributed differently between these forms when compared to nuclear recoils. For example, two-phase liquid xenon detectors exploit the large difference in the ionisation-to-scintillation ratio of electron recoils compared to nuclear recoils [73]. The efficiency of a discrimination technique is quantified by the electron discrimination factor, which is the estimated fraction of electron recoil events that will be incorrectly identified as nuclear recoil events, and hence potential WIMP interactions.

Electron discrimination efficiency varies widely across different target materials and discrimination techniques. The ZEPLIN-III collaboration, operating a two-phase liquid xenon detector, have an electron discrimination of  $\sim 10^{-4}$  from the ionisation-to-scintillation ratio [74]. The WARP detector has a target of liquid argon in which significantly better gamma-ray discrimination from the ionisation-to-scintillation ratio is possible. WARP have achieved an electron discrimination of  $\sim 10^{-8}$  in a 2.3 L prototype detector [75]. In the CDMS-II cryogenic detector, consisting of Ge and Si semiconductor targets, the ratio of ionisation-to-phonons produces an electron discrimination of  $\sim 10^{-4}$  above 10 keV [59]. In the DRIFT-II detector, with a gaseous target of low pressure  $\text{CS}_2$ , or  $\text{CS}_2\text{-CF}_4$  mixtures, the mean charge density along the length of the track,  $dE/dx$ , is used as a discriminant, where recoiling electrons have a much lower  $dE/dx$  than recoiling nuclei (see Section 3.3.1). Electron discrimination in the DRIFT-II detector has been measured to be better than  $8 \times 10^{-6}$  [76].

The total level of gamma radiation that exists in the detector, combined with the electron recoil/nuclear recoil discrimination power of the detector, determines the maximum sensitivity of the detector to WIMP-induced nuclear recoils.

### 2.2.2 Nuclear recoils

Neutrons, although a significantly less abundant background, are considerably more problematic for dark matter detection experiments as they can enter the target volume undetected and elastically scatter with nuclei in the target volume, creating nuclear recoils indistinguishable from the predicted WIMP-induced nuclear recoils.

Cosmic rays are a significant source of unwanted neutrons up to 100s of MeV. The upper atmosphere is constantly being bombarded by cosmic rays, consisting of mostly protons ( $\sim 89\%$ ), alphas ( $\sim 9\%$ ), and electrons ( $\sim 1\%$ ), with energies ranging from  $10^8$  to  $10^{21}$  eV [77]. These high energy particles interact with nuclei in the upper atmosphere (about 20 km above sea level) producing showers of secondary particles consisting mostly of pions ( $\pi^-$ ,  $\pi^0$  and  $\pi^+$ ). These secondary particles have two components: a *soft* component that consists mostly of neutral pions, which quickly decay into particles easily absorbed by the atmosphere; and a *hard* component that consists mostly of charged pions, which decay into high energy cosmic ray muons. Muons with energies  $> 3$  GeV have a mean decay length  $> 20$  km so are capable of travelling deep into the Earth before decaying. Such muons can interact with the detector or its surroundings producing neutrons. Dark matter detectors therefore benefit from operating deep underground, where the number of cosmic muons, and hence the muon-induced neutron background, is minimised. All competitive dark matter experiments are located deep underground,

at depths in excess of 1 km, where the number of muons present can be attenuated by  $\gtrsim 10^6$  [78].

A second source of potentially WIMP-mimicking ambient neutrons is radioactivity from natural uranium and thorium sources in the surrounding environment, typically dominated by the surrounding rock in an underground dark matter detector. These produce a background neutron population with energies up to  $\sim 10$  MeV through  $(\alpha, n)$  reactions and, to a lesser degree, through spontaneous fission of  $^{238}\text{U}$ . Dark matter detection experiments are therefore surrounded in materials with a high hydrogen content, such as water or polypropylene, to thermalise neutron backgrounds that remain underground. The DRIFT-II detector neutron shielding is described in Section 3.2.2. Since neutron events are indistinguishable from the expected WIMP signal, any remaining neutron background creates a limit on the potential sensitivity of the experiment.

## 2.3 Directional dark matter detection

As described in Section 1.4.2, the motion of the Earth through the WIMP halo determines the direction of incidence of WIMPs so that WIMP-induced nuclear recoils are expected to exhibit a directional bias. A dark matter detector capable of resolving the direction of WIMP-induced nuclear recoils could provide an unambiguous proof of the existence of dark matter particles in the galaxy. Low pressure gaseous targets, in which nuclear recoils create tracks of  $\sim$ mm length, are potentially capable of resolving this directionality.

**Track reconstruction** — Figure 2.8(a) shows the directional anisotropy of the predicted WIMP signal. Although the strength of this signal is clear there are a number of effects that act to reduce the measurable anisotropy. As shown in Section 2.1.1, a WIMP-nucleus collision can result in the nucleus recoiling at a range of angles relative to the incident WIMP, so although the direction of the incident WIMPs may be uniform, the resulting nuclear recoils are not. The effects of this are illustrated in Figure 2.8(b).

The nuclear recoil from a WIMP-nucleus interaction, particularly for low energy recoils, is also affected by *straggling*. This produces some uncertainty in determining the direction of the initial recoil from the ionisation track, thus reducing the strength of the directional anisotropy. In addition, the ionisation track suffers diffusion as it is drifted, typically over many cm, from the point of interaction to the detector readout plane. The diffusion acts to further reduce the clarity of the track and reduce the strength of the directional signal. Finally, when the track arrives at the pixellated readout plane it is reconstructed at a finite resolution (determined by the readout geometry), further

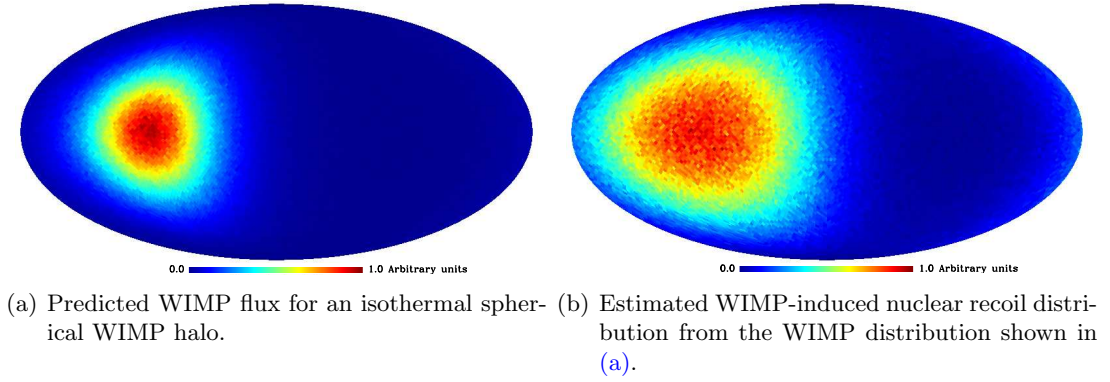


FIGURE 2.8: Estimated directional anisotropy of the WIMP signal assuming a  $^{19}\text{F}$  target and a  $100 \text{ GeV c}^{-2}$  WIMP. Images from Billard et al. [79].

reducing the ability to accurately measure the directional anisotropy of the WIMP signal. Despite such effects diluting the directional anisotropy, it has been shown, through simulation of a feasible directional dark matter detector, that the resulting signal would retain significant directionality. Figure 2.9 shows an estimate of how the nuclear recoil direction distribution, illustrated in Figure 2.8(b), may appear in a realistic directional detector with angular resolution of  $15^\circ$ . Figure 2.9 contains 100 WIMP events and 100 isotropic background events, from which a likelihood analysis identifies a galactic dark matter signal with high significance [79].

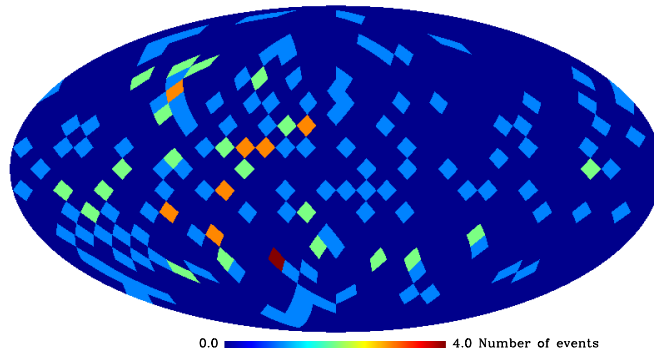


FIGURE 2.9: 100 WIMP-induced recoil events and 100 isotropic background events reconstructed with  $15^\circ$  angular resolution to mimic realistic directional dark matter detector. Assuming a  $^{19}\text{F}$  target and a  $100 \text{ GeV c}^{-2}$  WIMP. Image from Billard et al. [79].

Green and Morgan simulated a DRIFT-like dark matter detector to study aspects of directional detector design [80]. The strength of the directional signal is demonstrated by showing that a detector with a target of 40 Torr  $\text{CS}_2$ , a 20 keV threshold, zero background and with a readout capable of full 3D vector reconstruction of the recoil track is able to discriminate a WIMP signal from an isotropic background at 95% confidence with order of 10 events [80]. Morgen et al. considered detectors with 2D and 3D track

reconstruction capabilities and with axial and full 3D vector sensitivity. It was found that, while 3D track reconstruction reduces the total number of events required for a positive detection by a factor of  $\sim 3$  with respect to 2D reconstruction, having the ability to resolve the full vector direction of the recoil track, so-called head-tail sensitivity, in either case, reduced the number of events required by an order of magnitude [80].

**Head-tail sensitivity** — The charge density of tracks from high energy ionising radiation exhibits a *Bragg peak* [81] such that the vector direction of the track can be clearly identified. For WIMP-induced nuclear recoils of 10s of keV, however, the effect is much less pronounced and is less well understood. It is however expected that the  $dE/dx$  of the track slowly falls with the decreasing energy of the recoiling nucleus, and recent measurements have shown that this head-tail asymmetry exists, and is measurable at these energies in the DRIFT-II detector [82]. It has been shown that head-tail sensitivity is the most important parameter in reducing the required exposure time of a directional detector and a 2D reconstruction with head-tail may offer better sensitivity than full 3D reconstruction without head-tail [83]. However, the head-tail discrimination must be effective on an event-by-event basis at suitably low energies. While perfect head-tail discrimination gives approximately an order of magnitude reduction in the number of events required, success of  $\lesssim 70\%$  offers no improvement over axial readout.

**Energy thresholds** — The differential event rate of WIMP-induced nuclear recoils falls off exponentially with energy (Section 2.1.7), implying energy thresholds as low as possible are desirable. However, the ability to reconstruct the nuclear recoil track also decreases with lower energies. In a directional dark matter detector the improved angular resolution at high energies can compensate for the reduction in event rate. Thus there becomes a point at which reducing the threshold no longer has significant improvements in the sensitivity of the detector. Figure 2.10 shows the number of events required to reject isotropy for an idealised DRIFT-like detector with pure 40 Torr  $\text{CS}_2$  gas, in which the limit occurs at  $\sim 20$  keV. This optimal energy threshold will be lower for targets consisting of lighter nuclei. From Figure 2.10 it can also be seen that even degrading the energy threshold from 20 keV to 50 keV has the modest effect of reducing the required exposure time by a factor 2 [80]. Reducing energy thresholds may, therefore, not be a priority for directional detectors.

**Background events** — The ability of directional detectors to statistically distinguish nuclear recoils of galactic origin from nuclear recoils of terrestrial origin means that detection is possible with a higher signal-to-noise when compared with non-directional detectors. Green and Morgan showed that the number of signal events required to reject isotropy for a signal-to-noise ratio of 10, 1 and 0.1 respectively is 14, 27 and 170 [80].

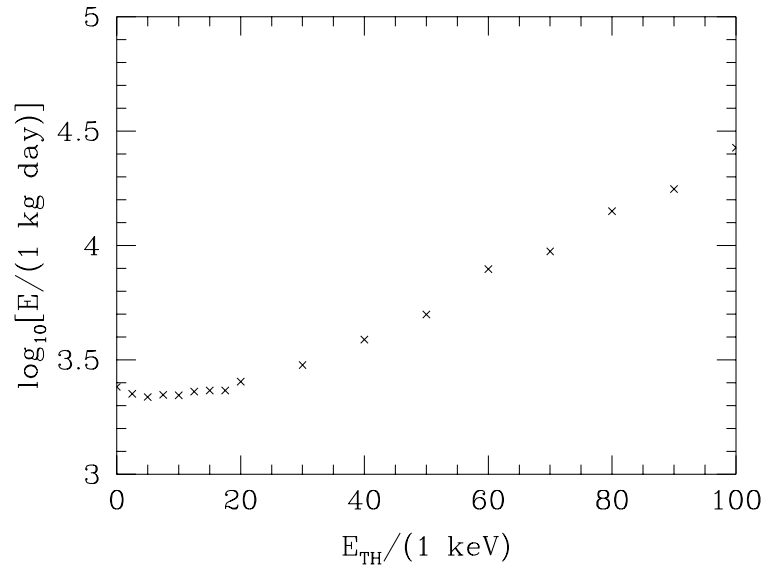


FIGURE 2.10: Exposure required to reject isotropy as a function of energy threshold for a DRIFT-like detector with 40 Torr  $\text{CS}_2$  target. Assuming a WIMP-nucleon elastic scattering cross-section of  $10^{-7}$  pb, a local WIMP density of  $0.3 \text{ GeV c}^{-2} \text{ cm}^{-3}$ , and a WIMP mass of  $100 \text{ GeV c}^{-2}$ . Plot from Green et al. [80].

For a signal-to-noise of less than 0.1 it becomes difficult to detect the anisotropy of the WIMP recoil events.

## 2.4 Existing directional dark matter detection experiments

Existing directional dark matter detectors are low pressure gaseous time projection chambers (TPCs). TPCs, discussed further in Section 3.1.1, consist of a volume of low pressure target gas in which WIMP-induced nuclear recoils are expected to produce tracks of ionisation of  $\sim$ mm length scale. The ionisation tracks are drifted in a constant electric field to a pixellated readout plane. This section discusses competing detector technologies for directional dark matter detectors based on this concept. A summary of the detectors is given in Table 2.2.

### 2.4.1 NEWAGE

The New Generation WIMP Search with Advanced Gaseous TPC Experiment (NEWAGE) detector is a low-pressure gaseous TPC dark matter detector operating in the Kamioka mine, Japan [84]. The current detector, NEWAGE-0.3a, is a prototype with a fiducial volume of  $0.0155\text{ m}^3$  of pure  $\text{CF}_4$  at a pressure of 152 Torr. The use of  $\text{CF}_4$ , which has a high drift velocity and thus low diffusion, combined with a relatively short drift distance makes high resolution 3D track reconstruction possible.

The NEWAGE detector uses a Micro Pixel Chamber ( $\mu$ -PIC) readout plane [85], a schematic of which is shown in Figure 2.11. Cathode strips with a series of holes of 0.25 mm diameter and 0.4 mm pitch are printed on one side of a PCB. On the other side perpendicular anode strips are printed with a series of  $50\ \mu\text{m}$  ‘dots’ that feed through the PCB and align on the centre of the cathode strip holes on the other side. High voltage is applied to the cathode strips creating a high field charge multiplication region between the anode dot and the cathode strip. Ionisation tracks arriving at the plane undergo multiplication in this region creating measurable charges on the anode and cathode strips. The perpendicular arrangement of the anode and cathode strips allows two-dimensional reconstruction of the ionisation track, with the third dimension possible through fast sampling of the charge deposition. This readout technology has the advantage that the entire charge multiplication and readout is on one robust PCB creating an extremely stable readout plane. PCB is a mature technology and, after potentially high start-up costs, mass production at low cost is feasible.

The present  $30.7 \times 30.7\text{ cm}^2$   $\mu$ -PIC readout consists of  $768 \times 768$  pixels of pitch  $400\ \mu\text{m}$ . The charge amplification in the  $\mu$ -PIC readout plane itself produces an amplification of  $\sim 10^3$ . A gas electron multiplier (GEM) plane is positioned 5 mm above the  $\mu$ -PIC plane for additional amplification [86]. The  $\mu$ -PIC has a total of  $2 \times 768$  strips, each of which is processed by an ASD (Amplifier/Shaper/Discriminator) chip producing a discriminated

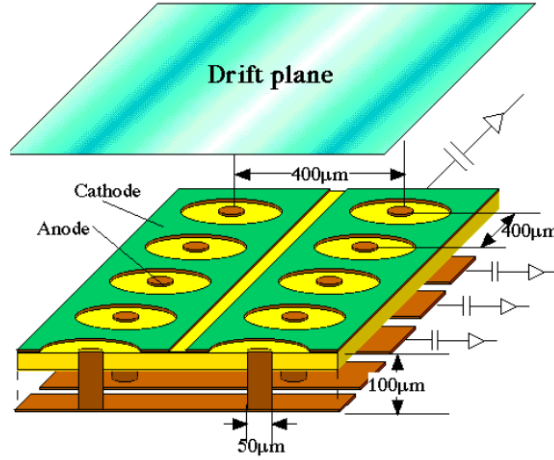


FIGURE 2.11: NEWAGE  $\mu$ -PIC readout plane. Anode strips (brown) with  $50\ \mu\text{m}$  ‘dots’ of  $400\ \mu\text{m}$  spacing and cathode strips (green) with  $0.25\ \text{mm}$  holes of  $400\ \mu\text{m}$  spacing are printed either side of a PCB (yellow). Figure from Miuchi et al. [84]

digital signal and an amplified analogue signal for each strip. The analogue signals from the anode are grouped together and used to trigger the readout electronics. Adjacent cathode strips are grouped by 16 and digitised at 100 MHz in order to determine the total charge in the track. The discriminated digital signals from both the anode and cathode strips are fed to a position encoding FPGA module with a sampling rate of 100 MHz that determines the individual hit positions via coincident signals on anode and cathode strips. The NEWAGE detector currently only has discriminated signals for individual pixels so is unable to determine charge distribution among individual pixels. The detector is, therefore, currently limited to axial track reconstruction, without head-tail sensitivity. The NEWAGE collaboration is developing position encoding electronics to enable measurement of charge distribution.

### 2.4.2 DMTPC

The Dark Matter TPC (DMTPC) collaboration operate a low-pressure gaseous dark matter detector at the WIPP Underground Laboratory in New Mexico [87]. The target volume is a 10-litre cylinder of 75 Torr  $\text{CF}_4$  with a fiducial target mass of 3.3 g. Figure 2.12 shows the top half of a symmetrical detector consisting of two back-to-back TPCs. Each TPC has a drift distance of 25 cm, from the  $-5\ \text{kV}$  cathode mesh at the top, to the grounded mesh electrode plane at the bottom. A constant drift field between these planes is maintained by stainless steel field shaping rings. The amplification region consists of a grounded mesh of  $28\ \mu\text{m}$  stainless steel wires of  $256\ \mu\text{m}$  pitch sitting 0.5 mm off the surface of a copper covered PCB sheet anode with fluorocarbon wire spacers. The copper plated central cathode is at 0.72 kV creating a field of  $14.4\ \text{kV cm}^{-1}$

in which electron avalanche occurs, producing both charge amplification of  $\sim 10^4$  and scintillation light.

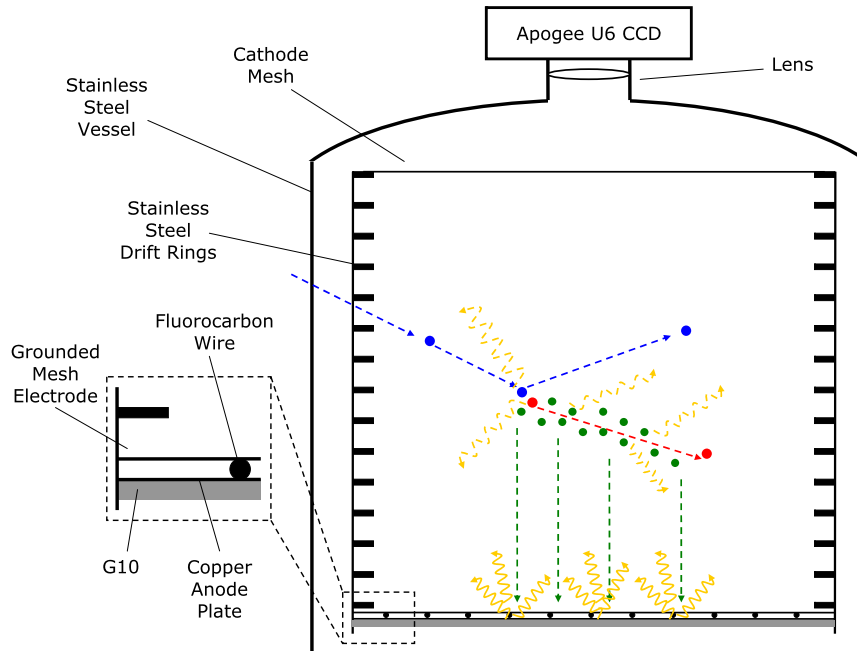


FIGURE 2.12: DMTPC 10-litre detector. Ionisation tracks in the target volume are drifted downwards to the high field region producing charge multiplication and scintillation that is captured by the CCD camera at the top. See text for details. Image from Ahlen et al. [87].

Scintillation photons are produced in numbers proportional to the charge in the avalanche region and are collected with a photographic lens and CCD chip. Each CCD chip has  $1024 \times 1024$  pixels each of which images a  $\sim 150 \times 150 \mu\text{m}$  area of the central anode giving a total area imaged of  $\sim 16 \times 16 \text{ cm}^2$ . A charge amplifier reads the integrated charge from the anode mesh, but this information is not currently used. To reduce potential contamination in the vessel the CCD and associated electronics are all located outside of the vessel. The detector currently only achieves 2D reconstruction of the track through the image of the projected track. The DMTPC experiment currently has a relatively high threshold of 100 keV, but at this energy head-tail sensitivity and an angular resolution of  $15^\circ$  have been demonstrated.

### 2.4.3 MIMAC

The Micro-TPC MAtrix of Chambers (MIMAC) collaboration is proposing a matrix of low pressure gaseous  $\mu$ -TPCs, each filled with either  $^3\text{He}$  or  $\text{CF}_4$ , for directional dark matter detection [88]. The current MIMAC prototype detector module, shown in

Figure 2.13, has a 6 cm drift region defined by five copper field shaping rings, a solid copper drift electrode and a bulk micromegas readout plane [89].

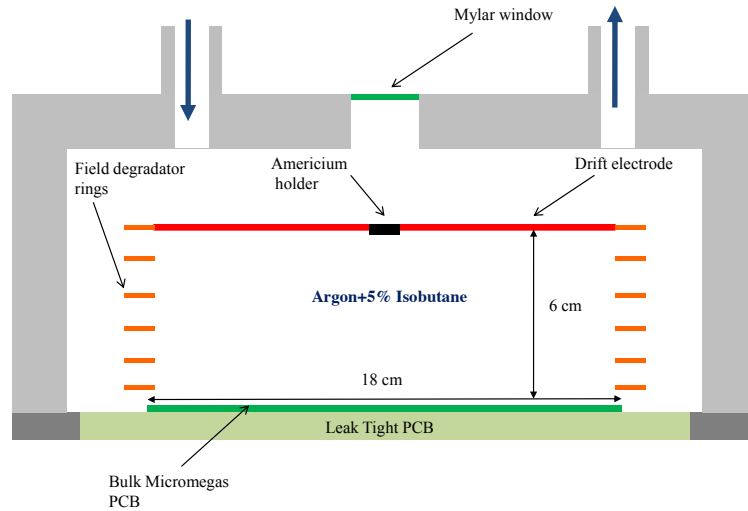


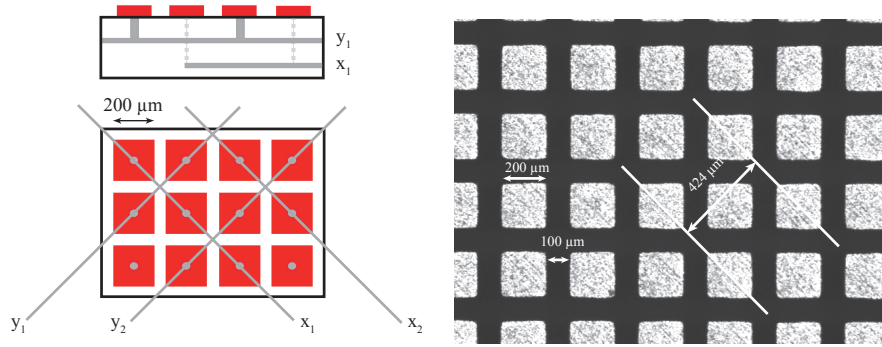
FIGURE 2.13: Prototype MIMAC detector. Ionisation electrons in the target volume drift downwards and are read out at the bulk micromegas readout plane. See text for details. Image from Iguaz et al. [90].

The bulk micromegas readout consists of a woven mesh cathode, with regularly spaced insulating pillars printed on it, mounted onto a pixellated anode readout PCB. The insulating pillars create a charge amplification region between the woven mesh and the PCB. The bulk micromegas in the prototype MIMAC detector has an area of  $10.8 \times 10.8 \text{ cm}^2$ . A voltage of 470 to 700 V is applied to a  $30 \mu\text{m}$  woven mesh, which is at a distance of  $256 \mu\text{m}$  from the readout PCB. As shown in Figure 2.14, the readout plane is a 1.6 mm thick PCB with  $200 \mu\text{m}$  square pixels separated by  $100 \mu\text{m}$ , each with a connection through the PCB [90]. The detector typically operates with an electric field of  $21.9 \text{ kV cm}^{-1}$  in the amplification region, resulting in a charge amplification of  $\sim 2 \times 10^4$ .

The bulk micromegas readout plane has 256 strips in each axis, each with  $424 \mu\text{m}$  pitch. Two-dimensional reconstruction is obtained from the track projection by detecting the charge created during the avalanche process in each pixel. The charge on each pixel is sampled at 40 MHz which, from the known drift velocity, gives the third dimension of the track.

The thick PCB detector plane is designed to withstand a vacuum such that it makes up one side of the vacuum vessel, as shown in Figure 2.13. This results in all readout electronics being located outside the vacuum vessel, minimising contamination in the detector. The detector modules have been designed to operate at both low pressures of

100s of mbar and high pressures of up to 3 bar to allow maximisation of either directional sensitivity or total mass.



(a) Schematic of the micromegas readout. Red squares indicate pixels on top layer of PCB, grey dots and lines indicate contacts and traces within PCB. (b) Photograph of micromegas readout. Light grey squares are pixels. White lines indicate traces within PCB.

FIGURE 2.14: Images of the bulk micromegas readout of the MIMAC detector. Images from Iguaz et al. [90].

	DRIFT-II	DMTPC 10-litre	MIMAC prototype	NEWAGE-0.3a
Location	Boulby, UK	WIPP, USA	LPSC, France	Kamioka, Japan
Gas	30-10 Torr CS <sub>2</sub> -CF <sub>4</sub>	75 Torr CF <sub>4</sub>	75 to 2250 Torr <sup>3</sup> He or CF <sub>4</sub>	152 Torr CF <sub>4</sub>
Fiducial volume	0.80 m <sup>3</sup>	0.01 m <sup>3</sup>	0.0007 m <sup>3</sup>	0.0155 m <sup>3</sup>
Fiducial Mass	136 g (32.6 g CF <sub>4</sub> )	3.3 g	0.3 to 7.6 g	11.5 g
Readout	MWPC (charge)	CCD (light)	Micromegas (charge)	GEM μ-PIC (charge)
Readout pitch	2 mm	256 μm	424 μm	400 μm
Dimension	3D	2D	3D	3D
Reference	This thesis	[91]	[90]	[84]

TABLE 2.2: Table of existing low pressure gaseous TPC experiments for directional dark matter searches.

## Chapter 3

# The DRIFT directional dark matter detector

The DRIFT collaboration is developing a directionally sensitive dark matter detector, which is potentially capable of using the strong directional anisotropy of WIMPs to provide unambiguous evidence for the existence of WIMP dark matter. The current iteration of the detector, the 1 m<sup>3</sup> DRIFT-II detector, operates underground at the Boulby Underground Laboratory.

This chapter begins with the theory of using a gaseous time projection chamber for directional dark matter detection (Section 3.1) and provides a full description of the experimental set up of the DRIFT-II dark matter detector (Section 3.2). The theory of track production in the detector volume through to track detection at the MWPC readout plane is discussed in Section 3.3. Following this, in Section 3.4, signal induction in the MWPC readout planes is investigated using a newly identified class of ‘spark-like’ events. Finally, in Section 3.5 a new method of measuring the reduced mobility of the target gas mixture, through these spark-like events during normal detector operation, is discussed. The results are compared to data from a dedicated single wire proportional counter experiment.

### 3.1 The DRIFT detector concept

#### 3.1.1 The time projection chamber

The *time projection chamber* (TPC), invented in 1974 by David Nygren of the Lawrence Berkeley National Laboratory [92], is a device for the detection and localisation of ionising particles. TPCs provide good spatial resolution over a large volume with high

efficiency using a fully digitised readout system.

Figure 3.1 illustrates a generic TPC with the detector volume defined by a high voltage cathode plane at one end, a lower voltage readout plane at the other, and a set of field shaping rings between the two to maintain a constant electric field throughout the drift volume. Any ionising particles entering the detector volume will create ionisation electrons which, in the constant electric field, drift uniformly to the detector readout plane. Various readout plane technologies exist (see Section 2.4) but, in general, the plane is a pixellated charge readout device that enables the localisation and reconstruction of the track in two dimensions. When combined with the time of charge arrival at the readout plane full three-dimensional positioning and reconstruction of the ionisation track can be achieved.

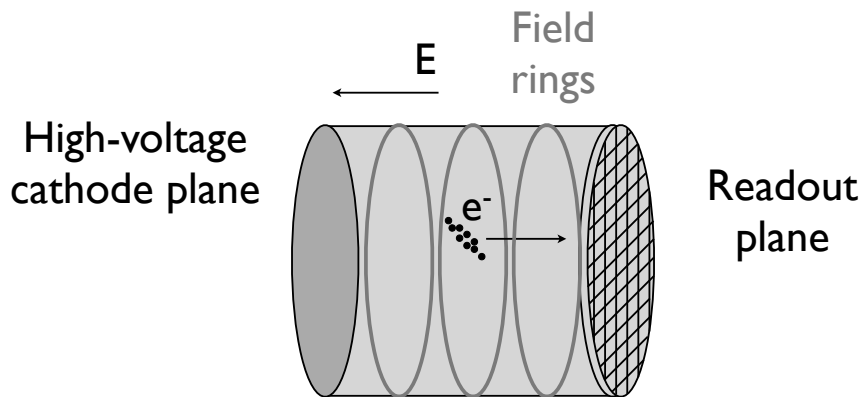


FIGURE 3.1: Schematic of a generic time projection chamber. Interactions in the target volume produce tracks of ionisation electrons that drift, in the uniform electric field, to the readout plane.

### 3.1.2 TPC for dark matter detection

The use of a low-pressure gaseous time projection chamber (TPC) for dark matter detection was conceived in 1994 by Buckland et al. [93]. The principle is that a WIMP-nucleus interaction in a low-pressure gas would create an ionisation track with a length of a few mm, compared to the  $\sim$ nm interactions that would occur in solid or liquid targets. The long track would potentially have an orientation that is resolvable and biased in the direction opposite to that of the incident WIMP. Such a detector may therefore be able to detect the strong directional anisotropy predicted in the WIMP signal, as discussed in Section 2.3.

The TPC used by Buckland et al. consisted of a  $0.125 \text{ m}^3$  cylindrical volume filled with a 20 Torr  $\text{CH}_4$  target gas and a readout plane consisting of an optically imaged multistage

parallel plate avalanche chamber [93]. The drift volume was surrounded in a superconducting magnet that produced a 0.45 T magnetic field in the direction of the electric field. This was required to suppress the transverse diffusion of the drifting electrons and hence preserve the directional information in the tracks. This experiment demonstrated the potential of the low-pressure gaseous TPC for WIMP detection but also demonstrated a significant restriction — the requirement of superconducting magnets around the drift volume to preserve directional information would severely limit the scalability and maximum target mass of a detector of this type.

A potential solution to this problem was suggested in 1999 when the low pressure negative ion time projection chamber (NI-TPC) was proposed for dark matter searches [67]. The NI-TPC uses an electronegative gas as a target material so that ionisation electrons rapidly attach to electronegative gas molecules to produce a track of negative ions. Massive ions, unlike electrons, remain in approximate thermal equilibrium with the gas, even in high drift fields. This means that both transverse and longitudinal diffusion of the track are suppressed to thermal levels as the track is drifted to the readout plane so that metre-scale drift distances are possible, without the need for strong magnetic fields [94].

### 3.1.3 Negative ion drift gas choice

A suitable gas for NI drift must have sufficient electronegativity that electron attachment occurs almost immediately, before the fast moving ionisation electrons have time to diffuse. However, it is equally critical that the electronegativity is small enough that the electrons will detach and avalanche in the high field region of the readout plane. A suitable gas for NI drift must therefore be mildly electronegative.

In order to be a suitable target for a dark matter detector, the target gas must also be stable, so as not to produce WIMP-like interactions intrinsically. For scalability to large volumes, the preferred gas must be available at an appropriate level of purity, at a reasonable cost, and must be gaseous at room temperature at the desired target pressure. An ideal target gas should also have a large atomic number for sensitivity to spin-independent (SI) WIMP interactions or an odd number of nucleons for spin-dependent (SD) WIMP searches. This is discussed in Section 2.1.6.

With an electron affinity of  $\sim 0.5$  to 1 eV and fast electron attachment [95], carbon disulphide ( $\text{CS}_2$ ) is understood to be a suitable NI-TPC target gas [96]. Sulphur, with an atomic mass of 32, provides reasonable sensitivity to SI WIMP-nucleus interactions. Carbon and sulphur are, however, dominated by isotopes with no unpaired nucleons, so the  $\text{CS}_2$  target is insensitive to SD WIMP interactions. Providing sufficient  $\text{CS}_2$  is present in the target gas for NI drift to be maintained, gases with more favourable

characteristics for dark matter searches may be added to enhance the sensitivity of the detector.

## 3.2 The DRIFT-II detector

The Directional Recoil Identification From Tracks (DRIFT) detectors, based on the NI-TPC concept, are the world's first large-scale directionally sensitive dark matter detectors. The current iteration is the  $1\text{ m}^3$  DRIFT-II [97]. From current limits on WIMP-nucleus cross-sections it is likely that DRIFT may ultimately require a volume on the order of  $\sim 10$  to  $100\text{ m}^3$  to achieve the target mass required to detect WIMP dark matter. For this reason the DRIFT detectors have been designed to be cost effective and scalable.

The DRIFT-II detector, shown in Figure 3.2, is symmetric about a  $1\text{ m}^2$  central cathode plane. On each side is a 50 cm field cage with a  $1\text{ m}^2$  multi-wire proportional chamber (MWPC) readout plane at the end. This creates two back-to-back TPCs, each with a volume of  $1 \times 1 \times 0.5\text{ m}^3$ . The structural support is constructed from transparent acrylic that is used for its high radiopurity. The detector sits on a bearing loaded stainless steel plate, which allows the detector to be easily moved into and out of a  $1.5 \times 1.5 \times 1.5\text{ m}^3$  stainless steel vacuum vessel, which is filled with the low-pressure target gas — typically 40 Torr  $\text{CS}_2$ .

### 3.2.1 Boulby Underground Laboratory

As with all operational dark matter detectors, DRIFT-II is situated deep underground in order to shield the detector from cosmic ray muon-induced neutrons (Section 2.2.2). DRIFT-II is located at the Boulby Underground Laboratory, an underground science facility located within the Boulby Mine, a working potash mine on the north east coast of England. The laboratory is at a depth of 1070 m ( $2805 \pm 45$  metres water equivalent), at which cosmic ray muons are attenuated by a factor of  $\sim 10^6$  relative to the surface, to levels of  $(4.09 \pm 0.15) \times 10^{-8}\text{ cm}^{-2}\text{ s}^{-1}$  [98]. Figure 3.3 shows a comparison of the depths and resulting muon flux of various international underground research facilities.

The cavern rock surrounding the Boulby Underground Laboratory, primarily NaCl salt, has been shown to be low in natural radioactivity with levels of  $67 \pm 6$  ppb uranium, and  $125 \pm 10$  ppb thorium [99]. The level of neutrons above 0.5 MeV coming from the rock surrounding the Boulby Underground Laboratory has been measured as  $(1.72 \pm 0.61(\text{stat}) \pm 0.28(\text{sys})) \times 10^{-6}\text{ cm}^{-2}\text{ s}^{-1}$  [100].

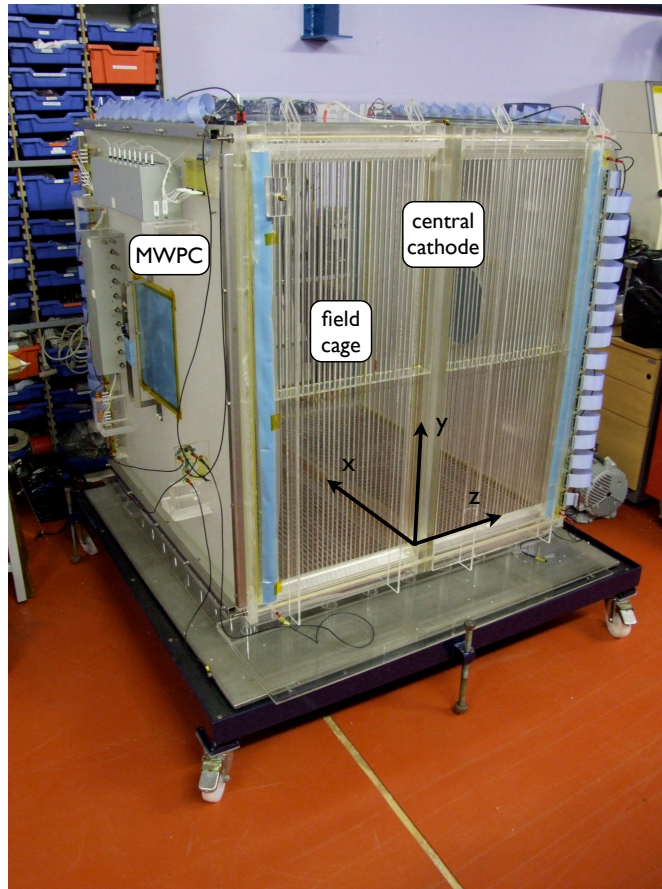


FIGURE 3.2: Photograph of the DRIFT-IIId detector underground at the Boulby Underground Laboratory. Arrows show the defined detector axes.

### 3.2.2 Detector hardware design

**Central cathode** — The high-voltage central cathode plane results in a drift field across the detector volume so that ionisation tracks occurring in the detector volume drift to the MWPC readout plane. The central cathode consists of a plane of 512 vertical  $20\ \mu\text{m}$  diameter stainless steel wires with a spacing of 2 mm across an open acrylic frame<sup>1</sup>. The wire plane is in contact with a hollow 6 mm diameter stainless steel tube (a field cage ring) that runs inside the acrylic frame. The cathode is held at a potential of  $-37.5\ \text{kV}$  via a high-voltage feedthrough in the roof of the vacuum vessel. The central cathode plane is in electrical contact with the field cage on either side, via a spring loaded  $33\ \text{M}\Omega$  resistor. The drift field between the central cathode and the MWPC readout plane is typically  $\sim 600\ \text{V cm}^{-1}$ .

**Field cages** — The two field cages, each 50 cm in length and located either side of the central cathode, are used to ensure a constant drift field throughout the target volume.

<sup>1</sup>Here the standard wire plane cathode is described. This has recently been replaced with a thin film cathode that is described in Section A.3.

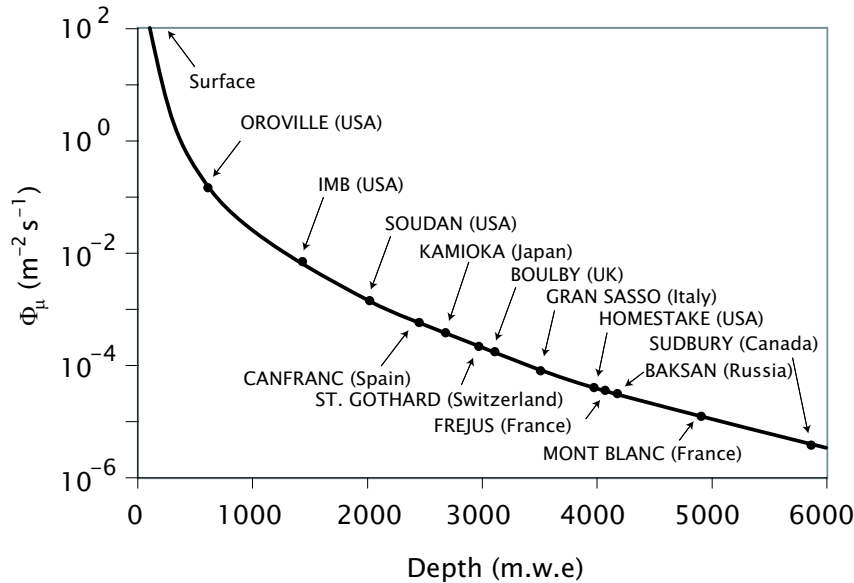


FIGURE 3.3: Depths of underground laboratories from around the world in metres water equivalent (m.w.e) against muon flux. Plot from Morales, J. et al. [101].

Each field cage consists of 31 hollow 6 mm diameter stainless steel tubes with 15 mm spacing in an acrylic support frame. Each field ring is in electrical contact with the next via a 33 M $\Omega$  resistor and the final field cage ring in the chain on either side is grounded via a 66 M $\Omega$  resistor. This resistor ladder steps the voltage down across each field ring to create a smooth electrical field from  $-37.5$  kV at the central cathode to  $-3$  kV at the MWPC readout plane. The acrylic frame of the field cages, as well as providing structural support for the field rings, provides electrical insulation to avoid sparking between the high-voltage field cage and the grounded metal vacuum vessel.

**MWPC readout planes** — The MWPC readout planes are used to amplify the charge created in the drift volume by the particle interaction and to provide localisation of the charges such that ionisation tracks can be reconstructed. The mechanism of this process will be discussed in detail in Section 3.3.1. Each MWPC consists of 3 planes of wires. The centre plane is the *anode* plane of 552 vertically oriented 20  $\mu\text{m}$  diameter stainless steel wires with a spacing of 2 mm. On either side of the anode plane, at a distance of 10 mm, is a *grid*<sup>2</sup> plane of 552 horizontally oriented 100  $\mu\text{m}$  diameter stainless steel wires, also with a spacing of 2 mm. The grid planes are held at a potential of  $\sim -3$  kV producing uniform electric field lines between the two planes, except in the immediate vicinity of the anode and grid wires.

The anode wire plane and the inner grid plane are instrumented with charge sensitive electronics (Section 3.2.3). The outer grid plane is required to ensure symmetric field

<sup>2</sup>The cathode planes of the MWPC are referred to as grid planes to avoid confusion with the central cathode.

lines on the anode wires but is not instrumented. Of the 552 wires in the anode plane the 11 outermost wires on each side act as *guard wires*, used to step the potential up from ground to 3 kV over three 33 M $\Omega$  resistors. This minimises distortions of the field that arise at the edges of the MWPC plane. The next 41 anode wires inwards are grouped together to form a *veto region*, used for tagging events that enter the drift volume from the outside. On the grid plane the outermost 52 wires are veto wires. The remaining 448 central wires of the anode and grid planes make up the fiducial area of the MWPC giving a 0.80 m<sup>3</sup> fiducial volume.

The MWPC wires are attached to PCBs mounted on an acrylic frame, supported by a thick acrylic backplate. The backplate, which has stainless steel support bars, is required to counter warping in the backplate caused by the tension of the MWPC wires. The backplate also houses the preamplifiers, grouping boards and a retractable <sup>55</sup>Fe calibration source.

**Shielding** — The exceptional gamma rejection capability of the DRIFT detectors means that gamma-ray backgrounds are negligible and lead shielding is not required [76]. This is crucial in maintaining a low modular cost of the detector. The neutron background in the underground laboratory is low, estimated as approximately one neutron-induced nuclear recoil per day in an unshielded DRIFT detector, from uranium and thorium in the cavern walls [102]. However, as neutrons produce events indistinguishable from the expected WIMP signal, neutron shielding to eliminate this background is essential. The entire vacuum vessel is surrounded by a plywood housing that is filled with loose polypropylene pellets providing a covering of at least 50 cm on all sides. This provides the equivalent of  $\sim 30$  cm of solid hydrocarbon shielding, reducing the neutron interactions in the detector by a factor of  $\sim 10^4$ . Simulations estimate the remaining neutron background from the cavern walls to be an acceptable level of  $< 0.3$  events per year [97].

**Gas system** — Although CS<sub>2</sub> is a stable TPC gas, even with relatively high levels of air contamination, detector stability has been shown to fall rapidly with contamination of  $\gtrsim 1\%$  [103]. In addition, radon emission by detector components leads to accumulation of radon in the target gas which, as discussed in Section 6.1.4, can result in WIMP-like nuclear recoils. To maintain adequate purity of the target gas, and to prevent accumulation of radon over long periods of operation, a continuous supply of target gas is flowed through the vacuum vessel. Reducing air contamination below 1% requires a flow equivalent to around one vessel (3375 L) of 40 Torr gas per day. Figure 3.5 shows a schematic of the standard gas flow system<sup>3</sup>. A scroll pump is attached to the vacuum vessel output and pumps continuously during normal operation, removing gas

<sup>3</sup>This section describes the standard gas flow system for operation with pure CS<sub>2</sub>. Recent operation with gas mixtures has required a new gas mixing system that is described in Section 4.3.



(a) With the front neutron shielding removed for access. (b) With the front neutron shielding constructed. Orange ports in the front are areas for insertion of neutron source.

FIGURE 3.4: Photos of the DRIFT-IIId vacuum vessel and neutron shielding housing.

at a fixed rate determined by a needle valve. The gas is continually replenished from a  $\text{CS}_2$  cylinder, attached to the vacuum vessel input via a mass flow controller (MFC). The MFC, which is coupled to the pressure of the vacuum vessel, varies the flow rate to maintain a constant pressure in the vessel. The  $\sim 400$  Torr vapour pressure of  $\text{CS}_2$  at room temperature is sufficient to maintain flow rates of up to  $\sim 5$  times the typical flow rate. Waste gas that is removed from the vessel is passed through a water trap that cools and condenses the gaseous  $\text{CS}_2$ , trapping  $>90\%$ . The output of the water trap is directed through a charcoal filter to absorb any remaining  $\text{CS}_2$ , before the clean air is vented to the mine. A  $\text{CS}_2$  gas monitor on the output ensures air from the charcoal filter is free from  $\text{CS}_2$ . A failure of the MFC, or exhaustion of the  $\text{CS}_2$  supply may result in a pressure drop in the vacuum vessel during operation. This lowers the breakdown voltage in the high-voltage MWPC readout planes, potentially leading to damage of sensitive preamplifier electronics, or, in severe cases, breakage of the  $20\ \mu\text{m}$  anode wires. A low-pressure hardware cutoff is therefore installed, which kills all high-voltage systems if pressure in the vacuum vessel falls below 39.5 Torr.

### 3.2.3 Detector readout electronics

**Wire grouping** — As described in Section 3.2.2, the fiducial area of the anode and grid planes within the MWPC are each defined by 448 wires with a spacing of 2 mm. Since a WIMP-induced nuclear recoil in the low-pressure gas is expected to have a maximum length of a few mm (Section 3.3.1), the resulting ionisation track will never traverse more than a few wires in either plane. To reduce the number of electronics channels required for readout, every eighth wire is grouped, as shown in Figure 3.6, to produce

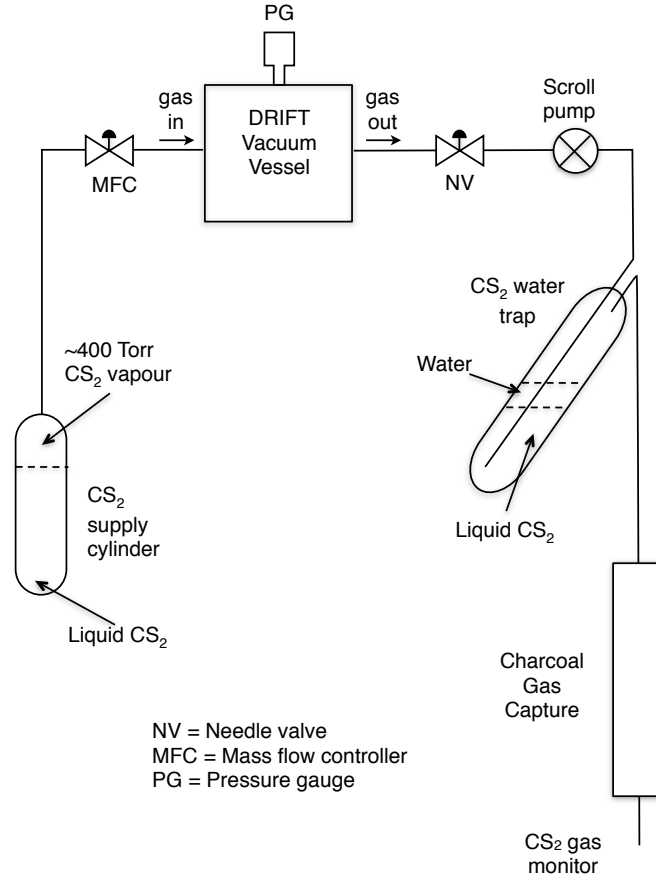


FIGURE 3.5: Schematic diagram of the standard gas flow system. A scroll pump attached to the vacuum vessel output operates continuously removing gas at a rate determined by the needle valve (NV). The  $\text{CS}_2$  cylinder attached to the input supplies the target gas at a rate determined by the mass flow controller (MFC), which is coupled to the pressure of the vacuum vessel. Waste gas passes through a water trap followed by a carbon trap. See text for full details.

eight readout lines per plane, where each line is connected to a total of 56 wires. The grouping of wires means that the  $0.80\text{ m}^2$  fiducial area of the MWPC can be read out with only 16 channels of electronics, essential in ensuring the cost effectiveness, and therefore scalability, of the DRIFT-II detector. The compromise of this wire grouping is that the absolute  $x$  and  $y$  coordinates of events within the detector volume are not known, only the  $\Delta x$  and  $\Delta y$ . The  $(x, y)$  position of the event, however, is not required information.

The veto regions — the 52 outermost wires on either side of the grid plane, and the 41 wires between the guard wires and fiducial wires on either side of the anode plane — are grouped together to form two veto channels per MWPC.

**Amplification electronics** — After grouping, all anode, grid, and veto lines are processed by identical electronics, with the exception that gains on the grid channels are

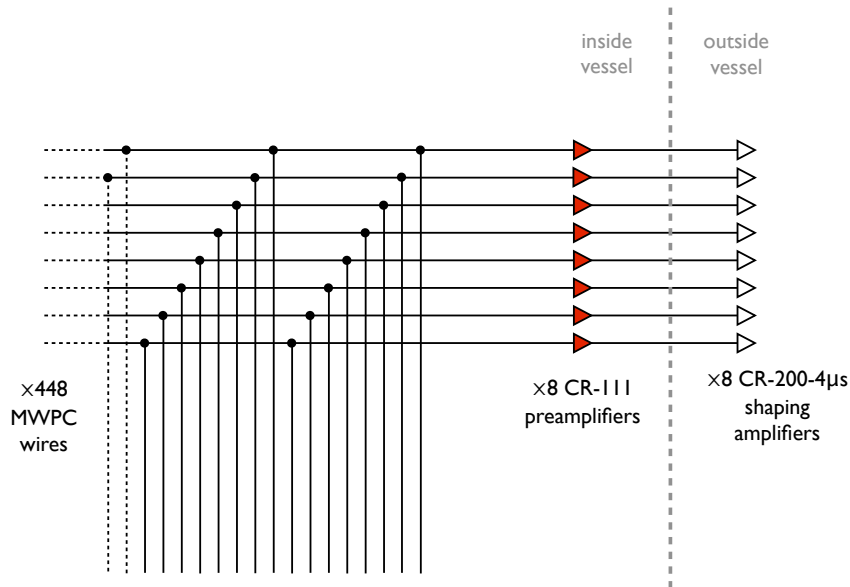
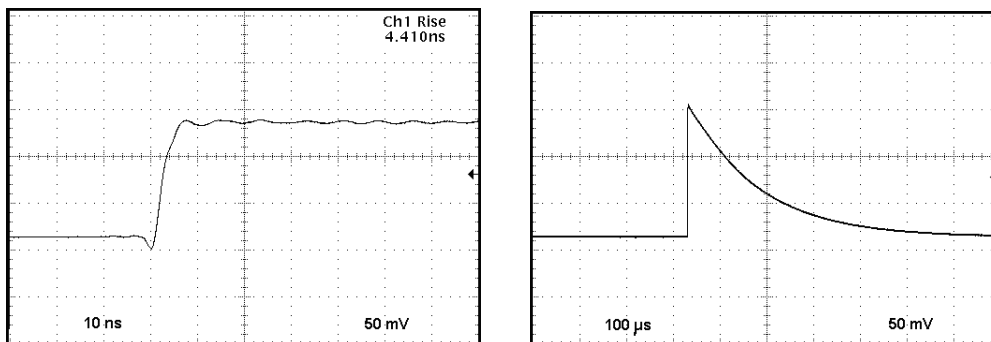


FIGURE 3.6: Schematic of the wire grouping in the fiducial volume of the detector.

set higher by a factor of four. Each line first passes through a Cremat CR-111 charge sensitive preamplifier circuit [104] that converts the charge to a voltage with a scale of  $0.15 \text{ V pC}^{-1}$ , as shown in Figure 3.7. The preamplifier circuits are mounted directly on the acrylic frame of the MWPC, as close as possible to the wires, in order to minimise cable distances and potential sources of signal interference.



(a) 10 ns timescale.

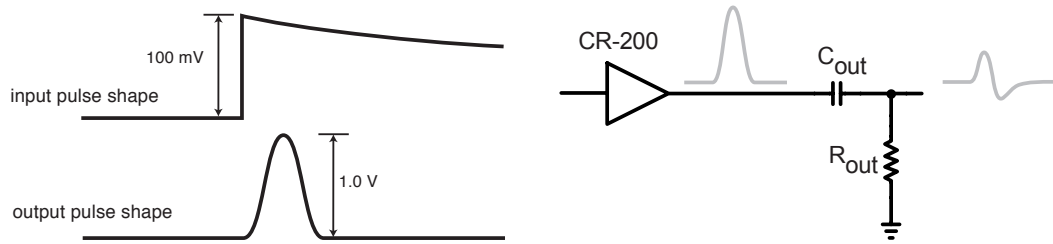
(b) 100 μs timescale.

FIGURE 3.7: Typical response to a fast square wave of the Cremat CR-111 charge sensitive preamplifier circuit [104].

The preamplifier output then passes through a Cremat CR-200  $4 \mu\text{s}$  shaping amplifier circuit [105]. This turns the slow exponential decay output of the charge amplifiers into a Gaussian profile with a FWHM of  $9.6 \mu\text{s}$  and an amplitude ten times that of the input

pulse as shown in Figure 3.8(a). The purpose of the shaping electronics is to boost the signal-to-noise ratio and to restore the pulse to the baseline quickly to prevent signal pileup. Though the DRIFT detector does not have high event rates, the grouping of the wires means that long tracks, such as alphas, create a number of pulses on a single channel in quick succession that may suffer from pileup without the baseline restoration of the shaping amplifiers. The amplification stage would ideally be physically close to the preamplification stage to avoid signal interference through pickup. However, the high power output of the shaping amplifiers would result in unacceptably high temperatures in the detector volume, so the preamplification stage is located outside the vacuum vessel. The DRIFT collaboration is currently investigating the replacement of this section of electronics for a less aggressive filtering solution that will more accurately preserve charge density information of the track.

After amplification the signal is passed through an RC high-pass filter to remove low frequency ( $\sim 50$  Hz) baseline wander which is suspected to come from mains pickup. Although this noise could in principal be removed in software afterwards, its removal is necessary so that the pulse height trigger can function. This filter has the effect of making the pulse bipolar, as shown in Figure 3.8(b). This not only has the undesirable effect of reducing the amplitude of the signal, but also adds another level of pulse shape manipulation leading to further loss of charge density information. Ways of removing this stage of filtering are also being considered.



(a) Input to shaping amplifiers has an exponential decay of time constant  $150 \mu\text{s}$ . Output is Gaussian with  $4 \mu\text{s}$  standard deviation. (b) Effect of the RC high-pass filter on the signal profile. In the DRIFT-IIId detector  $C_{\text{out}}=2200 \text{ pF}$  and  $R_{\text{out}}=50 \Omega$ .

FIGURE 3.8: Response of pulse shaping electronics to the output of the preamplifier.

**Data acquisition system** — DRIFT-IIId has two separate data acquisition (DAQ) systems. The *slow DAQ* system is used to monitor slowly changing environmental measurements such as the laboratory temperature, the vacuum vessel pressure and the currents and voltages of the high-voltage system. Each of the environmental monitoring devices outputs a voltage proportional to its reading that is recorded every  $\sim 10$  seconds using an Agilent 34970A data acquisition unit [106]. The slow DAQ runs continuously,

recording information crucial for real-time monitoring of detector stability, as well as information that may need to be considered later in data analysis.

The *fast DAQ* system consists of nine 4-channel 12-bit 1 MHz digitisation units that process the 36 signal channels of the two MWPC readout planes. The DAQ has no hardware trigger and all channels are digitised continuously during operation. A software trigger is implemented so waveforms are only recorded from the buffer to hard disk if the anode sum line crosses a predetermined voltage threshold. The software triggering system enables thresholds to be set remotely and allows thresholds to be automatically adjusted for different run modes. The collaboration is currently commissioning a new DAQ with increased computing power that will enabling a significant amount of digital signal processing, such as noise removal techniques, to be performed on-the-fly. The new DAQ will allow the replacement of some of the aggressive hardware filtering with digital software filtering, which will both simplify the detector hardware, and potentially result in improved preservation of track charge density information.

### 3.2.4 The DRIFT-II event file

Figure 3.9 shows a typical DRIFT-II event file containing a  $10\ \mu\text{s}$  duration ( $3\ \mu\text{s}$  pre-trigger,  $7\ \mu\text{s}$  post-trigger) of the 36 digitised waveforms (left and right MWPCs, each containing 8 anode fiducial lines, 1 anode veto line, 8 grid fiducial lines, and 1 grid veto line). Waveforms are sampled at 1 MHz so each line consists of 10000 12-bit integers. The event file is separated into two plots with the left and right plots containing the waveforms of the left and right MWPC respectively.

For each MWPC, 21 lines are plotted on a mV scale each with an arbitrary offset applied to each channel for visualisation. The lines are identified with labels on the right-hand side of each plot with the prefixes L and R corresponding to left and right MWPC respectively. A1 through A8 correspond to the anode fiducial lines. AS is the anode sum line — a virtual line produced by adding waveforms A1 through A8. VG and VA are the grid veto line and anode veto line respectively and VS is the virtual sum of VG and VA waveforms. An important consideration of the DRIFT-II event files is that anode waveforms are always shown inverted. This results in avalanches in the MWPC, which deposit negative charge on anode wires and positive charge on grid wires, producing positive going pulses on both anode lines and grid lines.

A typical neutron-induced nuclear recoil track can be seen in the lines of the right-hand side MWPC. The event results in charge on primarily two anode lines (RA3 and RA4) and two grid lines (RG1 and RG2). Vertical black markers on these lines, and on the anode sum line, indicate that these lines contain voltage samples that have

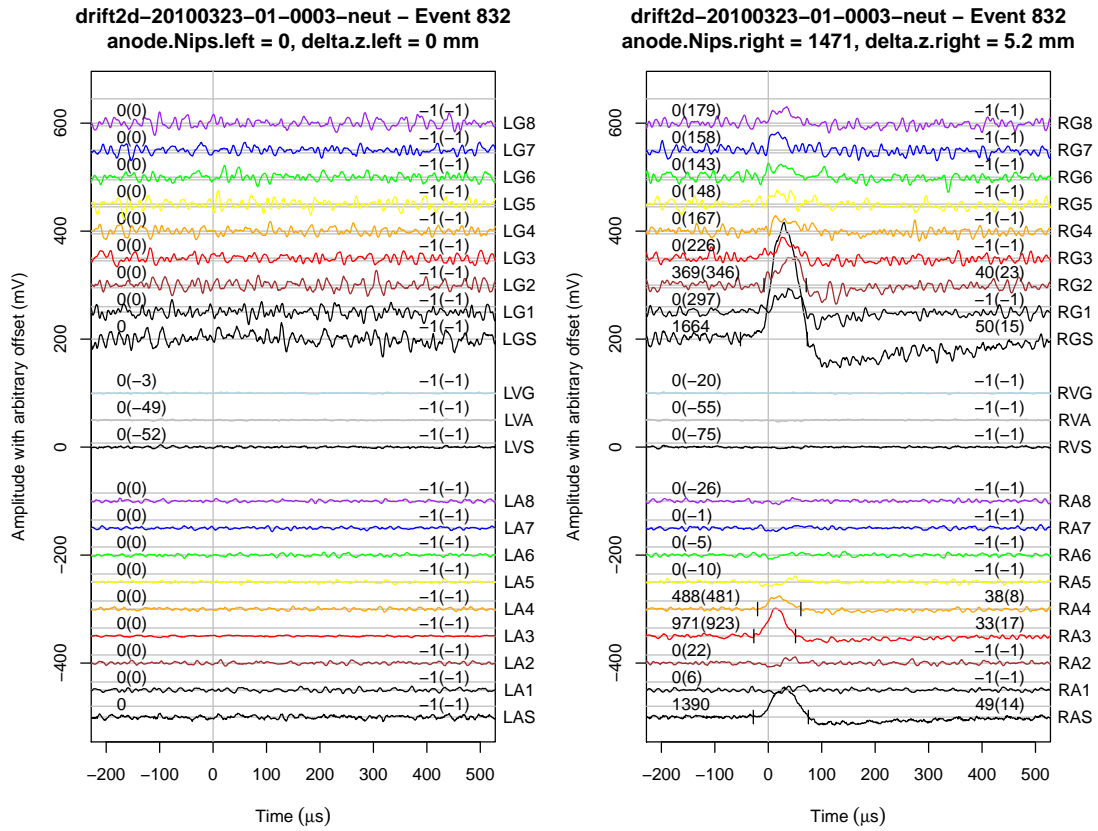


FIGURE 3.9: A typical DRIFT-II event file containing a neutron-induced nuclear recoil track. Only  $700\ \mu\text{s}$  of the  $10000\ \mu\text{s}$  event file is plotted. DAQ trigger time is  $\text{Time} = 0$ . Left and right plots correspond to left and right MWPC respectively. Waveform labels correspond to the line identity: L and R are left and right MWPC respectively, G1 to G8 correspond to the grid fiducial lines and VG the grid veto line. Similarly A1 to A8 correspond to the anode fiducial lines and VA the anode veto. GS, AS and VS correspond to the virtual sum of the eight grid fiducial lines, sum of the eight anode lines and sum of the two veto lines respectively. Anode waveforms are inverted so that charge depositions (which are negative on anode wires, positive on grid wires) appear as positive going pulses on all lines. See text for further details.

crossed the analysis threshold and the lines contain hits that have been parameterised. Parameterisation of events is discussed in detail in Section 5.3.1. Each signal line in the plot (except the sum lines) has four numbers above it corresponding to parameterisation of hits on that line. These indicate, from left to right, waveform parameters  $eventNips$ ,  $eventSumNips$ ,  $fwhm$  and  $risetime$ , definitions of which are given in Section 5.3.1.

### 3.3 Track production and readout in DRIFT

#### 3.3.1 Track production

**Ionisation** — At energies relevant to dark matter detection, particles may transfer energy to the target medium via two mechanisms: the *nuclear channel* — through collisions with the nuclei of the medium, and the *electronic channel* — through electromagnetic interactions with the atomic electrons in the medium.

The number of ion pairs (NIPs) liberated in an interaction is dependent on the energy and type of interaction that caused it. In an event that occurs entirely through the electronic channel, e.g. an electron recoil from a gamma-ray interaction, the NIPs produced is directly proportional to the energy  $E$  of the ionising particle, and is given by

$$\text{NIPs} = \frac{E}{W} \quad (3.1)$$

where  $W$  is the *W-value*, defined as the average energy required to create a single ion pair. The W-value is a property of the target gas and must be measured experimentally. The W-value for CS<sub>2</sub> is  $24.9 \pm 0.8$  eV [107].

For events in which energy is lost through both the electronic and the nuclear channels, such as nuclear recoils, the NIPs produced is not directly proportional to the energy of the ionising particle, and is instead given by

$$\text{NIPs} = Q(E) \cdot \frac{E}{W} \quad (3.2)$$

where  $Q(E)$  is the *ionisation quenching factor*.  $Q(E)$  is dependent on both the energy of the charged particle, and the medium through which it is travelling. Figure 3.10 shows the quenching factors of carbon and sulphur nuclear recoils in CS<sub>2</sub> from analytical calculations and from measurement and simulations [108].

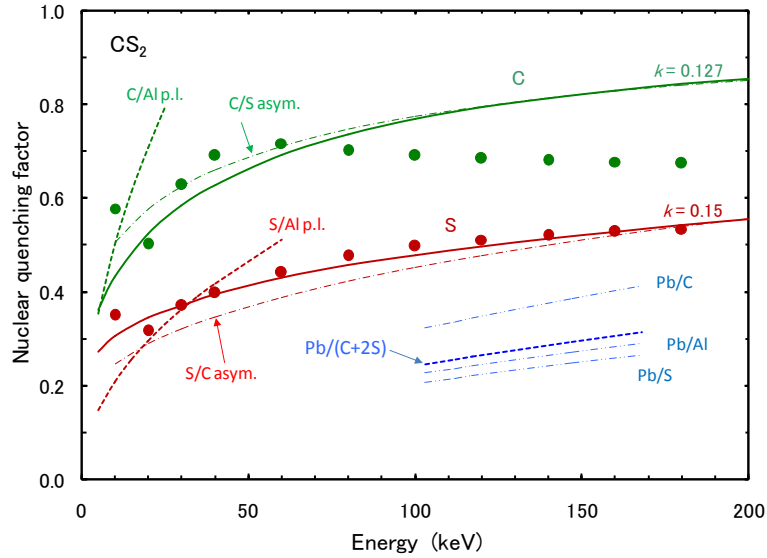


FIGURE 3.10: Quenching factors of carbon and sulphur recoils. Lines indicate estimates calculated by Hitachi et al. [108]. Solid lines: C recoils in C (green) and S recoils in S (red). Dot-dashed lines: C recoils in S (green) and S recoils in C (red). Blue lines are estimated quenching factors for heavy Pb ions in  $\text{CS}_2$ . Filled circles indicate results from measurement and part simulation performed by Snowden-Ifft et al. [109]: C in  $\text{CS}_2$  (green) and S in  $\text{CS}_2$  (red). Plot from Hitachi [108].

**Range** — The total ionisation produced in an event is distributed over the *range* of the track. The track range depends on the target medium, and the energy and type of particle. As illustrated in Figure 3.11, the range, if measured in conjunction with energy, offers a powerful method of particle identification. Low mass electrons, have ranges much longer than nuclei of the same energy, and similarly, alpha particles have a larger range than carbon and sulphur nuclear recoils. It is the significant difference in range between recoiling nuclei and recoiling electrons of the same energy that proves an extremely effective method of discriminating electron recoils from nuclear recoils in the DRIFT detectors.

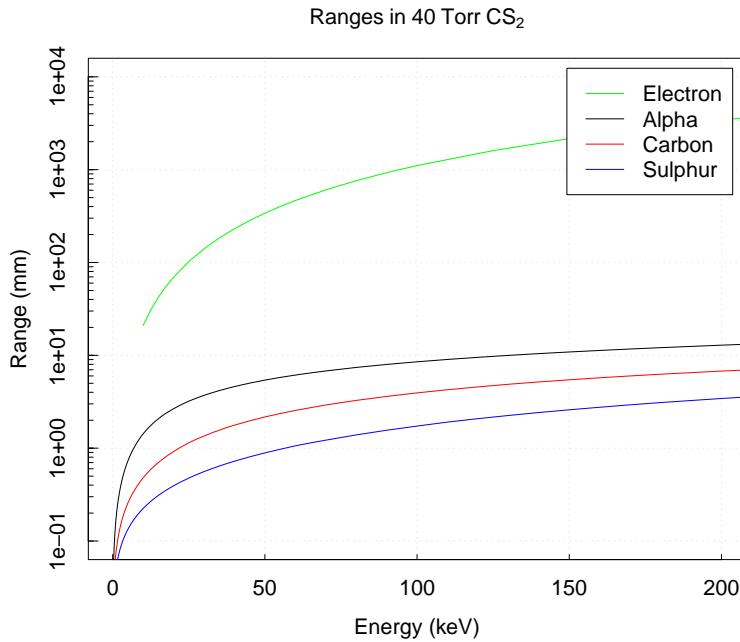
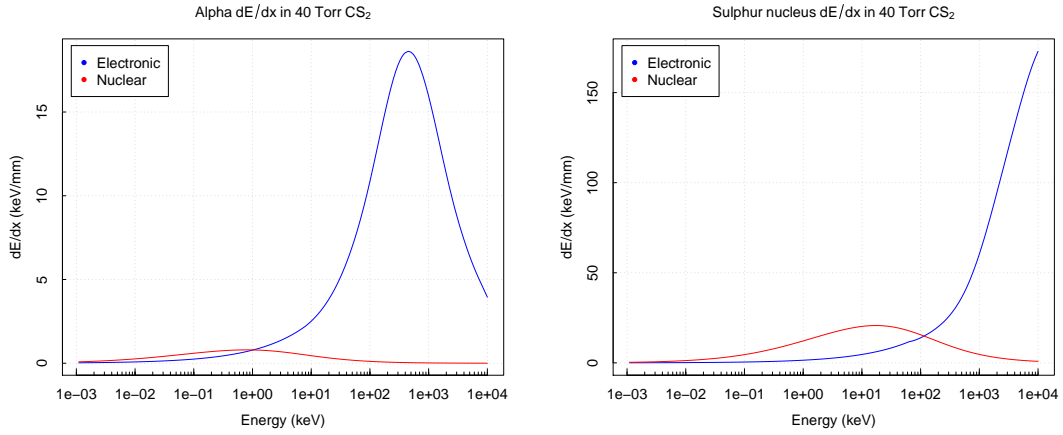


FIGURE 3.11: Simulated ranges of electrons, alphas, and carbon and sulphur nuclei in 40 Torr  $\text{CS}_2$ . Electron ranges simulated using ESTAR [110]. Ion ranges simulated using SRIM [111].

$dE/dx$  — As illustrated in Figure 3.12 the average energy loss per unit length in the target ( $dE/dx$ ) is dependent on the energy of the particle and is therefore not constant over the length of the track. This has the important consequence, for a directional dark matter detector, that it leads to a potential asymmetry in the ionisation track that may enable the full vector direction of the track to be determined. The energy dependence of  $dE/dx$  in the detectable electronic channel depends on the type of particle. In general the heavier the incident particle, the higher the point in energy where the nuclear channel begins to dominate over the electronic channel. Thus, as shown in Figure 3.12(a), for a typical  $\sim\text{MeV}$  background alpha interaction in 40 Torr  $\text{CS}_2$  a large head-tail asymmetry is observed. However, as shown in Figure 3.12(b), a  $\sim 100$  keV sulphur recoil, that might be expected from a WIMP-nucleus interaction, is below the peak of the electronic  $dE/dx$ , making it more difficult to resolve any head-tail asymmetry.

### 3.3.2 Track drifting and diffusion

Immediately after an ionising interaction in the DRIFT detector volume there exists a track of liberated ionisation electrons and corresponding positive ions. The total number and distribution of ion pairs in the track contains information on the type of interacting particle, its energy, and the direction in which it was travelling. Directional detectors, such as DRIFT, aim to extract as much of this information, as accurately as possible.



(a)  $dE/dx$  for an alpha particle in 40 Torr CS<sub>2</sub>. (b)  $dE/dx$  for a sulphur nucleus in 40 Torr CS<sub>2</sub>.

FIGURE 3.12: Electronic (blue) and nuclear (red)  $dE/dx$  values calculated using SRIM [111].

The constant electric field throughout the target volume drifts the ion pairs apart, minimising the amount of recombination of ionisation electrons with positive ions, which would reduce the observed ionisation. Due to the relatively high electronegativity of the CS<sub>2</sub> target gas in the DRIFT detectors, electron attachment, the attaching of each ionisation electron to a neutral target gas atom, occurs almost immediately. This happens before any measurable diffusion of the ionisation electrons [112], leaving a track of approximately equal numbers of negative and positive CS<sub>2</sub> ions. The positive ions, from which the ionisation electrons were liberated, drift to the central cathode plane. Since there is no charge readout instrumentation on the central cathode plane, the positive ions are lost. The negative CS<sub>2</sub> ions drift, whilst maintaining the structure of the track due to the constant electric field throughout the drift volume, towards the readout plane, where they are detected.

**Drift velocity** — From the constant electric field in the target volume, negative ions experience a force that accelerates them towards the MWPC. This acceleration is countered by a resistive force from collisions with the target gas molecules such that ions travel at a constant *drift velocity*. The drift velocity is dependent on the strength of the electric field, the number density of molecules in the gas, and the interaction cross-section. The drift velocity is given by

$$v_{\text{drift}} = \frac{\mu E}{p} \quad (3.3)$$

where  $\mu$  is the *reduced mobility*, an experimentally determined gas constant that contains information on nuclear cross-sections and number density. The drift velocity in DRIFT-II d is typically  $\sim 60 \text{ m s}^{-1}$  [113].

**Diffusion** — The random collisions encountered as negative CS<sub>2</sub> ions drift from the point of interaction to the MWPC readout plane also cause a point-like charge distribution to diffuse into a ‘cloud’ of charge. In the simplified case of the diffusion being equal in all dimensions this charge ‘cloud’ has a Gaussian density distribution. The *diffusion width*, the standard deviation of this distribution for a point-like charge drifting a distance of  $L$  in an electric field  $E$ , can be expressed as [114]

$$\sigma = \sqrt{\frac{4\epsilon L}{3eE}} \quad (3.4)$$

where  $e$  is the electronic charge and  $\epsilon$  is the energy of the diffusing body. Assuming that the body has only thermal energy, i.e.

$$\epsilon = \frac{3}{2}k_B T \quad (3.5)$$

at temperature  $T$ , Equation 3.4 becomes

$$\sigma = \sqrt{\frac{2k_B T L}{eE}}. \quad (3.6)$$

Measurements of  $\sigma$  in pure CS<sub>2</sub>, as well as other CS<sub>2</sub> mixtures relevant to DRIFT, have shown that diffusion of negative CS<sub>2</sub> ions is consistent with thermal diffusion [94, 112]. In DRIFT-IIId, with a maximum drift distance of 50 cm and an electric field of  $\sim 550 \text{ V cm}^{-1}$ , this leads to a maximum diffusion of  $\sim 0.6 \text{ mm}$ , in comparison with expected WIMP-induced nuclear recoil ranges on the order of a few mm. This estimate demonstrates a limit on the potential for track reconstruction precision and provides an approximate upper limit on the useful position resolution of the detector readout plane.

There are a number of additional effects that may reduce the precision with which the original recoil track can be reconstructed. As the electron drift velocity is a factor of  $\sim 1000$  greater than the CS<sub>2</sub> ion drift velocity, the diffusion in the direction of the drift field  $\sigma_z$  may be increased beyond thermal diffusion by the finite time taken for ionisation electrons to attach to the CS<sub>2</sub> ions. For currently used gas mixtures, this has been measured and has negligible effects [112]. *Anisochronicity* effects may also increase the measured  $\sigma_z$ . Figure 3.13 shows simulated field lines from the DRIFT detector target volume to the anode wires of an MWPC. As described in the figure caption, tracks with the same  $\Delta z$  can produce a range of  $\Delta t$  values due to the difference in path lengths taken as the positive ions pass follow the field lines. This leads to a range of possible measured  $\Delta z$  values for a given track, depending on position in the detector volume, that lead to an uncertainty of  $\sim 0.3 \text{ mm}$  in the  $z$  range [115].

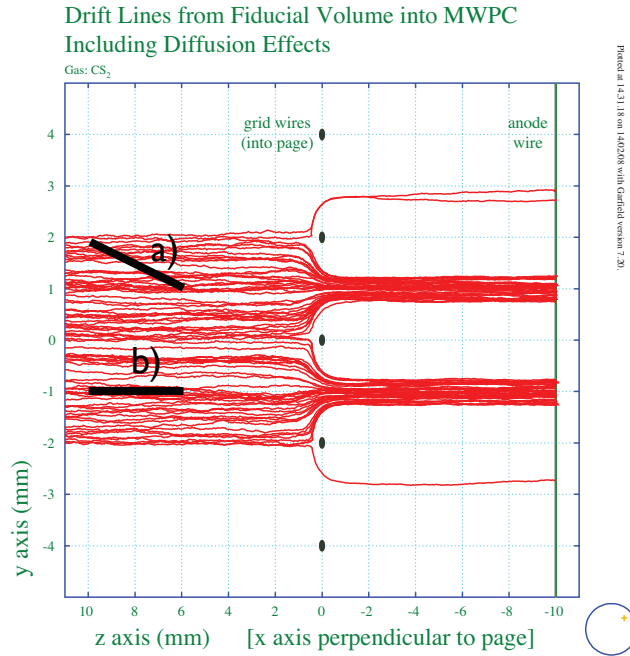


FIGURE 3.13: Drift lines from the drift volume to the anode wires of the MWPC. Two tracks of the same  $\Delta z$  are shown in black. Track b) passes directly between grid wires to the anode wires and the true  $\Delta z$  is determined from the drift velocity. For track a) the outer ions travel a longer distance arriving at the anode at a later time, increasing the measured  $\Delta z$ . Plot adapted from Muna [115].

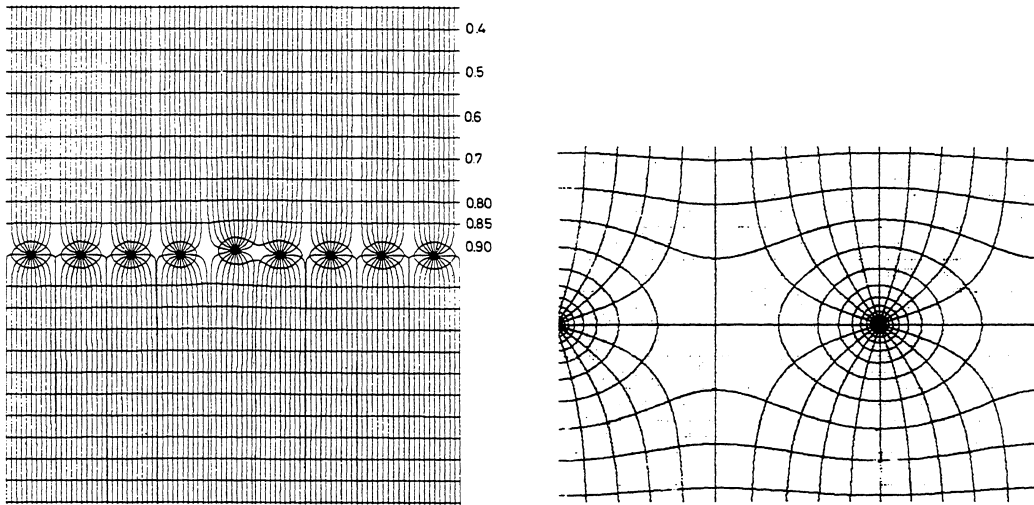
### 3.3.3 Charge multiplication

The anode wires in the MWPC have a radius that is small compared to the inter-wire spacing. As shown in Figure 3.14(b) this results in a strong coaxial electric field close to the wires such that each wire behaves as a single wire proportional counter [114].

Inside the MWPC plane the ion travels along the field lines towards the nearest anode wire. At a distance of a few tens of  $\mu\text{m}$  from the anode wire, the field is of sufficient strength to strip the electron from the negative CS<sub>2</sub> ion [116]. The freed electron continues to accelerate to a point where it has sufficient energy to free further electrons via collisions with CS<sub>2</sub> atoms. These electrons then accelerate and liberate further electrons creating an exponential multiplication of charge. This process, known as the *avalanche effect*, results in a single electron creating a large number of localised free electrons surrounding the anode wire. The number of electrons resulting from a single electron entering the MWPC is called the *gas gain* and, for the DRIFT detector, is of order 1000.

Assuming a single negative ion entering the MWPC, and a gas gain of  $10^3$ , the electron avalanche results in 1000 electrons collected on the anode wire and a cloud of positive ions close to the surface of the wire that form a tear shape as seen in Figure 3.15 [116].

The cloud of electrons is collected at the avalanche wire on a time scale of  $\sim$ ns [116], but the presence of the positive ions in the vicinity of the wire induces an opposing charge on the wire that initially cancels the signal from charge collection.



(a) Field lines remain parallel except within immediate vicinity of anode wires. (b) Coaxial field lines form close to the anode wires.

FIGURE 3.14: Electric field equipotentials and field lines within an MWPC readout plane with anode wires of diameter  $20\ \mu\text{m}$  and spacing of 2 mm. Images from Sauli [116].

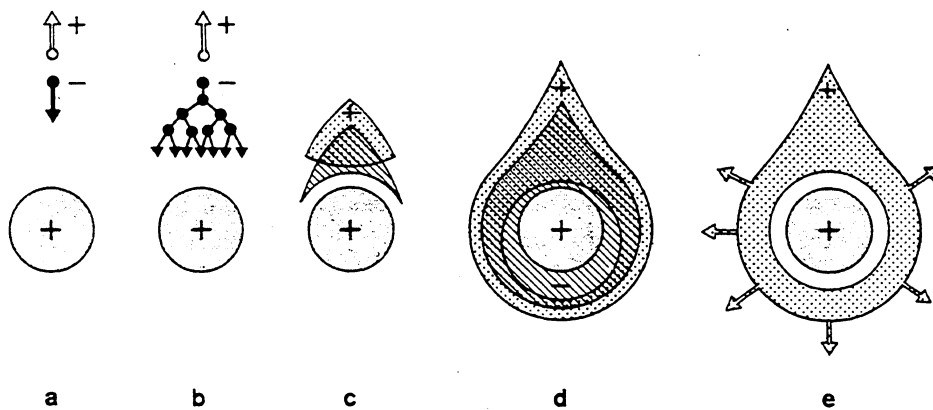


FIGURE 3.15: Evolution of charge in the vicinity of the anode wire. Anode wires are grounded, with positive potential relative to the surrounding  $-3\ \text{kV}$  grid wires (not pictured). **a-d** occur within approximately one wire radius and on a  $\sim$ ns timescale. Signal induction occurs from **e**. Images from Sauli [116].

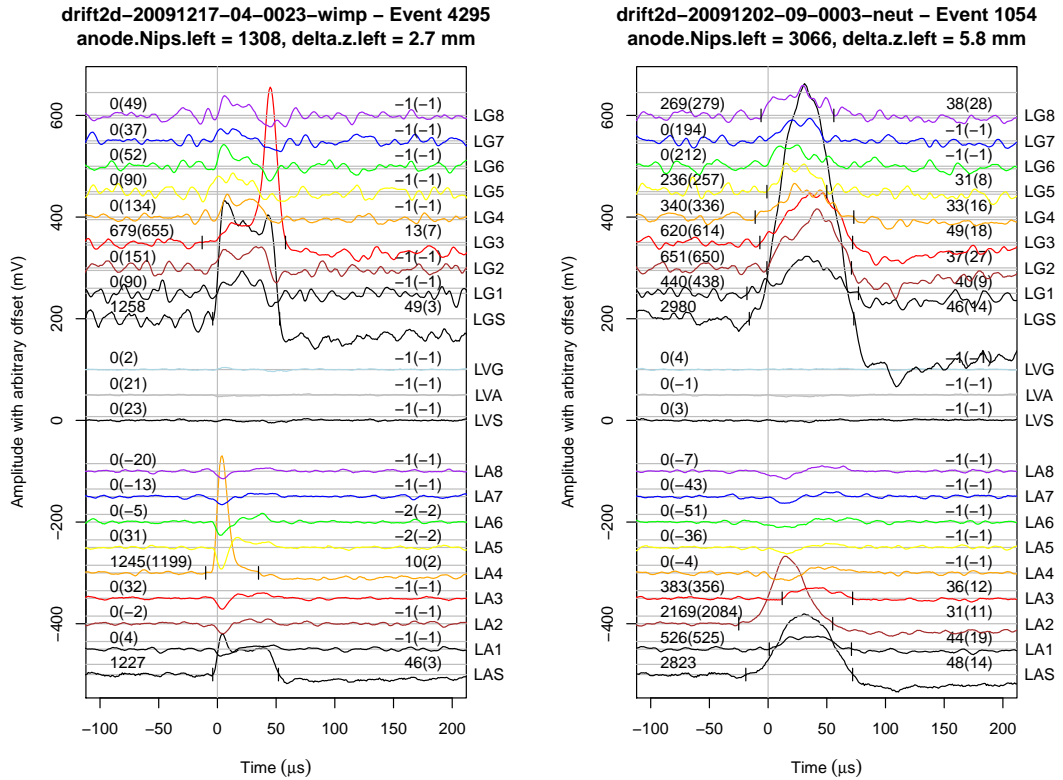
### 3.4 Response of MWPCs to spark-like events

During development of the DRIFT data reduction procedure, a class of spark-like events were discovered that appear to contradict the model established within DRIFT for the

signal induction in the MWPC. Although the dynamics of signal induction in the MWPC plane is complex, and likely requires simulation for a complete understanding, this section uses the spark-like events to discuss charge induction mechanisms and the possible consequences for DRIFT.

### 3.4.1 Identifying spark-like events

Figure 3.16(a) shows an event, identified during analysis, in which there is a large, fast pulse on a single anode wire. The full width at half maximum (FWHM) of the anode pulse is  $10 \mu\text{s}$ , consistent with the shaping time of the Gaussian shaping amplifiers [105]. This implies that the input to the shaping amplifiers was an approximate step-function, which in turn implies a fast, spark-like charge deposition recorded by the charge preamplifiers (see Section 3.2.3). Figure 3.16(b) shows a typical neutron event for comparison.



(a) A typical spark-like event on the left MWPC (b) A typical nuclear recoil event on the left MWPC from neutron run.

FIGURE 3.16: Comparison of a spark-like event compared to a typical nuclear recoil event. Recall that all anode lines are inverted, so that positive voltage indicates negative charge on the anode lines. See Section 3.2.4 for a full description of the event file.

The spark-like event has some interesting features. Firstly, it can be seen that there is a similarly fast pulse that occurs on a single grid line, but which appears much later

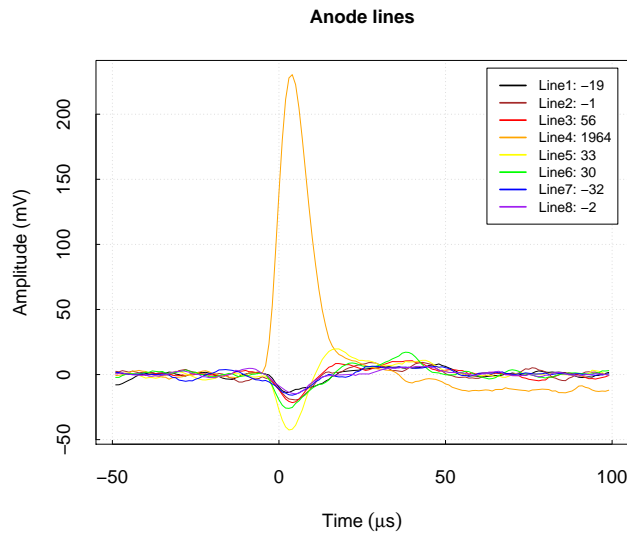
in time,  $\sim 40 \mu\text{s}$  after the trigger time. In addition, distinct signals can be seen on all other fiducial lines (both anode and grid) beginning at the time of the anode spike and ending at the time of the grid spike. This is seen most clearly on the anode and grid sum lines. These events are typically rejected in early analysis stages (as the fast signal is easily identifiable as being incompatible with nuclear recoil events), but removing some standard WIMP cuts reveals a significant number of these spark-like events with almost identical form. In each event a clear separation of  $\sim 40 \mu\text{s}$  between the anode and grid spikes is observed.

The  $\sim 550 \text{ V cm}^{-1}$  drift field throughout the detector target volume produces a constant ion drift velocity of  $5940 \text{ cm s}^{-1}$  [97]. Assuming the drift velocity remains directly proportional to the field strength, the drift field within the MWPC of  $\sim 2730 \text{ V cm}^{-1}$  results in an ion drift velocity of  $\sim 29500 \text{ cm s}^{-1}$ . This corresponds to a time of  $\sim 34 \mu\text{s}$  for  $\text{CS}_2$  ions to drift from the anode plane to the grid plane. This is sufficiently close to the time separation of the anode and grid spikes to suggest that the separation is caused by the time taken for positive ions, liberated during avalanche at the anode wire, to drift to the grid wire. This effect is significantly less visible in nuclear recoil events, due to the finite extent of the ionisation track.

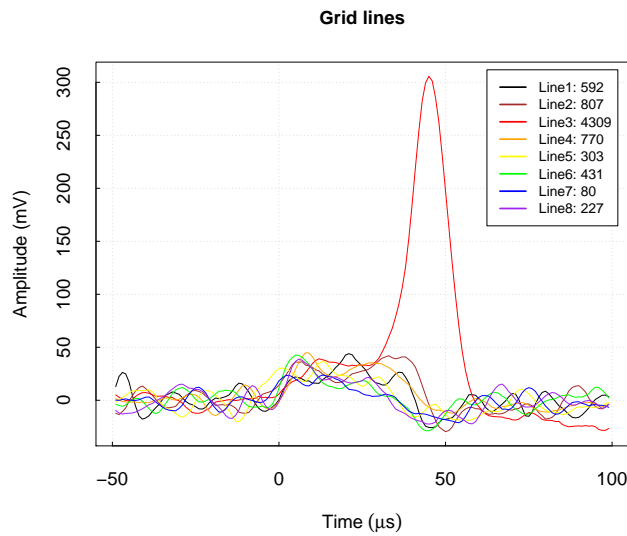
### 3.4.2 Qualitative analysis of spark-like events

The spark-like events from localised charge depositions are useful for investigating the signal induction mechanisms within the MWPC that may be hidden in nuclear recoil tracks by the extent of the ionisation track.

Figure 3.17(a) plots the anode fiducial lines only, with no voltage offset, from the spark-like event seen in Figure 3.16(a). Figure 3.17(b) similarly plots the grid fiducial lines with no voltage offset. These plots, characteristic of the spark-like event population, show that for both the anode and the grid lines, the seven lines without the main spike demonstrate a very similar pulse shape. For the purposes of gaining a qualitative understanding of these events, all lines without the main hit were averaged to a single line to improve signal-to-noise and reveal the underlying form. Each spark-like event is thus summarised by 4 lines, as shown in Figure 3.18: the anode hit line (LA4, in this case), the grid hit line (LG3, in this case), the average of the remaining anode lines, and the average of the remaining grid lines. A large number of spark-like events were individually studied in this way. All were found to be of the same form and represented well by the single event characterised by Figure 3.18. This event will be used to consider the signal induction process within the MWPC readout plane.



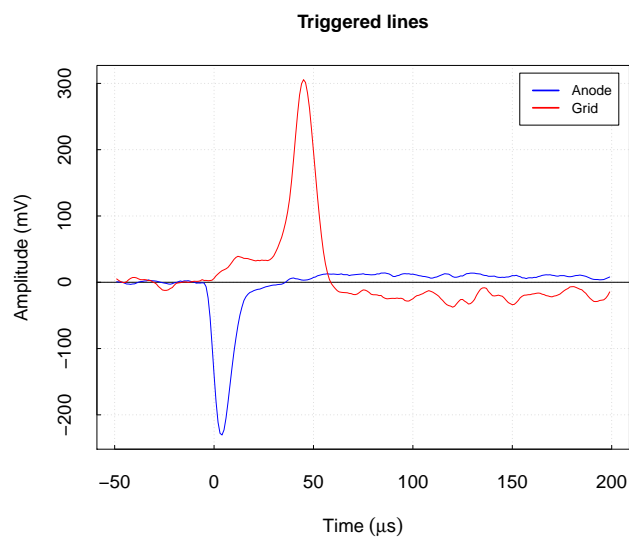
(a) Anode fiducial lines from Figure 3.16 with no voltage offset.



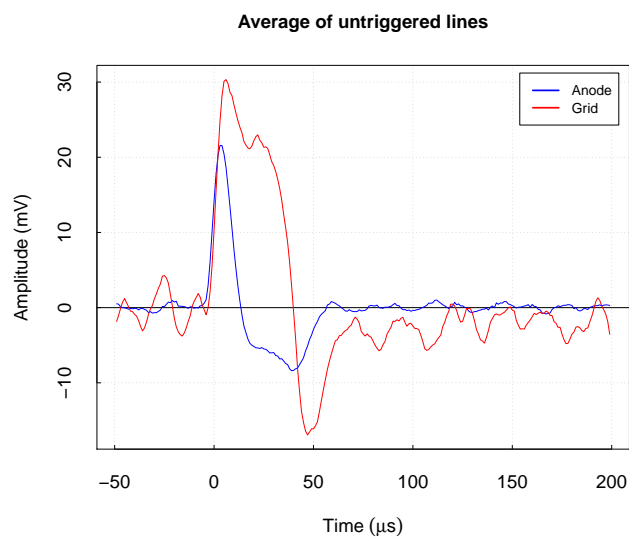
(b) Grid fiducial lines from Figure 3.16 with no voltage offset.

FIGURE 3.17: Grid and anode lines of a typical spark-like event. Legend contains the integrated voltage between  $-10$  and  $60 \mu\text{s}$  for each line.

The anode wire on which the avalanche occurs is first considered. This wire is represented by the single triggered anode line, shown by the blue waveform in Figure 3.18(a). The avalanche results in the deposition of negative charge on the anode wire, but simultaneously creates a cloud of positive ions close to the surface of the anode wire. The positive ions induce polarisation of the anode wire, which, for the  $\sim\text{ns}$  timescale whilst the positive ions are still very close to the anode wire, cancels the deposited negative charge. As the positive ions drift away, the polarisation of the anode wire is reduced.



(a) The single anode (blue) and grid (red) lines with identified hits.



(b) The average of the seven remaining anode (blue) and seven remaining grid (red) lines without identified hits.

FIGURE 3.18: Comparison of the direct hit to the average induced signal on anode lines (blue) and grid lines (red). Unlike all other event plots, in these plots the anode signal has not been inverted so negative voltage corresponds to negative charge.

There is no longer cancellation of the deposited negative charge, and a negative charge pulse on the anode wire results. The shape of this pulse is due to the combined effect of the dynamics of the positive ion cloud drifting from the anode wire, and the response of the charge readout electronics to the deposited charge. The fast movement of the positive ion cloud relative to the electronics response time means that the main pulse shape is dominated by the  $4\ \mu\text{s}$  shaping time of the shaping amplifiers.

The grid wire that receives the localised positive ion cloud is considered next. This wire is represented by the single triggered grid line, shown by the red waveform in Figure 3.18(a). The positive charge cloud drifts across the MWPC approaching one of the grid wires. As it approaches, the grid wire becomes increasingly polarised, with negative polarisation charge accumulating on the wire in proximity to the approaching positive ions producing a net positive charge on the grid wire readout. Once the positive charge arrives at the grid wire, it combines with the polarisation electrons, leaving net positive charge at the readout electronics. This positive charge quickly dissipates once the positive ions have gone.

Finally, the neighbouring anode and grid wires are considered. The neighbouring wires are represented by the average of the seven untriggered anode lines (the blue waveform in Figure 3.18(b)) and the average of the seven untriggered grid lines (the red waveform in Figure 3.18(b)). There is no direct charge deposition on these wires. There are, however, two competing polarisation effects: first, there is negative polarisation of the neighbouring wires due to attraction to the positive ion cloud — this results in a positive charge at the readout; second, there is positive polarisation of the neighbouring wires due to attraction to the negative anode wire system on which the avalanche occurred<sup>4</sup> — this results in a negative charge at the readout. The dominant polarisation component changes as the positive ion cloud drifts between the anode and grid plane resulting in the bipolar signals seen in Figure 3.18(b).

### 3.4.3 Consequences for DRIFT

These explanations are consistent with some preliminary signal induction simulations, performed previously within collaboration [117]. A full simulation, containing all fields and electronics effects, is likely required to fully understand all of these effects. Without this full simulation, however, some useful conclusions are made, which have a bearing on analysis.

The study of spark-like events shows that the response to grid wires is a positive going induced pulse on all grid wires from the time of the avalanche at the anode wire, followed by a larger positive pulse on a single grid wire at the time of the positive ions arriving at a given wire. This separation of induced and direct charge differs from the Gaussian distribution of charge across all grid lines currently used to model the grid response [118].

---

<sup>4</sup>The negative charge on the anode avalanche wire will redistribute to the anode wire system, which consists of the 55 other grouped anode wires and the capacitor coupling the wire to the integrating electronics.

This may explain discrepancies seen between simulation and data in Section 7.1.2, suggesting a modification to the standard DRIFT simulation to improve signal induction effects. This is the subject of ongoing discussions within the collaboration.

In addition, the identification of separation of induced charge and direct charge in the grid signals may have consequences for reconstruction of the  $\Delta y$  component of track range, which can not currently be determined accurately. For example, in the neutron event in Figure 3.16 the grid pulses on lines LG1, LG2 and LG3, appear to have larger pulses that peak later in time than the pulses on the rest of the grid wires. This implies that these lines received the bulk of the direct charge suggesting a track  $\Delta y$  of  $\sim 6$  mm. Preliminary attempts to separate the direct charge from the induced component in nuclear recoil events for  $\Delta y$  measurements resulted in some success only with selected neutron events. It is likely that improvement of the signal-to-noise ratio on the grid lines is required for these methods to yield significant improvements in track reconstruction.

## 3.5 In situ measurements of gas mobility

### 3.5.1 Drift time measurements

The spark-like events identified above present a way of measuring the drift velocity of  $\text{CS}_2$  ions within the MWPC, from the difference in time between the spikes on the triggered anode line and the triggered grid line. These events are relatively infrequent ( $\sim 1$  event per hour) so a significant livetime is required for reasonable statistical precision. Descriptions of datasets for four different detector configurations are given in Table 3.1.

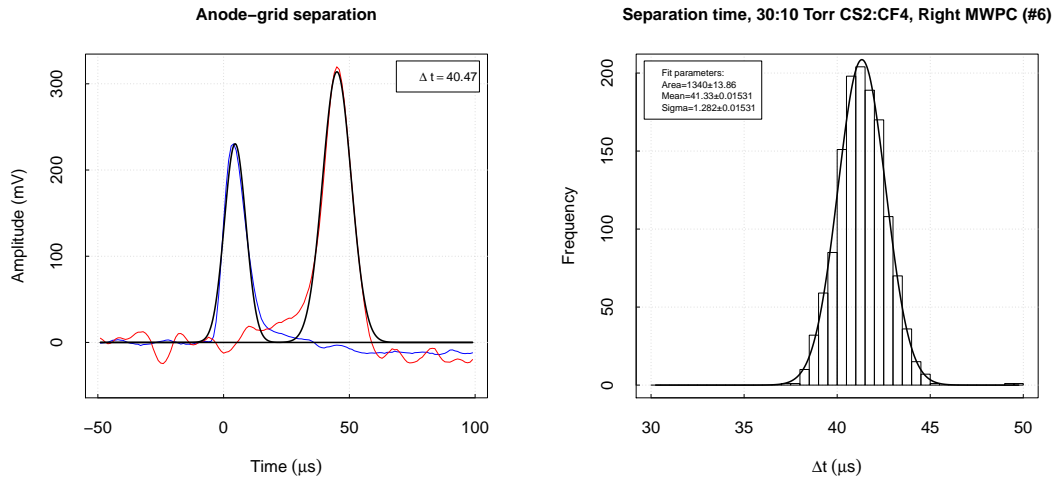
$\text{CS}_2\text{-CF}_4$ (Torr)	E ( $\text{V cm}^{-1}$ )	Livetime (days)	Number of events	Dates
30-10	2731	27.1	634	2009/12/16–2010/01/28
42-00	2884	25.6	190	2008/09/25–2009/02/11
41-00	2884	24.3	359	2008/04/18–2008/05/14
40-00	2884	22.3	386	2008/02/01–2008/04/15

TABLE 3.1: Descriptions of datasets used for positive ion drift time measurements. First column is the target gas mixture, second is the electric field within the MWPC plane.

To preferentially select spark-like events the standard WIMP event selection criteria was adapted for selection of spark-like events. Stages 1 and 2 of the standard WIMP cuts, described in detail in Section 5.3, are applied to remove events that are not fully contained within the fiducial volume, alpha events, and other anomalous unphysical events. Following this two additional cuts were performed. First, the anode pulse was

required to have an RMST of less than  $5 \mu\text{s}$ , thus selecting only events consistent with the  $4 \mu\text{s}$  shaping time of the amplifiers. Second, the largest grid wire amplitude was required to be at least 4 times larger than the second largest, ensuring that the majority of the positive ions liberated in the avalanche are received by a single grid wire.

In order to determine the time separation between the anode pulse and the grid pulse a Gaussian fit was performed to each, as shown in Figure 3.19(a). The separation in time  $\Delta t$  was defined as the distance between the means of these two fits and this was taken as the drift time of the positive ion cloud from the anode wire to the grid wire.  $\Delta t$  measurements were made for all events that passed the cuts described above and a histogram of drift times is produced for each MWPC separately. Figure 3.19(b) shows a histogram of  $\Delta t$  values on the right-hand side MWPC for 22.3 days livetime with 40 Torr  $\text{CS}_2$ . A Gaussian is fit to the histogram to determine the mean ion drift velocity.



(a) Measurement of  $\Delta t$  from Gaussian fits to triggered anode line (blue) and triggered grid line (red).  $\Delta t$  of this event is  $40.47 \mu\text{s}$ . (b) Mean  $\Delta t$  determined from Gaussian fit of all  $\Delta t$  measurements for 40 Torr  $\text{CS}_2$ . Mean  $\Delta t$  is  $41.33 \pm 0.02$ .

FIGURE 3.19: Separation of anode and grid pulses in spark-like events in 30-10 Torr  $\text{CS}_2\text{-CF}_4$ .

### 3.5.2 Drift time results

Table 3.2 shows measurements of the anode pulse to grid pulse separation ( $\Delta t$ ) for four different detector configurations. The errors shown in Table 3.2 include statistical uncertainties and the following estimated systematic errors: 1% uncertainty in the anode-grid wire plane separation from the MWPC construction precision; 1% uncertainty in the output of the high-voltage power supplies; 0.5% uncertainty in the target gas pressure.

It is apparent, from the measured  $\Delta t$  values in Table 3.2, that there are additional systematic uncertainties that have not been accounted for. First, since  $v_{\text{drift}} \propto p$  (Equation 3.3), the time taken for positive ions to drift between the anode and grid wires,  $\Delta t$ , is expected to increase by  $\sim 2.5\%$  between the pure  $\text{CS}_2$  runs of pressure 40, 41 and 42 Torr. This increase is not observed. In addition, since the two MWPCs share the same target gas, the drift time measurements should be the same in each MWPC. This is also not observed, with varying discrepancies between the left and right MWPC.

$\text{CS}_2\text{-CF}_4$	left $\Delta t$ ( $\mu\text{s}$ )	left $\mu$	right $\Delta t$ ( $\mu\text{s}$ )	right $\mu$
30-10	$37.65 \pm 0.66$	$0.512 \pm 0.009$	$41.33 \pm 0.64$	$0.466 \pm 0.007$
42-00	$41.64 \pm 0.65$	$0.460 \pm 0.007$	$42.72 \pm 0.69$	$0.449 \pm 0.007$
41-00	$41.90 \pm 0.66$	$0.447 \pm 0.008$	$44.97 \pm 0.69$	$0.417 \pm 0.009$
40-00	$40.64 \pm 0.64$	$0.449 \pm 0.007$	$43.11 \pm 0.68$	$0.423 \pm 0.007$

TABLE 3.2: Separation of anode and grid pulses in spark-like events for different gas mixtures. Reduced mobility measurements ( $\mu$ ) in units of  $\text{cm}^2 \text{atm V}^{-1} \text{s}^{-1}$ . Errors include statistical error and estimated systemic errors. See text for details.

Figure 3.20 shows the  $\Delta t$  measurements in Figure 3.19(b) plotted as a function of time, where the measured  $\Delta t$  is seen to vary over time. Although the slow control data reveals slight deviations in temperature and voltages during this time, no factors large enough to account for the  $\sim 3\%$  changes in  $\Delta t$  are found. Whilst the underlying cause has not yet been determined, it is clear there are some experimental conditions that are producing variations in the drift time measurement over time, of at least  $\sim 3\%$ , that limit the precision of these measurements.

Nonetheless, using Equation 3.3 and the measured drift time, reduced mobility values are calculated for each dataset. These are also shown in Table 3.2. Taking a mean of the measured values for each target gas, results in measured reduced mobilities of  $0.44 \pm 0.02$  and  $0.49 \pm 0.03 \text{ cm}^2 \text{atm V}^{-1} \text{s}^{-1}$  for pure  $\text{CS}_2$  and a 30-10  $\text{CS}_2\text{-CF}_4$  gas mixture respectively.

### 3.5.3 Comparison with existing measurements, and conclusions

Table 3.3 compares these results with previously measured reduced mobility values in  $\text{CS}_2$  and  $\text{CS}_2\text{-CF}_4$  gas mixtures. The table shows that two previous measurements within the DRIFT collaboration, using different experimental setups, have measured a significantly higher reduced mobility for these gas mixtures. The difference between the 40 Torr  $\text{CS}_2$  and the 30-10  $\text{CS}_2\text{-CF}_4$  measurements, however, is compatible. These results suggest further unaccounted-for systematic effects in the method detailed in Section 3.5.1. It is noted, however, that the pure  $\text{CS}_2$  measurement presented here

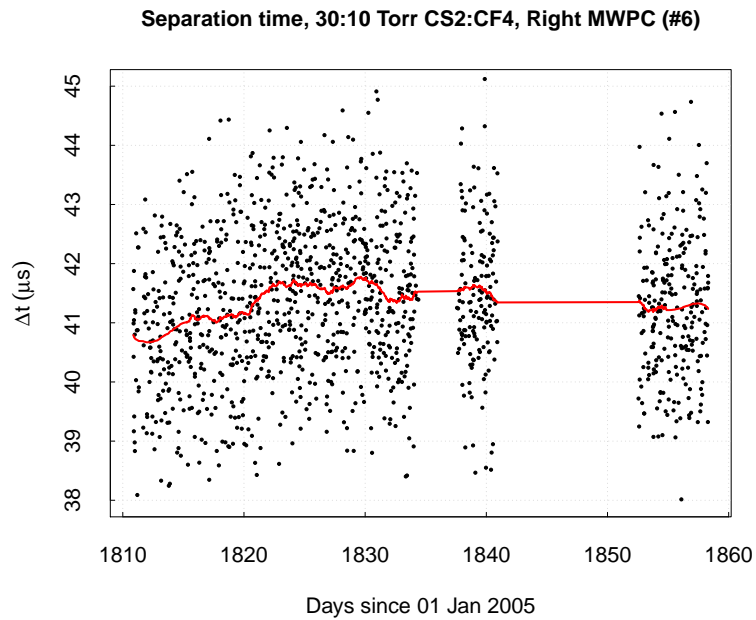


FIGURE 3.20: The  $\Delta t$  measurements in Figure 3.19(b) plotted as a function of time. The red curve shows the data smoothed revealing a  $\Delta t$  that is drifting over time.

is in agreement with a recently published mobility measurement from outside of the collaboration [119], adding further uncertainty to the situation.

Drift velocity measurements are crucial for accurate determination of the  $z$  component of the track range. Despite remaining uncertainties, a method has been presented that demonstrates the potential for continuous direct in situ measurements of the drift velocity in the DRIFT-II detector. The method has revealed variations over time in the drift velocity, demonstrating the merit of continuous in situ monitoring of the drift velocity in DRIFT.

CS <sub>2</sub> -CF <sub>4</sub> (Torr)	Reduced mobility $\mu$	$\mu$ (Pushkin [107])	$\mu$ (Gauvreau [112])	$\mu$ (Dion [119])
40-00	0.44±0.02	0.54±0.02	0.51±0.01	0.46±0.01
30-10	0.49±0.03	0.60±0.02	0.57±0.01	—
20-20	—	0.69±0.02	0.67±0.01	—
10-30	—	0.81±0.03	0.76±0.01	—

TABLE 3.3: Reduced mobility measurements ( $\mu$ ) in units of  $\text{cm}^2 \text{atm V}^{-1} \text{s}^{-1}$  presented in Section 3.5.2 compared to previous measurements from dedicated experiments. Second and third column contain measurements from the DRIFT collaboration with a single wire proportional counter experiment [107] and a small TPC with MWPC read-out [112] respectively. Fourth column contains measurements from a small TPC and micro-well detector [119].



## Chapter 4

# Development of spin-dependent $\text{CF}_4$ target for DRIFT-IIId

This chapter discusses spin-dependent WIMPs and the motivations for adapting the DRIFT detector for sensitivity to SD WIMP interactions. The addition of  $\text{CF}_4$  gas to the current  $\text{CS}_2$  target to achieve this sensitivity is considered. Results from a number of preliminary measurements on  $\text{CS}_2$ - $\text{CF}_4$  gas mixtures, and their consequences for the DRIFT detector are discussed.

In Section 4.2, results are presented from the first measurements, performed by the author in collaboration with Occidental College, from gas mixtures in a full-scale  $1\text{ m}^3$  DRIFT-II detector.  $^{55}\text{Fe}$  and neutron calibrations are presented. The author led the design, construction and commissioning of a new gas mixing system, required for long term operation of gas mixtures in DRIFT and this is presented in Section 4.3. Finally, in Section 4.4, results are presented of the long-term stability monitoring of the new gas mixing system since installation at the Boulby Underground Laboratory.

### 4.1 Spin-dependent WIMPs

#### 4.1.1 Spin-dependent vs spin-independent

WIMPs may interact with nuclei through spin-independent (SI) coupling, in which the WIMP interacts with the mass of the nucleus, or via spin-dependent (SD) coupling, in which the WIMP couples to the nuclear spin  $J$  (see Section 2.1.6).

Direct dark matter searches have typically focused on the search for SI WIMP-nucleus interactions. One reason for this is the ability to probe lower cross-sections due to the  $A^2$

enhancement of the WIMP-nucleon cross-section relative to the WIMP-nucleon cross-section. In addition, the majority of techniques suitable for low energy, low background nuclear recoil detection use target materials that have no unpaired nucleons, making it more attractive to focus on SI interactions. Figure 4.1 shows the current leading experimental limits on the allowed SI WIMP-nucleon interaction cross-section as a function of WIMP mass. Presently the most stringent upper limits come from XENON100, which has a minimum of  $7.0 \times 10^{-45} \text{ cm}^2$  for a WIMP of mass  $50 \text{ GeV c}^{-2}$  [120]. Favoured models, based on the assumption that WIMP-nucleon interactions are via Higgs boson exchange, predict WIMP cross-sections in the regions of  $\sim 10^{-46}$  to  $10^{-43} \text{ cm}^2$ . The grey shaded regions in Figure 4.1 illustrate regions favoured by CMSSM models [121], which are just beginning to be explored by direct detection experiments. The plot also contains the 90% C.L. acceptance regions of the positive results discussed in Section 1.4.2.

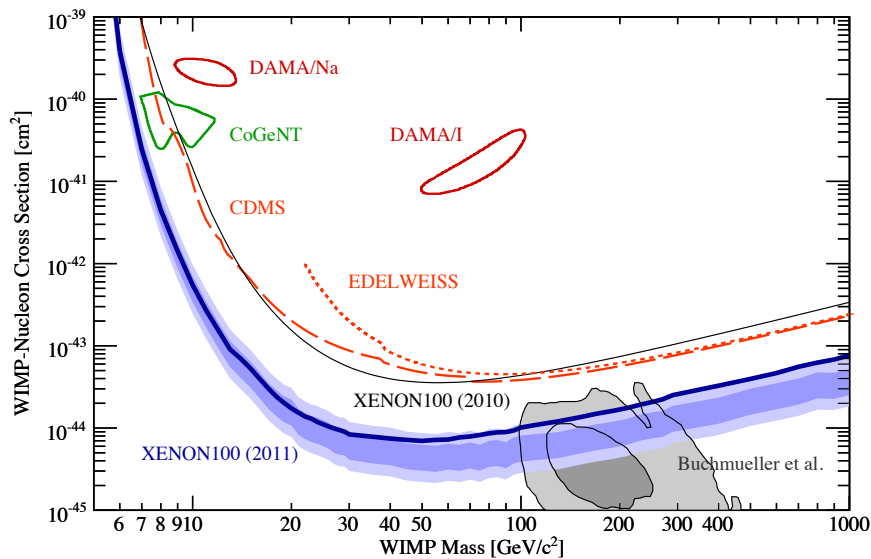


FIGURE 4.1: Spin-independent WIMP-nucleon cross-section as a function of WIMP mass. Blue line with 1 and 2 sigma regions is upper limit from XENON100 (2011) [120], black line is XENON100 (2010) [58], dotted orange line is EDELWEISS [60], and dashed orange is CDMS-II [59]. Grey shaded regions are expectations from CMSSM (68% and 95% C.L.) [121]. 90% C.L. areas favoured by CoGeNT [61] and DAMA [62] are also shown. Plot from Aprile et al. [120].

There are, however, reasons to pursue detection of WIMPs via spin-dependent interactions. SD WIMP-nucleon cross-sections are predicted to be larger than SI cross-sections by orders of magnitude, up to  $\sim 10^{-41}$  to  $10^{-38} \text{ cm}^2$  in many models [122, 123]. Furthermore, constraining the SD cross-section generally provides more stringent constraints on SUSY parameter space [124], and combining SD and SI measurements can be even more powerful [125].

Partly due to the  $A^2$  enhancement factor that SI dark matter detectors benefit from, but also due to the experimental focus on SI WIMP interactions, the upper limits on SD cross-sections are many orders of magnitude higher than SI limits. This is shown in Figure 4.2, where the best upper limits from direct detection experiments are at  $6.0 \times 10^{-38} \text{ cm}^2$  [126], and are over two orders of magnitude above theoretically favoured regions. Because current experimental limits are relatively high, DRIFT-II, despite its relatively low mass, has the potential to probe new SD limits with the addition of a target material with SD sensitivity [127].

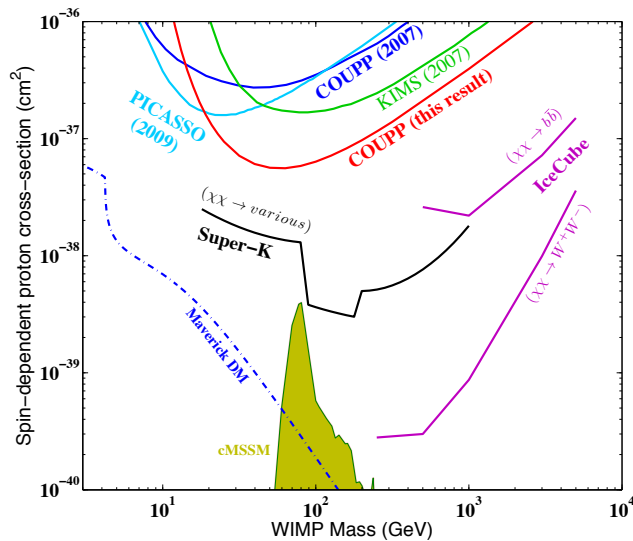


FIGURE 4.2: Current limits on spin-dependent WIMP-proton scattering cross-sections. Direct detection limits from COUPP (2007) [128] (dark blue), COUPP (2011) [126] (red), PICASSO [129] (light blue), and KIMS [130] (green), are shown. Also plotted are limits from WIMP annihilation in the Sun from IceCube [131] (magenta), and Super Kamiokande [51] (black), neutrino observatories, which have additional model dependencies. The gold region indicates favoured cross-sections from CMSSM [123]. The blue, dashed-dotted line is the expected cross-section for maverick dark matter [132]. Plot adapted from Behnke et al. [126].

#### 4.1.2 Spin-dependent sensitive target

Electronegative  $CS_2$  is an ideal gas for reducing diffusion of drifted ionisation tracks and preserving track information over large drift distances (Section 3.1.3). However,  $CS_2$  has negligible sensitivity to SD interactions, since isotopes with odd nucleons ( $^{13}C$  and  $^{33}S$ ) each have abundances of only  $\sim 1\%$ . It has been shown that the negative ion drift concept can be retained in gas mixtures with relatively small amounts of  $CS_2$  [107]. This suggests that gases with an unpaired nucleon, and therefore sensitivity to SD WIMP-proton scattering, could be mixed with the  $CS_2$  target gas, enhancing sensitivity to SD interactions, whilst retaining negative ion drift.

The element  $^{19}F$  is a favoured target for SD sensitivity [124, 133]. Table 4.1 shows the enhancement factors for typical targets of spin-dependent sensitive dark matter detectors, where  $^{19}F$  is seen to have a significantly higher WIMP-nucleus cross-section enhancement factor ( $C_N^{SD(p)}/C_p^{SD}$ ). Using  $^{19}F$  as a target is particularly attractive due to its complementarity with existing SD sensitive dark matter detectors. Whereas most current SD sensitive targets ( $^{23}Na$ ,  $^{127}I$ ,  $^{129}Xe$ ,  $^{131}Xe$ ) consist of targets with neutron and proton spin expectations of the same sign,  $^{19}F$  has neutron and proton spin expectations of opposite sign, i.e.  $\langle S_n \rangle / \langle S_p \rangle < 0$ . Combining these results has a large impact on the allowed WIMP-proton coupling ( $a_p$ ) vs WIMP-neutron coupling ( $a_n$ ) parameter space [125].

$CF_4$  has a high fluorine content and is a well known and effective fill gas for use in gaseous drift chambers [134, 135]. In addition,  $CF_4$  gas is cheap, available and, importantly for operation in an underground laboratory, inert and non-flammable.  $CF_4$  is therefore an ideal candidate as a mix gas to give the DRIFT detector sensitivity to SD WIMP interactions.

Nucleus	J	Abundance(%)	$C_N^{SD(p)}/C_p^{SD}$	$C_N^{SD(n)}/C_n^{SD}$
<b>unpaired proton</b>				
$^{19}F$	1/2	100	$7.78 \times 10^{-1}$	$4.75 \times 10^{-2}$
$^{23}Na$	3/2	100	$1.37 \times 10^{-1}$	$8.89 \times 10^{-4}$
$^{27}Al$	5/2	100	$2.20 \times 10^{-1}$	$1.68 \times 10^{-3}$
$^{127}I$	5/2	100	$1.78 \times 10^{-1}$	$1.05 \times 10^{-2}$
<b>unpaired neutron</b>				
$^{73}Ge$	9/2	7.8	$1.47 \times 10^{-3}$	$2.33 \times 10^{-1}$
$^{129}Xe$	1/2	26.4	$3.14 \times 10^{-3}$	$5.16 \times 10^{-1}$
$^{131}Xe$	3/2	21.2	$1.80 \times 10^{-4}$	$1.15 \times 10^{-1}$

TABLE 4.1: SD enhancement factors for WIMP-proton ( $C_N^{SD(p)}/C_p^{SD}$ ) and WIMP-neutron ( $C_N^{SD(n)}/C_n^{SD}$ ) interactions. Data from Tovey et al. [72].

### 4.1.3 Properties of $CS_2$ - $CF_4$ mixtures

The addition of  $CF_4$  to the  $CS_2$  fill gas of the DRIFT detector will have significant effects on the operation of the TPC. The ionisation produced by nuclear recoils in the target volume, the diffusion of the track as it drifts to the readout plane, and the charge multiplication from electron avalanche in the MWPC will all be effected by the addition of  $CF_4$ . These effects need to be understood before  $CS_2$ - $CF_4$  mixtures can be considered as suitable gases for use in DRIFT detectors. The critical gas parameters are discussed below:

**Negative ion drift and diffusion** — Negative ion drift must be preserved for any proposed gas mixture so that track diffusion is suppressed to thermal levels. Table 4.2 shows measured values of reduced mobility for various CS<sub>2</sub>-CF<sub>4</sub> mixtures that were measured using a small scale DRIFT-like TPC experiment [112]. For each mixture the measured mobilities are consistent with drifting of negative ions, which have mobilities three orders of magnitude lower than drifted electrons. For gas mixtures with less than 25% CS<sub>2</sub> (e.g. 5-35 Torr CS<sub>2</sub>-CF<sub>4</sub>) large diffusion was measured in the direction of drift, attributed to large fluctuations in electron attachment times. The drift fields used in the experimental setup are similar to those in the DRIFT detector, suggesting a minimum CS<sub>2</sub> concentration of ~25% is required to maintain low diffusion through negative ion drift in the full-scale DRIFT-II detectors.

Diffusion of point-like charge depositions were also measured and used to determine equivalent temperatures (Equation 3.6) of longitudinal and transverse diffusion in the gas mixtures. The measurements, also shown in Table 4.2, show no significant increase in diffusion with increasing CF<sub>4</sub> content.

**W-value** — The W-value, the mean energy required to liberate a single ion pair (Section 3.3.1), determines the ionisation yield from particle interactions, which in turn determines the sensitivity of the detector to low energy events. Table 4.2 shows W-value measurements made with a single wire proportional counter experiment [107]. The W-value increases with higher concentrations of CF<sub>4</sub>, implying a reduction in the ionisation yield for a given event.

Gas mix CS <sub>2</sub> -CF <sub>4</sub> (Torr)	W-value (eV)	Reduced mobility (cm <sup>2</sup> atm V <sup>-1</sup> s)	$T_x$ (K)	$T_z$ (K)
40-00	24.9±0.8	0.51±0.01	330±40	380±40
30-10	25.2±0.6	0.57±0.01	360±30	390±35
20-20	29.2±1.0	0.67±0.01	330±25	440±10
10-30	33.0±1.0	0.76±0.01		

TABLE 4.2: W-value measurements from a dedicated single wire proportional counter experiment [107]. Mobility measurements from a small (cube of side 30 cm) DRIFT-like TPC experiment [112].  $T_x$  is effective temperature of transverse diffusion,  $T_z$  is effective temperature of longitudinal diffusion.

**Gas gain** — The gas gain, the charge multiplication factor achieved in the avalanche of ionisation electrons within the MWPC (Section 3.3.3), is also strongly affected by the gas mixture used. Higher gas gains result in a higher ratio of signal to electronic noise, and potentially improved sensitivity to low energy events. Figure 4.3 shows measured gas gains of CS<sub>2</sub>-CF<sub>4</sub> mixtures where, for a fixed voltage, gas gains become significantly greater with increasing CF<sub>4</sub> content.

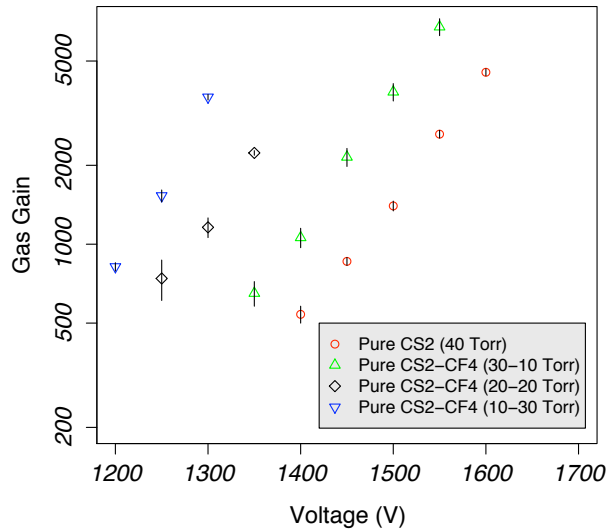


FIGURE 4.3: Gas gains in  $CS_2$ - $CF_4$  mixtures. Plot from Pushkin et al. [107].

**Nuclear recoil quenching factor** — For a nuclear recoil in a target medium the *nuclear recoil quenching factor*  $Q(E)$  is defined as the fraction of energy that is released through ionisation compared with its total kinetic energy

$$Q(E) = \frac{E_{\text{ionisation}}}{E_{\text{recoil}}}. \quad (4.1)$$

A quenching factor of 1 implies that no energy is “quenched” and the entire kinetic energy of the nuclear recoil goes into the liberation of ion pairs, which can be detected by DRIFT. Nuclear quenching factor estimates from measurements and simulation have been performed by the DRIFT collaboration for pure  $CS_2$  (Figure 3.10) but have not been made for  $CS_2$ - $CF_4$  mixtures. However, Hitachi [108] has made predictions regarding quenching factors of carbon and sulphur recoils in  $CS_2$  and carbon and fluorine recoils in  $CF_4$ . The calculations predict identical quenching factors for carbon recoils in  $CS_2$  and carbon recoils in  $CF_4$ . From this it is assumed that carbon nuclear recoils in arbitrary mixtures of  $CS_2$  and  $CF_4$  will have the same quenching factor as a function of energy. Furthermore it is assumed that the  $Q(E)$  for sulphur recoils in  $CS_2$  and the  $Q(E)$  for fluorine recoils in  $CF_4$  each hold for arbitrary  $CS_2$ - $CF_4$  mixtures. With these assumptions the nuclear recoil quenching factors of C, F and S recoils in arbitrary mixtures of  $CS_2$ - $CF_4$  are plotted in Figure 4.4.

**Ranges** — Figure 4.5 shows a SRIM [111] simulation of the ranges of nuclear recoils in pure  $CS_2$  and in a 30-10 Torr  $CS_2$ - $CF_4$  gas mixture. The track ranges of carbon and sulphur recoils are slightly reduced by the addition of  $CF_4$ . However, the measured mean

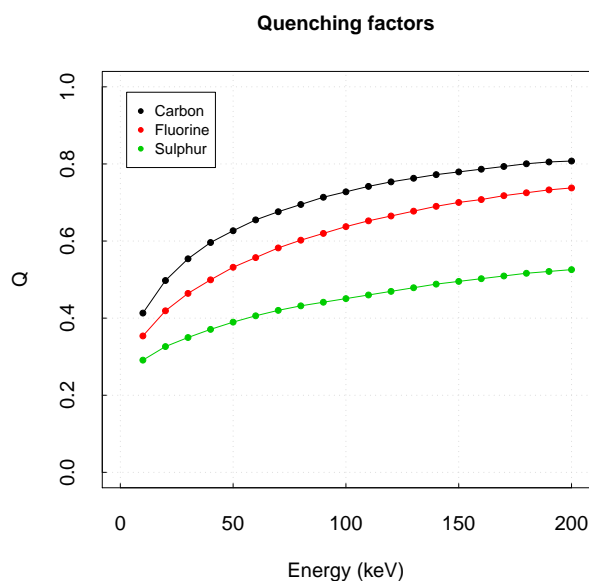


FIGURE 4.4: Nuclear recoil quenching factors for recoils of C (black), F (red), S (green) in arbitrary  $CS_2$ - $CF_4$  mixtures. Plot adapted from Hitachi [108].

track range in  $CS_2$ - $CF_4$  mixtures would be expected to increase due to the replacement of sulphur targets with fluorine targets, which have a substantially longer range.

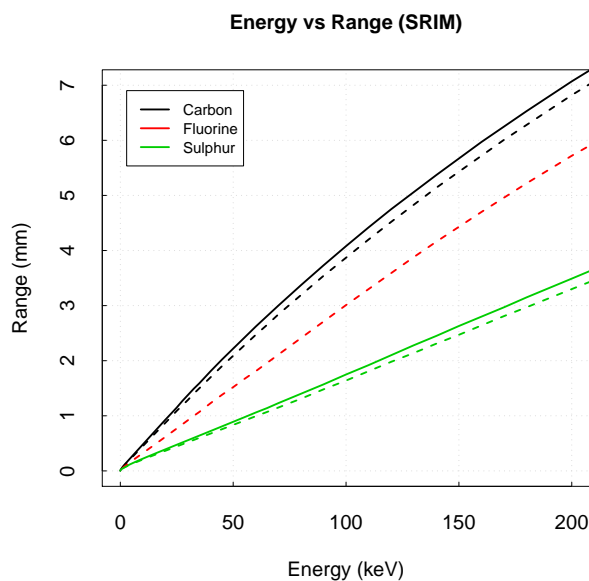


FIGURE 4.5: Track range as a function of recoil energy in  $CS_2$ - $CF_4$  gas mixtures. Solid lines shows ranges of C (black) and S (green) in 40 Torr pure  $CS_2$ . Dashed line shows ranges of C (black), F (red), S (green) in 30-10 Torr  $CS_2$ - $CF_4$  gas mixture.

## 4.2 Gas mixture tests in DRIFT-IIc

The measurements presented in the previous section showed that, in theory, the DRIFT detector would be operable with CS<sub>2</sub>-CF<sub>4</sub> gas mixtures. This section details new work performed in collaboration with Occidental College introducing, for the first time, CS<sub>2</sub>-CF<sub>4</sub> gas mixtures to a full-scale DRIFT detector. These measurements were made using the DRIFT-IIc detector, which is essentially identical to the DRIFT-IIId detector described in the previous chapter, but is located in a surface laboratory at Occidental College in Los Angeles.

### 4.2.1 <sup>55</sup>Fe calibrations

The slight increase in *W*-value, from the addition of CF<sub>4</sub> to the CS<sub>2</sub> target, results in a reduced number of ionisation electrons from particle interactions in the detector volume. However, the large increase in gas gain means that each ionisation electron undergoes a much higher multiplication in the MWPC and, overall, interactions are expected to produce larger ionisation signals in the detector. An <sup>55</sup>Fe calibration in which events of 5.9 keV are produced in the detector volume (Section 5.2) allows the measurement of these combined effects.

Initial tests with a 30-10 Torr CS<sub>2</sub>-CF<sub>4</sub> gas mixture in the DRIFT-IIc detector quickly revealed that stable detector operation would not be possible with the 3000 V MWPC operating voltage used for pure CS<sub>2</sub>. At voltages approaching 3000 V large current excursions in the MWPC power supplies were observed indicating electric discharges in the MWPCs. To achieve stability, and to minimise the risk of damage to sensitive preamplification electronics, MWPC operating voltages were reduced. Preliminary tests on various gas mixtures showed that the reduction in MWPC voltage required for stability cancelled-out much of the increased gas gain from the addition of CF<sub>4</sub>. It was therefore decided to tune the MWPC operating voltage for each gas mixture such that the effects of the lower *W*-value, the higher gas gain, and the lower operating voltage cancelled exactly. The result of this is that, in each CS<sub>2</sub>-CF<sub>4</sub> gas mixture, the MWPC signal produced by a recoil of a given energy is the same as that from the same recoil in pure CS<sub>2</sub> at 3000 V.

Figure 4.6 shows, for 3 different CS<sub>2</sub>-CF<sub>4</sub> gas mixtures, the measured mean pulse area of <sup>55</sup>Fe events as MWPC voltages were increased. In each case an MWPC voltage is reached in which the mean pulse area is within ~3% of the value in the standard pure CS<sub>2</sub> conditions. A gas mixture of 10-30 Torr CS<sub>2</sub>-CF<sub>4</sub> was attempted but, at a voltage of 2700 V, before <sup>55</sup>Fe calibrations could be performed, significant discharges

occurred in the MWPC readout planes that resulted in damage to a number of electronics components. The 20-20 mixture was thus determined as the maximum CF<sub>4</sub> content for the current detector configuration.

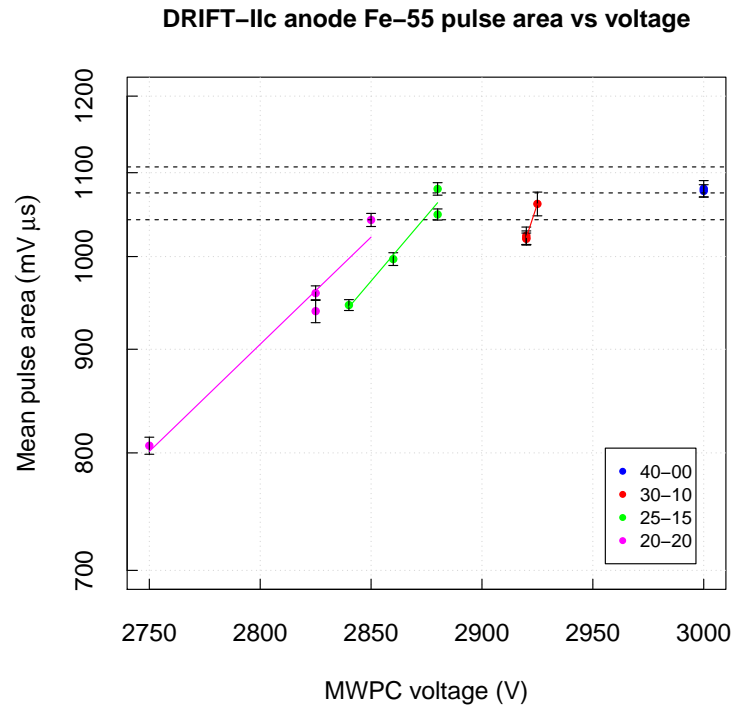


FIGURE 4.6: <sup>55</sup>Fe calibration plots from various gas mixtures in the DRIFT-IIc detector at Occidental College. For each gas mixture voltages are tuned to give a mean <sup>55</sup>Fe pulse area of 1075 mV μs to within 3% (black dashed lines).

## 4.2.2 Neutron calibrations

Neutrons from a <sup>252</sup>Cf source have been shown to produce nuclear recoils in DRIFT with an energy spectrum similar to that expected from massive WIMPs, making it an almost ideal calibration source [136]. Neutron calibrations of DRIFT-IIc were performed with three gas mixtures (40-00, 30-10 and 25-15 Torr CS<sub>2</sub>-CF<sub>4</sub>) and with the source at two different positions. As illustrated in Figure 4.7 this included an *x*-axis run, where the source was directly in front of the detector creating nuclear recoils biased in the direction of the *x*-axis; and a *z*-axis run where the source was placed directly behind the MWPC, creating nuclear recoils biased in the direction of the *z*-axis. In each case the source was placed 1.8 m from the detector, where the distance results in some collimation of the incident neutrons.

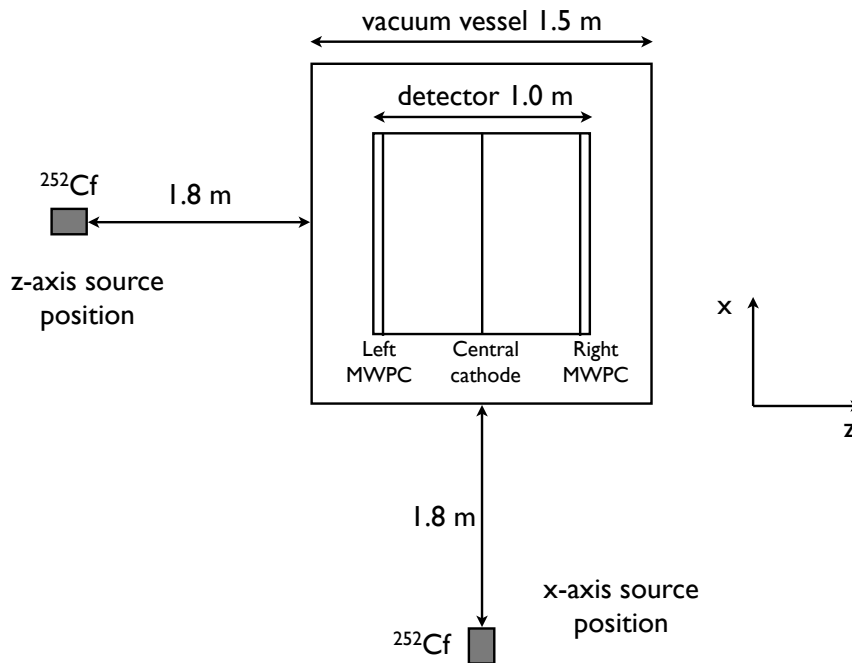


FIGURE 4.7: Schematic of neutron run geometry (not to scale) from a top-down viewpoint (refer to photograph in Figure 3.2 for reference). In the  $z$ -axis run the source is placed 1.8 m directly behind and in the centre of the left MWPC readout plane creating nuclear recoils biased in the direction of the  $z$ -axis. In the  $x$ -axis run the source is directly in front of the detector in the plane of the central cathode creating nuclear recoils biased in the direction of the  $x$ -axis.

Data from each run was analysed using the standard WIMP analysis cuts to select nuclear recoil events (Section 5.3). From the accepted nuclear recoil events the mean rate of nuclear recoils and the mean  $z$  component of the track range ( $\Delta z$ ) were calculated. Table 4.3 shows the mean rate of nuclear recoils detected for each gas mixture. A significant increase in event rate is observed with increased  $CF_4$  concentration. At fixed total pressure, volume and temperature, the number of molecules of gas in the detector is independent of the gas species. Increasing the partial pressure of  $CF_4$  relative to  $CS_2$ , therefore, has no effect on the number of carbon atoms in the detector volume but results in a decrease in the number of sulphur atoms. Since overall gains remain the same due to the voltage tuning, the increase in detected event rate must be attributed to the increased number of fluorine targets. This is evidence of sensitivity to fluorine recoils in the DRIFT-II detectors.

Table 4.4 shows the mean  $\Delta z$  for each of the neutron calibration runs, where  $\Delta z$  is seen to increase with  $CF_4$  concentration. Although this could be evidence of an increase in the mean range of tracks, as expected from the additional fluorine recoils, it could also be attributed to increased diffusion of the recoil tracks. However, the difference between  $\Delta z$  for the  $z$ -axis run and  $\Delta z$  for the  $x$ -axis run also increases with  $CS_2$ - $CF_4$  gas mixtures

Gas mix (CS <sub>2</sub> -CF <sub>4</sub> Torr)	C:F:S ratio	MWPC voltage (V)	Event rate (Hz)
40-00	4:0:8	3000	0.66±0.02
30-10	4:4:6	2925	0.84±0.02
25-15	4:6:5	2880	0.97±0.02

TABLE 4.3: Nuclear recoil event rates from neutron calibration runs of CS<sub>2</sub>-CF<sub>4</sub> gas mixtures.

relative to pure CS<sub>2</sub>. This implies that *directionality* is increasing, suggesting a larger mean recoil length, which is further evidence that fluorine recoils are being detected.

Gas mix	C:F:S ratio	MWPC voltage (V)	Source axis	$\Delta z$ (mm)
40-00	4:0:8	3000	<i>z</i> -axis	2.54 ± 0.02
		3000	<i>x</i> -axis	2.44 ± 0.02
30-10	4:4:6	2925	<i>z</i> -axis	2.77 ± 0.03
		2925	<i>x</i> -axis	2.59 ± 0.02
25-15	4:6:5	2880	<i>z</i> -axis	2.80 ± 0.02
		2880	<i>x</i> -axis	2.64 ± 0.02

TABLE 4.4: Measurement of  $\Delta z$  component of neutron induced nuclear recoils in CS<sub>2</sub>-CF<sub>4</sub> gas mixtures. Neutron source *x*-axis and *z*-axis positions illustrated in Figure 4.7.

### 4.3 Gas mixing system design and construction

In the 1 m<sup>3</sup> DRIFT-II detector a continuous flow of target gas is required to maintain target gas purity against the imperfect vacuum and to reduce build up of radon contamination and its associated backgrounds (Section 3.2.2). When operating with a target gas of pure CS<sub>2</sub> this is achieved with the relatively simple system described in Section 3.2.2. However, this system is not capable of a controlled supply of a mixture of gases to the vacuum vessel. This section describes the design and construction of a new automated gas mixing system to provide a continuous supply of arbitrary CS<sub>2</sub>-CF<sub>4</sub> gas mixtures to the DRIFT-II detectors.

#### 4.3.1 Hardware design

A gas mixing system is required to continuously supply premixed gas to the vacuum vessel at a minimum rate of approximately one vacuum vessel (3375 L) of 40 Torr gas per day. Figure 4.8 shows the schematic design of the new gas mixing system in which the mixing procedure is controlled and monitored by a system of four mass flow controllers (MFCs) and three capacitance manometer pressure gauges (PGs).

Assuming that the vacuum vessel and entire mixing system begin evacuated, with all mass flow controllers in the closed position, preventing gas flow, and assuming a typical gas mixture of 30-10 Torr CS<sub>2</sub>-CF<sub>4</sub>, the system operates as follows:

1. The mixing cylinder and supply cylinder valves are closed by hand and MFC1, MFC3 and MFC4 are opened such that CS<sub>2</sub> flows through the mixing system directly to the vacuum vessel, bypassing the mixing and supply chambers. MFC1 is closed when the vacuum vessel pressure gauge (PG3) shows that the desired CS<sub>2</sub> content (30 Torr) has been reached.
2. MFC2 is then opened, so that CF<sub>4</sub> flows directly to the vacuum vessel, and is closed when the desired total fill pressure (40 Torr) is reached in the vacuum vessel, measured by PG3.
3. All mass flow controllers are now closed and the valves on the mixing chamber and supply chamber are opened by hand.
4. The automated gas mixing cycle now begins. MFC1 is opened and the mixing chamber fills with CS<sub>2</sub> gas. When the desired pressure is reached in the mixing chamber MFC1 is closed.
5. MFC2 is then opened and CF<sub>4</sub> gas is added to the CS<sub>2</sub> in the mixing chamber. When the target pressure is reached, indicating the correct CS<sub>2</sub>-CF<sub>4</sub> mixture in the mixing chamber, MFC2 is closed.
6. MFC3 is opened and equilibrium occurs between the mixing and supply chamber.
7. The gas mixture is supplied to the vacuum vessel via MFC4 with a rate that maintains the 40 Torr operating pressure in the vacuum vessel.
8. When the pressure in the supply chamber falls below a predetermined level, MFC3 is closed, isolating the supply chamber from the mixing cylinder. The mixing process then repeats while the supply chamber continues to supply the vacuum vessel with the gas mixture.

So that the gas mixing system could be designed, built and tested on DRIFT-IIc at Occidental College, then shipped to the UK to be installed on DRIFT-IIId at the Boulby Underground Laboratory, it was required to be relatively portable. The gas mixing system was therefore designed so that the main components were in a self-contained 19-inch rack mountable panel, to which target gas cylinders and the mixing and supply chambers could be attached on location.

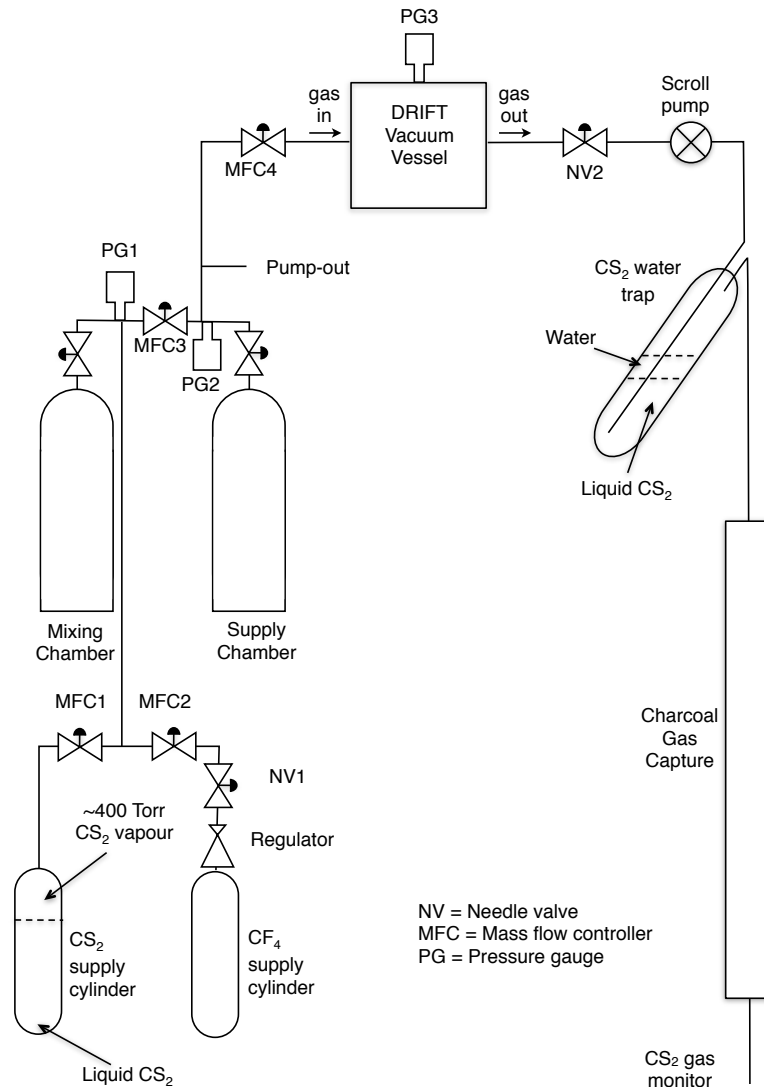


FIGURE 4.8: Schematic diagram of the  $CS_2$ - $CF_4$  gas mixing system. The supply cylinder isolates premixed gas during the fill cycle to allow continuous supply of target gas to the detector volume. During fill cycle MFC1 and MFC2 allow sequential controlled addition of  $CS_2$  and  $CF_4$  to the mixing chamber in the required partial pressures. The gas output system remains the same as that described in Section 3.2.2. See text for full details.

Figure 4.9 shows a to-scale design of the gas mixing panel. Four MKS Mass-Flo 1479A mass flow controllers [137] are mounted on the panel, each of which has an associated dual LED indicator light indicating the MFC status (open, closed or controlled flow). In addition there is an LCD display to show the gas flow rate through MFC4. Two MKS Baratron 626A capacitance manometer pressure gauges [138] are also mounted on the panel, each with an LCD display showing its pressure reading. Each MFC and PG is connected, via a D-sub connector, into a custom made PCB, which interfaces all required inputs and outputs with connections on the front of the panel, as well as providing  $\pm 15$  V power from the panel mounted DC power supply.

The panel has four 6 mm Swagelok connections on the back to which the supply and mixing chambers and the  $CS_2$  and  $CF_4$  cylinders are attached. The supply and mixing chambers currently used are standard 50 L steel high-pressure gas cylinders attached via CGA 580 to 6 mm Swagelok adapters. There are two 6 mm Swagelok connections on the front of the panel, one of which is to supply the mixed gas to the vacuum vessel; the other is so that a pump can be attached to directly evacuate the mixing system. All analogue communications with the gas mixing panel are through ten BNC connections on the panel front (two for each MFC and one for each PG) and all digital signals through a single 15 pin D-sub connection.

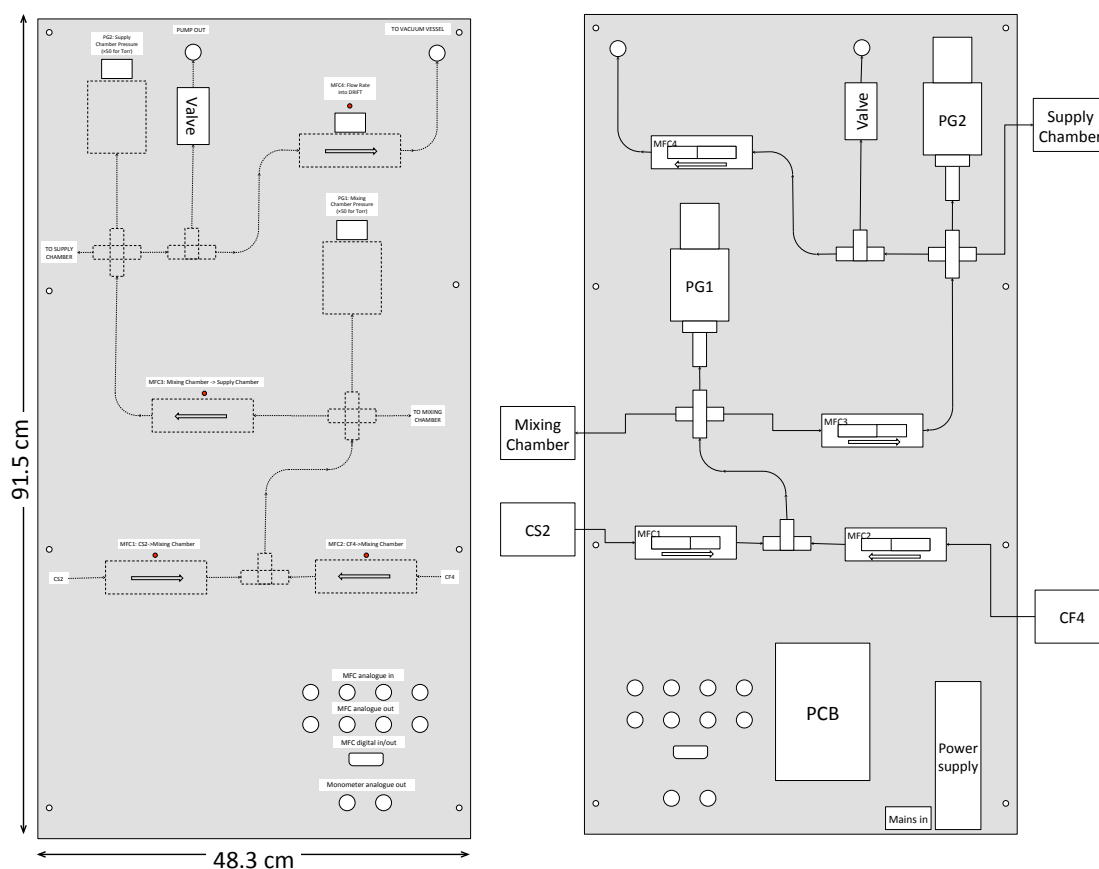


FIGURE 4.9: Scale diagram of gas mixing panel.

### 4.3.2 Electronics design

Each MFC is controlled by two lines of input. The first carries an analogue signal for the set point voltage. The second sets the MFC to either a *fully closed* position (connected to 0 V) a *fully open* position (connected to +5 V), or a *controlled flow* mode (floating), where the maximum rate of flow through the MFC is determined by the set point voltage. In addition each MFC has an analogue output of between 0 and 5 V, which corresponds

to the actual measured flow rate through the device. Each PG has only a single output — an analogue signal in the range 0 to 10 V corresponding to a pressure range of 0 to 1000 Torr.

Figure 4.10 shows a representative circuit design for the control of one mass flow controller and one pressure gauge. The pressure gauge connects to the PCB via a 15 pin D-sub connection, of which only six pins are used. Five of these pins provide power and ground connections. The remaining pin contains the single line of analogue output, which is split and goes to the panel mounted LCD display voltmeter, and a BNC bulkhead on the front of the panel. The mass flow controller connects to the PCB via a 9 pin D-sub connection, of which eight pins are used. Similarly, five of these pins provide power and ground connections to the MFC. The analogue output pin is split to both a BNC feedthrough and a panel mounted LCD display<sup>1</sup>. The analogue input pin, used for the set point voltage, is connected to a BNC bulkhead on the front of the panel. The remaining pin, controlling the MFC state and requiring a signal of 5 V (fully open), 0 V (fully closed) or floating (controlled flow) connects to a logic circuit that provides this signal via three TTL signals.

The logic circuit, shown in the top part of Figure 4.10, uses two AND gates (74LS08), an inverter (74LS04), and a tri-state buffer (74LS125) to achieve the required control, shown in Table 4.5. The ‘master’ channel is required to overcome an inherent behaviour of the multifunction DAQ card that sets all TTL signals to ‘high’ on a reboot of the PC. The digital inputs controlling the MFC state are connected to panel mounted LEDs, to indicate the state of each MFC. The PCB was designed to contain connections to all four MFCs and two PGs on a single 3” by 5” dual layer PCB. The board layout is shown in Figure 4.11.

TTL Inputs			Tri-state Output
O/C	F	Master	→ MFC state
1	0	0	+5 V → Open
0	0	0	0 V → Closed
0	1	0	Floating → Controlled flow
(1)	(1)	(0)	(Floating → Controlled flow)
X	X	1	0 V → Closed

TABLE 4.5: Logic truth table for TTL control of mass flow controllers.

The analogue and TTL outputs required for MFC control are provided by a National Instruments NI6024E multifunction DAQ PCI card [139], which is installed in the existing DRIFT control computer. The six analogue outputs of the gas mixing panel (four MFC

<sup>1</sup>Although only one LCD display, for MFC4, is installed in the panel, connections exist for all MFCs so they could be added later.

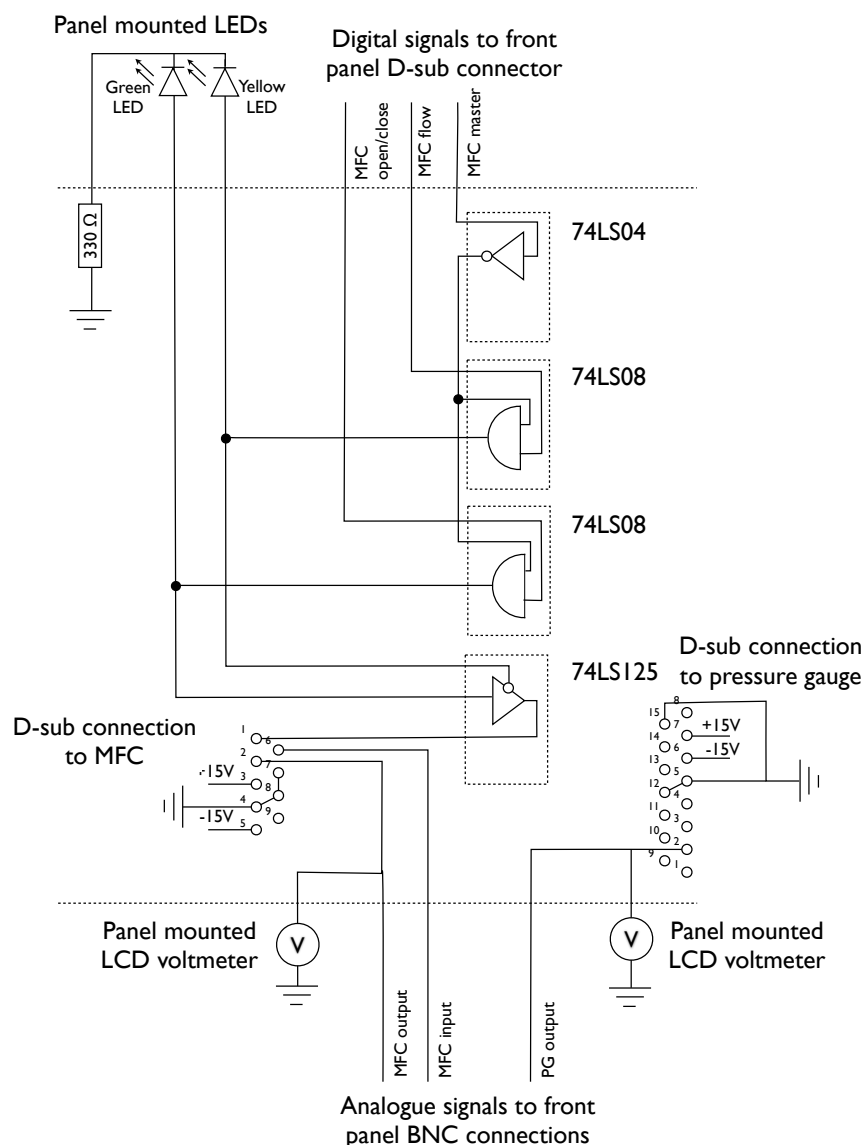


FIGURE 4.10: Representative circuit diagram for the gas mixing system control showing layouts for connections to one MFC and one PG. Connections at the top of the board connect to a D-sub connector on the panel and carry digital signals to control the MFC state. Connections at the bottom of the board connect to BNC feedthroughs on the panel and carry analogue signals. See text for full details.

and two PG) connect via the panel mounted BNC connections to the existing slow control system that takes continuous, high accuracy voltage measurements (Section 3.2.2). This integration into the existing slow control system means that the channels are continually recorded and added to a database that can be easily monitored via the existing web based system, or accessed by the custom gas mixing program. In order to achieve the required precision in voltage measurements, however, readings are made only every  $\sim 10$  seconds. This slow reaction to changes in pressure places constraints on the design of the gas mixing system control.

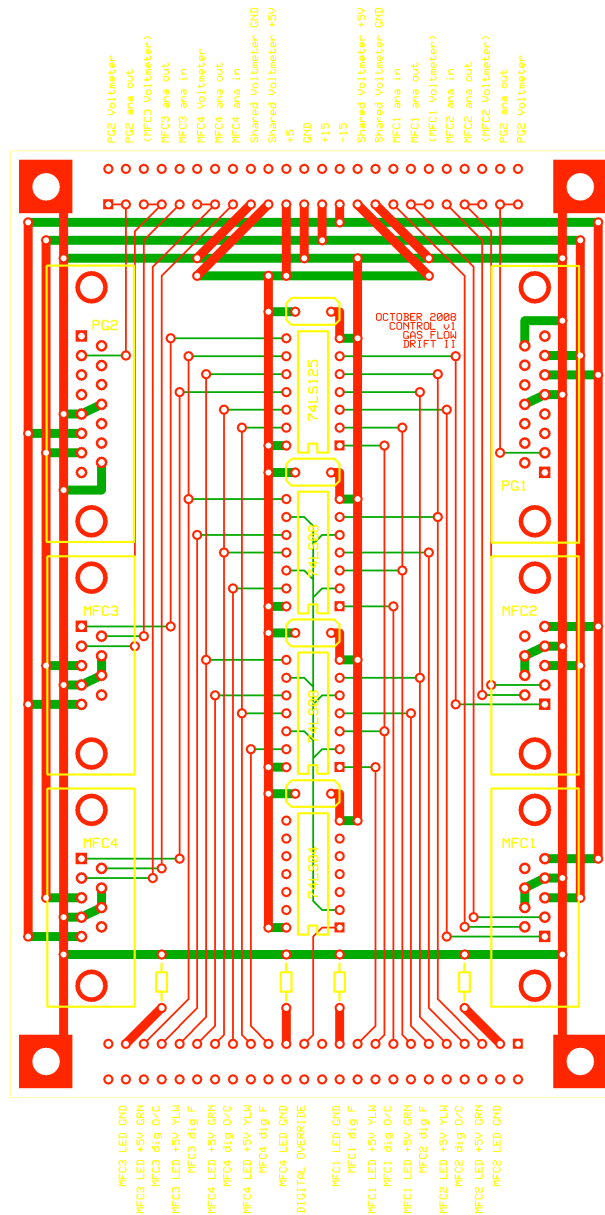
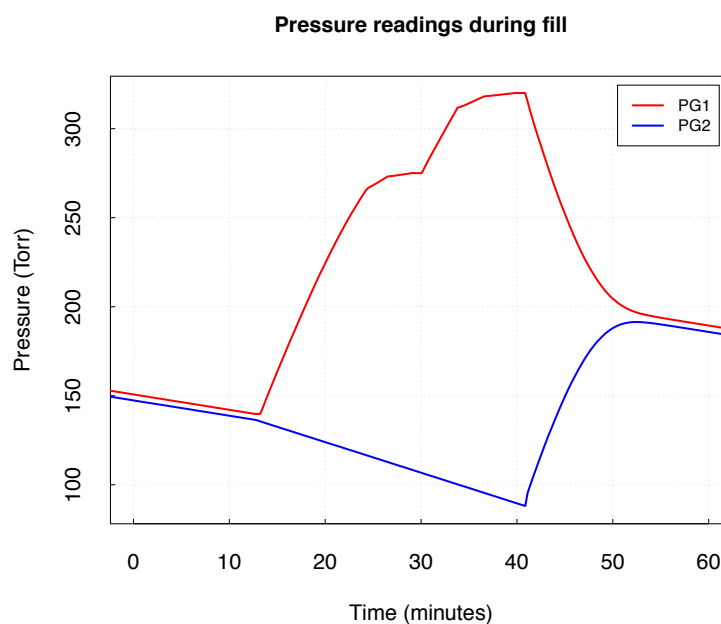


FIGURE 4.11: Schematic of PCB for control of gas mixing system. Red is top layer, green is bottom layer, yellow is silkscreen layer. Connections at top of board are to digital controls for MFC state, connections at bottom are for analogue signals.

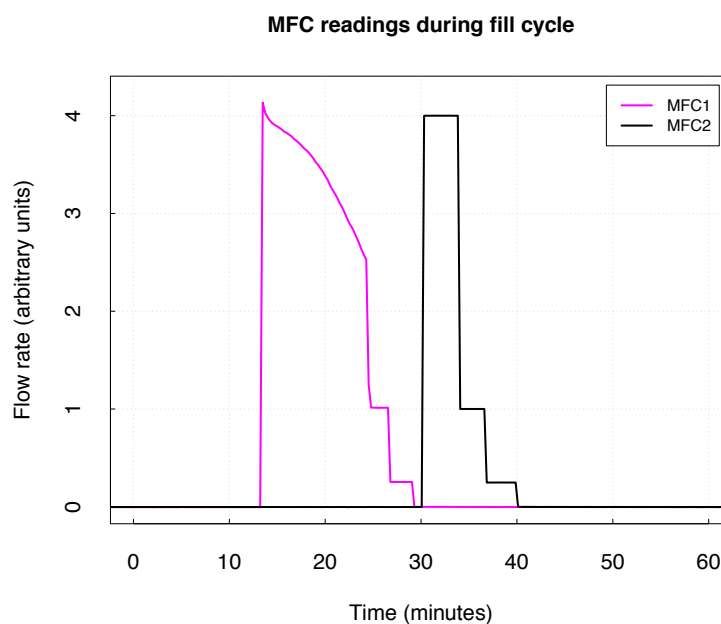
### 4.3.3 Software design

The gas mixing system, to be installed underground at the Boulby Underground Laboratory, is required to operate unsupervised for long periods, with the possibility of remote operator intervention if problems are suspected. A program, named *GasMix*, was written to provide both manual control of the gas mixing panel and to perform automatic and continuous fill cycles. The program was written in C using drivers and functions from the National Instruments NIDAQmx Base package [140].

**Automated operation** — GasMix was designed to perform continuously and automatically the gas mixing operation described in Section 4.3.1. A number of hardware constraints determined the fill cycle procedure. Firstly, the  $\sim 10$  second interval between pressure readings limited the speed at which precise fill operations could be completed. In addition, because the panel mounted PG1 is a significant distance from the mixing chamber ( $\sim 1$  m away connected by a 6 mm diameter flexible vacuum hose) the pressure gauge sees an overpressure during filling and hence greatly overestimates the actual pressure of the mixing chamber. A solution to both of these problems is to reduce the flow rate from the CS<sub>2</sub> and CF<sub>4</sub> supply cylinders. A graduated decrease of the flow rate was implemented to maximise fill accuracy whilst minimising the time taken for a fill cycle to complete. An efficient fill cycle is required to ensure that the gas mixing is completed before the gas in the supply chamber becomes too low to maintain the flow rate to the vacuum vessel. A suitable solution for the addition of each gas was to set the MFC to fully open until PG1 was within 50 Torr of its target value, 4/5 open to within 10 Torr, 1/5 open to within 2 Torr, and finally 1/20 open until the target pressure was reached. The stepped decrease in flow rate can be seen in Figure 4.12.



(a) Mixing chamber pressure (PG1, red) and supply chamber pressure (PG2, blue).



(b)  $CS_2$  flow rate (MFC1, magenta) and  $CF_4$  flow rate (MFC2, black).

FIGURE 4.12: One filling cycle as monitored by the slow control. In minutes: 0–12) Normal running, both chambers in equilibrium supplying the vacuum vessel with gas mixture; 12–29) MFC3 is closed isolating the supply cylinder from the mixing cylinder. MFC1 flows  $CS_2$  to the mixing cylinder (PG1) with stepped flow rate until target pressure is reached; 30–40) MFC2 flows  $CF_4$  to the mixing cylinder with stepped flow rate until target pressure is reached; 40–60) MFC3 is opened and gas mixture flows to supply chamber (PG2). Equilibrium is reached and normal running continues.

At room temperature, CF<sub>4</sub> is volatile so that the fill speed is limited only by the speed of the slow control measurements. The boil-off pressure of CS<sub>2</sub>, however, is only ~400 Torr, which is a limiting factor in the time taken in completing each fill cycle and the maximum pressure that can be achieved in the mixing chamber. As the liquid CS<sub>2</sub> evaporates during the CS<sub>2</sub> fill stage it cools, leading to a reduced boil-off pressure and hence a decreasing fill rate, as illustrated during minutes 12 to 24 in Figure 4.12(b). To achieve reasonable fill times it is only possible to reach pressures of around ~270 Torr of CS<sub>2</sub> in the mixing chamber. Due to this restriction, the maximum flow rate that can be achieved (so that the supply chamber does not run out of gas before the mixing cycle is complete) is approximately 2 vacuum vessel changes per day — twice the presently required flow rate. Higher flow rates may be achieved by, for example, heating the CS<sub>2</sub> input cylinder or sourcing a larger supply chamber.

As with the previous gas flow system (Section 3.2.2), the rate at which gas is flowed through the system is determined by the pump-out rate. In the previous system the CS<sub>2</sub> was replenished via a MFC that took a set point directly from the vessel pressure gauge. The red line in Figure 4.13 shows that, due to the large vacuum vessel and slow reaction time of the MFC this resulted in an oscillation of ±0.5 Torr about the target pressure of 40 Torr. As well as automating the gas mixing cycles, the GasMix program is now responsible for maintaining a constant pressure in the vacuum vessel by directly controlling the flow of mixed gas through MFC4 to the vacuum vessel. MFC4 is independent of the gas mixing cycles and, during normal running, is permanently in the controlled flow mode, with a flow rate that is adjusted every 10 seconds to maintain the vessel target pressure. The formula for the change in the set point voltage is given by

$$\Delta V_{\text{set}} = A(P_{\text{target}} - P_{\text{measured}}) + B \frac{d}{dt}(P_{\text{target}} - P_{\text{measured}}), \quad (4.2)$$

where  $P_{\text{target}}$  is the target pressure (typically 40 Torr) and  $P_{\text{measured}}$  is the measured pressure of the vacuum vessel.  $A$  and  $B$  are experimentally determined constants and, for the current detector configuration, are 500 V Torr<sup>-1</sup> and 1000 V Torr<sup>-1</sup> respectively. The combination of proportional and derivative terms has been found to be extremely stable, maintaining pressure to well within 40.00±0.01 Torr. Figure 4.13 shows the stability of the GasMix controlled MFC4 compared to the previous MFC with an inbuilt control. The system has also been shown to quickly return the vessel to a stable target pressure from significant pressure deviations of at least ±3 Torr that may occur due to, e.g., pump malfunctions.

**Graphical user interface** — Although the main function of GasMix is to automate fill cycles for continuous unmanned operation, to offer as much flexibility and control as possible, and to provide remote monitoring and operation, a graphical user interface

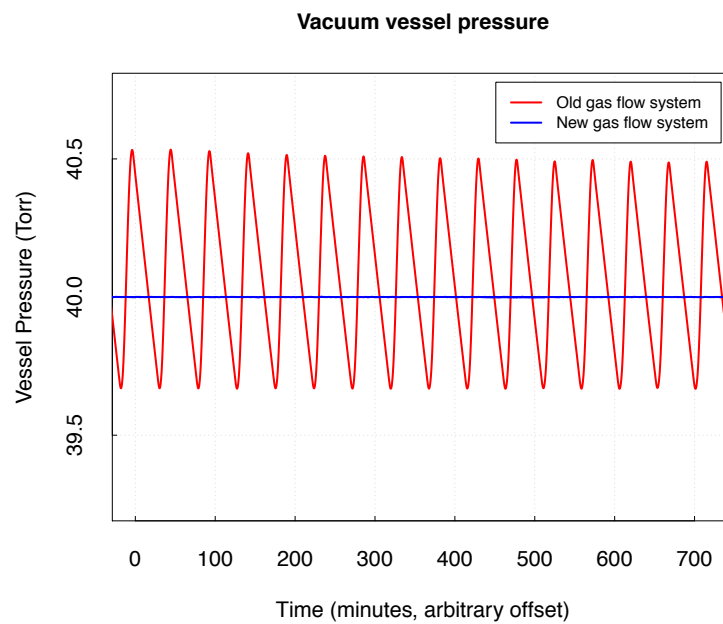
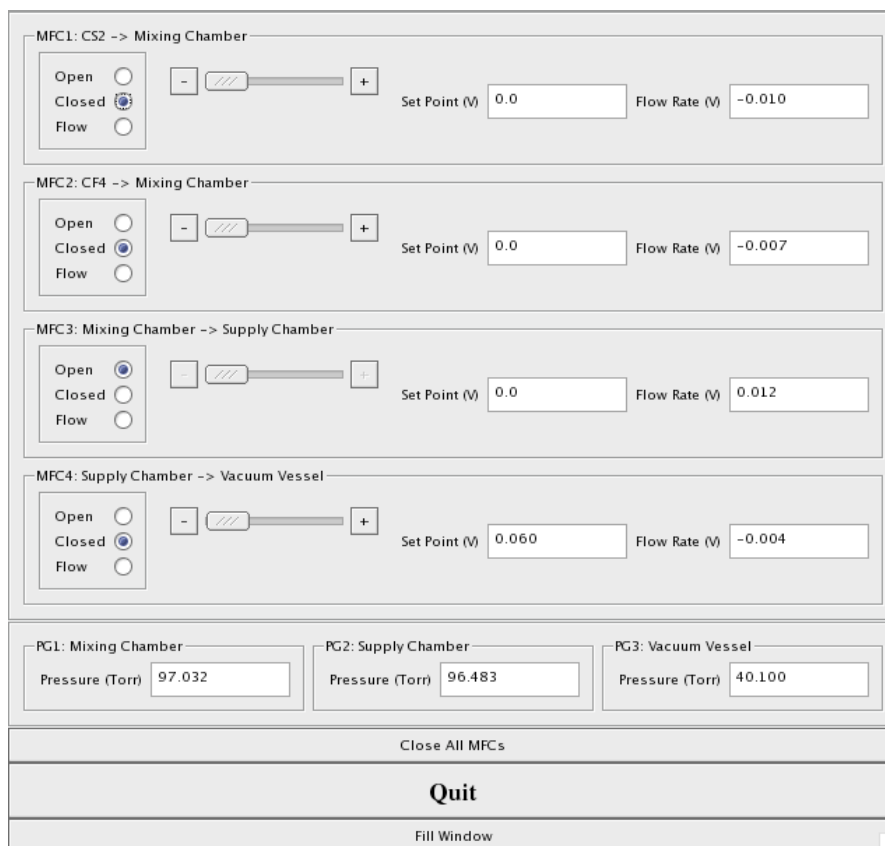


FIGURE 4.13: Comparison of vacuum vessel pressure during normal operation with the old MFC (red) compared to the GasMix controlled MFC (blue).

(GUI) was produced. The GUI was written in C++ using the Qt framework [141] and consists of two control windows. The main window, shown in Figure 4.14(a), is for the manual control and monitoring of each MFC and PG. The fill window, shown in Figure 4.14(b), is where the input parameters of the automated filling process are input and continuous operation is initiated.



- (a) Main window of GasMix GUI. Top section contains controls for each of the four MFCs, with selectable radio buttons for MFC state, a slider control for the controlled flow set point, and readings of the current set point and the current measured flow rate. The section under this shows the three pressure gauge readings.



- (b) Fill window of GasMix GUI. The PG1 pressure at which the fill cycle should start, the percentage of  $CF_4$  required and the total fill pressure are entered by the user. The 'Fill Once' button is used to perform a single fill cycle then stop and the check box turns on the continuous automated fill mode.

FIGURE 4.14: Screenshots of the GasMix GUI.

## 4.4 Gas mixing system underground on DRIFT-IIId

After the construction, development and testing of the gas mixing system at Occidental College, the system was shipped to the Boulby Underground Laboratory where it was installed on the DRIFT-IIId detector, as shown in Figure 4.15. The stability of the gas mixing system is crucial to ensure the correct gas mixture is maintained over long periods of operation. This section details a number of stability measurements since this installation.

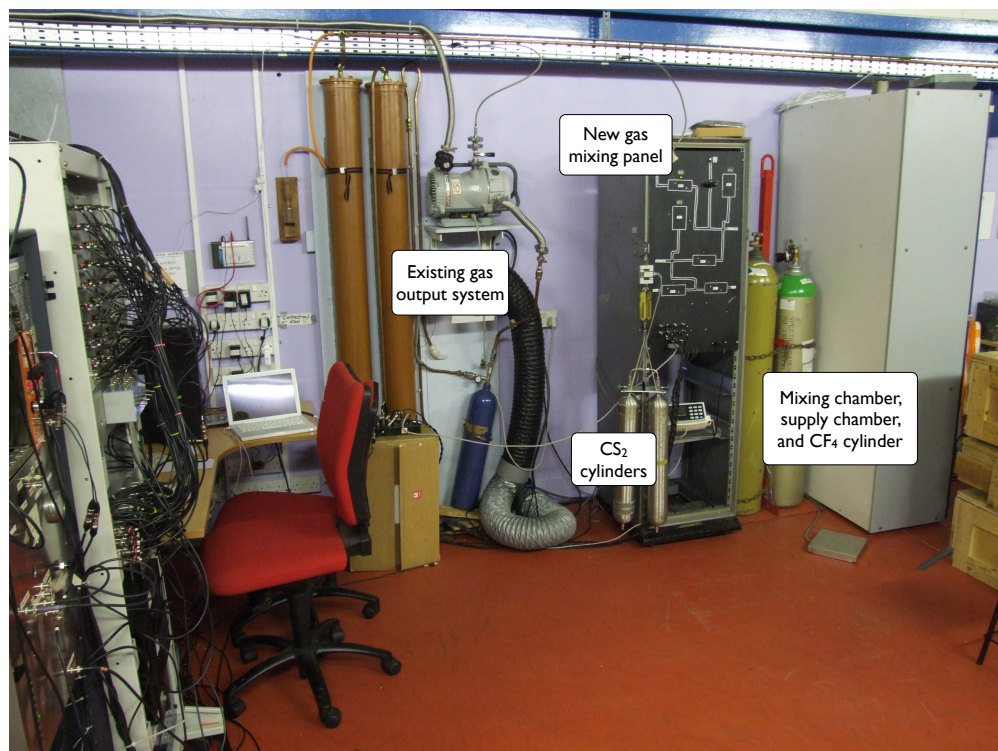


FIGURE 4.15: The gas mixing system installed at the Boulby Underground Laboratory.

### 4.4.1 Stability and monitoring

**Short term pressure monitoring via DRIFTwatch** — The integration of the gas mixing system with the existing slow control system means that the PG1 and PG2 pressures, which determine the fill ratio, can be viewed remotely via the existing *DRIFTwatch* web interface to monitor gas mixing system operation.

Figure 4.16 shows the PG1 and PG2 readings over 24 hours. The fill pattern is seen to be very regular and any irregularities in a particular fill cycle can usually be identified from periodic viewing of these plots. The DRIFTwatch slow control system has integrated alarms that send out warnings to collaboration members via email and SMS messaging

if readings occur outside preset limits. By setting alarms on the upper limit of PG1 (to warn of a fill overshooting its target) and the lower limit of PG2 (indicating that a fill is taking too long) any irregularities in a given fill cycle will immediately trigger the alarm. In the current configuration, if a fill cycle fails the alarm gives the operator  $\sim 45$  minutes to take appropriate action to resolve the problem until the supply chamber is no longer able to maintain the required flow rate. In the rare case in which the gas system and the alarm system may fail, or if an operator is unable to access the system, the hardware cut-off on the vacuum vessel pressure will kill all high voltages if the pressure in the vacuum vessel drops below 39.5 Torr.

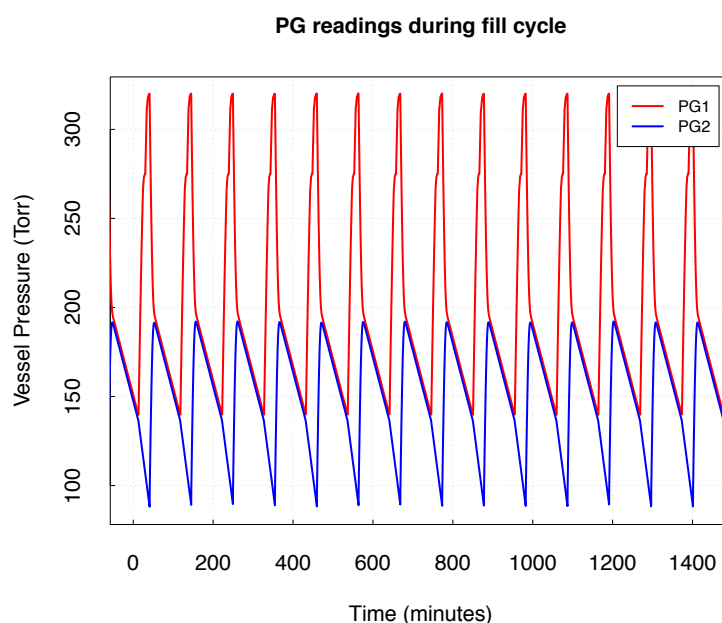


FIGURE 4.16: Mixing chamber (PG1, red) and supply cylinder (PG2, blue) pressures over a 24 hour period.

Figure 4.17 shows a situation in which the CS<sub>2</sub> supply cylinder is diminished. When the CS<sub>2</sub> level is low the cooling effects of evaporation on the remaining CS<sub>2</sub> are more severe and the boil-off pressure reduces. The CS<sub>2</sub> part of the fill cycle is seen to take progressively longer and, as a result, the supply chamber pressure reduces further with each fill. Although the mass of the CS<sub>2</sub> supply cylinders is monitored to avoid this situation, if CS<sub>2</sub> levels do run low the user is alerted at least 8 hours before the CS<sub>2</sub> level becomes too low to maintain the detector pressure, so the detector can be remotely shut down if needed.

**Long term monitoring via fill logs** — Although the slow control system enables the identification of significant errors during operation, slight systematic shifts in the

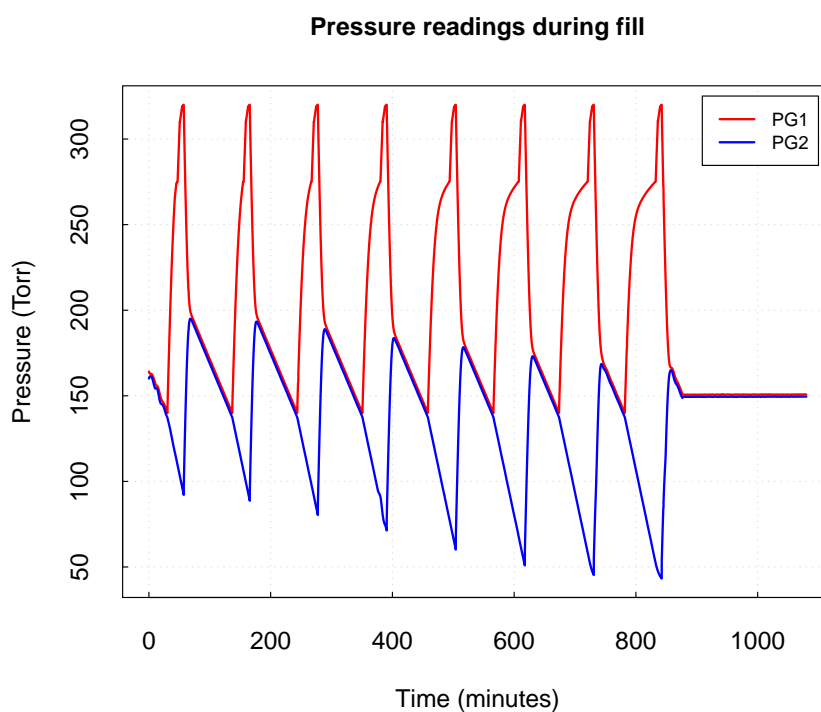


FIGURE 4.17: Mixing chamber (PG1, red) and supply cylinder (PG2, blue) pressures with a dwindling  $CS_2$  supply. With low  $CS_2$  levels, increased cooling occurs during evaporation leading to reduced evaporation and slower fill cycles. The longer fill time leads to a reduced minimum pressure in the supply chamber during the fill, which triggers the alarm.

fill pressures are unlikely to be noticed here. To enable long term monitoring of the gas mixing a record is made, for each fill cycle, of the fill start time and the mixing chamber pressure at each stage of the fill. Periodic analysis of the summary table allows the long term stability of the gas mixing procedure to be monitored. Figure 4.18 shows the ratio of  $CS_2$  to  $CF_4$  in each mixing cycle for 298 cycles over a period of one month, where the ratio is determined from the change in PG1 pressure over the  $CS_2$  and  $CF_4$  filling stages. The fill ratio is seen to vary from the nominal 3.0 (for a 30-10 Torr  $CS_2$ - $CF_4$  mixture) by no more than  $\pm 0.02$ . Figure 4.19 shows a histogram of 2393 fill cycles covering over 200 days of operation. A Gaussian fit to the data reveals a mean  $CS_2$  fraction of  $3.003 \pm 0.0002$  with a standard deviation of  $(7.5 \pm 0.1) \times 10^{-3}$ , indicating an extremely precise and stable gas mixing system performance.

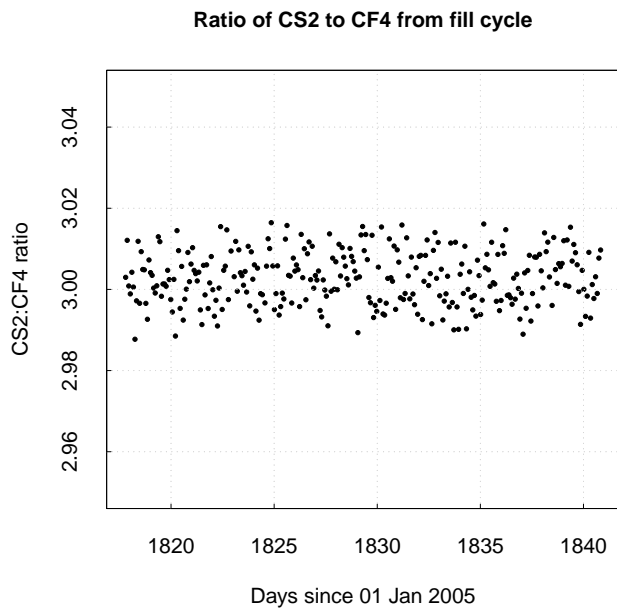


FIGURE 4.18: Ratio of CS<sub>2</sub> to CF<sub>4</sub> added to the mixture in each fill cycle.

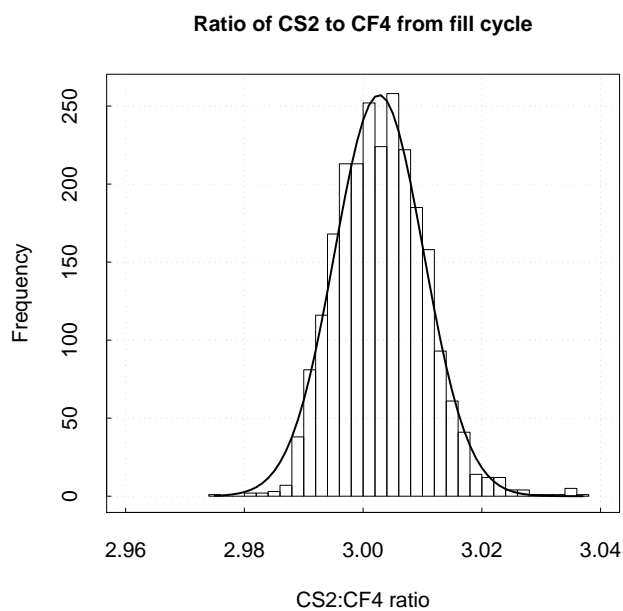


FIGURE 4.19: Histogram of CS<sub>2</sub> to CF<sub>4</sub> fill ratios from 2393 fill cycles covering  $\sim 200$  days of operation. Gaussian fit gives mean CS<sub>2</sub> to CF<sub>4</sub> ratio of  $3.003 \pm 0.0002$  and  $\sigma = (7.5 \pm 0.1) \times 10^{-3}$ .

**Monitoring gas mixture via <sup>55</sup>Fe calibration** — Increasing CF<sub>4</sub> content in CS<sub>2</sub>-CF<sub>4</sub> gas mixtures significantly increases gas gain, resulting in increased ionisation collected from <sup>55</sup>Fe interactions in the detector (Section 4.1.3). The standard six hourly <sup>55</sup>Fe calibrations therefore offer an independent method of monitoring the ratio of CS<sub>2</sub> to CF<sub>4</sub> in the vacuum vessel over long periods of operation.

Figure 4.20 shows gain curves from the underground DRIFT-IIId detector operating with 40-00 and 30-10 Torr CS<sub>2</sub>-CF<sub>4</sub> configurations. The gain curves show that, at the current standard operating voltage of 2840 V, changing the gas mixture from 30-10 Torr CS<sub>2</sub>-CF<sub>4</sub> to 40 Torr pure CS<sub>2</sub> results in a  $\sim 22\%$  decrease in ionisation produced in <sup>55</sup>Fe calibrations mean pulse area.

Figure 4.21 shows the mean pulse area from the 6 hourly <sup>55</sup>Fe calibration runs for a period of about one month, during which gains are seen to remain stable to within  $\sim 2\%$ . The fluctuations in the gain correlate with fluctuations in currents supplied by the MWPC high voltage supplies. These fluctuations limit the ability to detect small changes in gain that may be due to changing CF<sub>4</sub> content. Nonetheless, if the CF<sub>4</sub> content was systematically increasing or decreasing over long periods of time the <sup>55</sup>Fe calibrations should show this with a general increase or decrease in the mean pulse area of <sup>55</sup>Fe events over time. The  $\pm 2\%$  stability shows that the CS<sub>2</sub>-CF<sub>4</sub> ratio is not changing drastically over long time periods.

The collaboration is currently working on development of a residual gas analyser to enable continuous direct measurement of the gas composition, as well as measuring gas contamination.

#### 4.4.2 Conclusions

A gas system for maintaining a controlled mixture of CF<sub>4</sub> and CS<sub>2</sub> at a controlled overall pressure of 40 Torr in the drift vessel has been implemented. The majority of the design, construction, testing, installation and commissioning was performed by the author. The system has been running for 2 years, and has proved reliable, stable, and safe. This subsystem enables the operation of DRIFT as a detector for spin-dependent WIMP-nucleus interactions, a critical step for the experiment that has resulted in new publications for the collaboration [118].

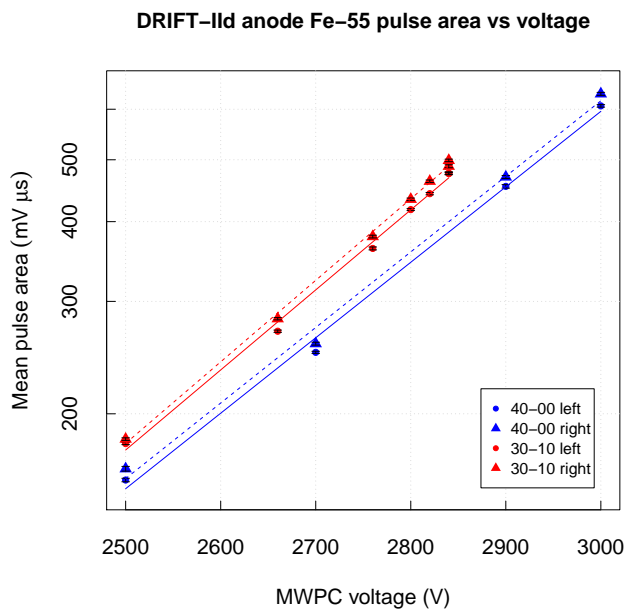


FIGURE 4.20:  $^{55}Fe$  gain plots from 40 Torr  $CS_2$  (blue) and 30-10 Torr  $CS_2-CF_4$  (red) gas mixtures in the DRIFT-II d detector. Circles (fit with solid line) and triangles (fit with dashed line) are measurements from left and right MWPCs respectively.

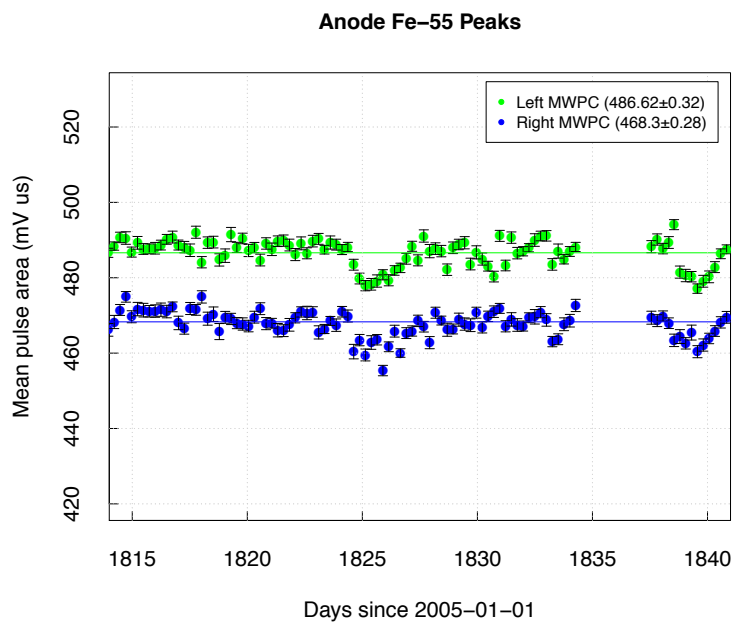


FIGURE 4.21: Mean pulse area produced by  $^{55}Fe$  events as a function time — showing a rate stable to approximately  $\pm 2\%$  over one month.

## Chapter 5

# DRIFT-II data analysis

The raw event rate from DRIFT-II during normal operation is  $\sim 1$  Hz. In this chapter event parameterisation and cuts are described, which result in a reduced set of WIMP-induced nuclear recoil candidates.

The energy calibration of DRIFT, via exposure to an  $^{55}\text{Fe}$  source, is described. An enhanced analysis procedure for  $^{55}\text{Fe}$  calibration is presented resulting in improved energy resolution and yielding a new technique for on-line monitoring of detector stability.

Finally, a data reduction procedure is developed with the motivation of improving efficiency of the existing data reduction process. This was performed using 47.36 days of data from DRIFT-II with a 30-10 Torr  $\text{CS}_2\text{-CF}_4$  gas mixture. New cuts developed here, and the tuning of existing cuts, produced a background-free signal region with a nuclear recoil detection efficiency improved by a factor of 2.4.

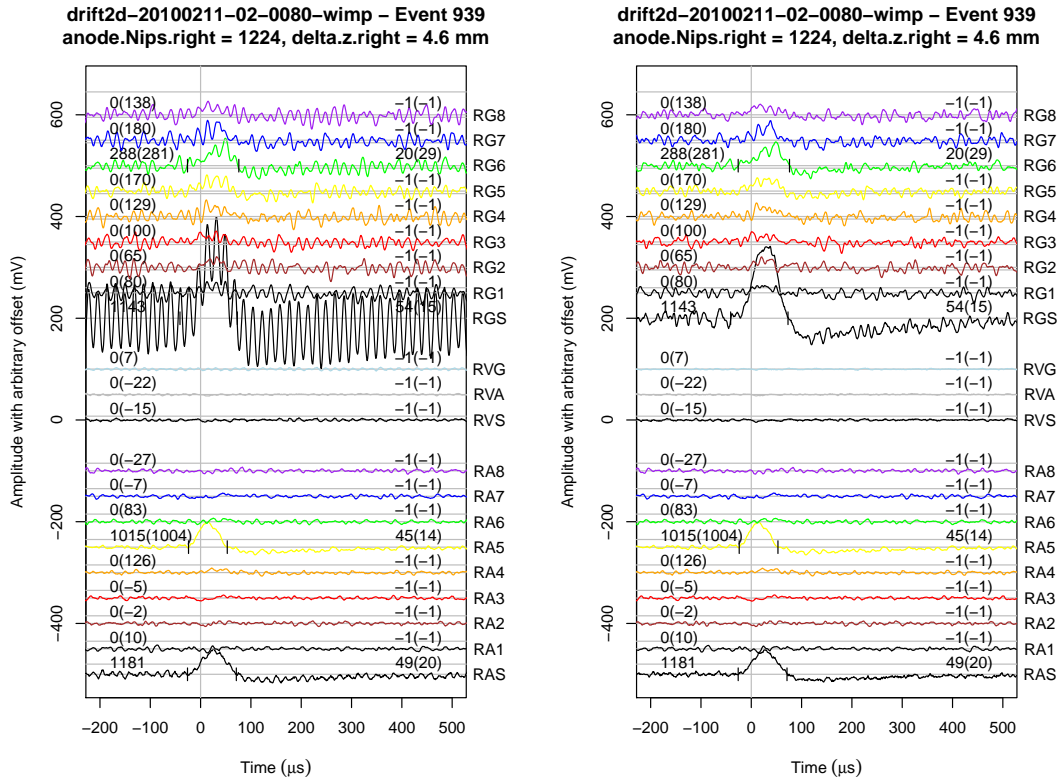
### 5.1 Waveform preprocessing

In Section 3.2.4 a typical event file was examined at the output of the preprocessing and digitisation electronics after some initial digital preprocessing to remove noise. This section describes well understood waveform filtering techniques used to improve signal-to-noise in all event waveforms before any parameterisation is attempted.

#### 5.1.1 High frequency noise removal

Figure 5.1(a) shows data from the right MWPC only from an event file in its raw form at the output of the digitisation electronics. Without the standard digital preprocessing each line can be seen to contain high frequency sinusoidal noise. A Fourier analysis of

the anode sum line reveals a clear peak in the power spectrum at a frequency of 55 kHz. The power spectrum of the grid sum line, shown in Figure 5.2, similarly has a peak at 55 kHz but also two further peaks at 110 and 165 kHz — harmonics of the 55 kHz noise.



(a) Data from right MWPC only prior to 55 kHz (b) The same data as in (a), but with 55 kHz noise removal.

FIGURE 5.1: Effects of 55 kHz noise removal on an event file containing a candidate nuclear recoil event. The effects of the noise removal, although present on each line individually, are seen most clearly on the grid sum line (RGS).

This high frequency noise is only present when the central cathode is at voltage, suggesting this is the source of the 55 kHz noise, despite the presence of a low-pass filter between the high voltage supply and the cathode. The noise is smaller on the anode lines, likely because of the shielding provided by the surrounding grid planes. Periodic Fourier analyses of data show that this high frequency noise has been present over the life of DRIFT-II and, although varying in amplitude, has remained at a fixed frequency of 55 kHz.

This regular sinusoidal noise is simple to remove in software with the use of a Fourier transform notch filter. For each line the discrete Fourier transform is taken and the 55 kHz noise and its harmonics are removed from the power spectrum. The inverse Fourier transform is then applied, returning the original line with the 55 kHz component

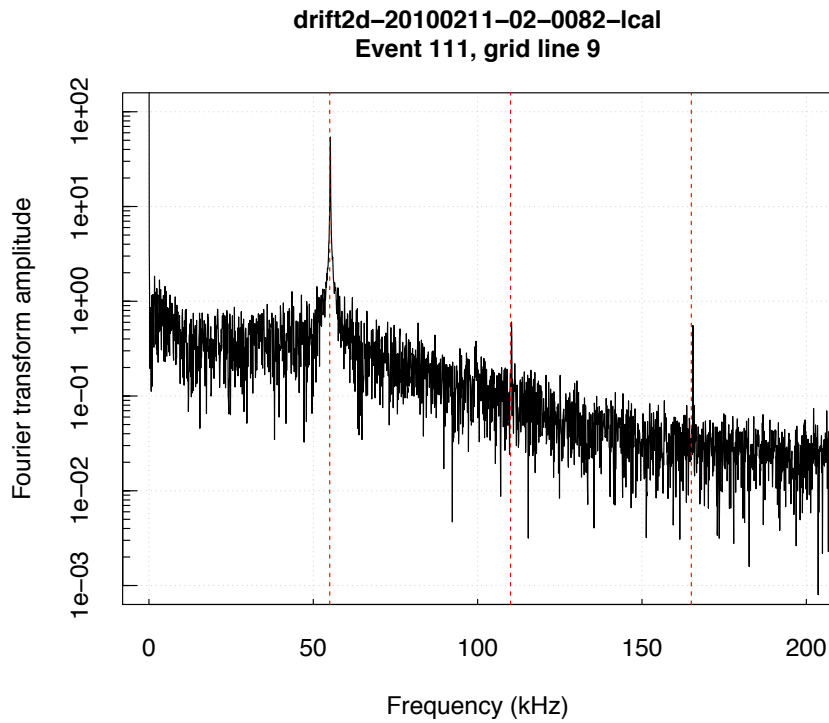


FIGURE 5.2: Power spectrum of grid sum line. Where peaks can be seen at frequencies of 55 kHz, 110 kHz and 165 kHz (marked with red dashed lines).

removed. Figure 5.1(b) shows the dramatic improvement in signal-to-noise that this produces.

### 5.1.2 Low frequency noise removal

Mains pickup at 50 Hz is next removed from the data using a nonlinear fit to a 50 Hz sine wave, which is subsequently subtracted from each data line. Figure 5.3 shows the effect of this noise reduction technique on the grid sum line.

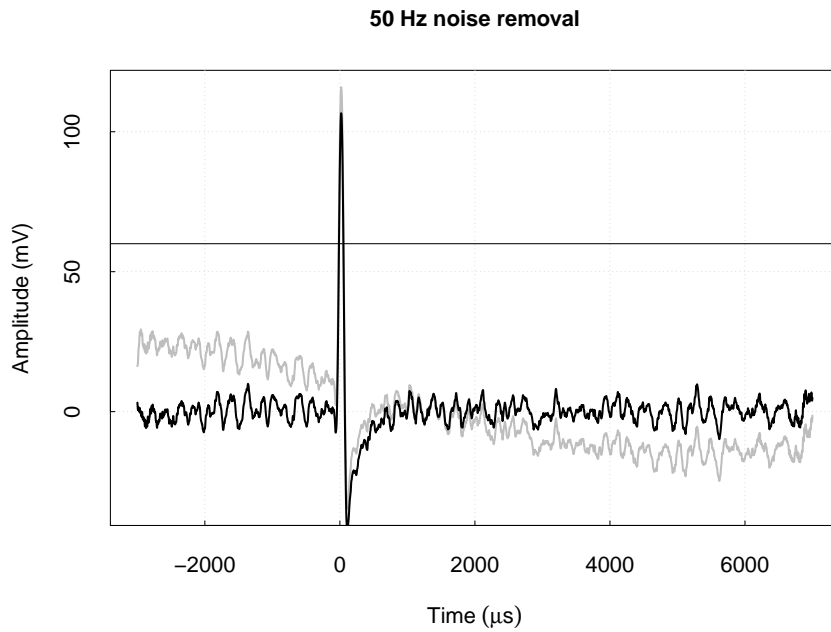


FIGURE 5.3: The grid sum line of a typical nuclear recoil event before (grey) and after (black) baseline correction from a nonlinear fit to a 50 Hz (20000  $\mu$ s) sine wave. Note that smoothing has been applied to better illustrate the change in baseline. Horizontal black line indicates grid sum threshold.

## 5.2 $^{55}\text{Fe}$ energy calibration

Each MWPC has a retractable  $\sim 100 \mu\text{Ci}$   $^{55}\text{Fe}$  source attached to its acrylic backplate. At regular 6 hourly intervals DRIFT enters an  $^{55}\text{Fe}$  calibration mode. Normal data acquisition is stopped and the  $^{55}\text{Fe}$  source is exposed to the detector volume for approximately 3 minutes. This section discusses the interactions that occur in the detector volume during this exposure and how these are used for energy calibration of the detector.

### 5.2.1 $^{55}\text{Fe}$ interactions in $\text{CS}_2$ and $\text{CS}_2\text{-CF}_4$ mixtures

$^{55}\text{Fe}$  decays to  $^{55}\text{Mn}$  with a half-life of  $\sim 2.7$  years via electron capture, resulting in emission of 5.90 keV x-rays. The likelihood of the x-rays interacting in the DRIFT target volume is determined by the mean free path,  $\lambda = 1/\mu\rho$  where  $\rho$  is the density of the target gas and  $\mu$  is the photoelectric absorption coefficient. Photoelectric absorption values for the carbon, fluorine and sulphur atoms relevant to the DRIFT detector are listed in Table 5.1.

**$^{55}\text{Fe}$  interactions in  $\text{CS}_2$**  — Sulphur has a photoelectric absorption  $\sim 20$  times greater than carbon, and in 40 Torr  $\text{CS}_2$ , the standard fill gas for DRIFT, a factor  $\sim 5$  larger

	Fluorescence yield	Auger yield	$\mu$ ( $\text{cm}^2 \text{g}^{-1}$ )	K shell binding energy (keV)	Auger kinetic energy (keV)
C	0.003	0.997	11.1	0.284	0.28
F	0.013	0.987	39.2	0.697	0.65
S	0.078	0.922	220.0	2.472	2.11

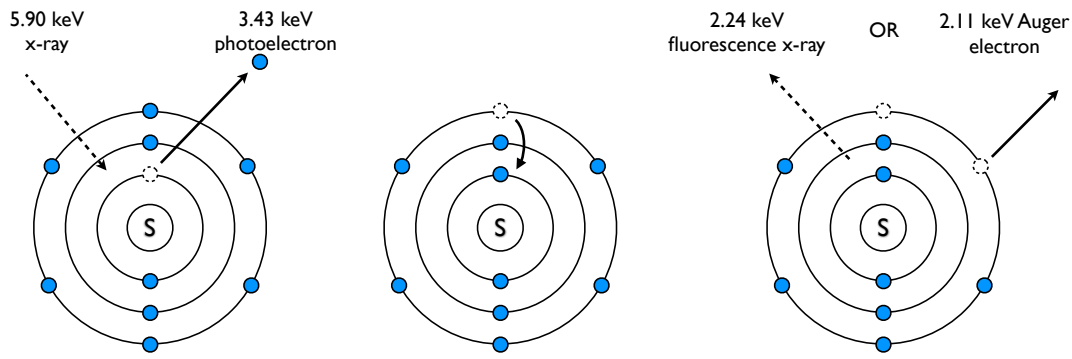
TABLE 5.1: Gas parameters for  $^{55}\text{Fe}$  interactions. Fluorescence and Auger yields from Krause et al. [142], photoelectric absorption coefficients ( $\mu$ ) for 5.90 keV gamma from the NIST database [143]. K shell binding energies from Table 1 of Bearden et al. [144]. Auger energies from the NIST database [145].

mass fraction. It is therefore assumed that all x-ray interactions occur with sulphur atoms and carbon interactions are neglected.

Figure 5.4 shows the principal interaction between a 5.90 keV x-ray and a sulphur atom. The x-ray is absorbed by the sulphur atom, which then emits an inner shell photoelectron of energy 3.43 keV, leaving the sulphur atom in an excited state. The atom partly relaxes with an outer shell electron filling this vacancy. The remaining energy is lost in one of two ways: either by the process of Auger emission [146], in which a second electron of 2.10 keV is emitted; or by fluorescence, releasing a photon of energy 2.24 keV. The Auger yield determines the probability that the atom will relax via Auger emission and is 0.922 for sulphur. Thus 92.2% of interactions will result in the full energy of the x-ray being deposited in two localised ionisation tracks that are seen as a single event by DRIFT. The detection of these events leads to a *full-energy peak* at 5.90 keV in the resulting  $^{55}\text{Fe}$  energy spectrum.

In the remaining 7.8% of interactions the excited sulphur atom de-excites by the emission of a 2.24 keV fluorescence x-ray. With a mean free path of 21 cm in 40 Torr  $\text{CS}_2$ , this x-ray will either escape the detector entirely, or produce a second event spatially separated from the first. This leads to additional structure in the  $^{55}\text{Fe}$  energy spectrum in the form of an *escape peak*, consisting of 3.43 keV events with an area 8.5% of the full-energy peak. In addition a fluorescence peak at 2.24 keV, caused by the fluorescence x-rays that do not leave the detector volume is also expected, with an area <8.5%.

**$^{55}\text{Fe}$  interactions in  $\text{CS}_2\text{-CF}_4$  mixtures** — Sulphur has an absorption coefficient  $\sim 6$  times larger than that of fluorine so, for the typical gas mixture of 30-10 Torr  $\text{CS}_2\text{-CF}_4$ , where the sulphur mass fraction is also 3 times greater than the fluorine, most x-ray interactions remain with sulphur. The high Auger yield of fluorine also means that 99% of interactions with fluorine result in contributions to the full-energy peak. The addition of  $\text{CF}_4$  therefore has minimal effect on the  $^{55}\text{Fe}$  spectrum at the typical levels of a 30-10  $\text{CS}_2\text{-CF}_4$  mixture. At higher  $\text{CF}_4$  concentrations no new features will be seen but a



(a) 5.90 keV x-ray absorbed by atom causing emission of 3.43 keV photoelectron. (b) Atom relaxes with core vacancy filled by outer shell electron. (c) Atom emits either a 2.24 keV x-ray or a 2.11 keV Auger electron.

FIGURE 5.4: Interaction between 5.9 keV x-ray and sulphur atom.

reduction in the size of the sulphur escape peak relative to the full-energy peak will result.

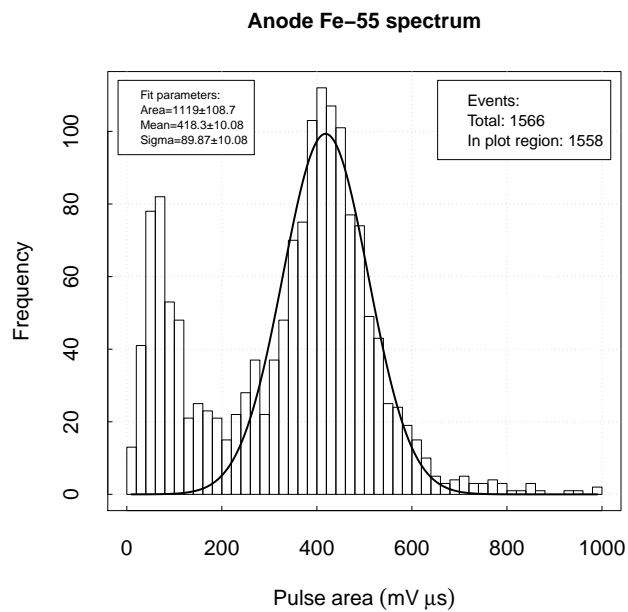
Although the addition of  $\text{CF}_4$  has only minor effects on the expected energy of events produced in  $^{55}\text{Fe}$  interactions, the ionisation measured at the MWPC (for a fixed voltage) changes drastically due to the changes in W-value and gas gain of  $\text{CS}_2$ - $\text{CF}_4$  mixtures compared with pure  $\text{CS}_2$  (Section 4.1.3).

## 5.2.2 Analysis, smoothing and thresholds

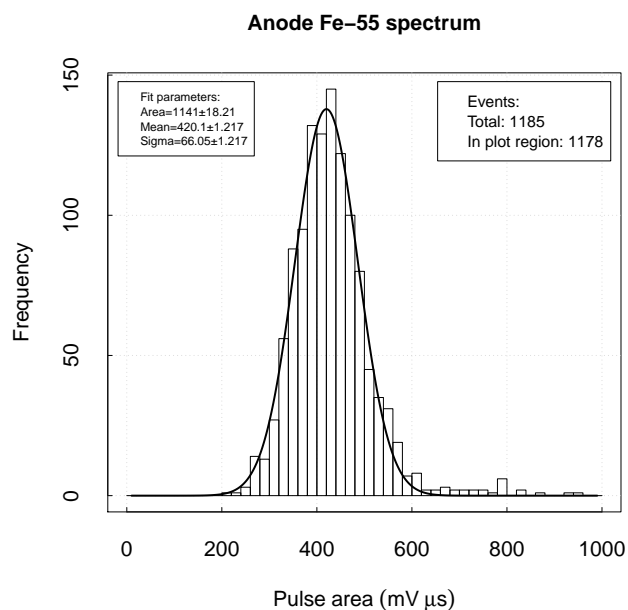
During  $^{55}\text{Fe}$  exposure the DRIFT DAQ runs in an untriggered mode, in which there is no threshold and event files are written to disk continuously. The rate of interactions from the  $^{55}\text{Fe}$  source is such that a number of events are typically seen in each 10 ms event file. Energy calibration of the DRIFT detector is performed by measuring the mean pulse area of events produced by the 5.90 keV interactions in the detector, where the pulse area is directly proportional to the ionisation produced in the detector volume. The W-value of the gas mixture is used to determine the number of ion pairs liberated by the 5.9 keV event resulting in a NIPs conversion factor — a multiplication factor to convert a measured pulse area in  $\text{mV } \mu\text{s}$  to the number of ion pairs produced in the initial event. The current  $^{55}\text{Fe}$  calibration procedure determines a separate NIPs conversion factor for each of the left and right MWPCs.

**Thresholds** — Figure 5.5(a) shows a typical  $^{55}\text{Fe}$  spectrum for the right MWPC that was analysed with a threshold of 2.0 mV. A clear full-energy peak can be seen with a mean of  $418 \pm 10 \text{ mV } \mu\text{s}$  clearly separated from the noise peak below  $\sim 150 \text{ mV } \mu\text{s}$ . There

may also be signs of additional structure at low pulse area that could be due to the escape peak (expected at  $\sim 240 \text{ mV } \mu\text{s}$ ). For calibration purposes however, only the full-energy peak is of interest. Figure 5.5(b) shows the same data with an analysis threshold of 5 mV. This threshold is high enough to exclude noise and smaller features, whilst not being so high as to clip the full-energy peak, as demonstrated by the mean of the full-energy peak remaining constant.



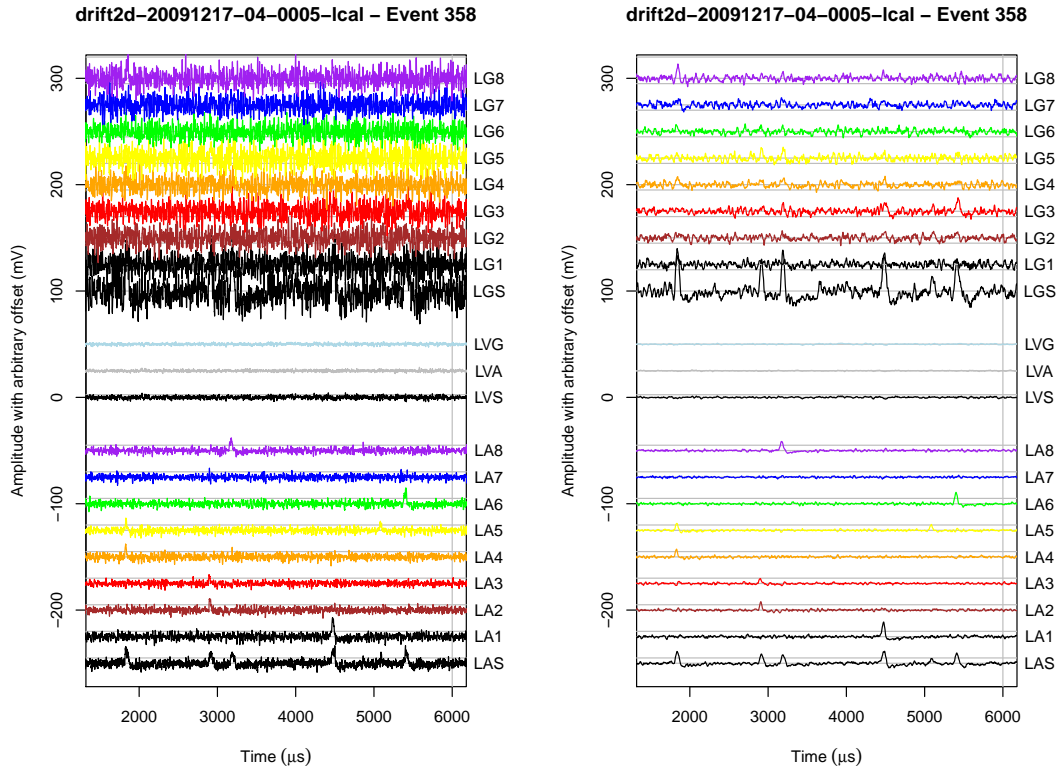
(a) Anode  $^{55}\text{Fe}$  spectrum with a reduced analysis threshold of 2.0 mV.



(b) Anode  $^{55}\text{Fe}$  spectrum with a standard analysis threshold of 5.0 mV.

FIGURE 5.5: Anode  $^{55}\text{Fe}$  spectra of a data file with reduced and standard analysis thresholds. The reduced threshold reveals the noise peak and possibly additional structure. The higher threshold isolates the  $^{55}\text{Fe}$  peak. The mean of the full-energy peaks are  $418 \pm 10$  and  $420 \pm 1$  mV  $\mu$ s for the reduced and standard analysis thresholds respectively.

**Smoothing** — For the purposes of  $^{55}\text{Fe}$  calibration, 60 sample boxcar averaging can be seen from Figure 5.6 to reduce the high frequency fluctuations underlying the longer timescale pulses. This allows lower analysis thresholds and improves accuracy of pulse parameterisation. Due to concerns of altering pulse shape features crucial for parameterisation, however, smoothing is currently only applied to  $^{55}\text{Fe}$  calibration data and not to data from normal operation.



(a) Waveforms of left MWPC only from a typical  $^{55}\text{Fe}$  event file prior to any smoothing. (b) Same waveforms as (a) after the application of  $60\ \mu\text{s}$  boxcar smoothing.

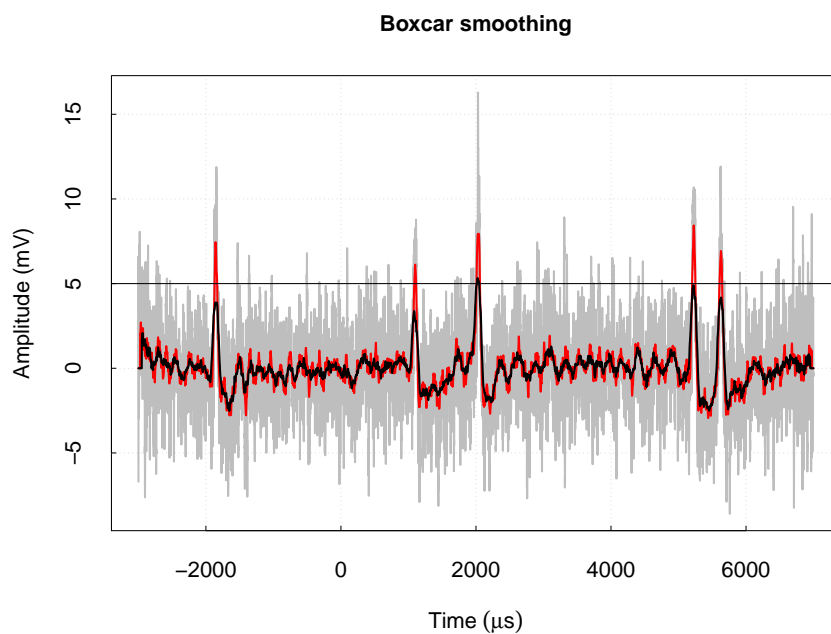
FIGURE 5.6: A typical  $^{55}\text{Fe}$  event file before and after boxcar smoothing with a  $60\ \mu\text{s}$  smoothing window

Even with  $^{55}\text{Fe}$  data, where pulse shape information other than the area is not required, the amount of waveform smoothing must be chosen with care as excessive smoothing can act to flatten and widen the pulse profile. This reduces the amplitude of the pulse, which has the same effect as increasing the threshold, and can reduce the measured pulse area.

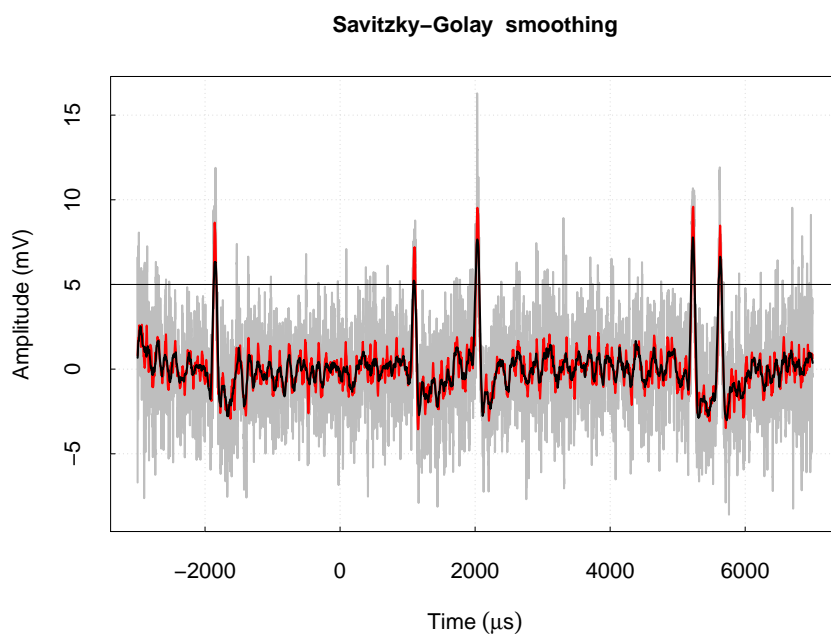
Currently, boxcar averaging is applied to  $^{55}\text{Fe}$  data prior to analysis. Boxcar averaging involves replacing each waveform sample with the mean value of a chosen number of adjacent samples, where the number of adjacent samples is determined by the smoothing window. The Savitzky-Golay smoothing filter [147] is a more advanced smoothing

algorithm that, instead of averaging the points within the smoothing window to a constant, uses a least-squares method to fit a higher order polynomial within the smoothing window. This algorithm is generally more effective at increasing signal-to-noise whilst preserving important pulse shape features such as amplitude and width. The Savitzky-Golay filter has been shown to be effective at revealing low energy features in DRIFT data [148].

Figure 5.7 compares the effects of the boxcar and Savitzky-Golay smoothing methods. In both cases there is a significant increase in signal-to-noise allowing analysis thresholds well below the noise level of the unsmoothed data. The Savitzky-Golay smoothing is seen to better preserve pulse amplitudes, with each of the five events in the waveform remaining above threshold for a smoothing window width of  $200 \mu\text{s}$ , compared to only two of the signals remaining above threshold for the of  $200 \mu\text{s}$  boxcar smoothed waveform.



- (a) A typical  $^{55}\text{Fe}$  event file before any smoothing (grey), after boxcar smoothing with a  $100\ \mu\text{s}$  window (red), and after boxcar smoothing with a  $200\ \mu\text{s}$  window (black).



- (b) The same  $^{55}\text{Fe}$  event unsmoothed (grey), after Savitzky-Golay smoothing with a  $100\ \mu\text{s}$  window (red), and after Savitzky-Golay smoothing with a  $200\ \mu\text{s}$  window (black). A comparable reduction in noise is achieved but pulse heights are affected less with all 5 events remaining above background for the  $200\ \mu\text{s}$  window.

FIGURE 5.7: Comparison between boxcar and Savitzky-Golay smoothing algorithms on the anode sum line of a typical  $^{55}\text{Fe}$  event.

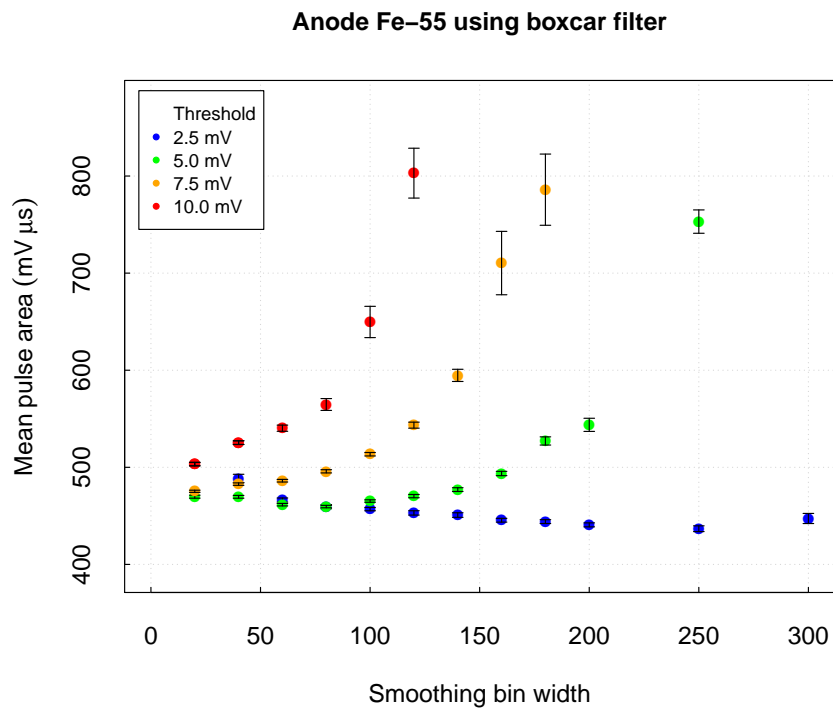
### 5.2.3 Stability of $^{55}\text{Fe}$ analysis configuration

It was suspected from inspection of calibration data that more careful choice of smoothing strategy might lead to more accurate  $^{55}\text{Fe}$  calibration results. Due to the relationship between the amount of smoothing performed and the analysis threshold, the effects of changing these parameters need to be considered in parallel. A single  $^{55}\text{Fe}$  data file, containing 1000 event files, was analysed with 96 smoothing–threshold permutations in order to determine an optimal configuration.

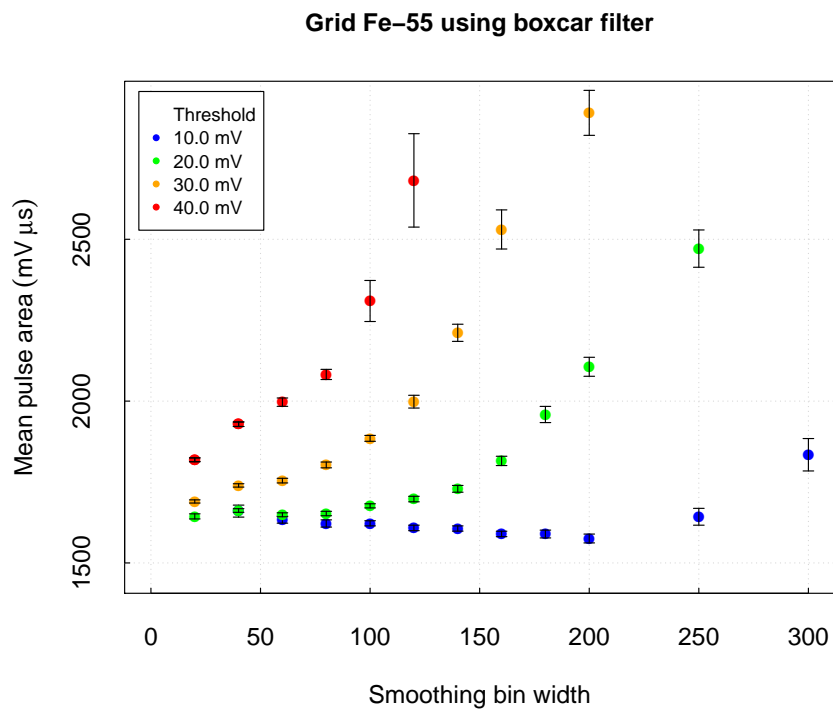
Figure 5.8(a) shows the effects of altering the smoothing window width for 4 different thresholds when using the boxcar smoothing method. With the analysis threshold set at 5.0, 7.5 or 10.0 mV, increased smoothing flattens smaller pulses below threshold so that only the largest events trigger the analysis, resulting in a largely overestimated mean pulse area. With an analysis threshold of 2.5 mV however, the majority of events are above analysis threshold even with the severe pulse shape flattening caused by boxcar smoothing of  $>200\ \mu\text{s}$ . Therefore, at this threshold, the reduction in the pulse area caused by increasingly aggressive smoothing is seen. The 5 mV threshold is most stable, with the mean pulse area measured remaining fairly constant for smoothing windows up to  $\sim 100\ \mu\text{s}$ . The mean pulse areas on the grid wires, Figure 5.8(b), shows very similar characteristics.

Figure 5.9 shows equivalent plots using the Savitzky-Golay smoothing filter. Although similar effects are observed, the measured pulse area is generally more stable over variations in threshold and smoothing window width. It is seen that for smoothing window widths up to  $\sim 100\ \mu\text{s}$  and for thresholds from 2.5 to 7.5 mV there is convergence in the measured pulse shape area to  $\sim 480\ \text{mV}\ \mu\text{s}$ . This indicates stability in the smoothing algorithm and indicates that a threshold-smoothing configuration within these values would be stable over significant changes in detector gain (as increased gain is equivalent to reduced thresholds).

These results suggest that for optimal stability in  $^{55}\text{Fe}$  calibrations a Savitzky-Golay smoothing filter with a smoothing window width of 40 to  $80\ \mu\text{s}$  should be used in conjunction with an analysis threshold of between 2.5 and 7.5 mV. A smoothing window width of  $60\ \mu\text{s}$  and a threshold of 5 mV are therefore used for  $^{55}\text{Fe}$  calibration throughout this thesis.

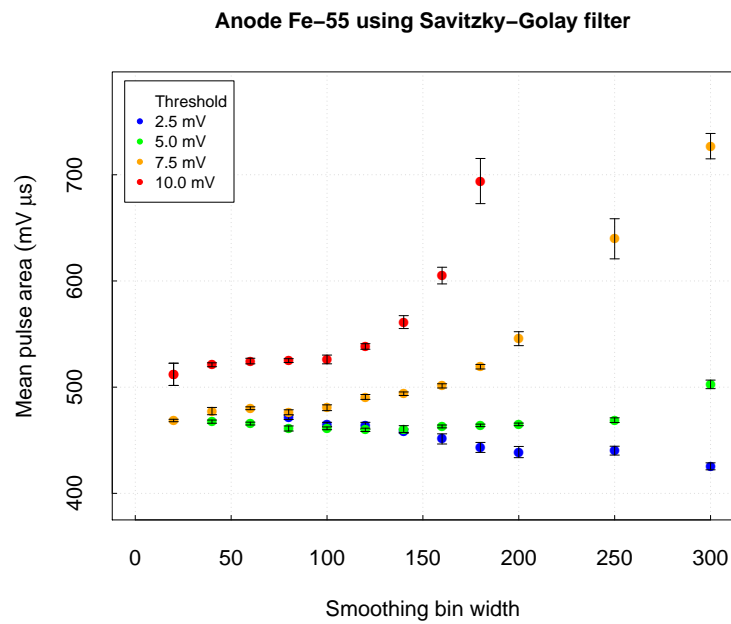


(a) Mean anode pulse area from  $^{55}\text{Fe}$  events as a function of smoothing window width.

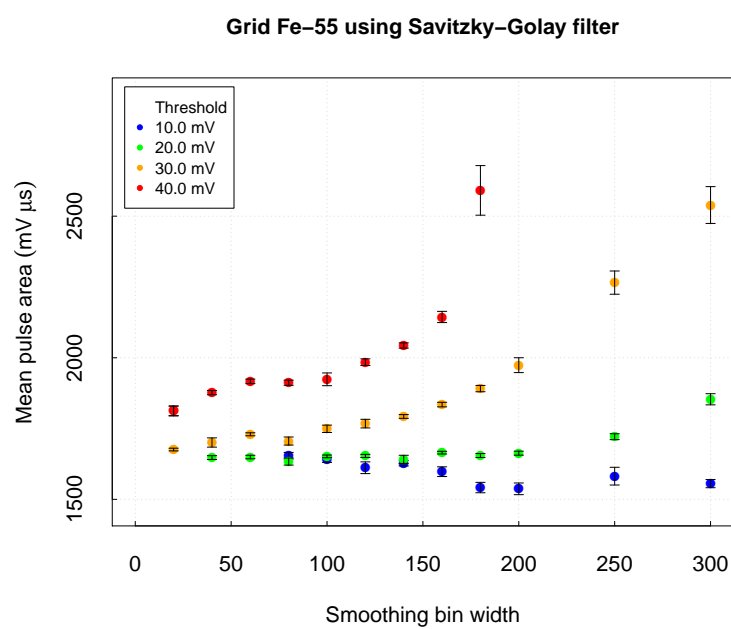


(b) Mean grid pulse area from  $^{55}\text{Fe}$  events as a function of smoothing window width.

FIGURE 5.8: Measured pulse area of  $^{55}\text{Fe}$  events as a function of smoothing window width for boxcar smoothing algorithm. Analysis was performed at various thresholds for each value of the smoothing window width.



(a) Mean anode pulse area from  $^{55}\text{Fe}$  events as a function of smoothing window width.



(b) Mean grid pulse area from  $^{55}\text{Fe}$  events as a function of smoothing window width.

FIGURE 5.9: Measured pulse area of  $^{55}\text{Fe}$  events as a function of smoothing window width for Savitzky-Golay smoothing algorithm. Analysis was performed at various thresholds for each value of the smoothing window width.

### 5.2.4 Energy calibration on a per-channel basis

The existing  $^{55}\text{Fe}$  energy calibration procedure determines a separate NIPs conversion factor for each of the left and right MWPCs, but assumes that each channel within the MWPC has equal gain. While developing cuts comparing the charge collected on anode wires compared to charge collected on grid wires (Section 5.4.1) it became apparent that this is not the case, and that gains on individual anode channels varied by up to  $\sim 20\%$ .

To study this further, the standard  $^{55}\text{Fe}$  analysis was developed to allow separation of  $^{55}\text{Fe}$  events for individual lines. A standard six-hourly  $^{55}\text{Fe}$  dataset contains insufficient events on a single line to allow a precise determination of the mean pulse area, so data from ten  $^{55}\text{Fe}$  datasets were combined. Figure 5.10 shows individual line calibrations for a combined dataset where variation between lines is evident with mean pulse areas ranging from 427 to 520  $\text{mV } \mu\text{s}$ .

It is clear from Figure 5.10 that the current procedure of grouping all lines within an MWPC together under the assumption that all channels have uniform gain results in a poor energy resolution in DRIFT.

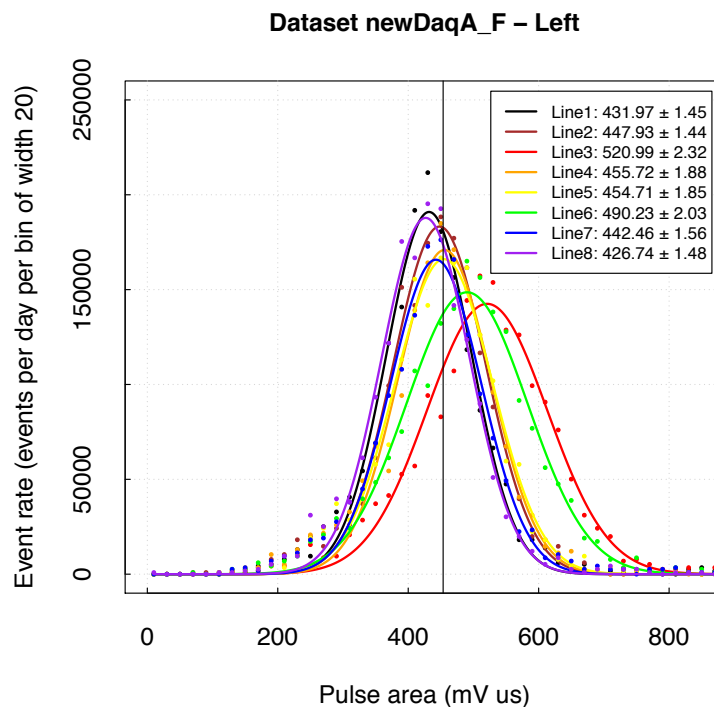


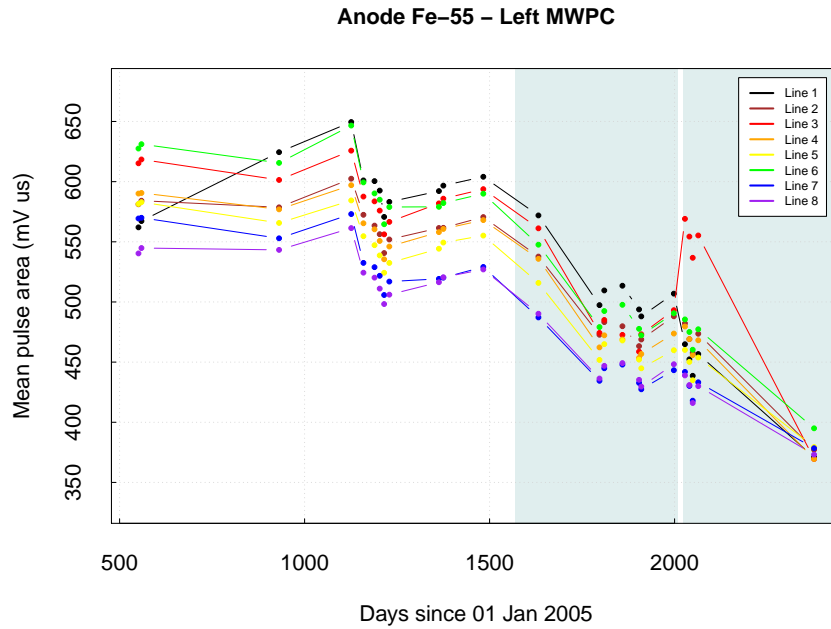
FIGURE 5.10:  $^{55}\text{Fe}$  calibration spectra of individual lines of left MWPC before tuning of the shaping amplifiers. Values in plot legend indicate the mean pulse area from the shown Gaussian fit.

### 5.2.5 Long term stability

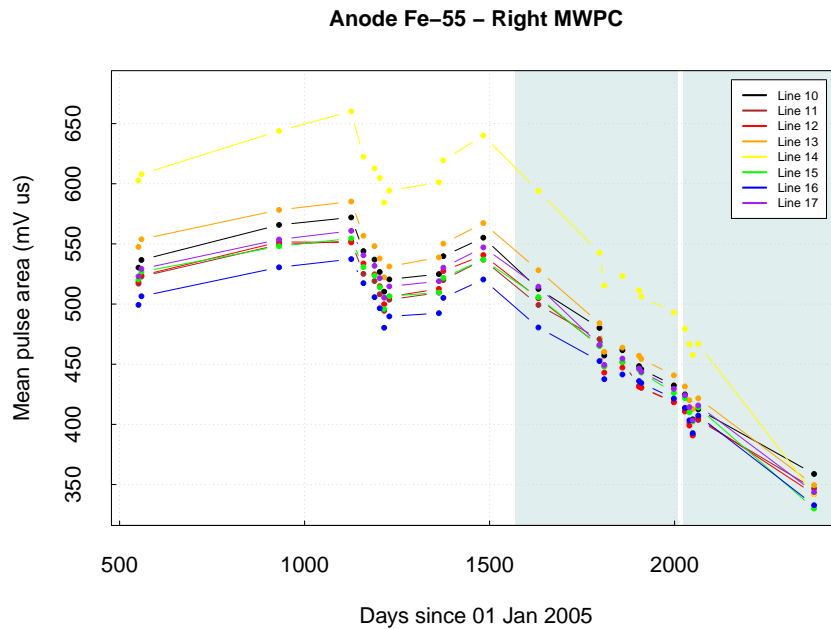
Having established non-uniformity in line gains, it is necessary to determine whether the gains are constant in time. If so, the preamplifiers can be tuned to match each other and all lines within an MWPC can continue to be grouped together in analysis. If the gains do drift in time, however, gains will have to be determined on a per-channel basis in analysis, which would require an increase in the amount of collected  $^{55}\text{Fe}$  data by factor  $\sim 8$ .

To investigate this, data from four years of  $^{55}\text{Fe}$  calibration runs were examined. The mean pulse area of  $^{55}\text{Fe}$  events as measured on each individual line is plotted as a function of time in Figure 5.11. It is observed that, although the overall gains change between runs, the relative gains between lines generally remains fairly constant. Exceptions can be seen in Figure 5.11 as lines that do not run parallel (see figure caption for details), where each of these exceptions can be traced back in the DRIFT log books to changes to the electronics, such as the replacement of damaged shaping amplifier chips.

The plots demonstrate that significant variations in gain of individual lines within an MWPC have always been present, with gains varying by  $\sim 10\%$  on each MWPC. Importantly this plot also demonstrates that the relative gains on each line are stable over long periods of time. This suggests that, once the gains of the shaping amplifiers are manually fine-tuned, the current method of producing a single NIPs conversion factor for each MWPC will be adequate. However, periodic analysis of  $^{55}\text{Fe}$  data on a per-channel basis, using the analysis techniques developed for this work, should be continued to monitor the stability of amplifiers individually.



(a) Left MWPC anode gains. Relative gains are generally stable from one run to the next. Exceptions are Line 1 (black) between 500 and 1000 days and Line 3 (red) at  $\sim 2000$  days. The DRIFT log book indicates replacement of shaping amplifiers at these times.



(b) Right MWPC anode gains. Line 14 is seen to have a significantly higher gain throughout, until the re-tuning of the amplifiers at day 2350.

FIGURE 5.11: Gains of individual anode lines over time. Relative gains are constant with anomalies explained by alterations to shaping amplifiers. The most recent data point at 2350 days is after the tuning of the shaping amplifiers.

### 5.2.6 Tuning shaping amplifier gains

Figure 5.12 plots the  $^{55}\text{Fe}$  spectra for individual lines after tuning the gains of all shaping amplifiers. Compared to Figure 5.10 the mean pulse areas have a significantly lower spread across the different lines, with a standard deviation of  $8.4\text{ mV } \mu\text{s}$ , compared to  $31.7\text{ mV } \mu\text{s}$  before tuning. In addition, the Gaussian fit to each of the single line datasets has a smaller sigma than before tuning. This is due to the way the  $^{55}\text{Fe}$  event pulse area is determined. An  $^{55}\text{Fe}$  event is defined as occurring on an individual line if only that line crossed the analysis threshold. However, to account for any residual charge on neighbouring wires that did not cross the analysis threshold, a region of the adjacent wire on either side is also added to the overall pulse area of the event. If the gain on neighbouring wires is different, as was the case before the tuning of the shaping amplifiers, this increases the uncertainty in the pulse area determination, thus leading to poorer resolution.

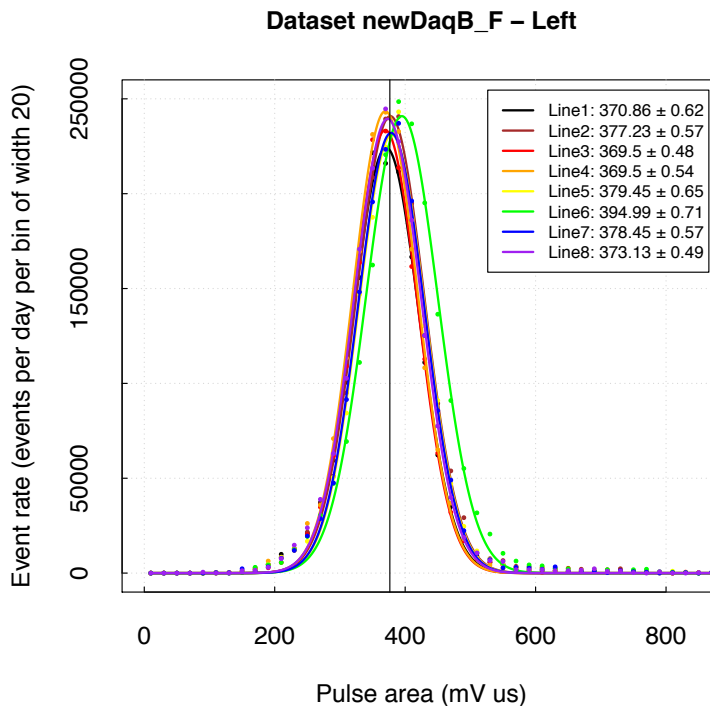


FIGURE 5.12:  $^{55}\text{Fe}$  calibration spectra of individual lines of left MWPC after tuning of the shaping amplifiers, to compare to Figure 5.10. Numbers in plot legend indicate the mean pulse area from the shown Gaussian fit.

Figure 5.13 compares the  $^{55}\text{Fe}$  spectrum for the left MWPC with all lines combined before and after the tuning of the shaping amplifiers, showing a significant improvement in energy resolution. Defining energy resolution as  $\sigma_E/E_0$ , where  $\sigma_E$  is the standard deviation and  $E_0$  is the mean, the left MWPC energy resolution improves from  $(17.8 \pm 0.3)\%$

to  $(13.8 \pm 0.1)\%$  and the right improves from  $(16.0 \pm 0.2)\%$  to  $(12.8 \pm 0.1)\%$  for data taken directly before and after the tuning. Because of the lower signal-to-noise on the grid lines a similar analysis of individual grid lines was not possible. Despite this, an accurate re-tuning of the grid shaping amplifiers was applied at the same time, resulting in a similar overall improvement in energy resolution from  $(21.7 \pm 0.5)\%$  to  $(16.8 \pm 0.4)\%$  from directly before and after the amplifier tuning.

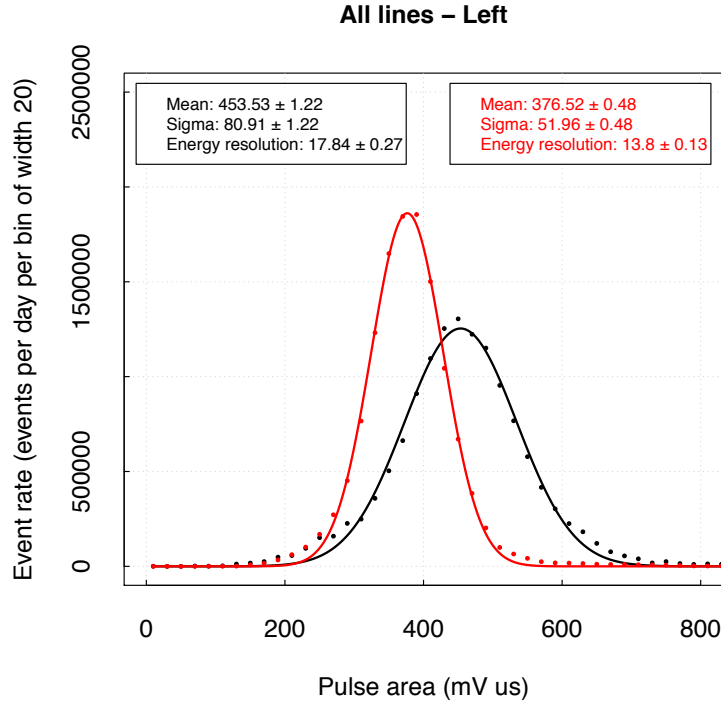


FIGURE 5.13:  $^{55}\text{Fe}$  spectrum of left MWPC (all lines combined) showing an improvement in energy resolution from  $(17.8 \pm 0.3)\%$  before the shaper tuning (black) to  $(13.8 \pm 0.1)\%$  after the shaper tuning (red).

### 5.3 WIMP analysis

In line with improvements to  $^{55}\text{Fe}$  calibration, improvement of the rest of the analysis chain was attempted. This began with restructuring a large proportion of the existing WIMP analysis code to make it more accessible and flexible to use, as well as enabling it to be run on a computing cluster. The goal was then to identify cuts that might be relaxed, removed, or replaced in order to improve efficiency for WIMP detection, without harming background rejection.

### 5.3.1 Parameterisation of hits

The data acquisition (DAQ) system described in Section 3.2.3 results in data from each line being written to disk, starting 3 ms before the trigger point and terminating 7 ms afterwards. The DAQ has a sampling rate of 1 MHz and a precision of 12 bits per sample. Each event consists of this raw data from each of 42 lines associated with a single trigger. These lines are the eight fiducial grid and eight fiducial anode lines for each of two MWPCs, plus four veto lines and six virtual lines that store the sum of each of the line types.

Offline analysis begins with the identification of hits caused by the deposition of charge on MWPC wires. This is done with the use of an analysis threshold, where an event file may contain no hits if the analysis thresholds are set above the DAQ trigger threshold. If the event was due to an extended particle trajectory in the target volume, several hits may be associated with the same particle trajectory, in this case the hits are collectively termed a track.

To remove artefacts at line edges from noise removal procedures, a region of interest (ROI) is defined from  $-0.5$  to  $4.5$  ms of the trigger time, with data outside of this region excluded from all parameterisation. Each line within the event file is processed individually. Derived hit parameters relevant to this WIMP analysis are described below:

**Minimum and maximum voltage samples** —  $V_{\min}$  and  $V_{\max}$  are the minimum and maximum voltage samples on a line within the ROI. The points in time at which these occur are  $t_{V_{\min}}$  and  $t_{V_{\max}}$  respectively.

**Hit duration** — For lines with identified hits, the  $t_{\min}$  and  $t_{\max}$  parameters define the full extent of the hit in time. The parameter  $t_{\min}$  is defined as the time of the last baseline crossing before the first threshold crossing, while  $t_{\max}$  is defined as the time of the first baseline crossing after the last threshold crossing.

**Hit pulse area** — The pulse area of a hit, in units of  $\text{mV } \mu\text{s}$ , has two definitions. Firstly  $\Sigma$  is defined only for lines with identified hits, and is given by the integral of the voltage between  $t_{\min}$  and  $t_{\max}$ . The parameter  $\Sigma_{\text{sum}}$  is defined, for a given fiducial line, as the integral of the voltage on that fiducial line between the  $t_{\min}$  and  $t_{\max}$  values calculated from the hit on the sum line. Thus, assuming the sum line crosses the analysis threshold,  $\Sigma_{\text{sum}}$  is defined for all lines making it useful for measuring residual charge on neighbouring lines on which there is insufficient charge to produce a hit.

**Voltage-weighted mean time** — A measure of the centre of the charge distribution in time is determined by the voltage-weighted mean time  $\bar{t}$  over the samples  $t_{\min}$  to  $t_{\max}$ ,

given by

$$\bar{t} = \frac{\sum_{t=t_{\min}}^{t_{\max}} (V_t \times t)}{\sum_{t=t_{\min}}^{t_{\max}} V_t} \quad (5.1)$$

where  $V_t$  is the voltage sample at time  $t$ .

**Smoothed derivative crossings** — The number of hits on an individual line is an important parameter. Ionisation tracks from WIMP-induced nuclear recoils are much less than 16 mm long, so only a single hit is expected on any given line. Therefore, for a WIMP search, a single line with more than one hit should be cut. In contrast, typical alpha tracks are 10s of cm in length and, due to the MWPC wire grouping (Section 3.2.3), usually result in multiple hits on a single line. In this case each hit on a line corresponds to charge deposition on a separate wire 8 mm from the first, so the number of hits provides the track range in  $x$ . Simply counting the number of times the line crossed a threshold was found to be ineffective, since it is affected by noise and is susceptible to baseline drifting during the event. A more accurate hit count comes from taking the derivative of the smoothed line (20  $\mu$ s boxcar smoothing) and counting the number of times this line crosses the threshold. The result is the parameter *sdCrossings*.

**Risetime** — The *risetime* of a hit is defined as the time taken for the hit to rise from 25% to 75% of  $V_{\max}$ <sup>1</sup>. The *risetime* at the output of the preamplifier would be of particular interest, since the shape of the leading edge should contain information on the charge density of the track as it arrives at the anode wire. The signal recorded here, after the aggressive filtering of the shaping amplifiers, however, contains much less of this information. It is, however, a useful parameter for identifying particularly fast pulses. Revisions of the electronics to remove aggressive pulse shaping electronics are in development within the collaboration

**First full width at half maximum** — The FWHM of a pulse is its width at half of its maximum amplitude, which may have more than one value. The parameter *FFWHM*, the first FWHM, is defined as the time difference between the first voltage sample below  $0.5V_{\max}$  on either side of  $t_{V_{\max}}$ . The parameter *FFWHM* thus characterises the spread of the core of the hit.

<sup>1</sup>Typically rise time is defined as the time taken for the leading edge to rise between 10% and 90% of the peak height [114], but the electronic noise in the DRIFT data currently does not permit this.

**Root mean square time deviation** — The *RMST* is a determination of the spread of the charge calculated by

$$RMST = \sqrt{\frac{\sum_{t=t_{\min}}^{t_{\max}} (V_t(t - \bar{t})^2)}{\sum_{t=t_{\min}}^{t_{\max}} V_t}} \quad (5.2)$$

where  $V_t$  is the voltage sample at time  $t$ , and  $\bar{t}$  is the voltage-weighted mean time defined in Equation 5.1.

In contrast to *FFWHM*, the *RMST* characterises the entire pulse from  $t_{\min}$  to  $t_{\max}$ , where the square of the deviation from the mean puts particular emphasis on the tails of the pulse. The combination of the *RMST* and *FFWHM* parameters has shown to be very effective in removing a particular class of background event, described in Section 5.4.

### 5.3.2 Rebound hits

Unphysical pulse shapes may appear as hits, particularly where the event involves deposition of a large amount of charge. Examples of this phenomenon are lines LA2, LA3 and LA4 in the event shown in Figure 5.14(a). Large charge depositions on all other lines have produced induced pulses of negative polarity on these lines that, due to the complex signal induction process and aggressive shaping electronics, acquire a significant positive overshoot. This positive overshoot crosses the analysis threshold and may be identified as a legitimate hit. Such hits are called rebound hits and are identified by  $|V_{\min}/V_{\max}| > 2$  and  $t_{V_{\min}} < t_{V_{\max}}$ . In a WIMP analysis rebound hits are excluded from parameterisation of the event. Alpha hits can occasionally mistakenly be tagged as rebound hits, so removal of rebound hits is not performed for analyses of alpha events.

### 5.3.3 Stage 1 cuts

After all events have had rebound hits identified and excluded from the defined track, the following cuts, each identified by a numerical index in parentheses, are applied:

**Zero NIPs cut** — *anodeZeroNipsCut* (1.1) removes any event in which no individual anode line registers a hit. This removes events where no anode line crosses the analysis threshold or where all lines with identified hits are excluded by the rebound cuts.

**Time cuts** — *anodeTminCut* (1.2), *anodeTmaxCut* (1.3), *gridTminCut* (1.5) and *gridTmaxCut* (1.6) remove events in which there is one or more hits that extends outside of the

ROI. This removes events that are not fully contained and hence may not be properly parameterised. This mostly acts to remove large unphysical events such as those caused by baseline wander or microphonics, but can also remove some alphas with particularly long  $\Delta z$  as shown in Figure 5.14(b).

**Clipping cuts** — *anodeClippingCut* (1.4) and *gridClippingCut* (1.7) remove any events in which one or more hit has a value of  $V_{\max} > 999$  mV or  $V_{\min} < -999$  mV. This removes events in which any hit exceeds the  $\pm 1$  V voltage range of the digitisers. It is not possible to accurately determine the ionisation of these events and no useful event occurring within the fiducial volume would produce sufficient  $dE/dx$  to exceed this voltage range. This cut mainly removes large sparks, an example of which is shown in Figure 5.15(a). In addition, hits out of the range of the digitisers may be caused by alpha tracks that pass through the MWPC plane. Such events may liberate ionisation electrons in the high field region surrounding the anode wires, in which electrons do not attach to negative ions but instead drift with high velocity to the anode wire. The electrons arrive in a very short time creating a spark-like charge deposition, as shown in the alpha event in Figure 5.14(b).

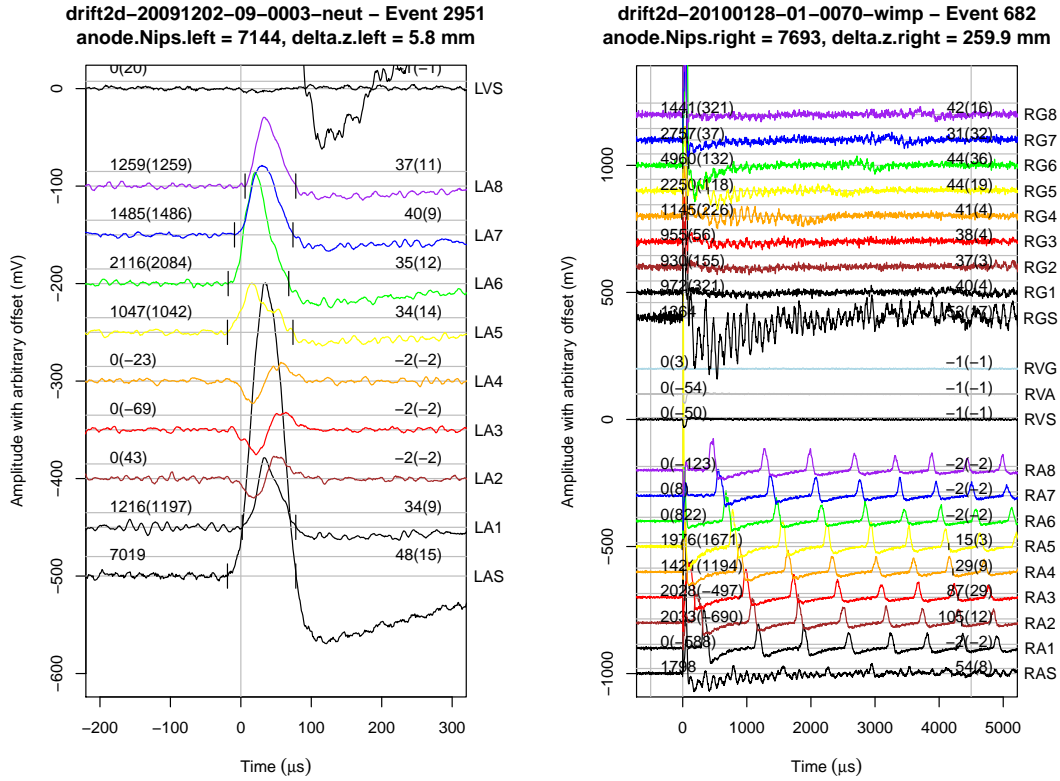
**Veto cuts** — *vetoCut* (1.8) removes events where the veto sum line exceeds 25 mV within the ROI. This cut excludes events that exit or enter the fiducial volume from outside, which would deposit charge on the veto line as a consequence. These events fail the requirement of full containment.

### 5.3.4 Parameterisation of events

The hit parameterisation stage characterises each identified hit within an event by a set of parameters. The event parameterisation stage is then performed for each event that passes the stage 1 cuts, and reduces the data further by characterising the entire event by a single set of parameters.

Some event parameters are determined directly from the set of hit parameters, as follows:

- *anodeHits* — the number of anode fiducial lines with an identified hit.
- *anodeNips* — the sum of  $\Sigma$  from all anode fiducial line hits multiplied by the anode NIPs conversion factor, determined by  $^{55}\text{Fe}$  calibrations as described in Section 5.2.2.
- *anodeSumNips* —  $\Sigma$  of the hit on the anode sum line multiplied by the anode NIPs conversion factor.

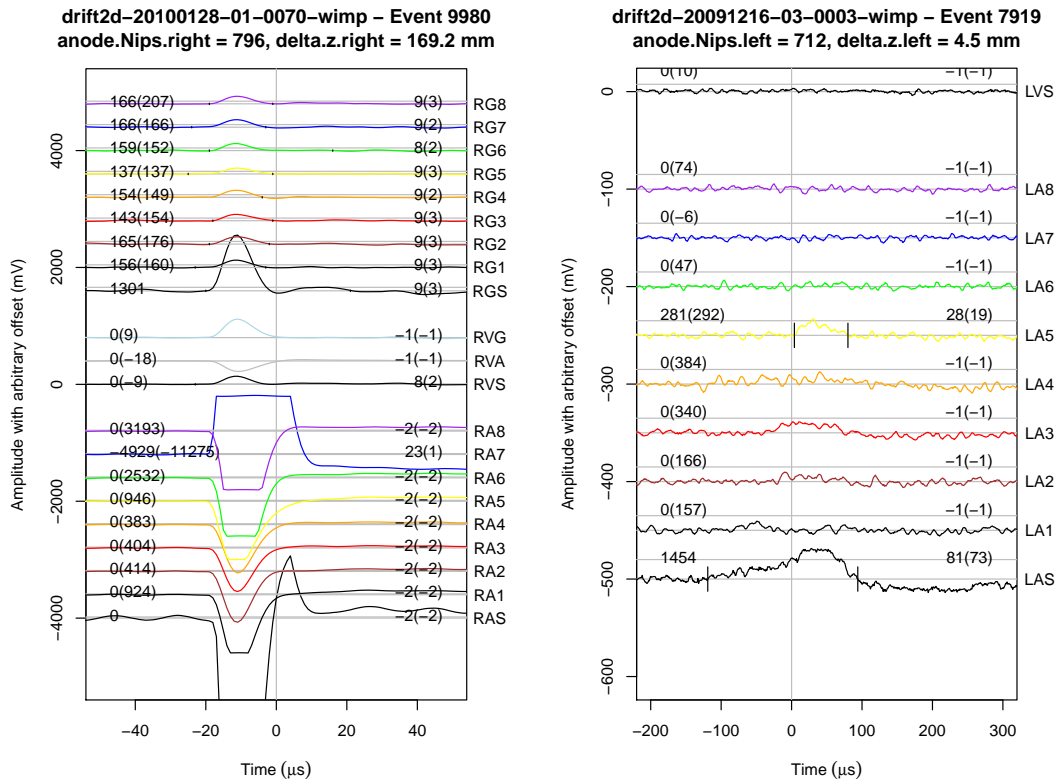


(a) A high energy neutron event. Although all lines cross the analysis threshold (horizontal grey lines), LA2 to LA4 are identified as rebound hits are not included in the parameterisation of the track.

(b) An alpha event that passes through the MWPC, railing the digitiser at  $t \approx 0$ , and extending out of the ROI with  $t_{\max} > 4500 \mu\text{s}$ .

FIGURE 5.14: An event with hits excluded by the rebound hits cut (a), and an event cut by both the stage 1 clipping cuts and the stage 1 time cuts (b).

- *gridSumNips* —  $\Sigma$  of the hit on the grid sum line multiplied by the grid NIPs conversion factor.
- *anodeMinTmin* and *gridMinTmin* — the minimum of all the  $t_{\min}$  values for hits on anode and grid fiducial lines respectively.
- *anodeMinRisetime* — the minimum of all *risetime* values for hits on anode fiducial lines.
- *anodeMinFwhm* — the minimum of all *FFWHM* values for hits on anode fiducial lines.
- *anodeMaxSdCrossings* — the maximum *sdCrossings* value from all anode fiducial lines.
- *gridPhRatio* — the ratio of the largest to the second largest  $V_{\max}$  from all the grid fiducial lines.



- (a) A large spark on RA7 produced a voltage spike (b) A track with low  $dE/dx$  deposits charge on a number of lines but a hit is identified only on LA5. Cross-induced pulses on adjacent wires are also out of the  $-1$  V range.

FIGURE 5.15: Example events removed by stage 1 clipping cuts (a), and by stage 3  $anodeNips$  to  $anodeSumNips$  cut (b).

Additional event parameters are derived from an additional virtual line, named the anode track line. This is formed by going back to the event file and summing the waveforms of all lines that contain hits. The anode track line is similar to the sum line, but does not contain the noise and induced pulses from lines containing no hits. The same parameters that were produced for individual lines, described previously in Section 5.3.1 are then generated for the anode track line. Parameters derived from this line are:

- $anodeTrackNips$  —  $\Sigma$  for the anode track line multiplied by the NIPs conversion factor.
- $anodeTrackRmst$  —  $RMST$  for the anode track line.
- $anodeTrackSigma$  — defined as  $FFWHM/2.35$  for the anode track line.

### 5.3.5 Stage 2 cuts

Stage 2 cuts select, from all the fully contained events that pass the stage 1 cuts, subsets of events of interest for a particular analysis. For example, alpha-like events, or WIMP-like events. The priority at this stage is to keep the vast majority of interesting events for the chosen analysis, particularly WIMP-like events, even if this means that some marginal backgrounds or unphysical events pass these cuts.

The stage 2 cuts used to select WIMP-like events are described here. Modifications of the cuts are also useful for identifying other (non-WIMP) event classes, which are also described. Each cut is again given a numerical index in parentheses.

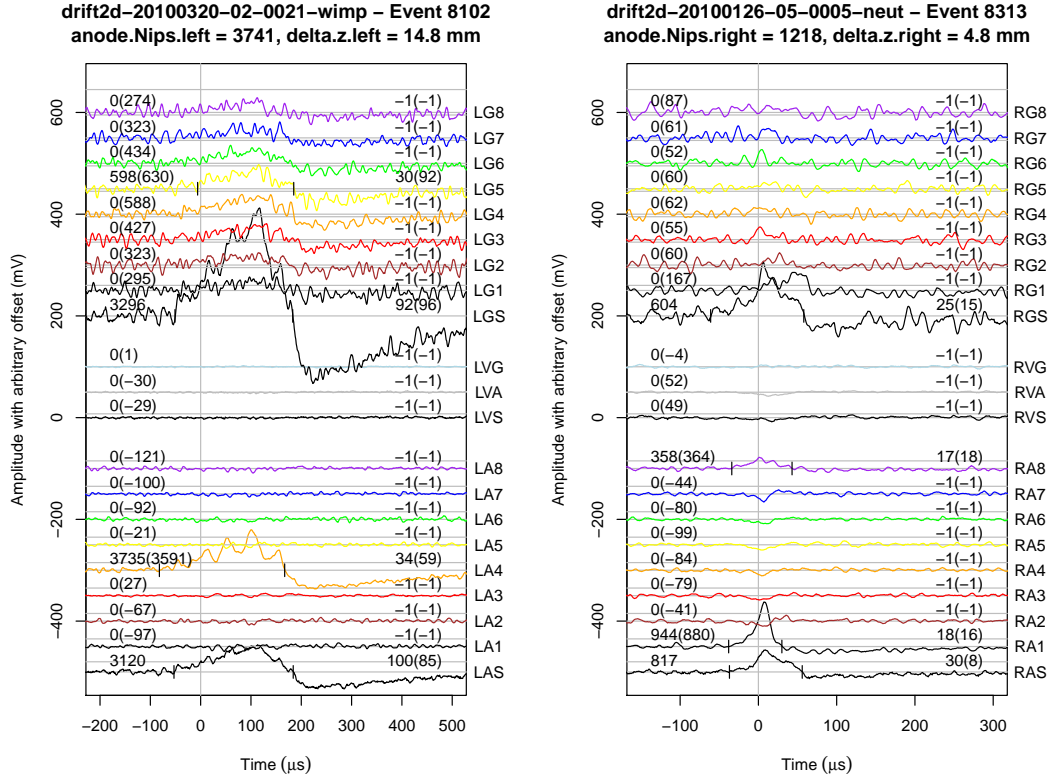
**Sides hit** — *singleSideCut* (2.1) removes events based on whether hits are identified on one or both MWPCs. For WIMP analyses this cuts events with at least one identified hit on each MWPC, since the probability of a WIMP interaction occurring twice in the detector is negligible, as is the probability of a WIMP-induced nuclear recoil crossing the central cathode plane.

**Lines hit** — *eightLineCut* (2.2) removes events where all 8 lines in the anode plane contain hits. WIMP tracks are expected to have a range less than the 16 mm distance between adjacent wires connected to a given line. The cut can be tailored for other event subsets. For example, when studying alpha tracks, requiring all 8 lines to have hits rejects non-alpha events with high efficiency.

**Adjacent hits** — *adjacentCut* (2.3) removes events in which the pattern of hits does not occur on adjacent wires. This is applied to all analyses for all event classes, since tracks are always expected to be continuous, and events containing more than one track are very rare.

**Hits per line** — *anodeMaxSdCrossingsCut* (2.4) removes events based on the maximum number of hits on a single anode fiducial line. For WIMP events there should be a maximum of one hit on an individual line corresponding to a cut of *anodeMaxSdCrossings*  $< 3$ , however because of the signal overshoot introduced by the cross-induced signals and amplification electronics, a cut of *anodeMaxSdCrossings*  $< 5$  is instead applied. This cut also removes so-called ‘ringer events’, an example of which is in Figure 5.16(a). These background events have similarities with nuclear recoil events, but with an oscillatory ‘ringing’ superimposed on the event pulse. These events have been present in the DRIFT detector for some time but their origin remains largely unknown [109], though their frequency appears to be correlated with periods of suspected gas contamination. The *anodeMaxSdCrossingsCut* is effective at detecting the multiple pulses present in

ringer events and is thus an effective parameter for removing them. A cut of  $anodeMaxSdCrossings > 5$  is used to preferentially select alpha events, which, due to the grouping of MWPC wires, typically produce many pulses on each line.



(a) An example of a ringer event cut by  $anodeMaxSdCrossingsCut$ . The event has similarities to a neutron event but has a 'ringing' oscillation superimposed on the event

(b) An event cut by both the  $anodeSumNips/gridSumNips$  cut and the  $anodeTrackSigma/anodeTrackRmst$  cut

FIGURE 5.16: Events cut by stage 2 and final stage cuts.

## 5.4 Final stage cuts

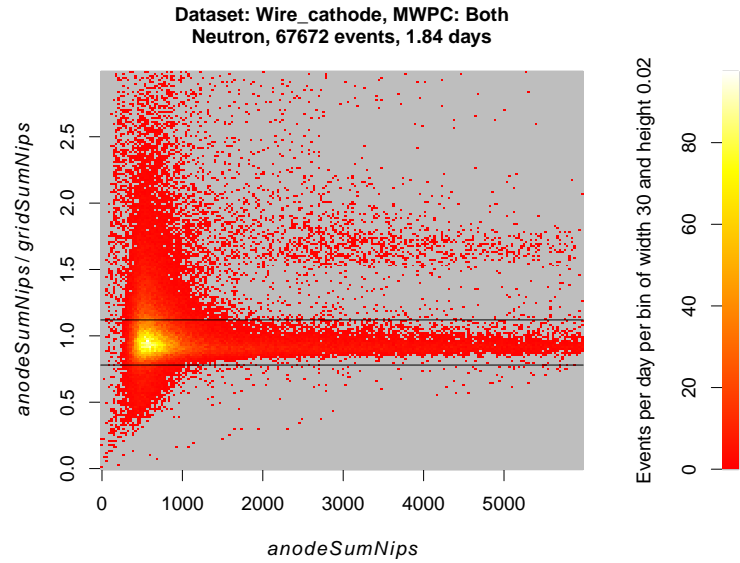
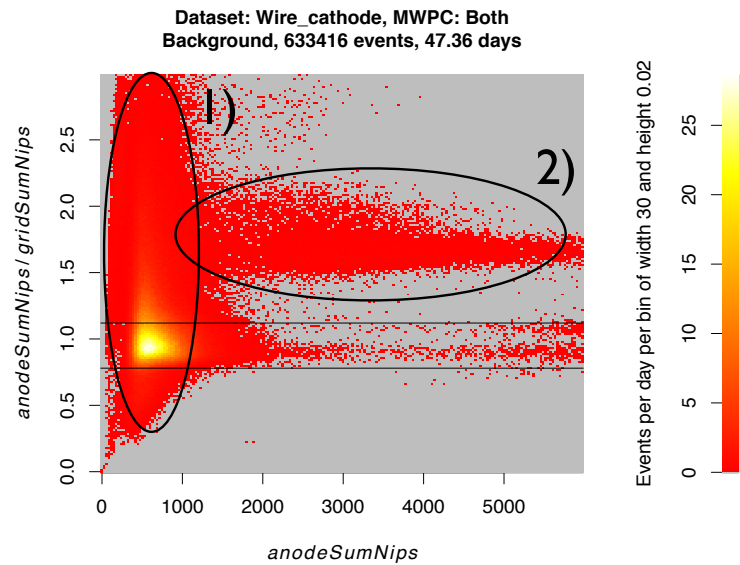
Data reduction proceeds on the assumption that all events remaining in the WIMP-search run are background events, and that neutron-induced nuclear recoils from  $^{252}\text{Cf}$  calibration runs closely mimic the expected WIMP-induced nuclear recoils. The final stage cuts are thus developed by comparison of the two datasets to eliminate events from the WIMP-search data whilst maximising the number of events retained from the neutron data. The following cuts were developed from WIMP-search data totalling 47.36 days livetime between 16 Dec 2009 and 15 Feb 2010, and three neutron calibration runs totalling 1.84 days livetime taken at the beginning, middle, and end of the WIMP-search data.

### 5.4.1 NIPs Ratio cuts

***anodeSumNips* to *gridSumNips* ratio (3.1)** — Events having a ratio of *anodeSumNips* to *gridSumNips* outside the range 0.78 to 1.22 are cut. As the avalanche caused by normal events should generate equal amounts of positive and negative charge, the ratio of the charge deposited on the anode and grid wires should be approximately 1. The accepted range is within 3 sigma of the *anodeSumNips* to *gridSumNips* ratio exhibited during neutron calibration runs, shown in Figure 5.17(a).

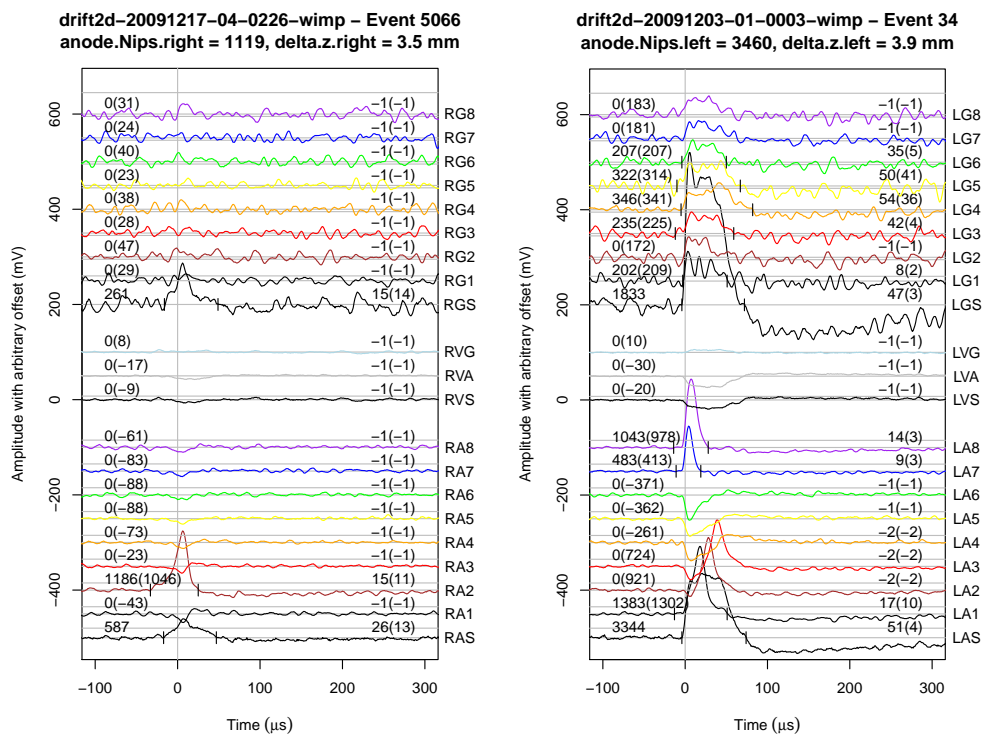
Figure 5.17(b) illustrates the two main event populations that this cut excludes from the WIMP-search data set. The first, labelled 1 in Figure 5.17(b), consists of events below  $\sim 1000$  NIPs, which span a range of *anodeSumNips* / *gridSumNips* values. Figure 5.18(a) shows a typical event from this population, in which there is a distinct signal on a single anode wire, but only a small charge distributed across all grid wires. The second population, labelled 2 in Figure 5.17(b), consists of events of all NIPs values and a *anodeSumNips* / *gridSumNips* value of  $\sim 1.6$ . A typical event from this population is shown in Figure 5.18(b) and consists of multiple anode hits, some of which have fast leading edges. The exact sources of these events are unknown but it is suspected that they originate from interactions on the surfaces of wires within the MWPC plane between the anode plane and the outer, non-instrumented grid plane. This would result in the full charge deposition being detected on the anode wires, but only a fraction of the charge reaching the inner, instrumented grid wires. It is suspected that the smaller population 1 events may be caused by recoiling nuclei from decays on the wire surfaces of the MWPC, whereas the longer population 2 events may be from alpha particles that originate within the MWPC but travel outwards so that they are only partially detected.

It is seen that, although the vast majority of population 2 events are removed by the cut, population 1 extends through the signal region such that a fraction of these events will remain after this cut. This cut reduces the WIMP-search run event rate by 48% whilst reducing the background subtracted neutron event rate by only 25%.

(a) Data from 1.84 days livetime with exposure to  $^{252}\text{Cf}$  neutron source.

(b) Data from 47.36 days livetime of WIMP-search runs.

FIGURE 5.17:  $anodeSumNips$  to  $gridSumNips$  ratio as a function of  $anodeSumNips$  for neutron and WIMP-search runs. Black lines indicate 3 sigma rejection region. Events outside of this region are cut. Circled regions illustrate the two separate background populations discussed in the text.



(a) A typical event from population 1 of Figure 5.17(b). (b) A typical event from population 2 of Figure 5.17(b).

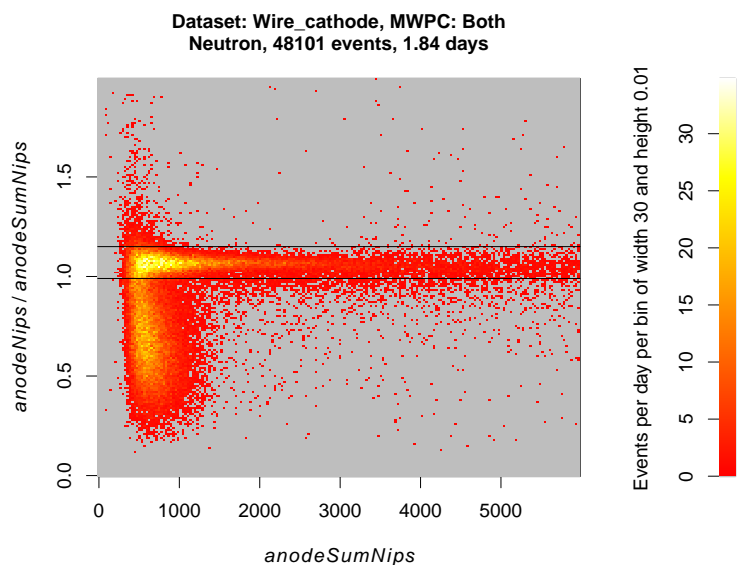
FIGURE 5.18: Two events cut by the *anodeSumNips* to *gridSumNips* ratio cut. It is suspected that these events originate from interactions within the MWPC between the anode plane and the uninstrumented outer grid plane.

***anodeNips* to *anodeSumNips* ratio (3.2)** — Events having a ratio of *anodeNips* to *anodeSumNips* outside the range 0.99 to 1.15 are cut, since the summed charge of individual anode fiducial line hits should approximately equal the charge of the hit on the anode sum line. The acceptance region, marked by the black horizontal lines in each figure, was determined from a 3 sigma fit to the neutron population in Figure 5.19(a).

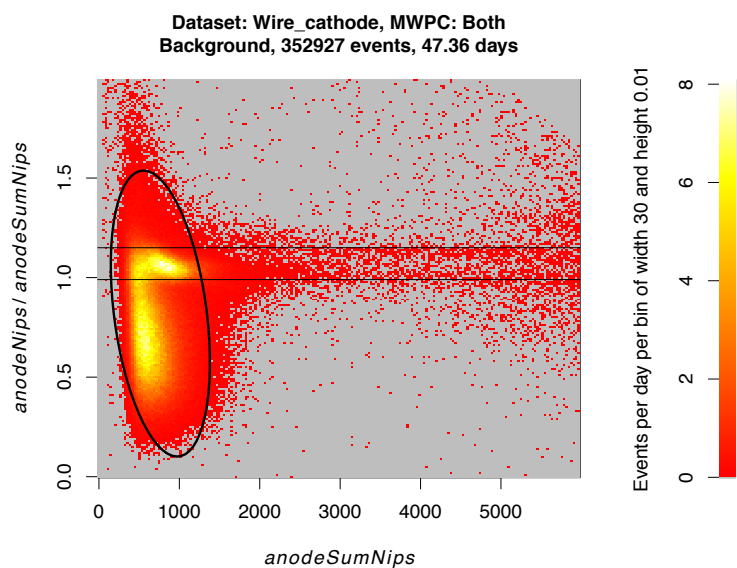
An *anodeNips* to *anodeSumNips* ratio below 1 implies ‘missing charge’. That is, there is insufficient charge in the identified anode fiducial line hits to account for the charge seen on the anode sum line. The majority of events that fail this cut occur at low energy, forming the population circled in Figure 5.19(b). These events are typically low charge density events, an example of which is shown in Figure 5.20(a). The low charge density results in a large fraction of the overall event charge appearing on lines in insufficient density to cross the analysis threshold, and hence is not included in the *anodeNips* calculation.

The low charge density and relatively high rate of these events is consistent with electron recoils from gamma events. This is also consistent with the observation that there is a higher rate of events in this region during neutron source exposure in comparison to WIMP-search data, as shown in Figure 5.19. Other events rejected by this cut include some higher energy events in which lines have been incorrectly identified as ‘rebounded pulses’ and hence are not included in calculation of the *anodeNips* parameter. This is usually caused by the effects of large cross-induced pulses, as shown in Figure 5.20(b).

This cut reduces the WIMP-search run event rate by a further 73% whilst reducing the background subtracted neutron event rate by 47%.

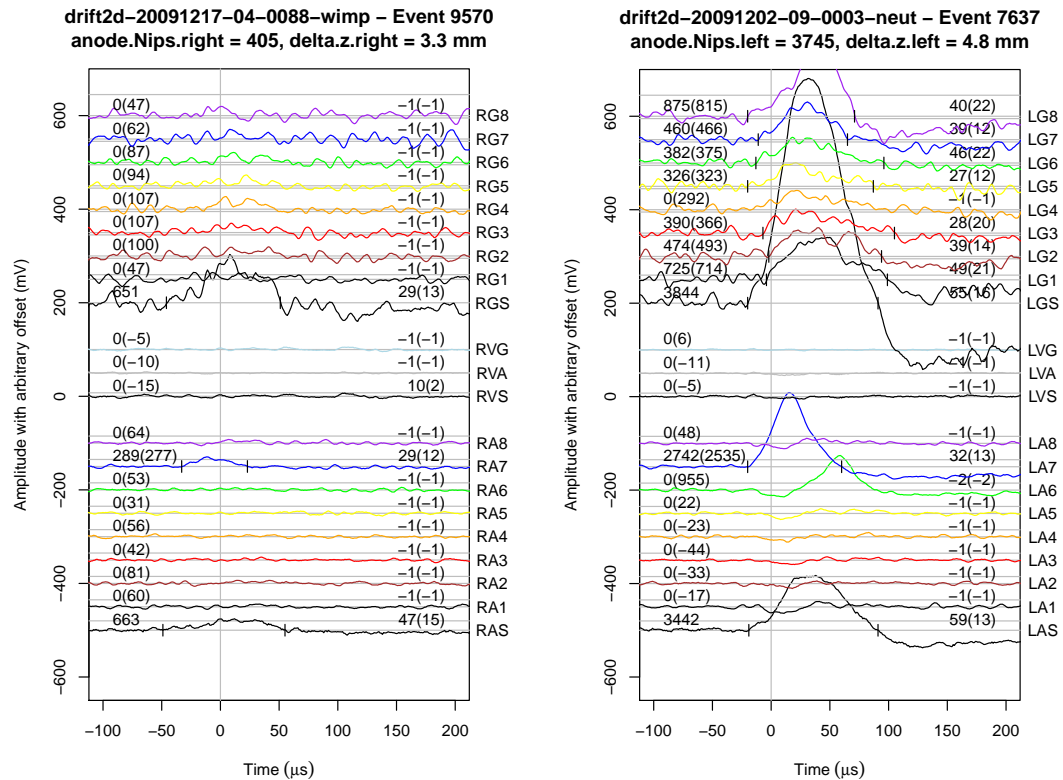


(a) Data from 1.84 days livetime with exposure to  $^{252}\text{Cf}$  neutron source.



(b) Data from 47.36 days livetime of WIMP-search runs.

FIGURE 5.19:  $anodeNips$  to  $anodeSumNips$  ratio as a function of  $anodeSumNips$  for neutron and WIMP-search runs. Horizontal black lines indicate 3 sigma rejection region. Events outside of this region are cut. Circled region illustrates a background population of low  $dE/dz$  events, discussed in the text.



- (a) An event with low charge density resulting in ‘missing charge’.
- (b) An event with ‘missing charge’ due to anode line LA6 mistakenly identified as a rebound pulse and thus not included in the *anodeNips* parameter.

FIGURE 5.20: Two events cut by the *anodeNips* to *anodeSumNips* ratio cut.

### 5.4.2 RMST vs. NIPs plots

The distribution of events in a plot of recoil range as a function of recoil energy has been shown to be effective in identifying different classes of events [118, 149]. In this work the distribution of events in the *anodeTrackRmst* vs. *anodeTrackNips* plane was found to be the best measure of this, where *anodeTrackRmst* is a measure of how long the track is in the direction parallel to the drifting charge, and *anodeTrackNips* is a measure of the charge, which is proportional to the recoil energy of the event. It should be noted that, since *anodeTrackRmst* is the range in the  $z$  direction only, it is affected not only by the total range of the track, but also by the track orientation.

Despite this, it has been shown that in this plane it is possible to achieve some separation between the population of events that occur during exposure to a  $^{252}\text{Cf}$  neutron source, and the populations of events that occur during a WIMP-search run. Because it is assumed that neutron-induced nuclear recoils closely mimic WIMP-induced nuclear recoils, a separation of events occurring during neutron runs from the backgrounds currently seen during WIMP-search runs, allows an acceptance region to be defined that is free of background events, but in which WIMP-induced nuclear recoils may occur.

Figure 5.21 plots the events remaining in the *anodeTrackRmst* vs. *anodeTrackNips* plane for neutron data (red) and WIMP-search data (blue), after application of cuts 1.1 through 3.2, as described above. Distinct populations of background events are seen in the WIMP-search run data that are not seen in the neutron data. Investigation into the sources of these populations is the subject of the next chapter. In this chapter the remaining cuts required to achieve a background-free acceptance region are discussed.

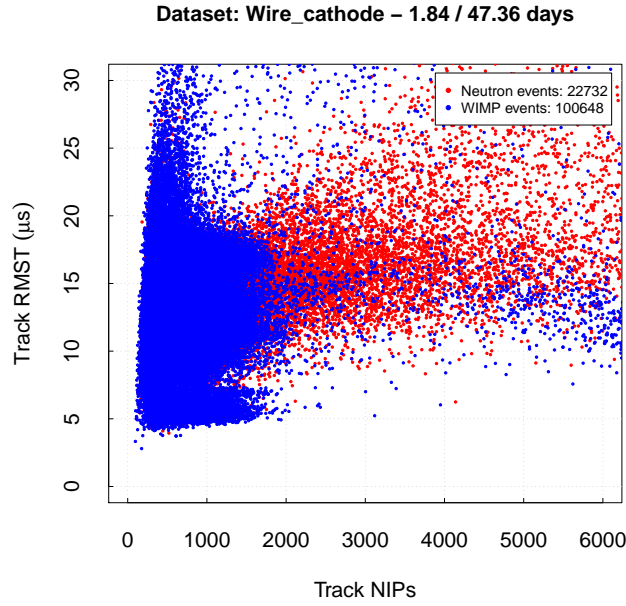


FIGURE 5.21: Events from neutron runs (red) and WIMP-search runs (blue) in the  $anodeTrackRMST$  vs.  $anodeTrackNips$  plane with cuts 1.1 through 3.2 applied.

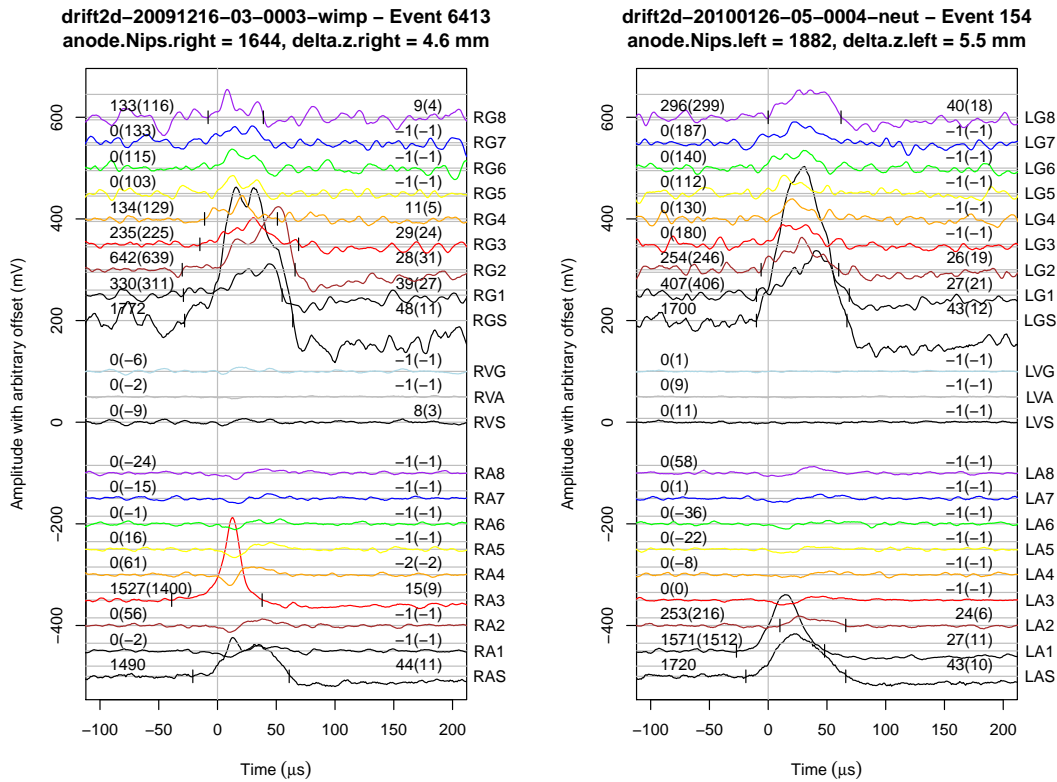
### 5.4.3 Pulse shape cuts

It is clear from Figure 5.21 that WIMP interaction searches using only the cuts described above would be ineffective, since the high level of remaining background events are directly over the region where WIMP events are expected. Attempts are made to remove as many of these background events as possible, whilst retaining the neutron-induced events, by cuts based on event pulse shapes. This is achieved through a manual search of event files to identify differences in events from WIMP-search runs and neutron runs in the same region of the RMST vs. NIPs plane. Differences between neutron and background events are particularly evident in the region of  $\sim 12 \mu\text{s}$  RMST. The following cuts are based on these observed differences.

**$anodeTrackSigma$  to  $anodeTrackRmst$  ratio (3.3)** — Events with  $anodeTrackSigma/anodeTrackRmst$  of below 0.9 are cut. Figure 5.22 compares a typical neutron event and background event of  $\sim 11 \mu\text{s}$ . It can be seen that the event from the neutron exposure has a more Gaussian profile, whereas the event from the WIMP-search run has a wider base and a narrower peak. The source of these events is investigated in the next chapter. A powerful discriminant for this type of event is found by comparing the  $anodeTrackRmst$  to the  $anodeTrackSigma$ . For the Gaussian profile of the events in the neutron runs, these values are approximately equal. However, for an event with a wide base and narrow peak, such as that in Figure 5.22(a), the  $anodeTrackRmst$  is considerably larger

than the  $anodeTrackSigma$ . Figure 5.23 shows that during WIMP-search runs the majority of events have  $anodeTrackSigma/anodeTrackRmst < 0.7$ . During neutron exposure, however, events are mostly distributed about  $anodeTrackSigma/anodeTrackRmst \approx 1$ , with events of lower values approximately consistent with background.

The background population appears to extend into the region in which neutron events occur, with no distinct separation. The cut is, however, very effective — removing 78% of the remaining background events, whilst reducing the background subtracted neutron rate by only 15%.



- (a) Typical event from a WIMP-search run with an  $anodeTrackRmst$  of  $10.6 \mu s$  and a  $anodeTrackSigma$  of  $6.80 \mu s$ . (b) Typical event from a neutron exposure with an  $anodeTrackRmst$  of  $11.8 \mu s$  and an  $anodeTrackSigma$  of  $11.9 \mu s$ .

FIGURE 5.22: Comparison of a typical background and neutron event of  $\sim 1700$  NIPs and RMST of  $\sim 11 \mu s$ . The event occurring during neutron exposure has a more Gaussian shape.

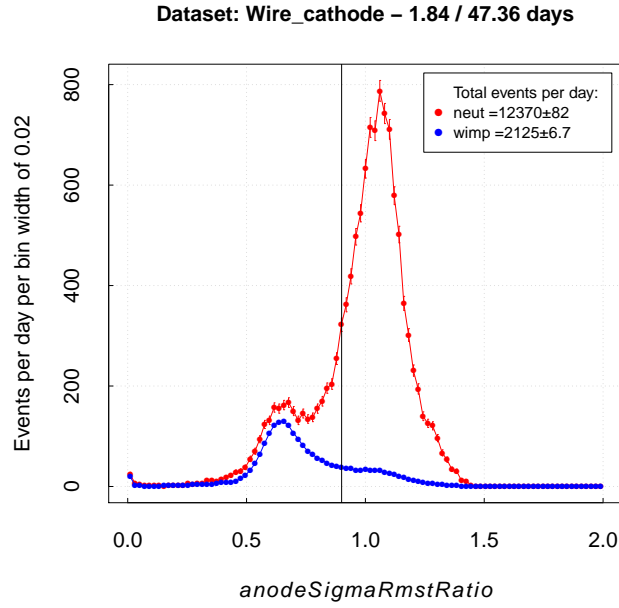


FIGURE 5.23: Ratio of  $anodeTrackSigma$  to  $anodeTrackRmst$  for events during neutron exposure (red) compared to events from WIMP-search data (blue). All events to the left of the black vertical line are cut, removing 78% of events from WIMP-search data whilst reducing the background subtracted neutron rate by only 15%.

***gridPhRatio* (3.4)** — The  $gridPhRatio$  parameter is the ratio of the largest to second largest  $V_{max}$  value from all grid fiducial lines. Events with a  $gridPhRatio$  greater than 1.4 are cut. This cut comes from the observation that events occurring during WIMP-search runs typically produce a particularly pronounced peak on one grid wire, as is seen in the event in Figure 5.22(a). This is in comparison to the event from the neutron run in Figure 5.22(b), in which similar charge is deposited on all grid wires. Figure 5.24 shows that above a  $gridPhRatio$  of 2 the neutron data is consistent with background, confirming that these events are not the result of nuclear recoils. However, again, there is no clear separation between this population and the peak in the neutron source data indicating the expected  $gridPhRatio$  of nuclear recoil events.

A cut at 1.4 is found to maximise rejection of background events whilst retaining reasonable efficiency of neutron events. This cuts 64% of events from the WIMP-search run while reducing the accepted background subtracted neutron rate by only 16% when applied independently to the  $anodeTrackSigma$  to  $anodeTrackRmst$  ratio cut.

When applied in conjunction with the  $anodeTrackSigma$  to  $anodeTrackRmst$  ratio cut, these form an extremely strong background removal technique reducing the rate during WIMP-search runs by 83% whilst reducing the background subtracted neutron event rate by only 28%. Figure 5.25 shows the remaining events on the NIPs vs. RMST plot

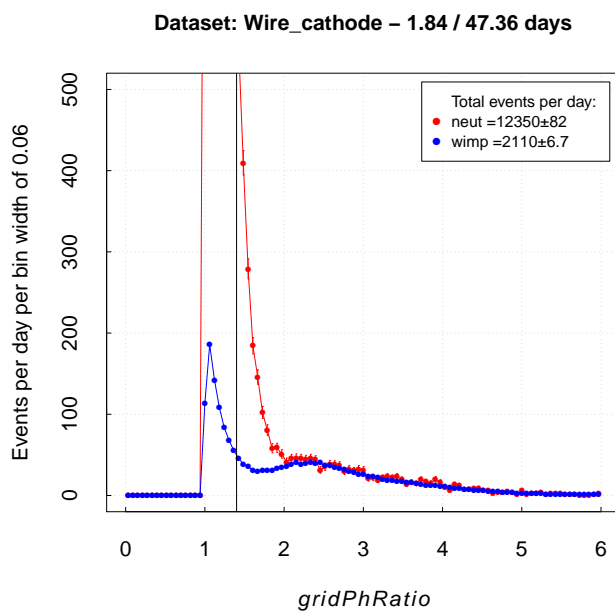


FIGURE 5.24: Frequency plot of *gridPhRatio*. Events with *gridPhRatio*  $\gtrsim 2$  have rates during neutron source exposure consistent with WIMP-search data. Events to the right of the black vertical line at *gridPhRatio* = 1.4 are cut, which reduces WIMP-search event rate by 64% while reducing the background subtracted neutron rate by 16%.

with all the above cuts applied. When compared to Figure 5.21 it is seen that cuts 3.3 and 3.4 have eliminated the majority of WIMP-search run events with an RMST of 8 to  $13 \mu\text{s}$  and NIPs above  $\sim 800$ , while a reasonable number of neutron events in that region remain.

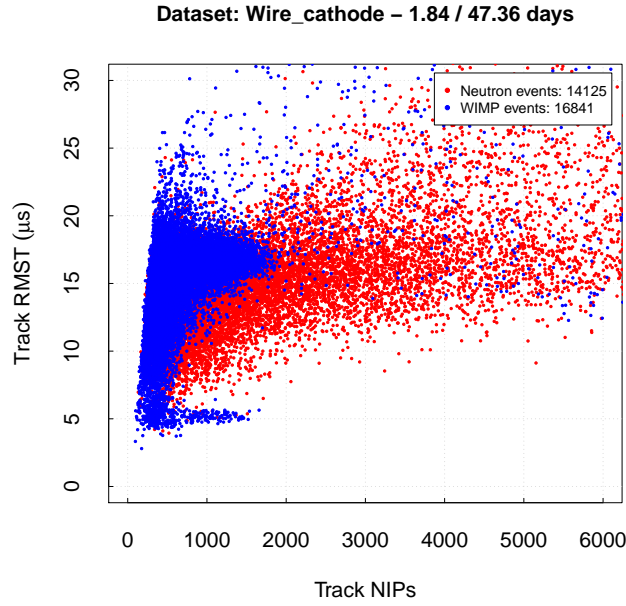


FIGURE 5.25: Events from neutron runs (red) and WIMP-search runs (blue) in the  $anodeTrackRMST$  vs.  $anodeTrackNips$  plane with cuts 1.1 through 3.4. Compared to Figure 5.21, the events from the WIMP-search run in the region  $\sim 8$  to  $12 \mu s$  and above  $\sim 800$  NIPs have largely been eliminated.

#### 5.4.4 Additional pulse shape cuts and signal region

**$anodeMinRisetime$  (3.5) and  $anodeMinFwhm$  (3.6) cuts** — Events with  $anodeMinFwhm < 26$  or  $anodeMinRisetime < 7$  are cut. This identifies and cuts events in which one or more hits on the anode fiducial lines are fast. This was due to the observation that, of the events remaining in the 8 to  $13 \mu s$  window that has opened up in the RMST vs. NIPs plane, they were found generally to consist of faster pulses.

These cuts are less discriminant than the pulse shape cuts described in Section 5.4.3 and, whilst achieving a 85% reduction in background events, also reduce the remaining background subtracted neutron rate by 46%. The combination of pulse shape cuts, however, eliminates the remaining lower RMST events from the WIMP-search runs leaving a background-free region in the RMST vs. NIPs plane, as illustrated in Figure 5.26.

The procedure developed here has resulted in a signal region in the RMST vs. NIPs plane, illustrated in Figure 5.26, in which no events occur during the 47.36 days of WIMP-search data. In the 1.84 days of neutron exposure data 1995 events occur within the signal region implying sensitivity to WIMP-induced nuclear recoils. A previous DRIFT analysis, to be published, consisted of the same 47.36 days WIMP-search data but used a single neutron run consisting of 0.82 days livetime on 16 Dec 2010 [118].

This previous analysis resulted in 1830 events from the neutron exposure passing all cuts and a background-free signal region that contained 228 events from the neutron exposure. The analysis presented here, considering the same 0.82 days livetime neutron run, results in 2422 events passing all cuts (1.1 through 3.6), and a signal region that contains 538 events.

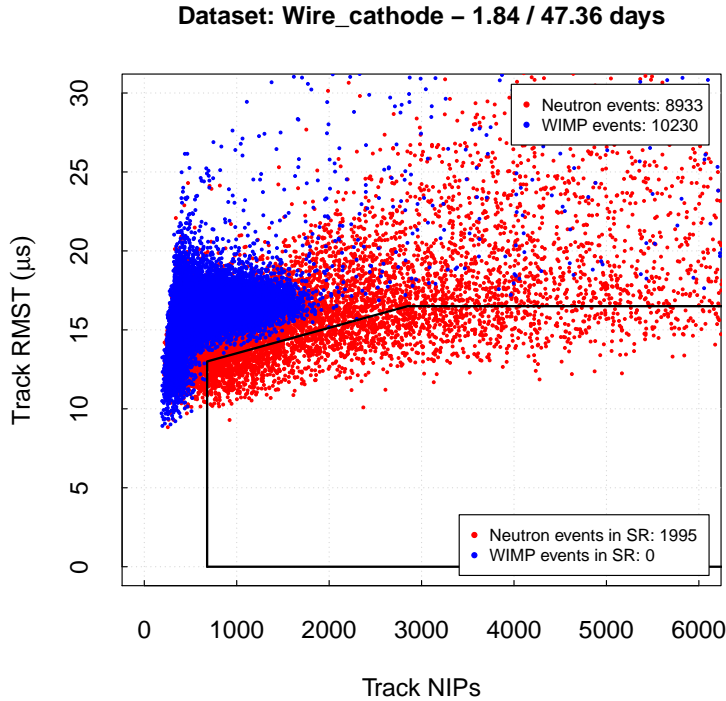


FIGURE 5.26: Events from neutron runs (red) and WIMP-search runs (blue) in the *anodeTrackRMST* vs. *anodeTrackNips* plane after all cuts. Signal region contains no events from the 47.36 days of WIMP-search data but 1995 events from the 1.84 days of neutron data.

## 5.5 Conclusion

A significant restructuring of existing code has been performed to increase the efficiency and flexibility of the DRIFT analysis software. Within the optimised analysis framework all existing cuts have been investigated and removed, tuned, or replaced with newly developed cuts. The resulting cuts are summarised in Table 5.2. The overall effect of the new cuts and procedures results in an increase in the neutron efficiency by a factor of 2.4 — translating into increased sensitivity to WIMP dark matter interactions. The zero background signal region that has been developed will be used to determine a limit on the WIMP-proton interaction cross-sections in Section 7.2.

Cut	Events per day		
	WIMP- search	Neutron	Back. sub. neutron
Total triggered events (no cuts)	96520±45	153120±250	56600±250
All stage 1 cuts	33450±30	70780±200	37330±200
All stage 2 cuts	15100±18	41080±150	25980±150
<i>anodeSumNips/gridSumNips</i> cut (3.1)	7923±13	27340±120	19420±120
<i>anodeNips/anodeSumNips</i> cut (3.2)	2127±7	12370±80	10240±80
<i>anodeTrackSigma/anodeTrackRmst</i> cut (3.3)	470±3	9130±70	8660±70
<i>gridPhRatio</i> cut (3.4)	356±3	7680±70	7320±70
<i>anodeMinRisetime</i> cut (3.5)	249±2	5940±60	5690±60
<i>anodeMinFwhm</i> cut (3.6)	216±2	4860±50	4640±50
Events in signal region	0	1084±24	1084±24

TABLE 5.2: Effect of cuts on event rates. Showing the event remaining after each cut (first column, with cut index shown in parentheses) for WIMP-search data (second column), neutron data (third column), and background subtracted neutron data (fourth column).



## Chapter 6

# Long-term study of backgrounds in DRIFT-IIId

The previous chapter introduced selection cuts that permit separation of a portion of neutron-induced nuclear recoil events from all backgrounds. In developing these cuts it was observed that, in the RMST vs. NIPS plane, the background separates into four distinct populations. In this chapter, a systematic study of over three years of data is undertaken for two of these populations, with the aim of understanding the sources of these backgrounds. Ultimately it is hoped to reduce or eliminate these backgrounds, permitting an increase in the size of the acceptance region, leading to a corresponding improvement in WIMP detection efficiency. This is the first systematic long-term study of backgrounds attempted in the collaboration.

Section 6.1 outlines the known backgrounds in DRIFT-IIId. Section 6.2 introduces new methods developed by the author for measuring rates of these backgrounds. Rates of the identified backgrounds over long time periods are presented in Section 6.3 and conclusions from this analysis are drawn in Section 6.4.

### 6.1 Background events in DRIFT-IIId

A general discussion of backgrounds in direct dark matter detectors is covered in Section 2.2. In DRIFT, backgrounds can be classified by considering the energy and range of the identified track. *Recoil-like* tracks are tracks with a range of a few mm consisting of a few hundreds to thousands of negative ion pairs (NIPs). *Alpha-like* tracks have a range of a few cm and consist of many thousands to tens of thousands of NIPs.

### 6.1.1 Alpha-like background events

Alpha particles in DRIFT originate in the Uranium and Thorium decay chains. U and Th are present in the cavern rock, the materials used in the construction of the lab, the stainless steel vacuum vessel and components of the detector itself. Alpha particles generated in these bodies, however, have too little penetrating power to enter the DRIFT detector volume. The dominant mechanism for alphas in DRIFT is therefore from impurities deposited on surfaces inside the detector, and radon, a radioactive gas generated in the U and Th decay chains, that decays via alpha emission.

Alphas entering the detector fiducial volume from outside will cause hits in the veto and be cut at stage 1 reduction (Section 5.3). Alphas contained within the fiducial volume produce a distinctive long track, resulting, because of the grouping of every eighth MWPC wire (Section 3.2.2), in periodic deposition of charge on each of the eight lines. Figure 6.1 shows a typical alpha event in DRIFT-II, which has a range of  $\sim 240$  mm. In a WIMP analysis alpha tracks are cut by the *eightLineCut*, since they hit all eight lines, and also by the final acceptance region, since the RMST of an alpha will typically be very long. Alpha tracks are, therefore, trivial to separate from WIMP interactions.

Although direct alphas can be cut, a far subtler and more problematic background is caused by alpha decays on detector electrodes where the alpha particle is emitted into the electrode, and the daughter nucleus recoils into the detector volume. These recoiling nuclei produce events potentially indistinguishable from WIMP-induced nuclear recoils, and so are a troublesome background for DRIFT and other direct dark matter detectors. These events, termed radon progeny recoils (RPRs), are discussed further in Section 6.1.4.

### 6.1.2 Alpha events as a diagnostic for DRIFT

Although typical alpha events can be eliminated by cuts, they are interesting for the purposes of characterising the detector. Alpha tracks in the DRIFT detector can be considered in three categories:

**1MWPC alpha events** — Alpha events that are fully contained within a single side (left or right) of the fiducial volume are defined as 1MWPC alpha events. Such events are defined as having no hits on the veto channels so cannot be from emanation from the vacuum vessel walls and must originate from inside the fiducial volume. Such events must, therefore, originate from radioactive decays in the target gas, or on the surface of the electrode wires that define the fiducial volume. The alpha event in Figure 6.1 is a typical 1MWPC alpha event.

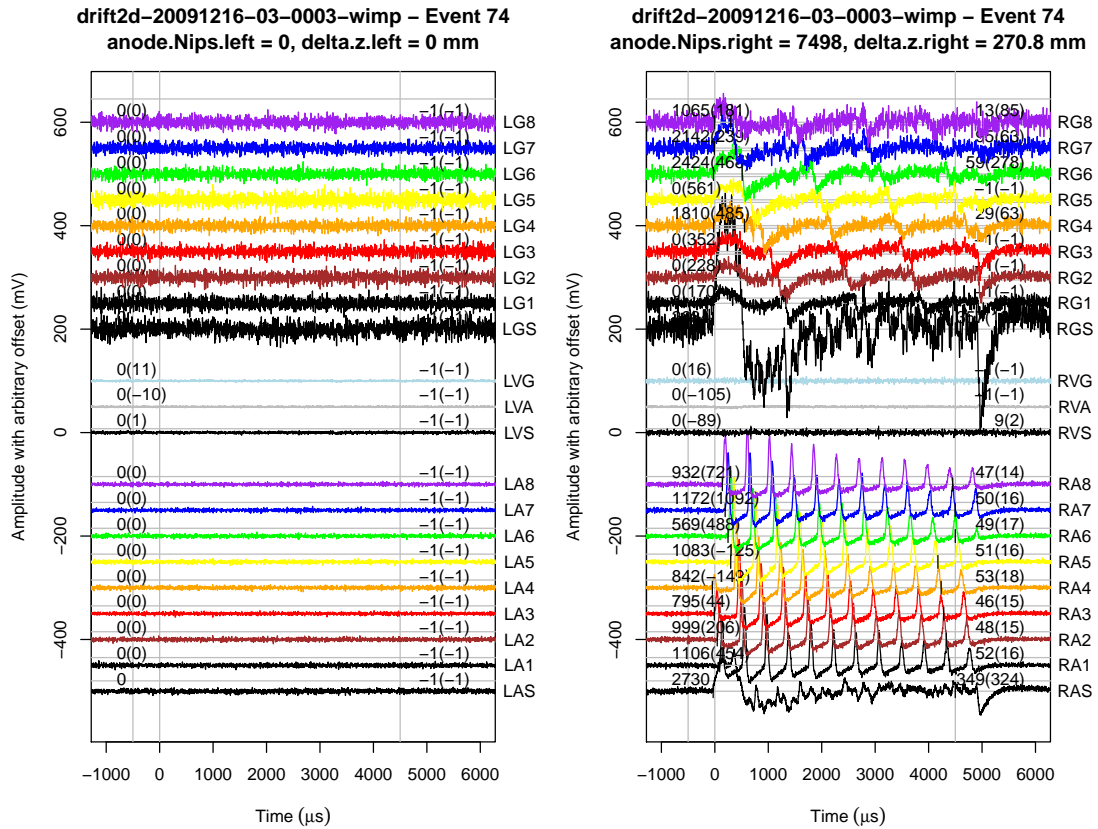


FIGURE 6.1: Event file for a typical alpha event. No charge is deposited in the left-hand side of the detector but a large event is seen on the right MWPC. The grouping of every eighth MWPC wire results in periodic charge deposition on each line, where each hit corresponds to charge deposition on a separate wire 16 mm away.

**Gold-plated cathode-crossing alphas** — The decay of an atom that is suspended in the target gas may produce an alpha track that is fully contained within the fiducial volume and passes through the central cathode. Such an event will result in alpha tracks in both MWPCs — a signature that can only be produced by the decay of radionuclides suspended in the target gas. These events are referred to as gold-plated cathode-crossing (GPCC) events, because of their well defined source. The rate of GPCCs is therefore a direct measure of the level of radon contamination in the target gas. Figure 6.2 shows a typical GPCC event where the alpha track is split over both MWPCs. The coincidence in the end time of the tracks on each side (at  $\sim 3500 \mu\text{s}$ ) confirms that these are two halves of the same track, and not two separate alphas in coincidence.

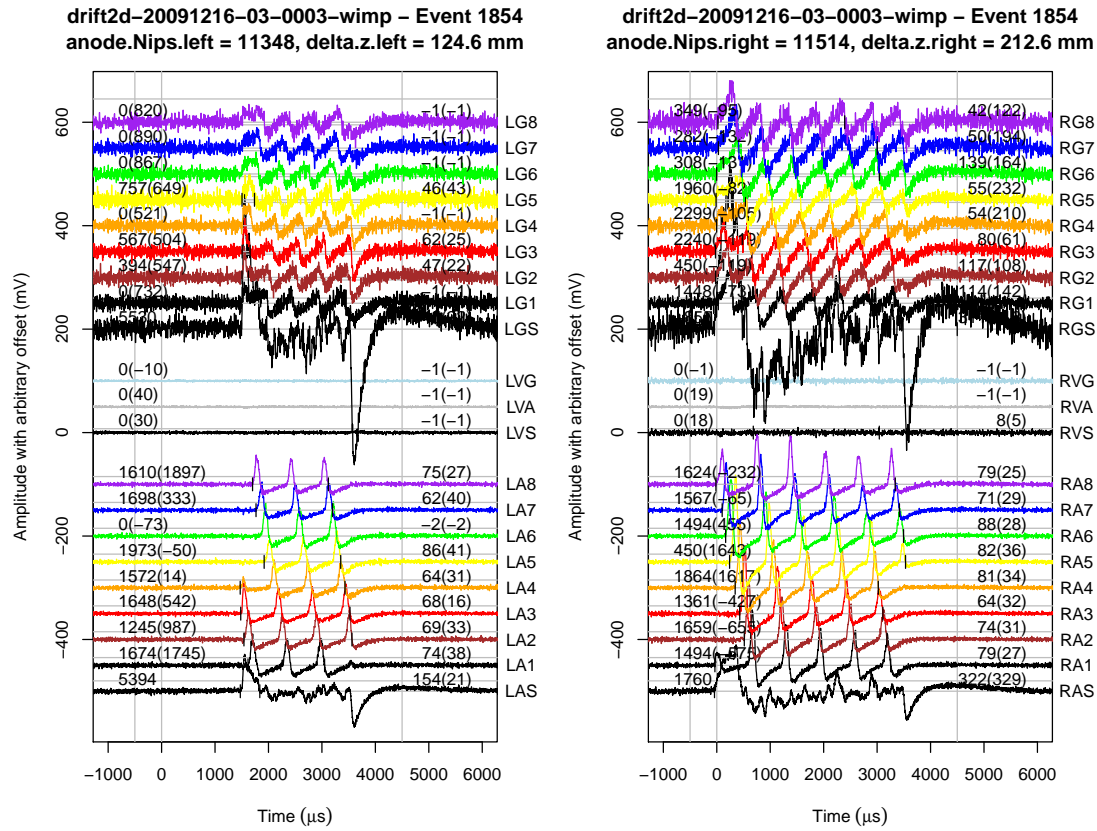


FIGURE 6.2: A typical GPCC event in which a distinct alpha signal is seen on both MWPCs. The track ends simultaneously on each side, at  $\sim 3500 \mu\text{s}$ , indicating that these are two halves of the same track.

**Alpha-tagged recoil events** — The random orientation of alpha emission from a radioactive isotope on the surface of a wire can lead to a variety of ionisation tracks in the fiducial volume. One track type of particular interest is that where a decay on the surface of a central cathode wire results in an alpha being emitted into one side of the fiducial volume, whilst the daughter nucleus recoils into the other side. This type of event can only be created by the decay of an atom on the surface of the central cathode wire and thus offers a direct measure of contamination on the central cathode wires. It should be noted that a cathode-crossing alpha event that is almost entirely on one side, with only a few mm on the other, could look identical to an alpha-tagged recoil event. However, the rate of these events is estimated to be small compared to the overall alpha-tagged recoil event rate. A typical alpha-tagged recoil event is shown in Figure 6.3.

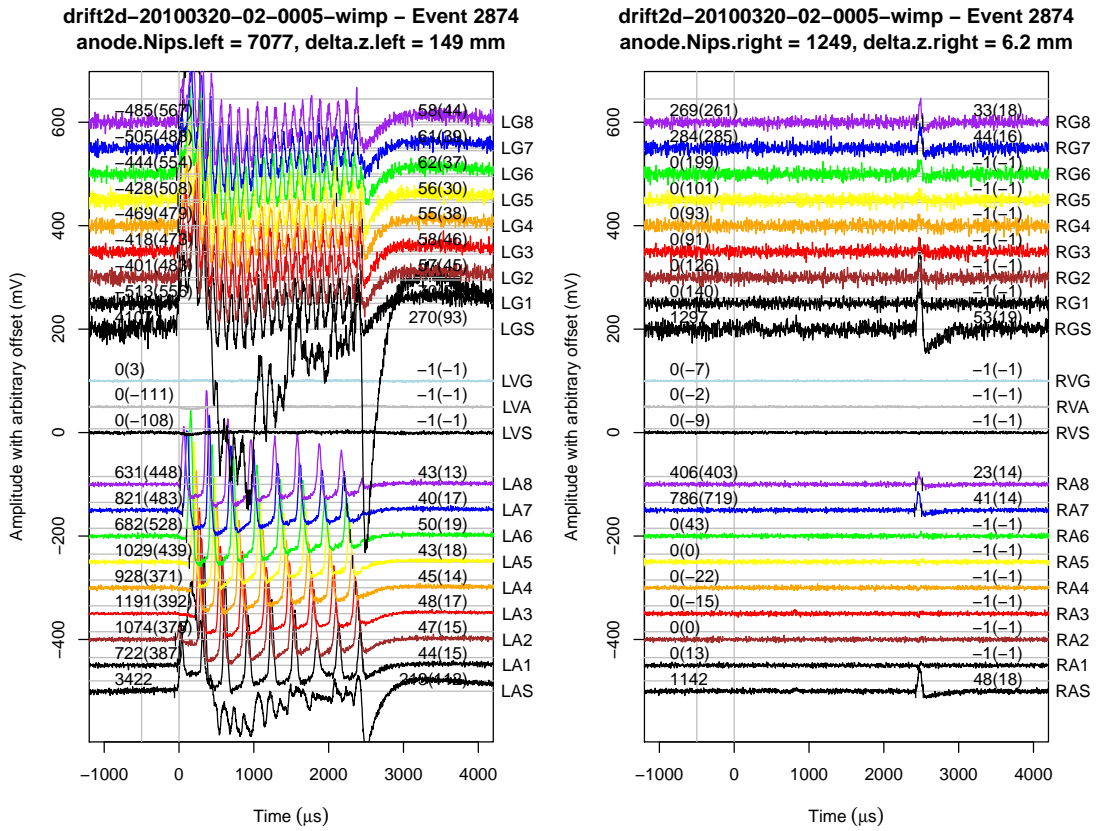


FIGURE 6.3: A typical alpha-tagged recoil event. The left-hand side MWPC contains an alpha track and the right-hand side contains a recoil-like event that passes all the WIMP analysis cuts defined in Section 5.3. The coincidence in time between the alpha event on the left and the recoil-like event on the right, at  $2500 \mu\text{s}$ , confirm that these are two parts of the same event, separated by the central cathode.

### 6.1.3 Recoil-like background events

The decay of a hypothetical radionuclide contaminant on the surface of a wire (either in the central cathode or an MWPC) could result in a recoil-like event if the alpha particle is ejected into the wire, while the recoiling daughter nucleus is emitted into the fiducial volume. Alpha emissions from the U and Th decay chains have energies ranging from 5.9 to 9.0 keV. From conservation of momentum, the recoiling nucleus, with an atomic mass of  $\sim 200$ , has an energy of  $\sim 100$  keV. A nuclear recoil of this energy scale is precisely what is expected from a WIMP-induced nuclear recoil, making this background potentially indistinguishable from dark matter signal events on an event-by-event basis. A typical recoil-like event from a neutron exposure is shown in Figure 6.4.

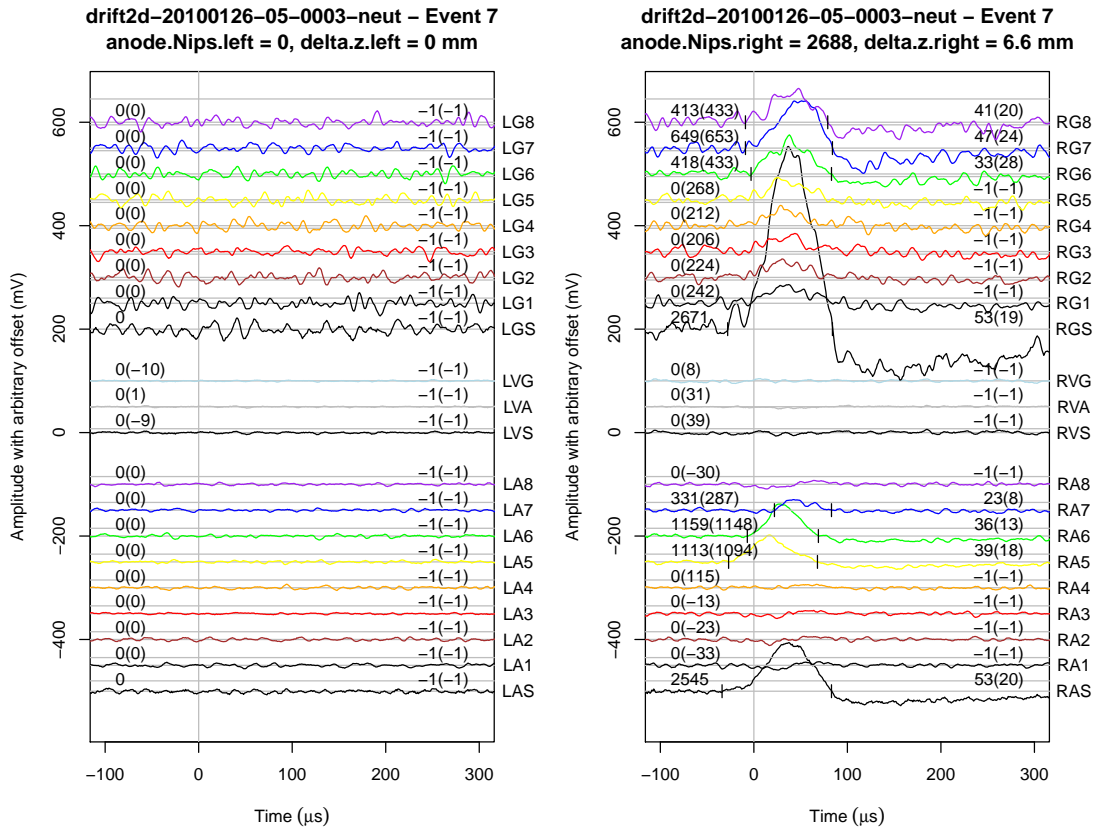


FIGURE 6.4: A typical recoil-like event from a neutron calibration run. The event spans anode lines RA5 to RA7 in the right-hand side MWPC.

### 6.1.4 Radon progeny recoils in DRIFT

As shown in Section 5.3, the selection cuts leave a population of nuclear recoil-like events in the dataset. It has long been suspected that nuclear recoils from decays of radionuclides on the central cathode wires are a significant source of recoil-like events in DRIFT. A long-standing hypothesis for the source of radionuclides on the central cathode wires is that they originate from radon contamination in the detector volume. This background is termed the radon progeny recoil (RPR) background.

Radon isotopes  $^{222}\text{Rn}$  and  $^{220}\text{Rn}$  are gaseous radioactive isotopes from the uranium and thorium decay chains respectively. Radon gas is known to be present in the Boulby Underground Laboratory and is expected to penetrate the imperfect seals of the vacuum vessel, contaminating the target volume. In addition, some detector components, such as circuit board materials and wire insulation, are known to contain trace elements of U and Th that are a source of further radon contamination in the fiducial volume [113]. The detection of cathode-crossing alphas, described in Section 6.1.1, is direct evidence of radon contamination in the target volume.

Figure 6.5 illustrates how radon contamination could lead to recoil-like background events in DRIFT with target gas contamination of the radioisotope  $^{222}\text{Rn}$ . The particle, suspended in the gas, decays via the emission of a 5.6 MeV alpha, which can easily be identified as such in DRIFT. However, the daughter product is an unstable  $^{218}\text{Po}$  atom, which may be produced positively charged [113]. In this case the  $^{218}\text{Po}^+$  ion would be attracted to the negatively charged central cathode plane, where it would plate-out on the wire surface.

The  $^{218}\text{Po}$  isotope on the surface of the cathode wire then decays, with a half-life of 3.10 minutes, by emission of a 6.11 MeV alpha. An alpha of this energy has a range of  $\sim 14\ \mu\text{m}$  in the stainless steel of the  $20\ \mu\text{m}$  central cathode wires. This geometry, illustrated in Figure 6.5, and the random orientation of the alpha decay result in a number of possible event types from this decay, including a WIMP-mimicking recoil-like event.

Furthermore, as shown in Figure 6.6, the  $^{222}\text{Rn}$  decay chain results in further radioisotopes that may be produced positively charged and hence plate out on the central cathode wires. Finally, the decay chain leads to  $^{210}\text{Pb}$ , which decays to  $^{206}\text{Pb}$  by emission of a 5.41 MeV alpha with a half-life of 22.3 years. This process therefore may result in long-term accumulation of  $^{210}\text{Pb}$  on the central cathode wires.

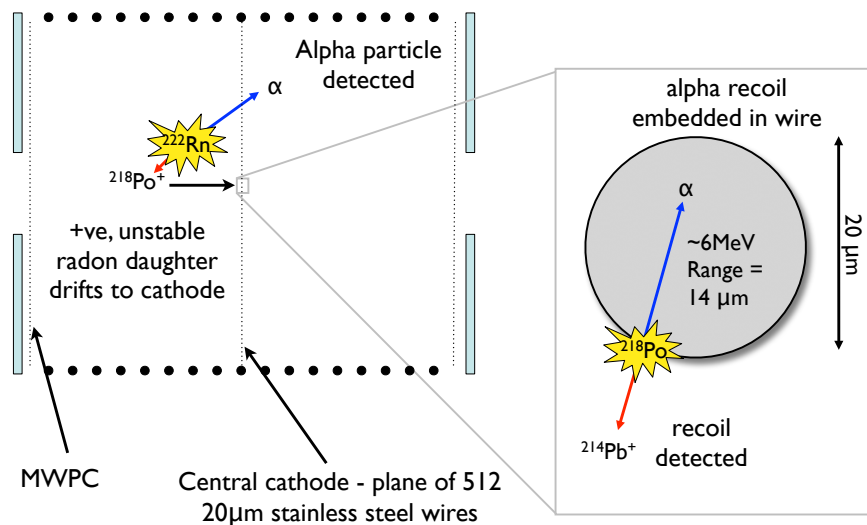


FIGURE 6.5: Schematic of the radon progeny recoil (RPR) background in the DRIFT-II detectors. Radon decay in the detector volume can result in an unstable, positively charged ion that drifts to, and plates out on, the surface of the  $20\ \mu\text{m}$  stainless steel wires of the  $1\ \text{m}^2$  central cathode plane. The unstable radon daughter on the wire surface then decays by alpha emission, which, if the alpha is oriented into the wire, can result in detection of a WIMP-like nuclear recoil without the tell-tale alpha event.

The RPR hypothesis therefore predicts, from the contamination of radon, a prompt RPR background of WIMP-like recoils within minutes or hours of the decay of the radon isotope in the gas, and a cumulative RPR background of WIMP-like recoils that

gradually increases over time due to the accumulation of the long-lived  $^{210}\text{Pb}$  on the wires, and remains long after the radon is removed from the detector.

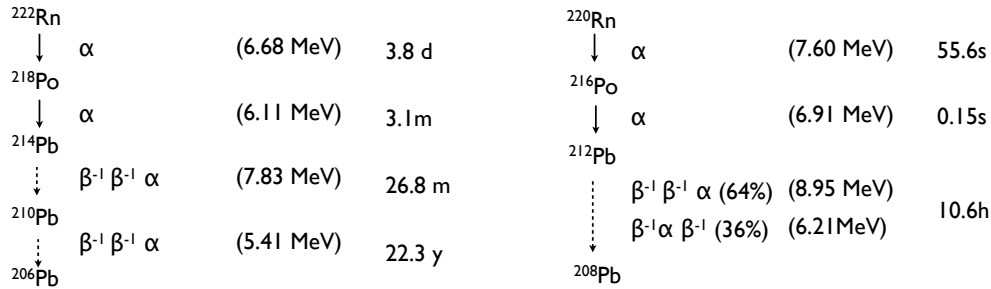


FIGURE 6.6: Sections of the U ( $^{222}\text{Rn}$ ) and Th ( $^{220}\text{Rn}$ ) decay chains relative to backgrounds in DRIFT.  $^{222}\text{Rn}$  produces four alpha particles with energies of 5.4 to 7.8 MeV.  $^{220}\text{Rn}$  produces three alpha particles with energies of 6.2 to 9.0 MeV. Data from Nuclear Data Services [150].

### 6.1.5 DRIFT-II detector operations

The first operational DRIFT-II module was installed in the Boulby Underground Laboratory in 2005. The underground detector has been subject to numerous upgrades to improve performance. Those actions which have demonstrably affected the background event rates are listed below, with the time of the action, in days since 1 January 2005, indicated in parentheses.

1. 9 February 2008 (day 1134) — The central cathode wire plane was etched in nitric acid to remove radioactive surface contamination such as  $^{210}\text{Pb}$ . This procedure was based on background reduction techniques found to be successful in the EXO-200 experiment [151]. In all time-based plots presented in Section 6.3 this action is indicated by the first red dashed line at day 1134.
2. 1 July 2008 (day 1277) — The MWPC readout planes were similarly etched in nitric acid. This action is indicated by the first black dashed line at day 1277 in the time-based plots in Section 6.3.
3. 22 September 2009 (day 1725) — The replacement of the right-hand side MWPC, which was exhibiting unstable behaviour, with one from a prototype DRIFT-II detector at Occidental College. This action is indicated by the second black dashed line at day 1725 in the time-based plots in Section 6.3.

4. 1 March 2010 (day 1885) — The subsequent replacement of the original right-hand side MWPC after its repair. This action is indicated by the third black dashed line at day 1885 in the time-based plots in Section 6.3.
5. 6 March 2010 (day 1890) — Replacement of the wire plane central cathode for a cathode constructed from a  $20\ \mu\text{m}$  aluminium coated mylar thin film. The thin film cathode is highly transparent to alpha particles and so should reduce the number of recoil-like events from the process described in Section 6.1.4. In all time-based plots presented in Section 6.3 this action is indicated by the second red dashed line at day 1890.

## 6.2 Characterising recoil-like backgrounds

### 6.2.1 Identification of background recoil-like populations

In the previous chapter it was shown that by careful selection of cuts a number of separate populations of background events can be resolved. Figure 6.7 shows both neutron and background data in the NIPs vs. RMST plane after applying cuts 1.1 through 3.2, which, as detailed in Section 5.3, retains only well parameterised recoil-like events that are fully contained in the fiducial volume. While the remaining events in the neutron data form a single population, the events from the background runs consist of four distinct populations, which are labelled in Figure 6.7(b).

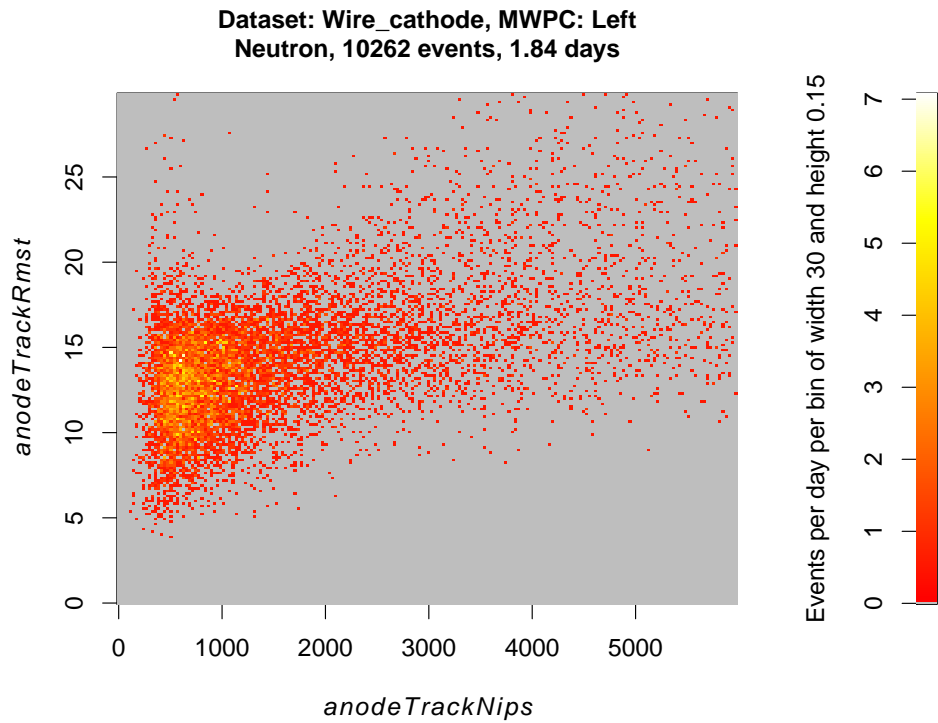
**Population 1 recoil-like events** — The population 1 events, with an RMST of  $\sim 5\ \mu\text{s}$  are the spark-like events discussed in Sections 3.4 and 3.5. They have pulse shapes consistent with the  $4\ \mu\text{s}$  shaping time of the shaping amplifiers — indicating that they are from short, fast charge depositions. A possible source of these events are nuclear recoils from radioactive contamination on the surface of anode wires in the MWPCs. A nuclear recoil produced in the high field region surrounding the anode wire may result in an ionisation track in which the electrons do not attach to  $\text{CS}_2$  molecules. In this case, the fast drifting electrons would produce a spark-like event with a shape determined by the response of the shaping amplifiers. Since these events are clearly separable from the neutron-induced nuclear recoils, and can be removed with minimal loss to neutron efficiency, they are not the focus of this section.

**Population 2 recoil-like events** — Events in this background population were found, in Section 5.4.3, to have different pulse shape characteristics to neutron-induced recoils in the same region of the NIPs vs. RMST plane. Although these pulse shape differences were used to essentially eliminate this population, the cuts used resulted in a significant

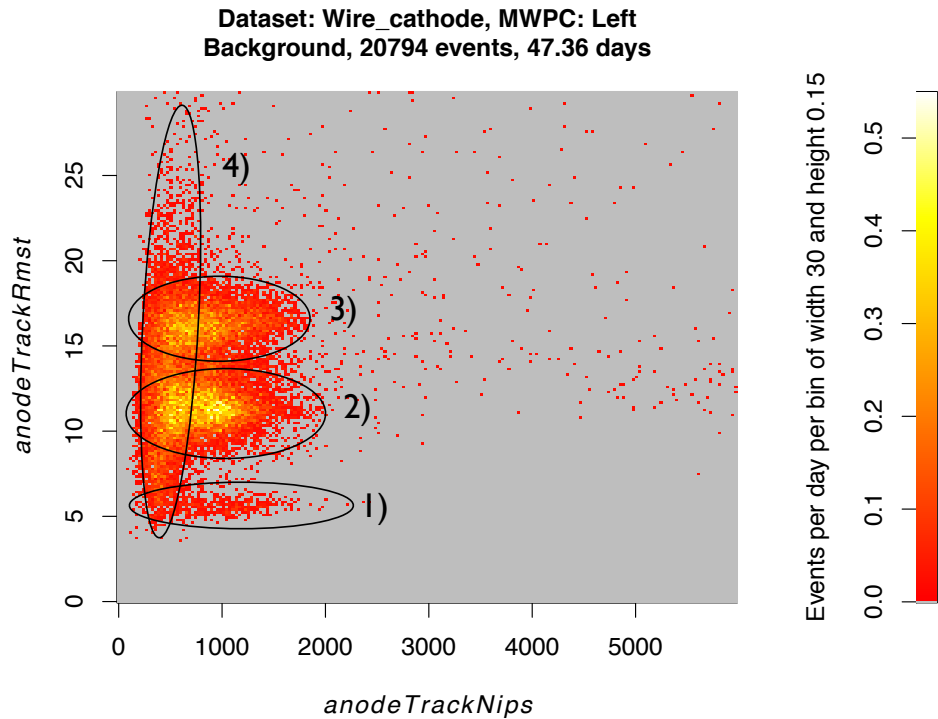
reduction in the nuclear recoil detection efficiency, and hence sensitivity to WIMP interactions, of DRIFT. Improving understanding of the population 2 events is therefore a focus of this chapter, with the motivation of improving, and ultimately removing the need for, the lossy pulse shape cuts described in Section 5.4.3.

**Population 3 recoil-like events** — No difference has been established between the population 3 events from WIMP-search runs and the neutron-induced nuclear recoils from  $^{252}\text{Cf}$  exposure in this region. Since population 3 events are indistinguishable from neutron-induced nuclear recoils it is suspected that they are true nuclear recoils, from decays on the central cathode plane. The signal region in the NIPs vs. RMST plane required to exclude these events (Figure 5.26) also severely reduces the nuclear recoil detection efficiency of DRIFT. Improving understanding of this population is a core motivation for the work in this section.

**Population 4 recoil-like events** — It is thought that the population 4 events may be due to electron recoils from gamma-ray backgrounds. Evidence for this came from a full WIMP analysis of 40 minutes of livetime data from the routine six-hourly  $^{55}\text{Fe}$  exposures. The events from this analysis are plotted in the NIPs vs. RMST plane in Figure 6.8, where a cluster of events above background is seen with a distribution consistent with the population 4 recoil-like events — suggesting that population 4 may also be gamma-ray related. This population has large implications for future DRIFT detectors that may be run at low threshold — the large range of RMST values associated with this population might make it challenging to cut such events in analysis if they cannot be reduced by shielding or improved radiopurity of the detector.



(a) Data from 1.84 days of neutron source exposure with reduced cuts. Events are seen to be distributed over a wide range of NIPs and RMST values.



(b) 47.26 days of WIMP-search run data with reduced cuts. The remaining background events consist of four distinct populations.

FIGURE 6.7: A comparison of WIMP-search run data to neutron data with a reduced set of cuts (1.1 through 3.2) as detailed in Section 5.4.

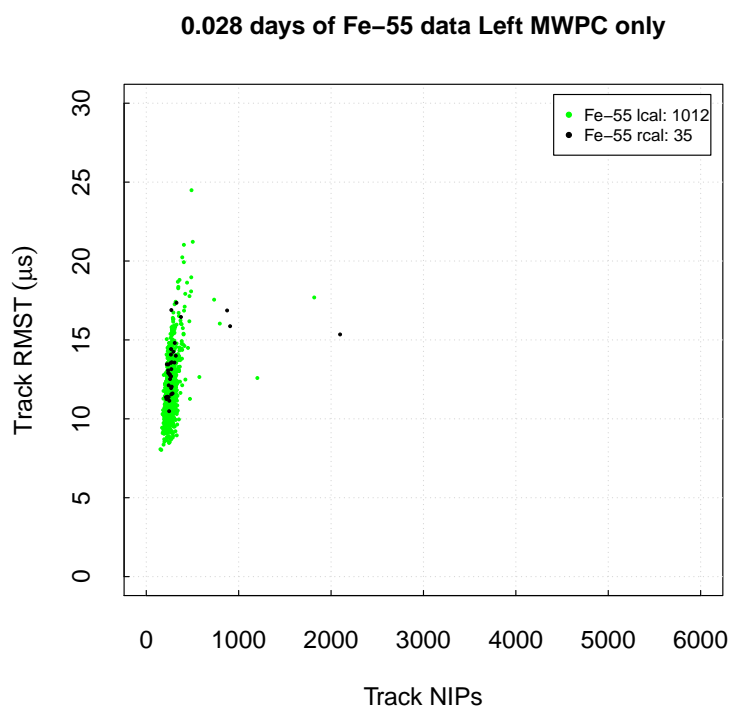


FIGURE 6.8: Data from a standard WIMP analysis of  $^{55}\text{Fe}$  calibration data. Only data from the left MWPC is analysed. Green points are events from 40 minutes of  $^{55}\text{Fe}$  source exposure, in which events are detected with a rate of  $0.42 \pm 0.01$  Hz and a distribution similar to the population 4 background events identified in Figure 6.7(b). Black points are events from 40 minutes of background data in untriggered mode in which an event rate of  $0.014 \pm 0.002$  Hz is observed.

### 6.2.2 Quantifying backgrounds

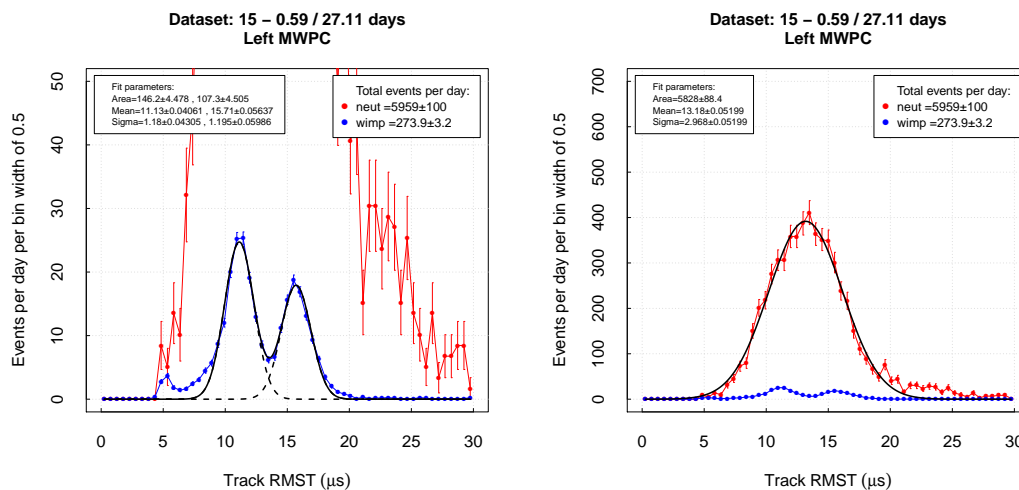
For the purpose of determining the event rate of each of the backgrounds defined in the previous sections an alpha event is defined as an event that passes all stage 1 cuts (defined in Section 5.3), hits all eight anode fiducial lines, and has  $anodeSdCrossingsMax \geq 6$ . A recoil-like event is defined as an event that passes all stage 1 and stage 2 cuts and has a charge deposition greater than 700 NIPs (to exclude population 4 events).

Events may pass either the alpha event cuts or the recoil-like event cuts in either MWPC, or in both MWPCs simultaneously. An event is defined as a 1MWPC alpha event if the event passes the above alpha event definition in a single MWPC only, or a GPCC event if it passes the above alpha definition in both MWPCs, and in addition has  $t_{max}$  for the two MWPC signals separated by  $< 150 \mu s$ . The additional  $t_{max}$  requirement is to ensure that both tracks originated from the same  $z$ , and are therefore likely to be two halves of the same track that crossed the cathode plane between the two MWPCs. An event is defined as an alpha-tagged recoil event if it passes the alpha event cuts in one MWPC and the recoil-like event cuts in the other. Again, it is required that  $t_{max}$  for the two MWPCs to be separated by  $< 150 \mu s$ . Alpha-tagged recoils are treated as a separate population from 1MWPC recoil-like events.

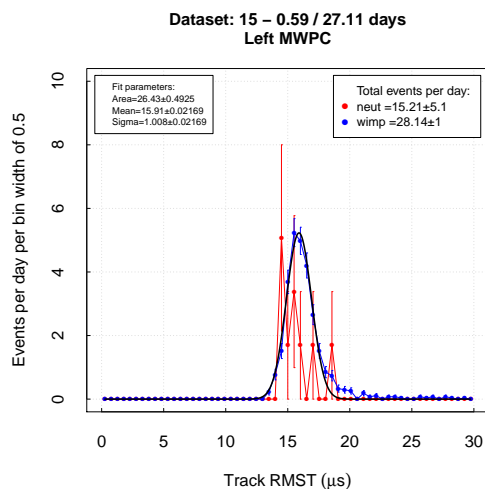
In the recoil-like event class, a 1MWPC recoil-like event is an event that passes the cuts for a recoil-like event in a single MWPC only, with no detected charge in the other MWPC. The separate rates of the population 2 and 3 recoil-like events are determined by projecting the RMST of 1MWPC recoil events into a frequency plot. A double Gaussian is then fitted to the two populations. Figure 6.9(a) shows the results of this double Gaussian fit for an 27.1 day livetime WIMP-search run. The Gaussian fit enables extraction of an estimate of the number of events in each of populations 2 and 3, and the mean RMST, with associated error, for each of these two populations. The fits yield estimates of the event rate for each MWPC separately. For the data shown in Figure 6.7(b) left MWPC, the event rates for populations 2 and 3 were  $146.2 \pm 4.5$  events per day and  $107.3 \pm 4.5$  events per day, respectively. In the right MWPC (not illustrated) the corresponding rates were  $690.3 \pm 27.3$  events per day and  $87.4 \pm 23.8$  events per day, respectively.

Figure 6.9(b) shows an overlaid frequency plot of 1MWPC recoil events from a run with a neutron source, with a Gaussian fit to the single population of neutron recoils from the detector. The mean event rates in the left and right MWPC neutron runs were  $5828 \pm 88$  and  $3067 \pm 87$  events per day. The mean RMST is  $13.18 \pm 0.05 \mu s$  in the left MWPC and  $13.36 \pm 0.10 \mu s$  in the right MWPC.

Figure 6.9(c) shows the RMST distribution of the recoil component of alpha-tagged recoil tracks. The mean event rate is  $26.43 \pm 0.4925$  events per day and the RMST is  $15.91 \pm 0.02 \mu\text{s}$ .



- (a) Two-Gaussian fit to population 2 and population 3 events in WIMP-search run data (blue). See text for details.
- (b) Gaussian fit to events from neutron exposure (red). WIMP-search data (blue) is plotted for comparison. See text for details.



- (c) Gaussian fit to recoil component of alpha-tagged recoil events (blue). Rate of events during neutron exposure (red) is consistent with background.

FIGURE 6.9: Gaussian fits to recoil-like events to determine event rate and mean RMST of population 2 and population 3 recoil-like events, and alpha-tagged recoil events.

## 6.3 Long term background studies

In Section 6.2, the use of cuts to select alpha-like and recoil-like events from the data was demonstrated. Overlapping Gaussian fits were then used to decouple the population 2 and population 3 event statistics for recoil-like events. The statistics of interest, as calculated for a single dataset, are the rates of each event subclass, and, for the recoil-like events, the duration in time of the anode signals, determined by the mean value of the *anodeTrackRmst* parameter.

In this section these methods are applied to a large amount of data, with the aim of observing any trends in these parameters over long time periods and resulting from detector modifications. A description of the detector configuration in each of the datasets used in this analysis is given in Appendix B.

### 6.3.1 Population 3 recoil-like events

Figure 6.10 shows the rates of population 3 events from 1MWPC recoil-like events in runs distributed over more than 1200 days of DRIFT-IIId data. There are three clearly delineated regions, separated by the actions at days 1144 and 1890, both marked by red dashed lines. At each of these actions, the rate of population 3 events drops, at the first action by a factor of about 2, and at the second by a further factor of about 10. The first action is the use of nitric acid to etch the central cathode wire plane, as described in Section 6.1.5. The second action is the replacement of the central cathode wire plane with a thin film cathode, also discussed in Section 6.1.5.

The numerical values for the background reductions are given in the caption of Figure 6.10. The acid etching procedure reduced the population 3 event rate to 54% of its pre-etch value, and the use of a thin film cathode further reduced it to 6.5% of its pre-etch value. These results provide confirmation of the hypothesis that population 3 background events originate on the central cathode. In addition the results demonstrate the success of the thin film cathode in reducing the background, and the effectiveness of using dilute nitric acid for removal of radioactive contamination.

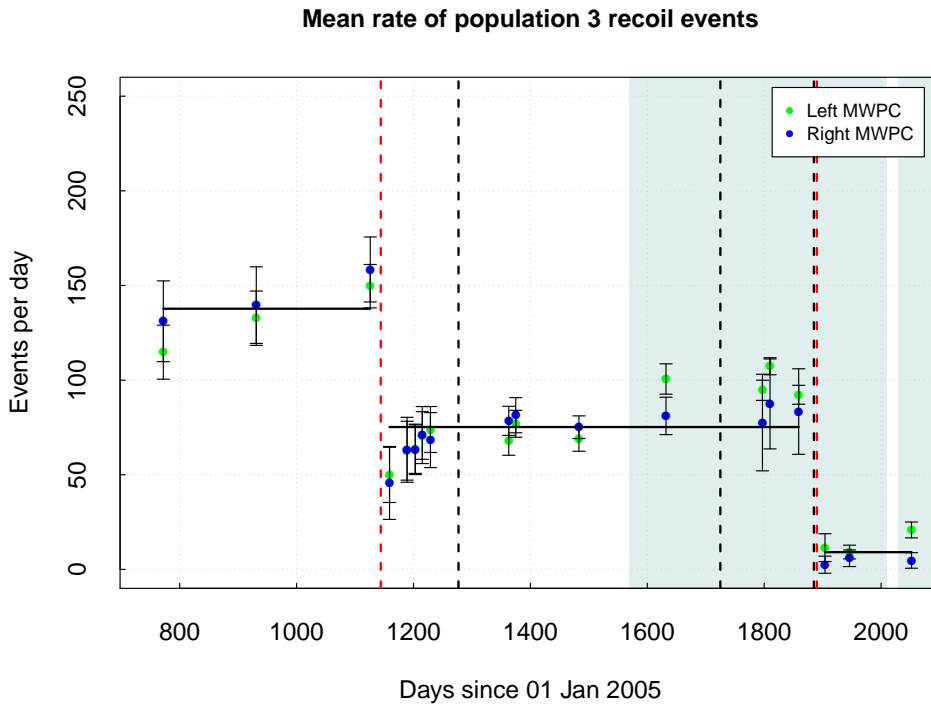


FIGURE 6.10: The mean event rate of population 3 recoil events. The mean event rate, shown by the black horizontal lines is  $138 \pm 6$  with the wire central cathode prior to etching,  $75 \pm 3$  with the wire central cathode after etching and  $9 \pm 3$  with the thin film cathode. Vertical dashed lines indicate the actions described in Section 6.1.5. Blue shaded region is  $\text{CS}_2\text{-CF}_4$  data, unshaded region is pure  $\text{CS}_2$ .

**Mean RMST** — Figure 6.11 shows the distribution of the RMST parameter in population 3 events from 1MWPC recoil-like events over the same 1200 day period. There is a discontinuous change to a higher mean RMST after the cathode etch, which then falls back to its previous average exponentially with a time constant of about 100 days. Re-examining Figure 6.10, this period appears to be accompanied by a rise in the event rates from the two MWPCs at the same time. The cause of the behaviour during this period is unknown. This is discussed further in Section 6.3.6.

It is noted that the 54% reduction in background from the central cathode acid etching procedure presented here, is significantly lower than that of previous analyses, in which a reduction by a factor of  $6.7 \pm 1.0$  was observed [152]. The reason for this discrepancy is the drastic change in the RMST of population 3 events caused by the central cathode etch. In previous analyses this resulted in the events not being recognised as part of the central cathode background population, leading to the conclusion that the background had been reduced by a much larger factor.

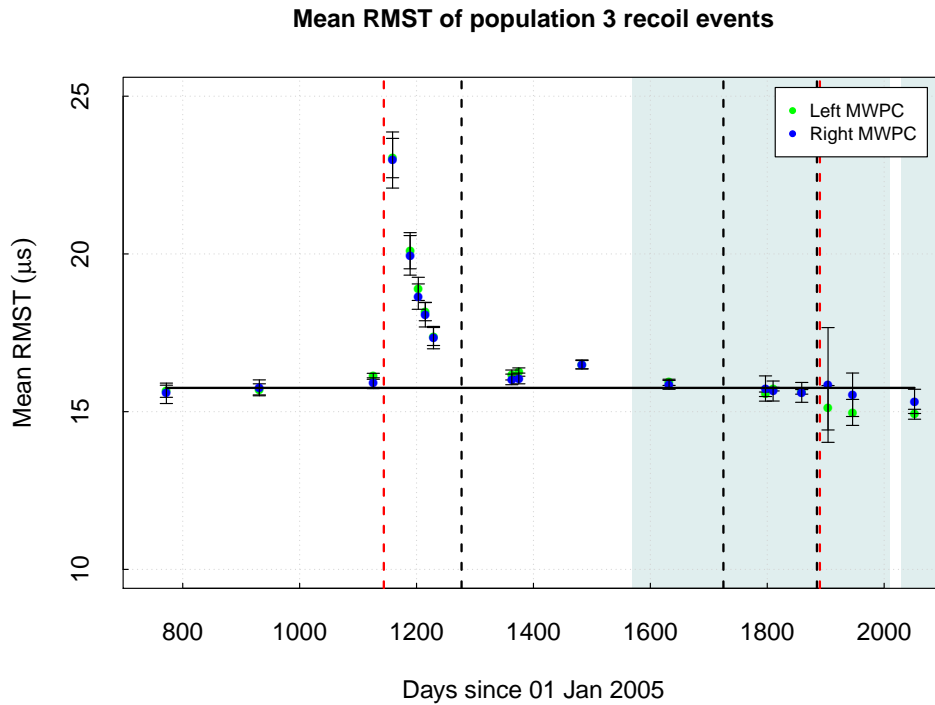


FIGURE 6.11: The mean RMST of population 3 recoil events. A dramatic deviation from the mean is seen directly after the acid etch of the central cathode plane. Vertical dashed lines indicate the actions described in Section 6.1.5. Blue shaded region is  $\text{CS}_2\text{-CF}_4$  data, unshaded region is pure  $\text{CS}_2$ .

### 6.3.2 Alpha-tagged recoil events

The RPR hypothesis predicts that radon progeny on the surface of the central cathode wires is responsible for both recoil-like events and alpha-tagged recoil events. The results in the previous section showed that the population 3 recoil-like events originate from the central cathode. It is therefore of interest to explore similarities between the population 3 recoil-like events and the alpha-tagged recoils.

**Mean RMST** — Figure 6.12 shows the mean RMST of alpha-tagged recoil events. A striking correlation can be seen between this plot and the mean RMST of the population 3 events shown in Figure 6.11. Although the reasons for the dramatic increase in mean RMST following the acid etch are unknown, the identical behaviour of the mean RMST in each population is clear evidence that population 3 recoil-like events and alpha-tagged recoils are from the same source.

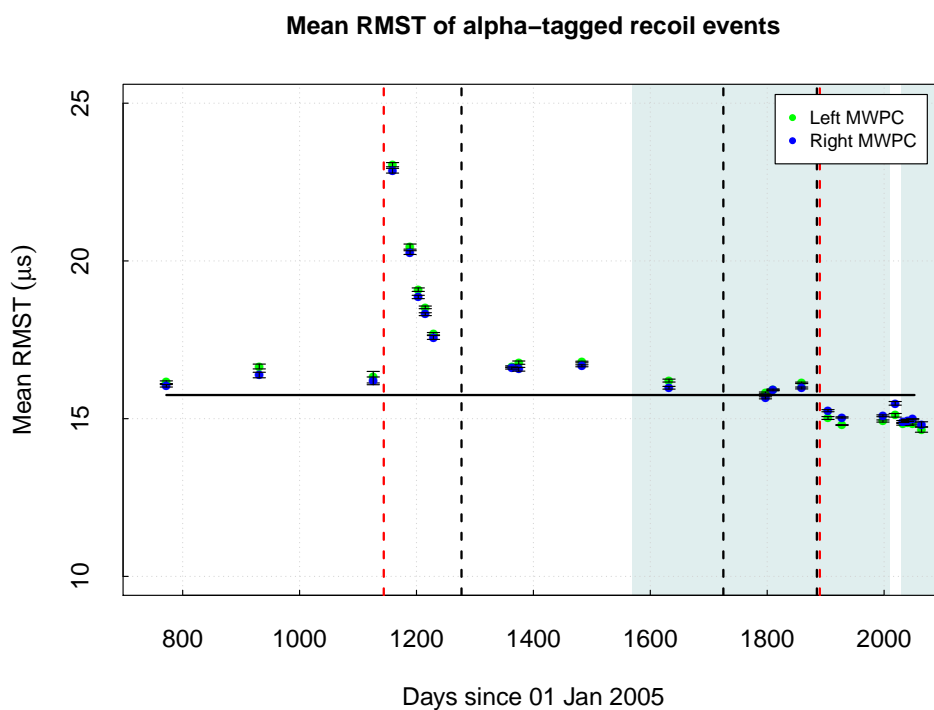


FIGURE 6.12: Mean RMST of the recoil component of alpha-tagged recoil events. The deviation following the acid etch is almost identical to that in the population 3 events, shown in Figure 6.11. Vertical dashed lines indicate the actions described in Section 6.1.5. Blue shaded region is  $\text{CS}_2\text{-CF}_4$  data, unshaded region is pure  $\text{CS}_2$ .

**Event rate** — Figure 6.13 shows the rate of alpha-tagged recoils over the 1200 day period of the long-term study. Although this rate does decrease somewhat at the cathode clean, it then rises again at the replacement with the thin film cathode. The alpha-tagged recoil rate increase on installation of the thin film cathode is consistent with the hypothesis that alphas are less likely to become confined in the thin film of the new cathode than in the wires of the previous cathode. Indeed, this is the reason for the replacement of the central cathode.

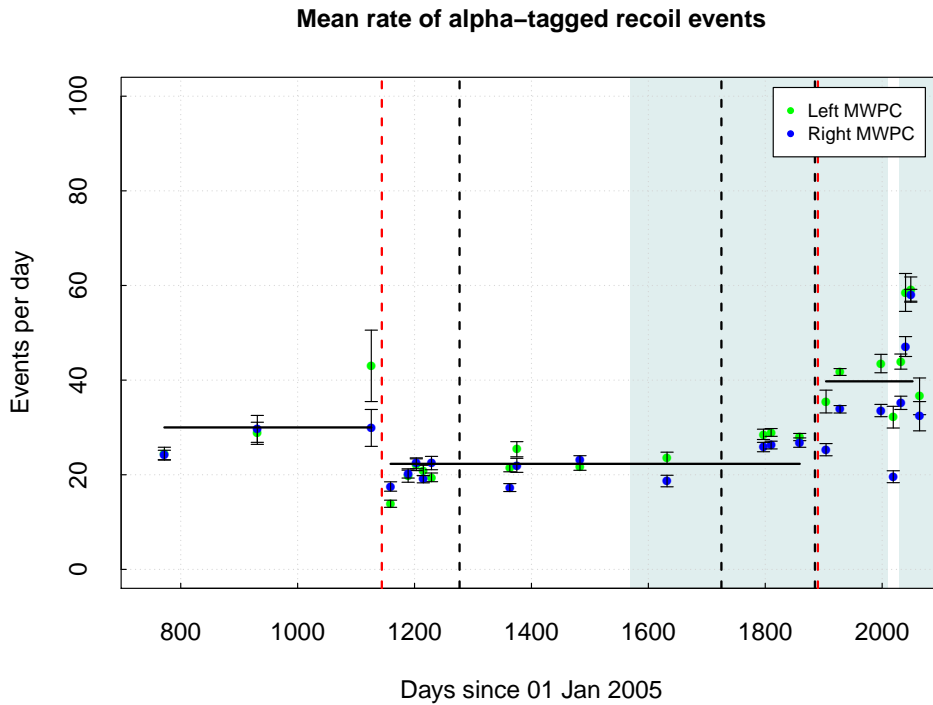


FIGURE 6.13: The mean event rate of alpha-tagged recoil events. The mean event rate shown by the black horizontal lines is  $30.8 \pm 2.8$  with the wire central cathode prior to etching,  $22.3 \pm 0.8$  with the wire central cathode after etching and  $39.7 \pm 2.9$  with the thin film cathode. Vertical dashed lines indicate the actions described in Section 6.1.5. Blue shaded region is  $\text{CS}_2\text{-CF}_4$  data, unshaded region is pure  $\text{CS}_2$ .

### 6.3.3 Population 2 recoil events

**Event rate** — Figure 6.14 shows the mean event rate of population 2 recoil-like events. The marked difference between the results for the left and right detectors immediately suggests that the MWPCs are the source of population 2 recoil-like events, since, of the possible background sources (gas mixture, central cathode, MWPCs), the only component not common to both drift chambers is the MWPC.

Recall that the red dashed vertical lines in Figure 6.14 at days 1134 and 1890 indicate the times of the cathode etch and the switch to the thin film cathode, respectively. The black lines at days 1277, 1725 and 1885 correspond respectively to the etching of both MWPCs in nitric acid, the substitution of the right-hand side MWPC and the subsequent replacement of the original right-hand side MWPC. It is thus seen, in Figure 6.14, that no significant change in the population 2 recoil-like events results from the central cathode etch, but a drop in rate by a factor of  $1.62 \pm 0.07$  ( $2.02 \pm 0.16$ ) in the left (right) detector is observed when the MWPC is cleaned. This lends further support to the hypothesis that the population 2 recoil-like events originate from contamination of

the MWPCs and again demonstrates the effectiveness of nitric acid etching for removal of radioactive contamination.

As alluded to in Section 6.1.5, on day 1140 the right MWPC was replaced with one taken from the DRIFT-II prototype detector above ground at Occidental College. In this configuration a factor  $3.4 \pm 0.2$  increase is seen in the rate of population 2 recoil events on the right MWPC, with no change in the number of population 2 events detected on the left side of the detector, and no increase in the rate of population 3 events. When the original MWPC is replaced, on day 1885, the rate reduces again. This is clear evidence that the population 2 recoil-like background is indeed due to the MWPC.

It is noted that the right detector has consistently higher rates in population 2 recoil events than the left detector. In the past, MWPC performance has been seen to depend on the history of the MWPC, including factors such as storage conditions and the wire used in the MWPC construction. It is, therefore, not surprising to see two similar MWPCs with different background contamination levels.

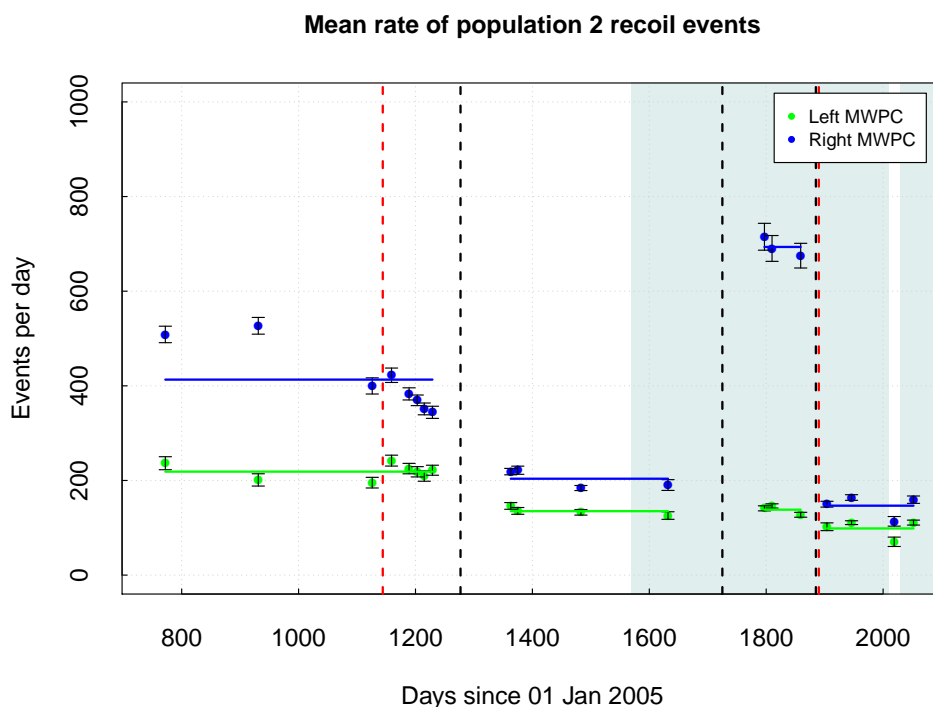


FIGURE 6.14: The mean event rate of population 2 recoil-like events. Event rate on the left (right) MWPC is  $219 \pm 6$  ( $413 \pm 25$ ) events per day before the MWPC etching,  $135 \pm 4$  ( $204 \pm 10$ ) events per day after the MWPC etching,  $138 \pm 6$  ( $693 \pm 12$ ) events per day with the replacement MWPC on the right and  $99 \pm 10$  ( $147 \pm 11$ ) events per day with the original MWPC replaced. Vertical dashed lines indicate the actions described in Section 6.1.5. Blue shaded region is  $\text{CS}_2\text{-CF}_4$  data, unshaded region is pure  $\text{CS}_2$ .

### 6.3.4 1MWPC alpha events

As discussed in Section 6.1.1, the background of alpha events fully contained within one side of the detector consists of alpha decays of radioactive nuclei suspended in the target gas, on the surface of the central cathode plane and on the surface of the MWPC wires.

The rates of one-sided alpha events are plotted in Figure 6.15. The large asymmetry between the left and the right sides of the detector immediately suggests that the MWPCs are also the dominant source of the 1MWPC alpha event background. Further evidence for this is the fact that the etching of the central cathode has no effect on the one-sided alpha population, and that no reduction is seen during the run starting on day 931, which was conducted with nine times the typical gas flow rate, drastically reducing any gas contamination. As with the population 2 recoil event rate, a particularly large increase (a factor  $2.9 \pm 0.2$ ) in the number of one-sided alpha events is observed on the right-hand side detector, between days 1725 and 1885 when the replacement MWPC was in use. This compares to a factor  $3.4 \pm 0.2$  increase seen in the population 2 recoil event rate. The large and approximately equal increase in relative rates of one-sided alpha events and population 2 recoil events strongly suggests that these two backgrounds are closely related. It is suggested here that the dominant source of both populations is the decay of radionuclides on the surface of the MWPC wires. When the alpha is oriented into the detector volume a one-sided alpha event is produced and when it is oriented into the MWPC wire the alpha is lost and the recoiling daughter nucleus produces a population 2 recoil event (Section 6.1.4).

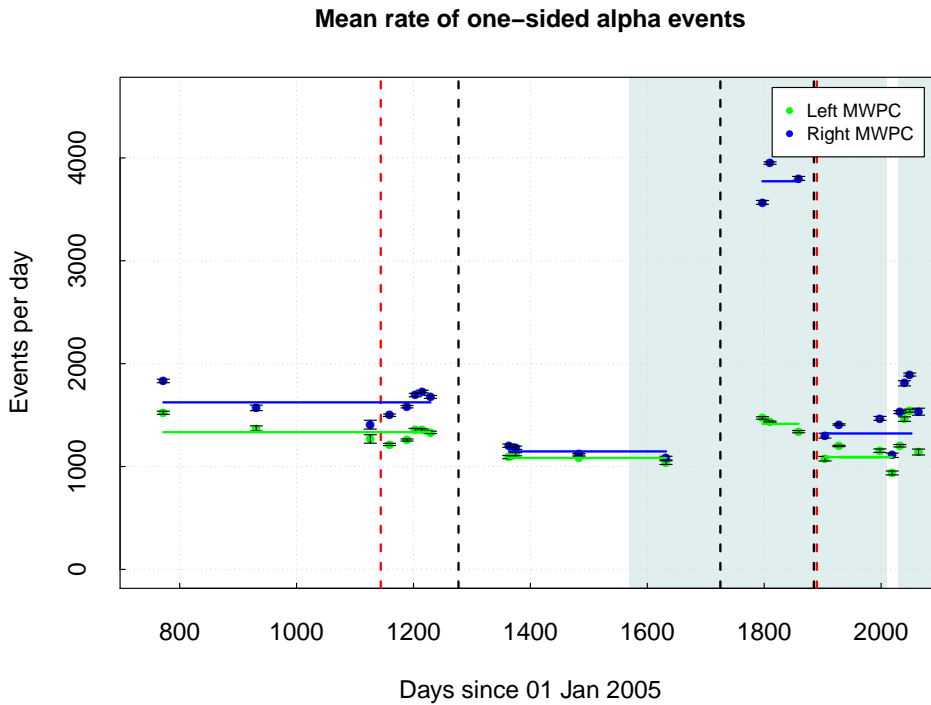


FIGURE 6.15: The mean event rate of 1MWPC alpha events. Event rate on the left (right) MWPC is  $1334 \pm 33$  ( $1624 \pm 48$ ) events per day before the MWPC etching,  $1084 \pm 17$  ( $1147 \pm 28$ ) events per day after the MWPC etching,  $1415 \pm 40$  ( $3773 \pm 111$ ) events per day with the replacement MWPC on the right and  $1092 \pm 57$  ( $1321 \pm 79$ ) events per day with the original MWPC replaced. Vertical dashed lines indicate the actions described in Section 6.1.5. Blue shaded region is  $\text{CS}_2$ - $\text{CF}_4$  data, unshaded region is pure  $\text{CS}_2$ .

### 6.3.5 GPCC events

The rate of gold-plated cathode-crossing (GPCC) events, as discussed in Section 6.1.1, provides a measure of the radon contamination of the gas. Figure 6.16 shows the measured rate of GPCCs where the mean rate over all runs is  $54 \pm 3$  events per day.

The dataset at day 931 has a particularly low rate of GPCC events of  $20 \pm 3$  events per day. This run was undertaken with a flow rate nine times faster than the typical flow rate. This has the effect of flushing out the radon contamination of the gas (from the emanation of internal components) before it has time to decay, resulting in a lower GPCC count. There is no measurable reduction in any other background population during the nine times flow run. This suggests that the recoil-like background events are dominated by long-lived contamination already on the surface of the detector wires, and not the prompt RPRs discussed in Section 6.1.4.

Conversely, when a flow rate of half the nominal value is used, for the two datasets on days 2040 to 2064, the rate of GPCCs is above base rate with a mean of  $70 \pm 1$  events per day, showing a build-up of radon contamination. The GPCC rate is also above the base rate from days 1725 to 1885, when the replacement MWPC was in use. This suggests that the MWPC, shown to have high levels of contamination on its wire surfaces, also caused contamination of the target gas.

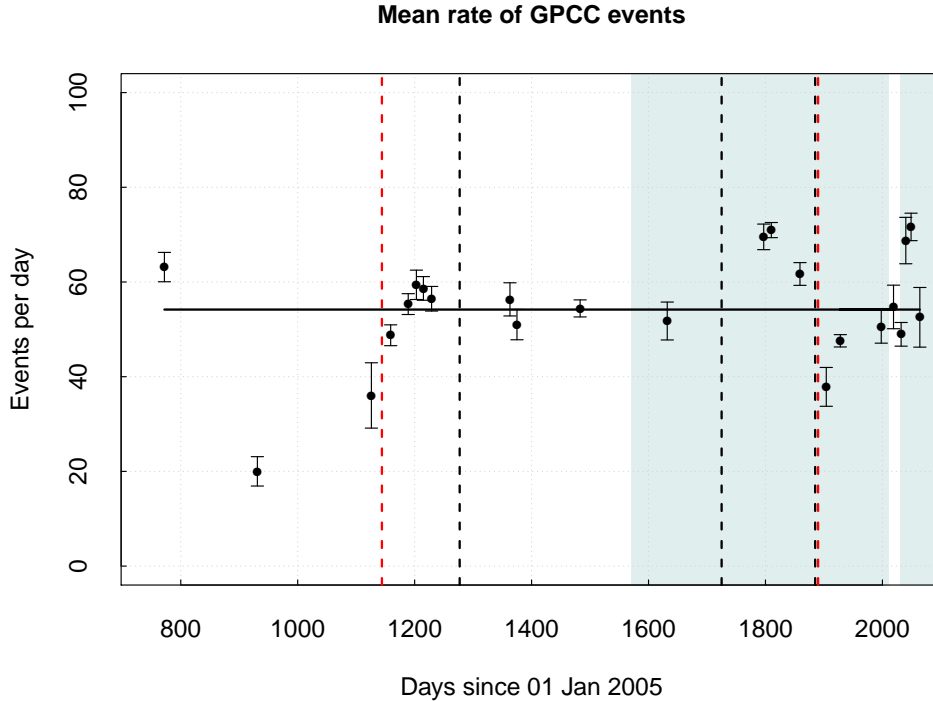


FIGURE 6.16: The mean event rate of GPCC events. Mean rate of  $54 \pm 3$  events per day is indicated by the horizontal black line. The dataset at day 772 is a run with nine times the regular flow rate in a reduced mean rate of  $20 \pm 3$  events per day is seen. The two high ones at the end are datasets with a half flow rate. Vertical dashed lines indicate the actions described in Section 6.1.5. Blue shaded region is  $\text{CS}_2\text{-CF}_4$  data, unshaded region is pure  $\text{CS}_2$ .

### 6.3.6 Further discussion of RMST effects in recoil-like events

The large deviation in the otherwise stable mean RMST of population 3 recoil events, caused by the etching of the central cathode, shown in Figure 6.11, is currently not well understood. There are two plausible explanations for the increase in the mean RMST, which corresponds to an increase in the measured  $z$  component of the track range. One is that recoil tracks are being extended as they drift from the central cathode to the MWPC readout plane by increased levels of diffusion in the 100 days following the cathode etch. The cathode frame consists of a large amount of acrylic, which was

submerged in dilute nitric acid during the etching procedure. This could be outgassing into the target volume, with the contaminants leading to higher diffusion. This seems unlikely, however, since no significant increase in the mean RMST of neutron calibration data is seen during this period. In addition, a similar etching of the MWPC planes, also constructed from acrylic, did not produce any change in the RMST of population 3 recoil events. An alternative, and currently favoured, interpretation of the increased RMST is an increased range of recoils from the central cathode in the 100 days following the central cathode etch. A possible explanation for this is that the wire surfaces are normally contaminated — potentially with carbon and sulphur compounds from the CS<sub>2</sub> target. Such contamination may reduce the range of recoiling radionuclide daughters on the cathode wire surface. The acid etch would remove these contaminants resulting in larger ranges, which would gradually decrease again as contamination of carbon and sulphur compounds re-accumulates on the cathode wires.

Figure 6.17 plots the mean RMST of population 2 recoil events over time. In the unshaded regions of the plot, corresponding to pure CS<sub>2</sub> runs, the RMST has a mean of  $8.3 \pm 0.1 \mu\text{s}$ . A considerably larger mean RMST, of  $11.1 \pm 0.1 \mu\text{s}$ , is observed during runs with a 30-10 CS<sub>2</sub>-CF<sub>4</sub> gas mixture, indicated by the blue shaded regions. The reason for this significant shift in RMST of MWPC-originating population 2 recoil-like events, while the cathode-originating population 3 recoil-like events remain unchanged is currently not understood and is a subject of ongoing investigation.

The two aforementioned RMST effects, though not well understood are significant for DRIFT. Figure 6.18 plots WIMP-search (blue) and neutron (red) data for datasets at day 1159 with a 40 Torr pure CS<sub>2</sub> target immediately after the cathode etch (Figure 6.18(a)), and at day 1810 with a 30-10 Torr CS<sub>2</sub>-CF<sub>4</sub> target after the cathode RMST effects had passed (Figure 6.18(b)). The plots demonstrate the significant advantage of the former configuration where the population 2 events are largely below the region in which neutron events are seen (and hence WIMP events would be expected), and the population 3 events are largely above this region. This is in comparison to the latter plot in which the population 2 and population 3 events show a large overlap with the neutron data, thus highly contaminating the expected WIMP signal region. Further investigation into the causes of these effects is therefore warranted, with the hope that it may be possible to control such effects, significantly reducing the backgrounds in the most sensitive region of DRIFT.

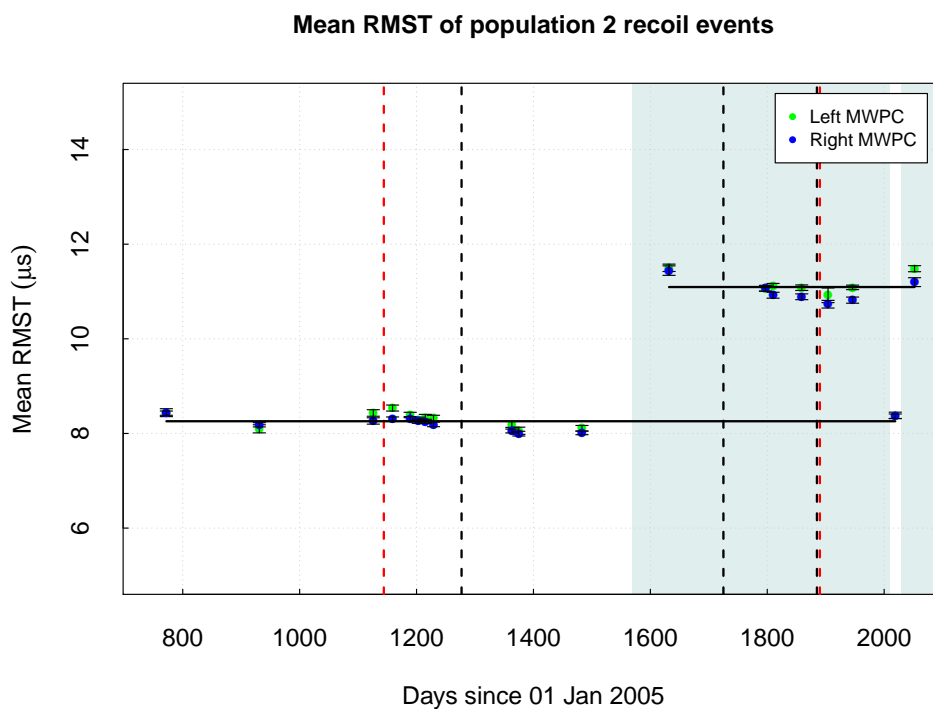
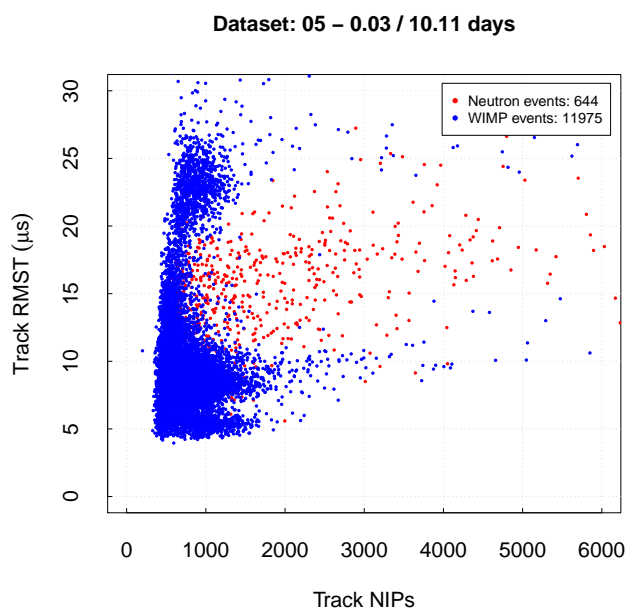
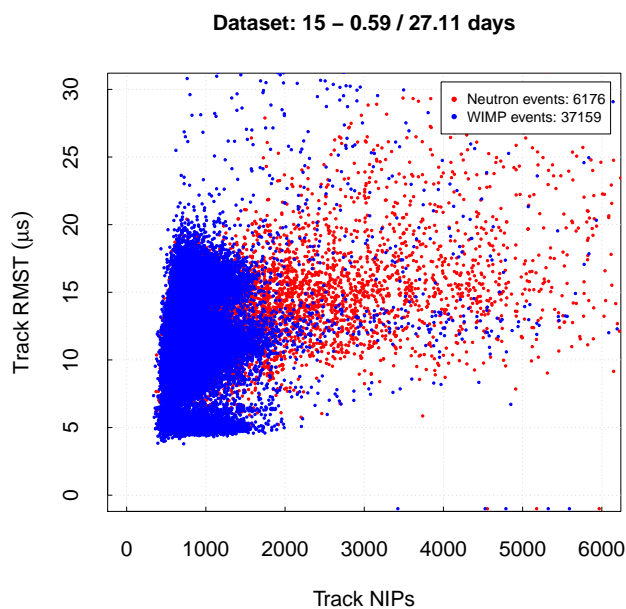


FIGURE 6.17: The mean RMST of population 2 recoil events. Mean rate during 40 Torr pure  $\text{CS}_2$  data is  $8.3 \pm 0.1 \mu\text{s}$ . Mean rate during 30-10 Torr  $\text{CS}_2\text{-CF}_4$  runs is  $11.1 \pm 0.1 \mu\text{s}$ . Vertical dashed lines indicate the actions described in Section 6.1.5. Blue shaded region is  $\text{CS}_2\text{-CF}_4$  data, unshaded region is pure  $\text{CS}_2$ .



- (a) 10.11 (0.03) days WIMP-search (neutron) data with 40 Torr pure  $\text{CS}_2$  from 05 March 2008 (day 1159) after etching of central cathode plane. Population 2 events have a low RMST due to the pure  $\text{CS}_2$  target gas and population 3 events have a high RMST due to the effect of the acid etch of the central cathode. A large separation is seen between the two populations leaving a large window for accepted neutron events.



- (b) 27.11 (0.59) days WIMP-search (neutron) data with 30-10 Torr  $\text{CS}_2\text{-CF}_4$  from 16 December 2009 (day 1810). Population 2 events have a high RMST due to the  $\text{CS}_2\text{-CF}_4$  target gas and population 3 events have the standard lower RMST. The two recoil-like background populations significantly overlap the neutron event population.

FIGURE 6.18: WIMP-search (blue) and neutron (red) data in the RMST vs. NIPs plane showing the effects of gas change and cathode cleaning on separation of event populations.

## 6.4 Conclusions

For the first time a consistent analysis of DRIFT data has been performed covering several years and many detector configurations. The results provide new insights into the nature and sources of the backgrounds in DRIFT-II. The dominant recoil-like backgrounds are found to be from four distinct populations. Strong evidence is presented that population 3 recoil events are recoils of decay daughters on the surface of the central cathode plane and population 2 events are recoils of decay daughters on the surface of the MWPC readout planes. In addition a WIMP analysis of  $^{55}\text{Fe}$  data has shown that population 4 recoil-like events are likely due to electron recoils from gamma-ray interactions.

The acid etching of the central cathode resulted in a reduction of population 3 recoil events, but of a smaller magnitude than previously determined — a discrepancy caused by the drastic change in RMST of the population 3 events. This new finding, although requiring further investigation, may have significant consequences for future background reduction. Finally, the replacement of the wire plane central cathode with a thin film plane has substantially reduced the rate of recoils in the population 3 class, which is an important advance.



## Chapter 7

# Dark matter results

This chapter discusses the use of DRIFT-IIId to search for elastic, spin-dependent collisions of WIMPs from the local halo with  $\text{CF}_4$  molecules in the target gas of the detector.

In Section 7.1 a simulation of DRIFT, written by collaborators, is described. As results from this simulation will be used to deduce the sensitivity of the search, the simulation is verified through various tests, which will be described. In Section 7.2, a non-blind analysis of 47.36 days of data from operation with a 30-10 Torr  $\text{CS}_2\text{-CF}_4$  gas mixture is presented, leading to a 90% confidence upper limit on the cross-section for spin-dependent interactions of halo WIMPs with fluorine nuclei. In Section 7.3, results from a blind analysis of a further 53.07 days of data from DRIFT-IIId, following installation of an improved low background thin film cathode, are presented. Finally, conclusions are drawn in Section 7.4.

### 7.1 The DRIFT-IIId event simulator

The simulation used for this work was first developed for the DRIFT-IIa detector [76] and has been further developed to model the present DRIFT-IIId detector [103]. This section presents a comparison between simulated neutron data and experimental neutron data from the DRIFT-IIId detector.

#### 7.1.1 The DRIFT-IIId detector simulation

The simulation, like DRIFT itself, uses neutrons as a prototype for WIMPs interacting with the target gas. The most recent version of this simulation creates the nuclear recoil data in GEANT4 [76], in which the detector geometry, surrounding environment and

$^{252}\text{Cf}$  are accurately modelled. The simulation produces the following parameters from neutron scatters in the detector target: kinetic energy transferred to the target molecule, the location of the interaction, and the recoil direction.

These values are passed to a separate, in-house simulation of the DRIFT-IIId detector [109]. The first stage of the detector simulation process is to convert the energy of the recoiling nucleus to the number of ionisation electrons liberated by it. This conversion uses the W-value of 25.2 eV for 30-10 Torr  $\text{CS}_2\text{-CF}_4$ , as measured by Pushkin et al. [107], and the energy dependent quenching factors calculated by Hitachi [108], with the assumptions stated in Section 3.3.1. The Stopping and Range of Ions in Matter (SRIM) simulation [111] is used to determine the range of the recoil in 30-10 Torr  $\text{CS}_2\text{-CF}_4$  from the nuclear recoil energy. The ionisation electrons are then distributed along a track of this range with the orientation determined by the GEANT4 simulation. Each ionisation electron is then given a random displacement in all three dimensions, governed by a Gaussian distribution of standard deviation  $\sigma_{\text{thermal}}$ , to mimic the thermal diffusion suffered by negative ions drifting from their initial location to the MWPC plane. This is based on measurements that the diffusion of negative  $\text{CS}_2$  ions in a 30-10 Torr  $\text{CS}_2\text{-CF}_4$  gas mixture is thermal, with an equivalent temperature of 375 K [112].

Each simulated ionisation electron lands on an anode wire determined by its  $x$  position in the fiducial volume and at a given time determined by its  $z$  position and the  $59.4 \text{ m s}^{-1}$  drift velocity of  $\text{CS}_2$  ions in 30-10 Torr  $\text{CS}_2\text{-CF}_4$ . As each ionisation electron reaches the anode wire the avalanche mechanism is simulated by multiplication with a random factor determined by a Polya distribution [114] with an average of 1000 — the approximate gain of the MWPC. The charge amplification process is then approximated by convolving each avalanche with a Gaussian of sigma of  $4 \mu\text{s}$  (the shaping time of the shaping amplifiers in DRIFT-IIId) and a height determined by the gain of the electronics chain.

Thus the nuclear recoil from the GEANT4 simulation is turned into a voltage trace on the eight anode fiducial lines of a simulated DRIFT-II MWPC. The grid signals are then approximated as induced pulses, by a Gaussian with a width of 0.245 cm determined by the geometry of the MWPC readouts [114]. Finally, an approximation of the electronic noise of the amplifiers is added to each line. The lines are then written to a standard DRIFT data file in the same format as data from the real DRIFT-IIId detector.

### 7.1.2 Simulated vs. experimental neutron data

The following list summarises the reduced data parameters derived from the hits identified in the raw event files, and their definitions, as discussed in Section 5.3. This will be useful in the following discussion of analysis of the reduced data.

- *anodeNips* — the sum of  $\Sigma$  from all anode fiducial line hits multiplied by the anode NIPs conversion factor, where  $\Sigma$  is the integral of voltage over the extent of the hit.
- *anodeSumNips* —  $\Sigma$  of the hit on the anode sum line multiplied by the anode NIPs conversion factor.
- *gridSumNips* —  $\Sigma$  of the hit on the grid sum line multiplied by the grid NIPs conversion factor.
- *anodeMinRisetime* — the minimum of all *risetime* values for hits on anode fiducial lines.
- *anodeMinFwhm* — the minimum of all *FFWHM* values for hits on anode fiducial lines.
- *anodeMaxSdCrossings* — the maximum *sdCrossings* value from all anode fiducial lines.
- *gridPhRatio* — the ratio of the largest to the second largest  $V_{\max}$  from all the grid fiducial lines, where  $V_{\max}$  is the maximum voltage sample of a given line.
- *anodeTrackNips* —  $\Sigma$  for the anode track line multiplied by the NIPs conversion factor, where the anode track line is a virtual line from the sum of all lines that contain hits.
- *anodeTrackRmst* — *RMST* for the anode track line.
- *anodeTrackSigma* — *FFWHM*/2.35 for the anode track line.

Validation of the simulated neutron data is undertaken by comparison to data from a routine exposure of the detector to a sealed  $^{252}\text{Cf}$  neutron source. The  $^{252}\text{Cf}$  used to calibrate DRIFT is contained within a cylindrical lead canister, of length 11 cm, diameter 5 cm and wall thickness of 1.3 cm, to shield gamma-rays emitted by the source. This lead canister is placed in a hollow 10 cm pipe through the hydrocarbon pellet shielding so that it sits directly on top of the stainless steel vacuum vessel, inline with the central cathode plane. A run of 0.82 days livetime was taken with the source in this position on 16 Feb 2010, at which time the neutron source had an activity of  $3700 \pm 200$  neutrons per second [76]. This geometry was modelled in the GEANT4 simulation.

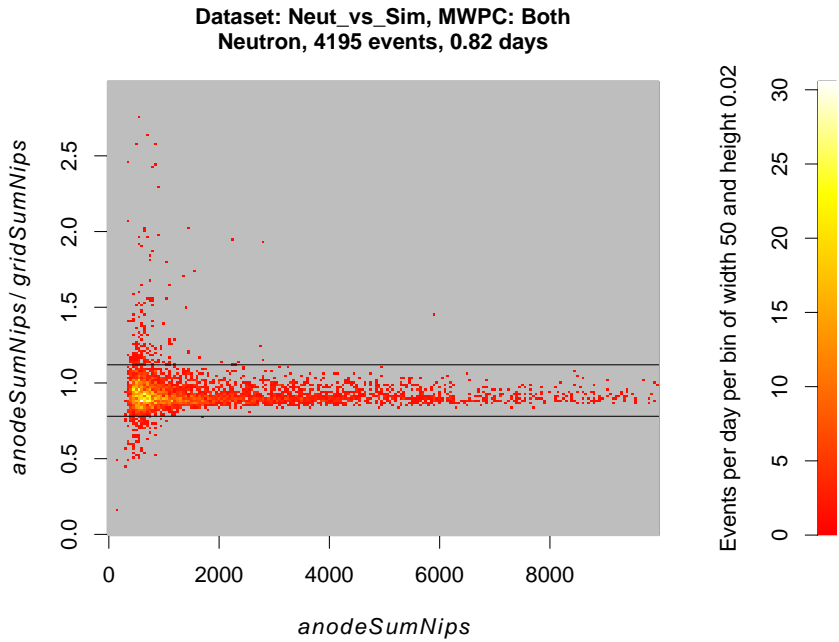
The simulated data, which is packaged in identical form to real DRIFT data, is processed by the analysis procedure up to the final stage cuts, described in Section 5.3. At this point the simulated data, consisting of 117055 event files from simulated nuclear recoils of all energies, is reduced to 23011 events. The vast majority of simulated events

being rejected by cut 1.1, as no line had sufficient charge density to cross the analysis thresholds. Since all of the events simulated are nuclear recoils however, very few are lost through the remaining stage 1 and stage 2 cuts, which are designed to remove only events that appear non-physical or not fully contained in the fiducial volume.

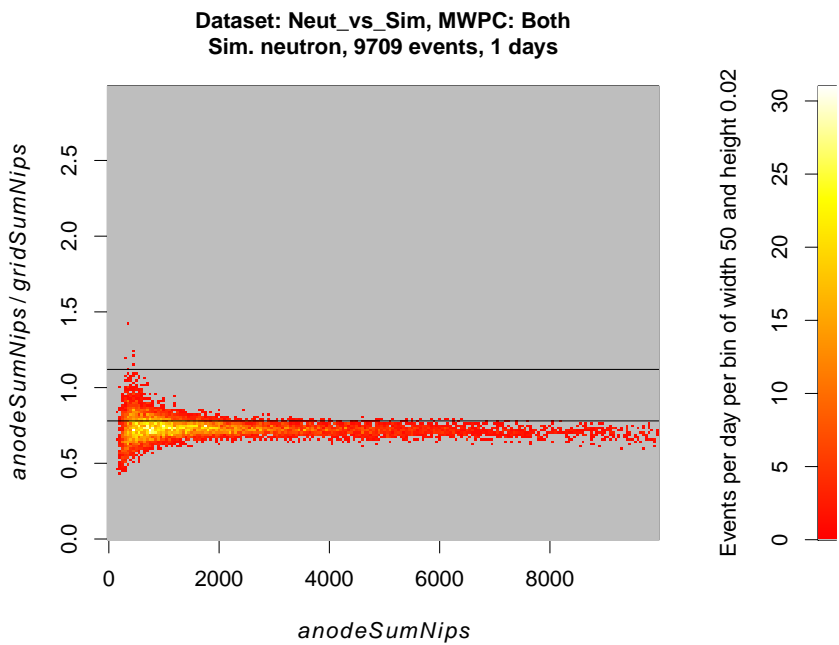
Ideally the simulated and real data would continue to be analysed identically, both undergoing the final stage cuts, which remove background events at the expense of recoil detection efficiency (see Section 5.3). However, the simulation is not entirely realistic in its treatment of the response of the detector to avalanching at the anode wires nor the response to the subsequent drifting of positive ions, a matter which needs addressing by the collaboration. Differences between the simulation output and the detector output are therefore described in the following sections, which motivate the omission of some cuts applied to real data in the analysis of the simulated data in some cases (Section 7.1.3), and correction factors in others (Section 7.1.4).

### 7.1.3 Grid signals and the anode sum line

Figure 7.1 plots the ratio of  $anodeSumNips$  to  $gridSumNips$  as a function of  $anodeSumNips$  for experimental data (Figure 7.1(a)) and simulated data (Figure 7.1(b)). The horizontal black lines indicate the cuts imposed on the real data by cut 3.1. Figure 7.2 similarly plots the ratio of  $anodeNips$  to  $anodeSumNips$  as a function of  $anodeSumNips$ , with horizontal black lines indicating the cuts imposed on the real data by cut 3.2. In both cases, there is a clear difference between simulated and experimental data.

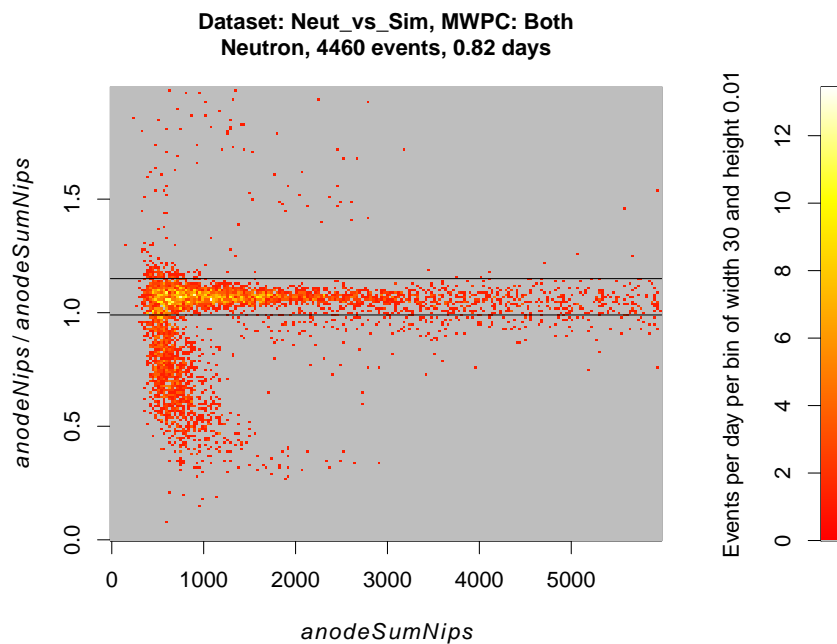


(a) Real data from a neutron exposure of 0.82 days livetime. Events outside of the horizontal black lines are removed by cut 3.1 (Section 5.4).

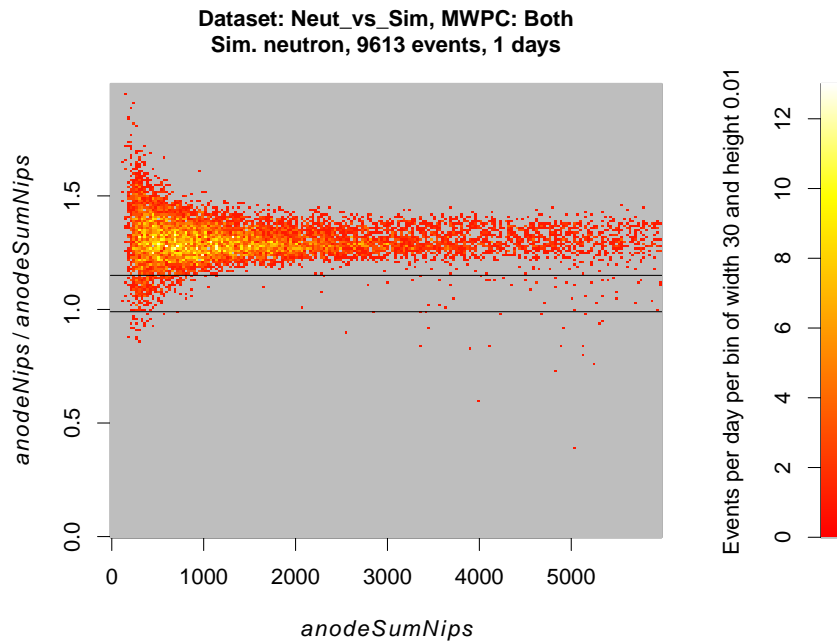


(b) Simulated nuclear recoil data. Horizontal black lines indicate region of cut 3.1, which is not applied to simulated data.

FIGURE 7.1: Plot of  $anodeSumNIPs$  to  $gridSumNIPs$  ratio as a function of  $anodeSumNIPs$  for simulated and real data.



- (a) Real data from a neutron exposure of 0.82 days livetime. Events below  $\sim 1000$  NIPs that spread down to low  $anodeNips / anodeSumNips$  values are the low  $dE/dz$  background events identified in Figure 5.19. Events outside of the horizontal black lines are removed by cut 3.2.



- (b) Simulated nuclear recoil data. Horizontal black lines indicate region of cut 3.2, which is not applied to simulated data.

FIGURE 7.2: Plot of  $anodeNIPs$  to  $anodeEventNips$  ratio as a function of  $anodeSumNIPs$  for simulated and real data.

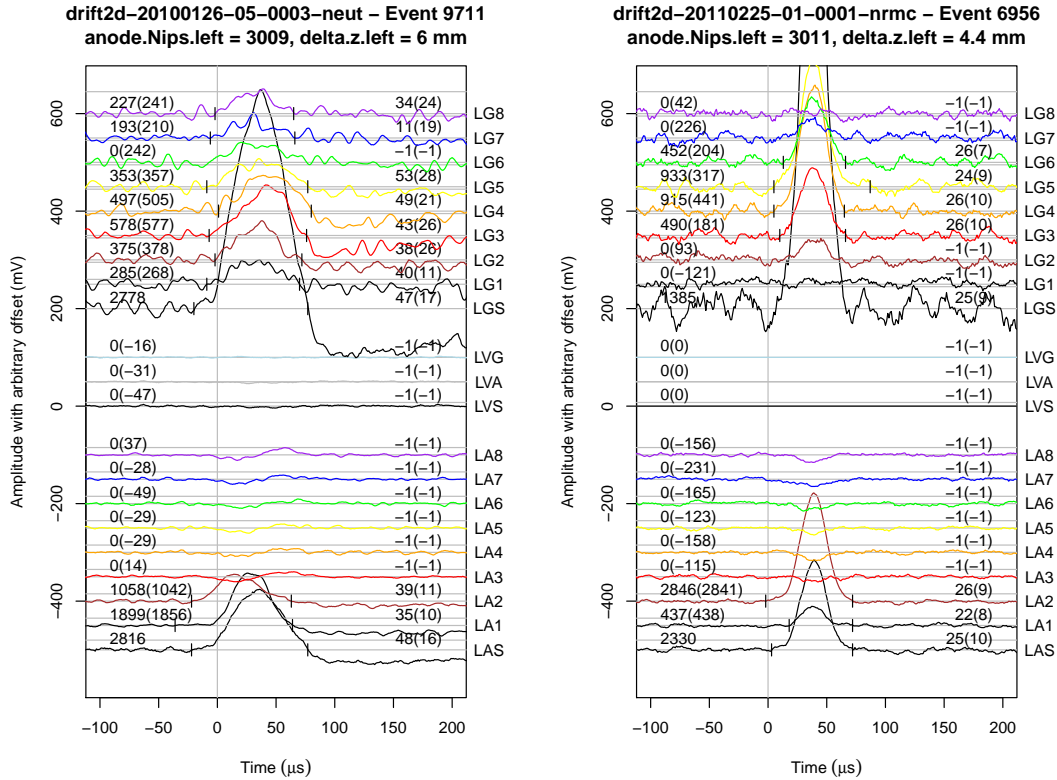
The underlying cause of these differences is believed to be the unrealistic treatment of the charge induced on neighbouring anode lines and grid wires after avalanching at the anode. Figure 7.3 shows the event display of a real (left) and simulated (right) 3000 NIP event. The gross features of the simulated event are seen to be similar to the real neutron event. There are, however, differences which result in the discrepancies in the event parameter distributions previously discussed. Both events contain hits on two anode fiducial lines and have an *anodeNips* value of  $\sim 3000$ . Although the pulse shapes of the hits on the anode lines look similar, a distinct difference is seen in the neighbouring anode lines without hits. In the real event (Figure 7.3(a)) bipolar cross-induced pulses can be seen. Their bipolar shape means that they have little overall effect on the area of the hit on the anode sum line. The result is an *anodeSumNips* value of 2816, only slightly lower than the *anodeNips* value of 3000. In the simulated data (Figure 7.3(b)), however, only the negative part of the induced pulse is simulated. Each line therefore has a considerable negative effect on the area of the pulse on the anode sum line resulting in an *anodeSumNips* value of 2330, significantly lower than the 3000 *anodeNips* value.

As discussed in Section 3.4, the signal on the grid lines is thought to consist of an induced component, which results in charge distribution across all grid lines, and a direct component, depositing charge on only the grid lines that receive positive ions. This effect is visible in the real event in Figure 7.3(a) where lines LG3 and LG4 appear to contain most of the direct charge, with pulses that occur later in time and have a different shape to the remaining lines. The purely Gaussian distribution used to produce the grid signals in the simulated event files, such as that in Figure 7.3(b), therefore leads to the discrepancy in the *anodeSumNips* to *gridSumNips* ratio observed in Figure 7.1. As would be expected from the suspected inaccuracies in the simulation of the grid signals, the *gridPhRatio* parameter distributions also do not match up well for real and simulated data.

Steps are underway within the collaboration to improve simulation of the cross-induced pulses on the anode lines and the signals on the grid lines. It is hoped that the present signal simulation will be replaced with a more accurate simulation that is able to model charge induction from drifting of positive ions within the MWPC geometry. The Garfield simulation package [153], appears to be a suitable tool for this purpose.

Without re-writing the simulation, there is no simple way to correct the simulated data so that the distributions of the *anodeNips/anodeSumNips*, *anodeSumNips/gridSumNips* and *gridPhRatio* parameters match the experimental data. The three cuts that rely on these parameters, namely cuts 3.1, 3.2 and 3.4 are therefore simply omitted in analysis of simulated data. The combined application of cuts 3.1, 3.2 and 3.4 to the experimental neutron exposure data, after application of all other cuts, results in a reduction in

accepted events above the 700 NIPs threshold, by a factor of 0.65. To account for the omission of cuts 3.1, 3.2 and 3.4 in the simulated data analysis, a correction factor of 0.65 is applied to the final event rate of simulated data. It is noted that the correction factor makes the assumption that, for the experimental data, all events rejected by cuts 3.1, 3.2 and 3.4 are genuine nuclear recoils. The factor 0.65 reduction to simulated data is therefore a very conservative estimate of the effects of the omitted cuts on neutron-induced nuclear recoil events.



- (a) Experimental nuclear recoil candidate. Cross-induced pulses are observed on anode lines LA3 to LA8 with an amplitude of  $\sim 15$  mV but with a bipolar profile. The contribution of these lines therefore has little effect on the pulse area of the hit on LAS (the sum of lines LA1 to LA8).  $anodeSumNips = 2816$ .
- (b) Simulated nuclear recoil. Cross-induced pulses are simulated of approximately correct negative magnitude but are unipolar. Induced signals on lines LA3 to LA8 therefore add to reduce the total pulse area of the hit on LAS.  $anodeSumNips = 2330$ .

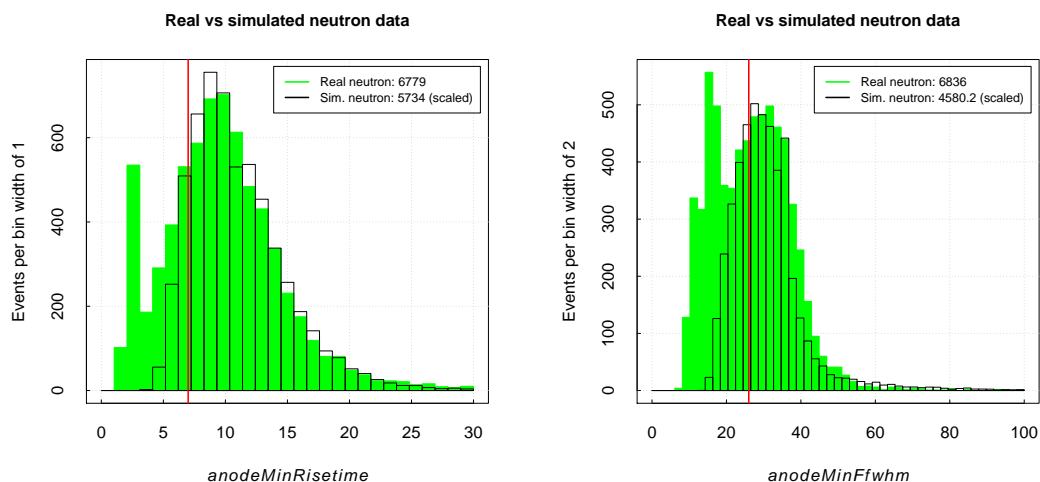
FIGURE 7.3: Comparison of experimental nuclear recoil candidate event to a simulated nuclear recoil event.

#### 7.1.4 Corrections to other simulated data parameters

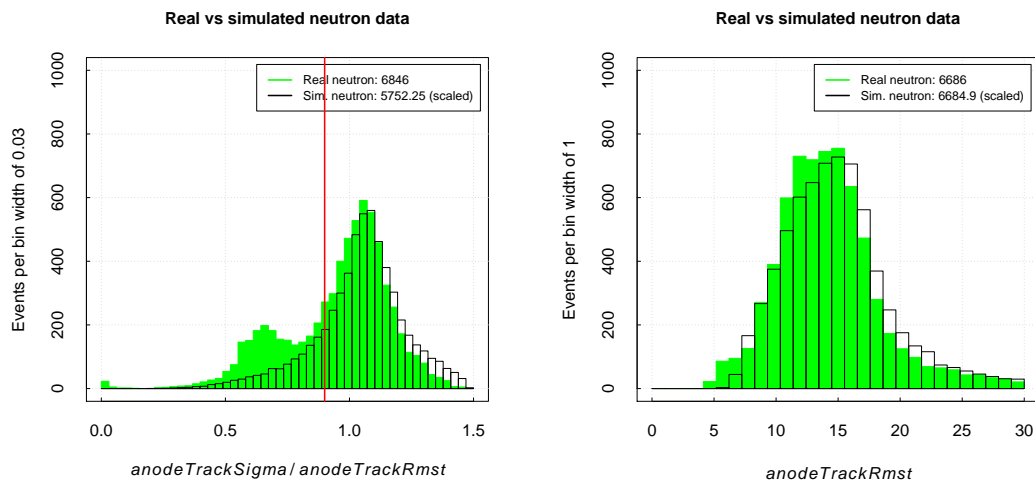
As discussed in Section 7.1.3, the shapes of anode and grid pulses on individual lines in the simulation do not perfectly match the equivalent signals in the experimental data. These mismatches were compensated for by applying physically motivated corrections

to certain reduced parameters from the simulated data files. First,  $2 \mu\text{s}$  was added to *anodeMinRisetime*, a correction derived from fits to the peak of this parameter in the simulated vs. real data. Similarly,  $7 \mu\text{s}$  was added to *anodeMinFwhm* in the simulated data using the same method. In the case of the parameter *anodeTrackRmst*, an energy dependent correction was made to the simulated data of  $2.85 + 0.0004 \times \text{anodeTrackNips}$ . This correction was made by making a scatter plot of the *anodeTrackNips* parameter for simulated data vs. experimental data, and finding a straight line that related the two.

Figure 7.4 shows a comparison of real vs. simulated data for the four remaining pulse shape parameters used in this analysis for cuts and characterisation of events. In each case the real and simulated data have undergone the same parameterisation and analysis procedure, with the exceptions of the omitted cuts detailed in Section 7.1.3 and the correction factors described above. Figures 7.4(a), 7.4(b) and 7.4(c) plot the parameters *anodeMinRisetime*, *anodeMinFwhm* and the ratio of *anodeTrackSigma* to *anodeTrackRmst* respectively. In each case a vertical red line indicates the cut value, below which all events are cut. In each of these plots there are differences between the real and simulated data below this value. This is expected, since events in the real data below the red line are not nuclear recoils, and are therefore not present in the nuclear recoil simulations. The event distributions above the red line are all reasonable fits to the real data, validating the combination of the DRIFT detector simulation and correction factors discussed above.



(a) *anodeMinRisetime*. Simulated data has a  $+2\ \mu\text{s}$  correction. (b) *anodeMinFwhm*. Simulated data has a  $+7\ \mu\text{s}$  correction.

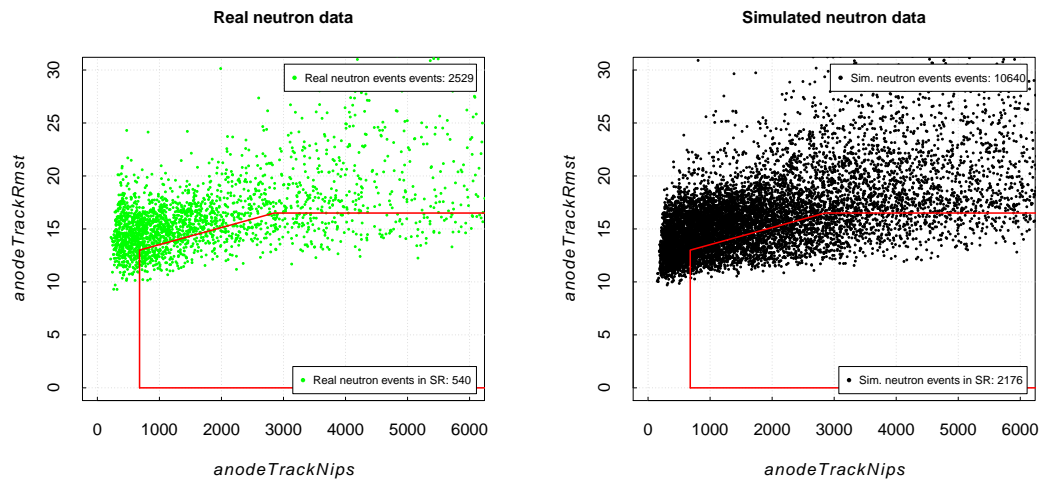


(c) *anodeTrackSigma / anodeTrackRmst*. (d) *anodeTrackRmst*. Simulated data has a  $2.85 + 0.0004 \times \text{anodeTrackNips}$  correction.

FIGURE 7.4: Comparison of anode pulse shape parameter distributions for real (green) and simulated (black) data. Neutron data has been scaled by an arbitrary number to visually compare distribution with the real data. For each parameter events below the red vertical line are cut (for both real and simulated data).

### 7.1.5 Simulated vs. experimental data in the RMST vs. NIPs plane

After reduction and cuts, real and simulated data are plotted in the RMST vs. NIPS plane. Figure 7.5 shows the results for an experimental  $^{252}\text{Cf}$  neutron source exposure of 0.82 days (Figure 7.5(a)) and from a simulation of neutron interactions with the same geometry (Figure 7.5(b)). Figure 7.6 shows the same data in histogram form, which shows a reasonable match between the real and simulated neutron-induced nuclear recoil data distributions. The signal acceptance region, chosen in Section 5.4, is illustrated by the red box. From the experimental data,  $21.4 \pm 1.0\%$  of events are in this acceptance region, compared to  $20.5 \pm 0.5\%$  of simulated events. The agreement shows that the simulation produces an event distribution in the NIPs vs. RMST plane that closely matches experimental data from a  $^{252}\text{Cf}$  exposure. Since neutron-induced nuclear recoils from a  $^{252}\text{Cf}$  source are a good approximation of nuclear recoils from massive WIMPs [136], this implies that the simulated detector will also produce a reasonable estimate of the distribution of events from simulated WIMP interactions. This in turn will allow an estimate of the total efficiency of the DRIFT detector, including the entire analysis process and effective signal region, to WIMPs.



- (a) Data from neutron exposure of 0.82 days live- (b) Data from 117055 simulated neutron events.  
time. 2529 events pass all cuts, of which 540 10640 events pass all cuts, of which 2176  
( $21.4 \pm 1.0\%$ ) are in the signal region. ( $20.5 \pm 0.5\%$ ) are in the signal region.

FIGURE 7.5: Comparison of real and simulated data in the RMST vs. RMST plane.

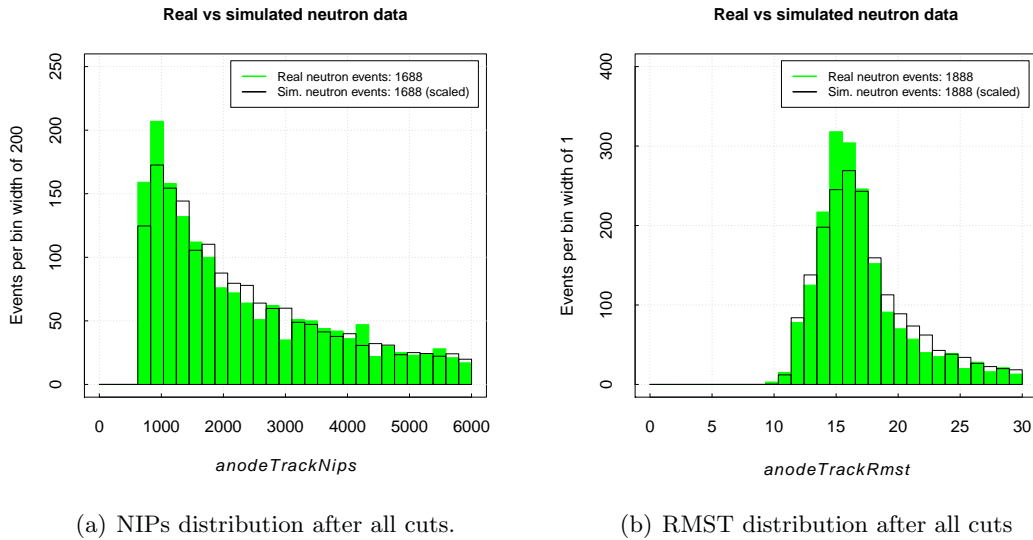


FIGURE 7.6: Comparison of real (green) and simulated (black) neutron data. Data is the same as in Figure 7.5 and shows a good match between real and simulated neutron data distributions.

## 7.2 A non-blind limit on the spin-dependent WIMP-proton cross-section

The derivation of a non-blind limit on the spin-dependent WIMP-proton cross-section begins with the concluding plot of Chapter 5. That is, 47.36 days of WIMP-search data that has been parameterised, reduced to only nuclear recoil candidates, and plotted in the RMST vs. NIPs plane. An exclusion region has been chosen to maximise the efficiency for detection of nuclear recoils from neutron runs, but has zero signal in the WIMP-search data. Effectively, this means the assumption of no signal. Blinded searches making no such assumption are discussed in Section 7.3.

The efficiency for detecting WIMPs during this zero-signal WIMP-search data period must be calculated. The agreement between real and simulated neutron data, presented in the previous section, shows that the DRIFT detector simulation is adequate for converting simulated nuclear recoil events into realistic DRIFT event data files. Therefore, in this section the simulated neutron-induced nuclear recoils are replaced with simulated WIMP-induced nuclear recoils. The analysis of ‘data’ from simulated WIMP events results in an estimate of the efficiency of DRIFT-II<sub>d</sub>, including the whole analysis chain, to WIMP-induced nuclear recoils. Combining the WIMP detection efficiency with the null signal from 47.36 days of experimental data results in limits on the SD WIMP-proton cross-section.

The WIMP induced nuclear-recoils are generated using the WIMP halo characteristics detailed in Section 1.3.2, i.e., a Maxwell-Boltzmann velocity distribution with  $v_0 = 230 \text{ km s}^{-1}$ ,  $v_E = 244 \text{ km s}^{-1}$  and  $v_{\text{esc}} = 600 \text{ km s}^{-1}$ , and a local halo density of  $\rho_0 = 0.3 \text{ GeV c}^{-2} \text{ cm}^{-3}$ . To determine the response of the detector to WIMPs of all masses, the simulation is repeated 31 times, each with a different WIMP mass in the range  $11 \text{ GeV c}^{-2}$  to  $10000 \text{ GeV c}^{-2}$ . 9000 WIMP-induced nuclear recoils are produced for each WIMP mass. The nuclear recoil information from each simulation is converted to standard DRIFT event files, as described in Section 7.1.1.

### 7.2.1 DRIFT-IIId detection efficiency for 100 GeV WIMPs

Each assumed WIMP mass is analysed separately. The 100 GeV WIMP mass data file is considered here to demonstrate the process.

The simulated data file, containing 9000 100 GeV WIMP-induced nuclear recoil events, undergoes the same analysis process as the simulated nuclear recoils, described in the previous section. This results in the NIPs vs. RMST plot shown in Figure 7.7. The plot shows that from 9000 simulated WIMP-induced nuclear recoils in the detector volume, 2407 produce events that cross the analysis thresholds and pass all the analysis cuts, and 461 of these lie in the acceptance box. Reducing this by a factor 0.65 to account for the cuts omitted from the simulated data analysis, as derived in Section 7.1.3, this gives 300 out of 9000 simulated events, giving an efficiency to 100 GeV WIMP-induced nuclear recoils of 3.33%.

The total rate of 100 GeV WIMP-nucleus interactions expected in the DRIFT-IIId fiducial volume (calculated using the equations discussed in Section 2.1) is 361 events per year, for an arbitrarily chosen WIMP-nucleus cross-section of  $\sigma_{WN} = 100 \text{ pb}$ .

Given detection of zero events in the acceptance box, and assuming zero leakage from the cuts detailed in Section 5.3, it is 90% probable that the box would on average contain less than 2.44 events [154]. Therefore, at 90% confidence, any WIMP model which would place more than 2.44 WIMP events in the acceptance box during 47.36 days livetime, or 18.82 events per year, can be excluded. With an assumed WIMP-nucleus cross-section of 100 pb, the number of events expected in the acceptance box is 361 times the efficiency of the box at detecting 100 GeV WIMPs (0.0333). Hence 12.02 events are expected in the box per year. The arbitrarily chosen WIMP-nucleus cross-section of 100 pb is then scaled by the ratio of the actual 90% confidence upper limit on the number of events in our box per year (18.82) divided by the expected number of events that a WIMP-nucleus cross-section of 100 pb predicts in the box (12.02), yielding a 90% confidence upper limit on the WIMP-nucleus cross section of 157 pb. Finally, to enable

comparison with other experiments, this can be scaled to a target independent WIMP-proton cross-section. Using Equation 2.59 and the enhancement factor of Fluorine of  $(C_N^{SD(p)})/(C_p^{SD}) = 0.778$  (see Table 4.1), this results in an upper limit of  $\sigma_{Wp}^{SD} = 0.75$  pb for a 100 GeV WIMP.

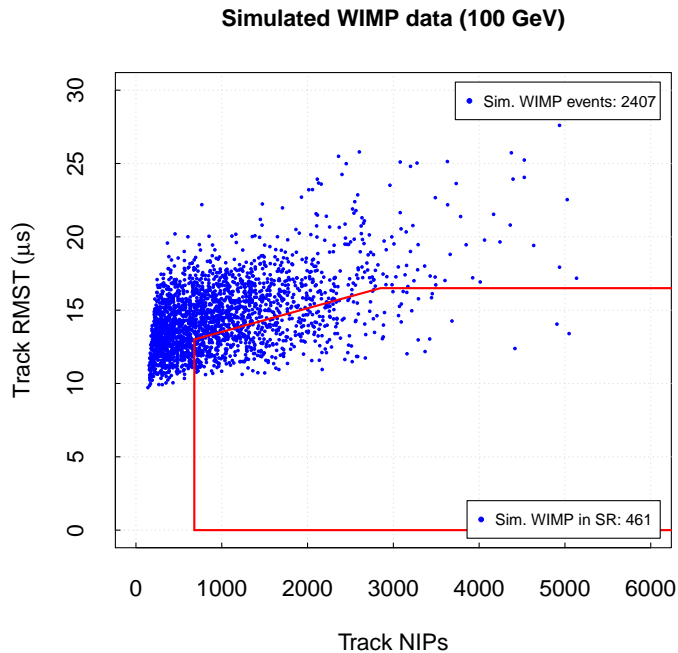


FIGURE 7.7: Simulated fluorine recoils from 100 GeV WIMP interactions. Of 9000 simulated events 2407 cross the analysis thresholds and pass all cuts, of which 461 are in the accepted signal region.

### 7.2.2 Spin-dependent WIMP-proton limit plot

The procedure detailed in Section 7.2.1 for 100 GeV WIMP interactions is repeated for the 31 simulated WIMP data files, each of which contains 9000 recoils from a WIMP of different mass. Table 7.1 shows, for a selection of WIMP masses: the total number of fluorine recoils expected in DRIFT-IIId in one year, the number of simulated WIMP events that pass all cuts and are in the signal region, and the corresponding detection efficiency. These values, with 24 other WIMP masses in-between, are used to produce the DRIFT limit plot, shown in Figure 7.8.

Also plotted in Figure 7.8 are leading upper limits on the SD WIMP-proton cross-section from other experiments, which are described briefly below:

WIMP mass (GeV)	Rate (no. per year)	No. in signal region	detection efficiency (%)
10000	3.6	705	$5.09 \pm 0.19$
1000	36.1	714	$5.16 \pm 0.19$
500	72.3	500	$4.68 \pm 0.18$
100	361.5	461	$3.33 \pm 0.15$
50	723.0	273	$1.97 \pm 0.12$
20	1807.5	59	$0.36 \pm 0.05$
11	3286.4	2	$0.014 \pm 0.010$

TABLE 7.1: Simulated WIMP statistics. Including the estimated total WIMP interaction event rate, The number of the 9000 simulated events that pass all analysis cuts and are in the NIPs vs. RMST acceptance region, and the resulting efficiency, taking into account the factor 0.65 reduction discussed in Section 7.1.2.

**NAIAD** — The NaI Advanced Detector (NAIAD) experiment ran at the Boulby Underground Laboratory from 2000 to 2003. The detector consisted of 7 NaI(Tl) scintillator crystals, each coupled to two 5 inch diameter low background photomultiplier tubes (PMTs) via light guides. The PMTs detected scintillation light from particle interactions in the crystals, where pulse shape discrimination was used to statistically separate neutron recoils from electron recoils. The experiment ran for a total exposure of 16399 kg days [155], with both  $^{23}\text{Na}$  and  $^{127}\text{I}$  contributing to the SD WIMP-proton sensitivity. The relatively poor limit from such a large exposure, in comparison to DRIFT, is due to the inability to separate electron recoils from nuclear recoils on an event-by-event basis, and demonstrates the power of efficient electron discrimination.

**KIMs** — The Korea Invisible Mass Search (KIMS) experiment is a scintillation detection experiment using low background CsI(Tl) crystals. In comparison to NaI(Tl), CsI(Tl) is more easily obtained in large crystals and has better pulse shape discrimination properties, but suffers from intrinsic backgrounds from, e.g.  $^{137}\text{Cs}$ , which must be well understood. The present KIMs detector consists of four 8.7 kg low background CsI(Tl) crystals with PMTs mounted at both ends of each crystal. As with NAIAD, pulse shape discrimination is used to statistically separate nuclear recoils from electron recoils, so long exposures are required for competitive limits, despite a large target mass of spin-dependent sensitive isotopes  $^{33}\text{Cs}$  and  $^{127}\text{I}$ . The KIMs limit shown in Figure 7.8 is from an exposure of 3409 kg days [130].

**PICASSO** — The Project in Canada to Search for Super-Symmetric Objects (PICASSO) experiment is based on the classic bubble chamber technique developed during the 1950s [156], in which ionising radiation can be detected in a superheated liquid target by triggering a phase transition. In contrast to traditional bubble chambers, which use a bulk target mass, the PICASSO detector target consists of superheated droplets

of  $\text{C}_4\text{F}_{10}$ , approximately 50 to 100  $\mu\text{m}$  in diameter, suspended in an elastic polymer. The temperature and pressure are chosen such that a WIMP interaction in a droplet may trigger a phase transition resulting in an acoustic pulse, which is measured by nine piezoelectric sensors. After an interaction the elastic polymer is compressed, returning the  $\text{C}_4\text{F}_{10}$  to its superheated liquid state. Since a relatively high  $dE/dx$  is required to trigger this process the detector can be made inherently insensitive to electron recoils, whilst retaining sensitivity to WIMP-induced nuclear recoils. As in DRIFT,  $^{19}\text{F}$  provides good sensitivity to spin dependent WIMP-proton interactions. The latest limit from PICASSO, shown in Figure 7.8, is from an exposure of  $13.75 \pm 0.48$  kg days [129].

**COUPP** — The Chicagoland Observatory for Underground Particle Physics (COUPP) experiment uses a more traditional bubble chamber technique with a bulk superheated liquid target. The target is contained in a synthetic fused silica bell jar, found to minimise surface nucleations. Four piezoelectric sensors attached to the bell jar record acoustic emissions from bubble nucleations. The acoustic signal is used to trigger two CMOS cameras, which photograph the formed bubbles at a rate of 100 frames per second. The spatial coordinates of bubbles, and therefore the particle interactions, within the chamber can be reconstructed from these images. Following a triggered event the target is compressed to recondense the  $\text{CF}_3\text{I}$  vapour. The COUPP experiment operated a 3.5 kg liquid  $\text{CF}_3\text{I}$  target for a total exposure of 28.1 kg days [126], obtaining the limits shown in Figure 7.8 — currently the most stringent limits on spin-dependent WIMP-proton interaction cross-sections.

The DRIFT limit presented here corresponds to an exposure of 1.75 kg days of  $\text{CF}_4$ . The competitive result with a relatively low mass is a demonstration of the powerful discrimination of the DRIFT detectors. It is also noted that other experimental limits shown here are from solid and liquid targets that do not have directional sensitivity. The most stringent limits set by other directionally sensitive experiments are orders of magnitude higher than the limit presented here. DMTPC have produced a limit on the SD WIMP-proton cross-section with a minimum of 2000 pb for a  $115 \text{ GeV } c^{-2}$  WIMP from 0.0357 kg days exposure [87], while NEWAGE have a limit with a minimum of 5400 pb for  $150 \text{ GeV } c^{-2}$  WIMPs from an exposure of 0.524 kg days [84]. While the directionality of DRIFT has not been utilised in this analysis, it has not been compromised and this result is the first competitive limit on WIMP interaction cross-sections from a directionally sensitive dark matter detector.

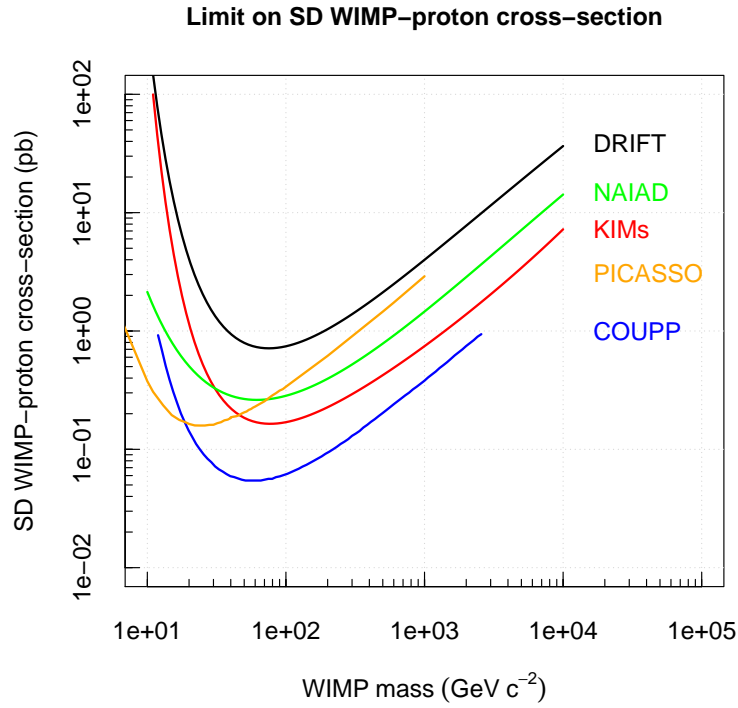


FIGURE 7.8: 90% C.L. upper limits on the spin-dependent WIMP-proton cross-section from a non-blind analysis of 47.36 days of DRIFT-II<sub>d</sub> data with a 30-10 Torr CS<sub>2</sub>-CF<sub>4</sub> target. Also plotted are upper limits from KIMs [130], NAIAD [155], PICASSO [129], and COUPP [126]. See text for details.

### 7.3 A first blind search for WIMP-proton interactions in DRIFT-II<sub>d</sub>

To ensure impartiality in analysis techniques and development of cuts it is customary for dark matter experiments to perform blind analyses. That is, deciding on conditions for accepted WIMP signals based on a subset of non-blind data then analysing the blinded data with the fixed analysis configuration to reveal the number of WIMP events detected. This process is called ‘opening the box’.

The limit presented in the previous section was from a non-blind analysis, in which the cuts were chosen based on the whole dataset and then a signal region was selected to exclude all events. In this section a blind analysis is performed from a total of 64.75 days of data. The detector configuration is the same except that the wire plane central cathode is replaced with a thin film central cathode, which was shown in Section 6.3 to result in a significant decreased in the number of WIMP-mimicking background events.

From the 64.75 days of data 11.68 days was selected as non-blind. The non-blind data includes the first 6.65 days of livetime with the thin film cathode, which was analysed

initially to ensure stability with the new set-up, and  $\sim 2$  hours per day over the following 55 days of livetime. This data is selected to be representative sample of the entire dataset, that will be used to define the WIMP signal acceptance region. The remaining 53.07 days of data were kept blind, only to be analysed once all the analysis techniques and the signal region have been fixed.

### 7.3.1 Setting parameters for the blind WIMP search

Figure 7.9 shows the NIPs vs. RMST plot for the 11.7 days of non-blind data from the WIMP-search run with the new thin film cathode. The box in this plot is the search region employed in the previously described non-blind search with the wire cathode.

The first observation from this dataset, compared to the wire cathode dataset (Figure 5.4.4), is that the large population of events around  $15 \mu\text{s}$  RMST and under 2000 NIPs, is largely eliminated. Figure 7.10 shows the alpha-tagged recoil events for this dataset. The distribution of alpha-tagged recoil events from the thin film cathode data closely match the background events observed during the wire cathode data, strongly indicating, as discussed in Section 6.1.5, that events which previously produced nuclear recoil events with the alpha hidden in the central cathode wires, now result in alpha-tagged recoils, due to the transparency to alphas of the new thin film cathode.

The second observation from the non-blind thin film cathode data in Figure 7.9 is that the indicated acceptance region, which was free of background for 47.36 days of WIMP-search data with the previous wire cathode configuration, contains 11 events for the 11.68 days of thin film cathode data. This indicates a change in the detector background with the installation of the thin film cathode. Ten of the events in the signal region are at high NIPs values, with an RMST of  $\sim 15 \mu\text{s}$ . This new background is suspected to be caused by decays on or within the new central cathode, which have a different form due to the geometry of the thin film cathode compared to the wire plane cathode. The signal region for the blind thin film cathode data needs to be adjusted to remove this new background, which is the subject of the next section.

A third observation is the existence of a single event from the non-blind WIMP-search runs that is inconsistent with the identified background populations, and is well within the signal region. The event, which has a NIPs value of 1450 and an RMST of  $13.24 \mu\text{s}$ , comfortably passes all WIMP cuts and does not display any unusual characteristics. Because of its position in relation to the expected neutron spectrum it is extremely unlikely to be a nuclear recoil from an ambient neutron interaction. For now, it is assumed that the anomalous event is not part of any known background, and it is

disregarded in consideration of the signal region. This will be discussed further in Section 7.3.3.

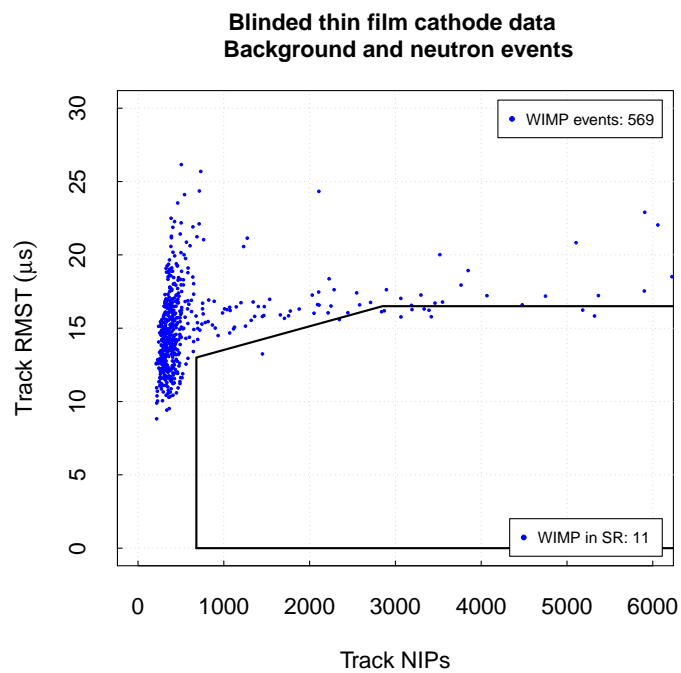


FIGURE 7.9: 11.68 days of non-blind thin film cathode WIMP-search data in RMST vs. NIPs plane. The illustrated accepted signal region is that from the previously described non-blind analysis of wire cathode data. The signal region, which was empty for 47.36 days of wire cathode data, contains 11 events.

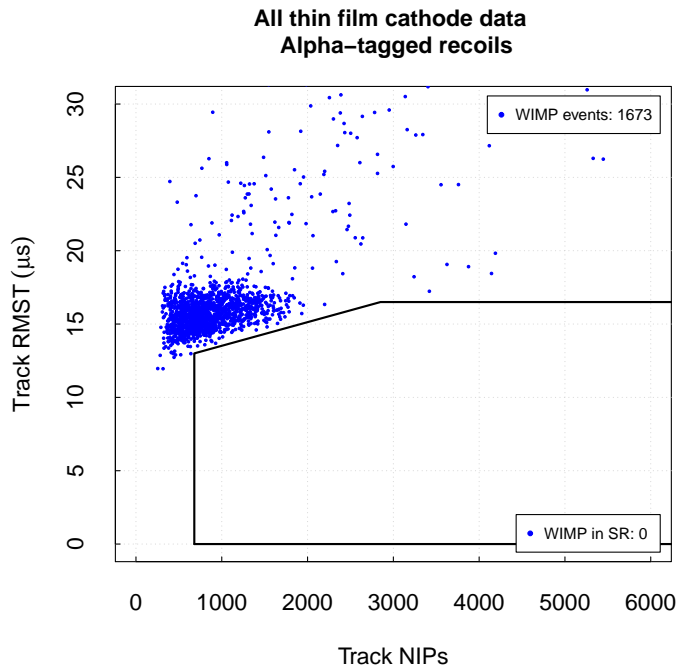


FIGURE 7.10: Alpha-tagged recoils from the full 64.75 days of WIMP-search data with the thin film cathode. The events show the same distribution in the RMST vs. NIPs plane as the background events in the wire cathode run. The wire cathode signal region is shown for reference.

### 7.3.2 Defining acceptance box for blind thin film cathode data

In Section 7.3.1 it was shown that the detector backgrounds have changed with the introduction of the thin film cathode. The aim of this section is to choose a new acceptance box in the RMST vs. NIPs plane for the blind thin film cathode data. The box is chosen using predictions of the backgrounds expected in the 53.07 days of blind data based on events from non-blind data.

The backgrounds observed in the non-blind thin film cathode data, after all cuts, consist of three populations: A low NIPs population, (population 4 in Section 6.2), thought to be from gamma-ray interactions; a population of high RMST and  $< 2000$  NIPs values (population 3 in Section 6.2), events from decays on the central cathode surface, which are now much fewer in number due to the thin film central cathode; and a new background from the thin film cathode consisting of  $\gtrsim 2000$  NIPs events with RMST of  $\sim 15 \mu\text{s}$ .

The signal region for the blind analysis of thin film cathode data is, therefore, considered in three parts that are combined to form the final acceptance box.

**NIPs threshold** — The NIPs threshold for the wire cathode data was chosen to be 700 NIPs to remove all low NIPs events from the 47.36 days of WIMP-search data. Assuming the low NIPs background population has not been altered by the new central cathode, the wire cathode data plus the non-blind thin cathode data gives a total of 59.04 days of data in which no events from this population contaminate the signal region. This implies that there should be  $\sim 0$  events from this population above 700 NIPs in the the 53.07 days of blind thin film data. In addition, Figure 7.11 shows that the low NIPs background population in the non-blind thin film cathode data has a distribution in NIPs that is reasonably approximated by a Gaussian distribution. The number of events in the population deduced from the fit is  $448 \pm 21$  and the 700 NIP threshold is  $\sim 4\sigma$  from the mean of this distribution. Scaling by a factor of 4.6 for the difference in livetimes gives a 90% C.L. upper limit of 2255 low NIPs events expected in the 53.07 days of non-blind WIMP-search run data. Assuming a Gaussian distribution,  $< 0.03$  events from this population are expected above the 700 NIPs threshold.

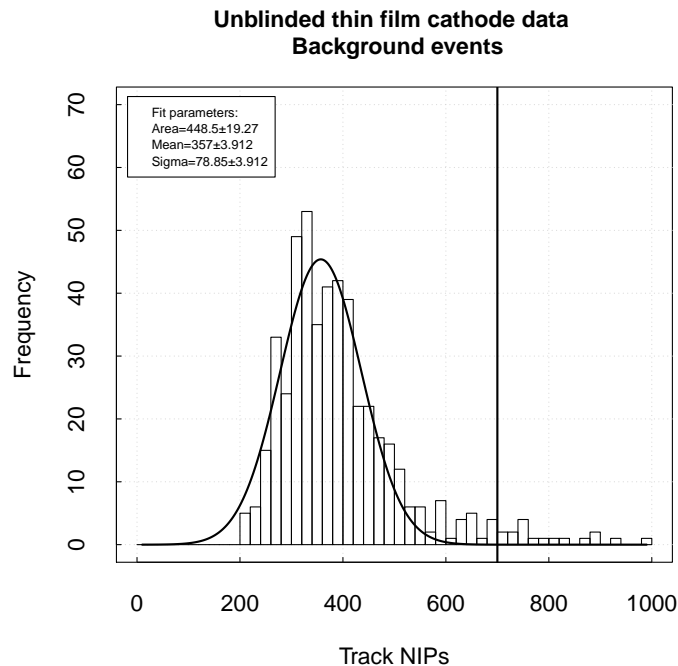


FIGURE 7.11: Histogram of low NIPs event population from the 11.68 days non-blind WIMP-search data. Curve shows the Gaussian fit and the vertical line shows the 700 NIP threshold.

**700 to 2000 NIPs** — The events occurring during the wire cathode WIMP-search runs in the 700 to 2000 NIPs region were shown, in Section 6.3, to be decays on the central cathode plane. In Section 7.3.1 it was shown that these events have been largely eliminated, and that the majority of events on the surface of the cathode result in alpha-tagged recoils instead. There are however, some remaining events in this region.

It is assumed that all of the events between 700 and 2000 NIPs in the WIMP-search data are recoils from decays on the surface of the thin film cathode. Figure 7.12 plots the recoil-like events from the non-blind WIMP-search data (black) and the alpha-tagged recoil events from the entire 64.75 days of thin film cathode data (red). As was previously demonstrated in Section 6.3.2, the alpha-tagged recoil events are a close match to the background distribution in this region. The alpha-tagged recoil events, which have a much higher rate in the thin film cathode, are therefore a useful model of the background in this region, and are used to determine the signal region.

The distribution of the alpha-tagged recoil events was determined by segmenting the data into 200 NIPs bins from 400 to 2200 NIPs, with the last two bins combined due to low statistics. For each NIPs bin the data was projected onto a histogram in RMST and was fitted with a Gaussian to determine the mean and the sigma of the distribution. The dashed line in Figure 7.13 shows the resulting mean of the event population as a function of NIPs.

The 11.68 days of non-blind WIMP-search data contains  $37 \pm 6$  recoil events in the region of 700 to 2000 NIPs. Scaling this for the 53.07 days of blind WIMP-search data results in an upper limit of 226 events expected (90% C.L.) in this population. Removing all events within 2.6 sigma of the mean of the event distribution, therefore, results in  $< 1.0$  events expected from this background event population in the blind dataset. The solid black region in Figure 7.13 shows the signal region defined as 2.6 sigma below the mean of the plotted alpha-tagged recoil data.

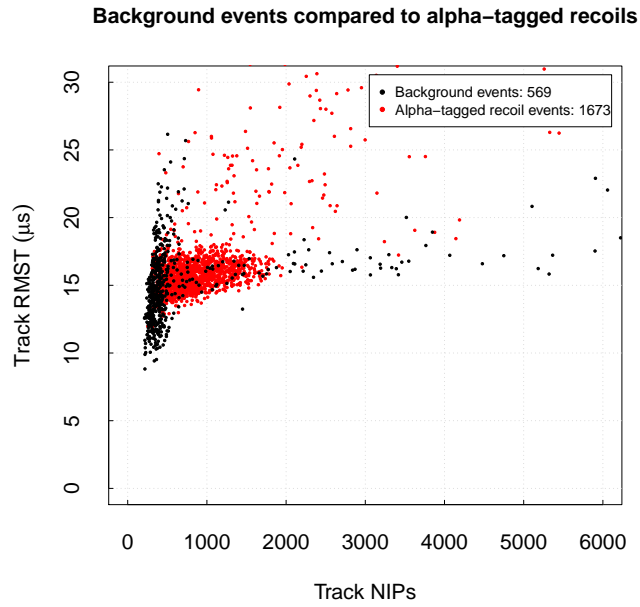


FIGURE 7.12: Non-blind WIMP-search data (black) and alpha-tagged recoil events (red) in the NIPs vs. RMST plane. The alpha-tagged recoil events are a good model for the background distribution in the 700 to 2000 NIPs region.

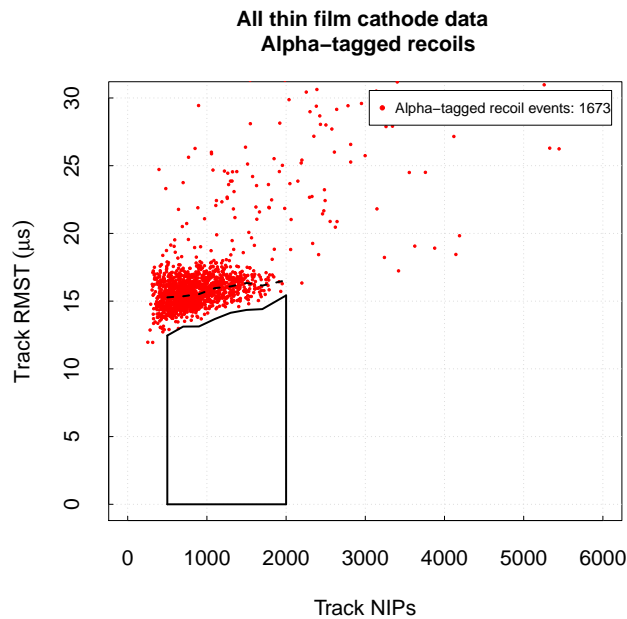
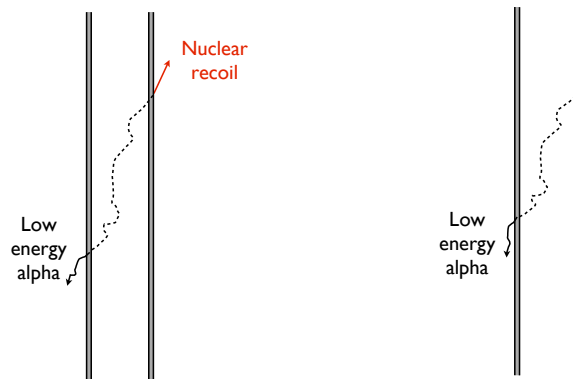


FIGURE 7.13: Alpha-tagged recoil events from the 64.75 days of WIMP-search data. Dashed line shows the mean RMST of the data distribution from Gaussian fits to events in bins of width 200 NIPs. Signal region set at 2.6 sigma from the mean of the alpha-tagged recoil population. Predicting a maximum of 1.0 events in signal region of the blind WIMP-search run data with 90% C.L..

**2000 to 10000 NIPs** — The events occurring in the 11.68 days of non-blind WIMP-search data above 2000 NIPs form a background population that is not seen in the 47.36 days of data with the wire central cathode. The background events are closely clustered around  $\sim 15 \mu\text{s}$  in RMST with NIPs values extending up to  $\sim 10000$  NIPs.

Since this background population was not observed in the 47.36 days of data with the wire central cathode, it is highly likely that the thin film cathode is the source. In coincidence with the appearance of this background population, a class of events termed double-recoils — events consisting of a recoil-like track on both MWPCs simultaneously — was also discovered. It is suspected that the source of both of these event classes may be low energy alphas (LEAs) originating in the aluminised surface of the thin film central cathode. As illustrated in Figure 7.14, the alpha decay of a radionuclide contaminant in the aluminised coating of the thin mylar film may result in a single or double recoil-like event if the alpha enters the fiducial volume after first losing most of its energy in cathode.

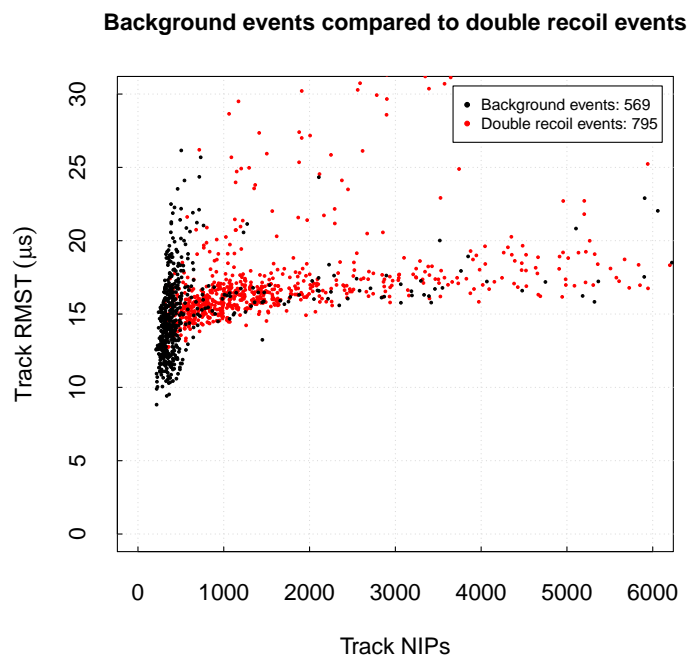


(a) Alpha decay of nuclei on surface of aluminium coating resulting in double-recoil event. (b) Alpha decay of nuclei under the surface of the aluminium coating resulting in a recoil-like LEA on one side.

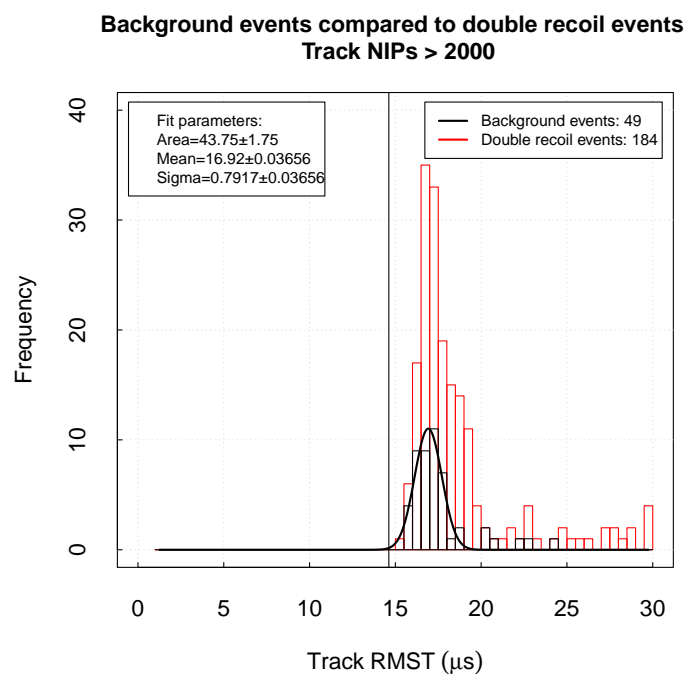
FIGURE 7.14: Illustrations of how radioactive contamination of the aluminium coating on the  $0.9 \mu\text{m}$  mylar sheet may result in double-recoil events or WIMP-mimicking low energy alpha (LEA) events.

Figure 7.15(a) plots the recoil-like events from the non-blind WIMP-search data (black) and the double-recoil events from the entire 64.75 days of data with the thin film cathode (red) in the RMST vs. NIPs plane. In the double-recoil data the event in each MWPC is parameterised separately, each of which undergoes the standard WIMP analysis described in Section 5.3. Figure 7.15(b) shows a histogram in RMST of this data for events above 2000 NIPs, showing that the populations have a similar event distribution. Although the double-recoil events appear to be a reasonable model for the new background

population and could potentially be used to determine this part of the signal region, a more cautious approach was taken of simply extrapolating the background population from the non-blind data. A Gaussian was fitted to the recoil-like events above 2000 NIPs from the 11.68 days of non-blind WIMP-search data. The population contains  $44 \pm 7$  events suggesting, in the 53.07 days of blind data, an upper limit of 267 events (90% C.L.). Removing all events within 2.9 sigma of the mean of this event population, i.e. rejecting events with  $\text{RMST} > 14.62 \mu\text{s}$ , results in an upper limit of 0.5 events expected in the blind dataset from this population.



(a) Comparison of recoil events from non-blind data (black) to double-recoil events from all data (red).



(b) Histogram of events in (a) in the range 2000 to 10000 NIPs.

FIGURE 7.15: Comparison of recoil events from non-blind data (black) to double-recoil events from all data (red). Double-recoil events are a reasonable match to the recoil-like background events above 2000 NIPs.

**Combined signal region** — Combining the acceptance regions detailed in this section results in the complete signal region shown in Figure 7.16. The three background populations used to derive the signal region are also shown. Double-recoil events (green) model the background events above 2000 NIPs. A maximum of 0.5 events from this population are expected to land in the signal region in the 53.07 days of blind data. Alpha-tagged recoils (red) model backgrounds between 700 to 2000 NIPs. A maximum of 1.0 events are expected in the accepted signal region from this population. The 11.68 days of non-blind WIMP-search data (blue) were used to model the backgrounds below 700 NIPs. A maximum of 0.03 events from this population are expected in the signal region in the blind data. The total signal region shown in Figure 7.16 is therefore expected to contain a maximum of  $\sim 1.5$  events in the 53.07 days of blind data when the box is opened.

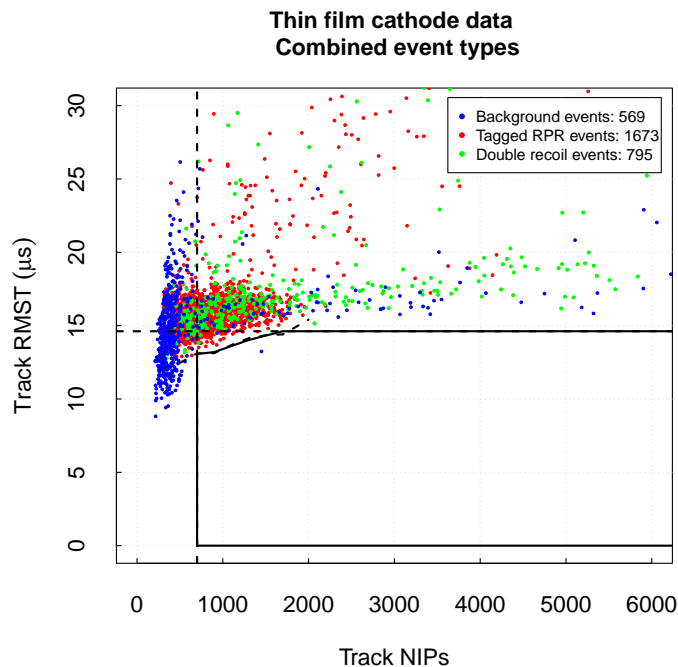


FIGURE 7.16: The total signal region with the three classes of event from which the signal region was derived. Recoil events from non-blind data (blue) used to determine energy threshold, alpha-tagged recoil events from all data (red), used to determine signal region from 700 to 2000 NIPs and double recoil events from all data (green), used to determine the signal region above 2000 NIPs.

### 7.3.3 Opening the box

Figure 7.17 reveals the distribution of events from 53.07 days of WIMP-search data after ‘opening the box’. As expected, the total number of background events has increased in

proportion with the increased livetime. A single event is observed in the signal region with a NIPs value of 803 and an RMST of  $10.97 \mu\text{s}$ .

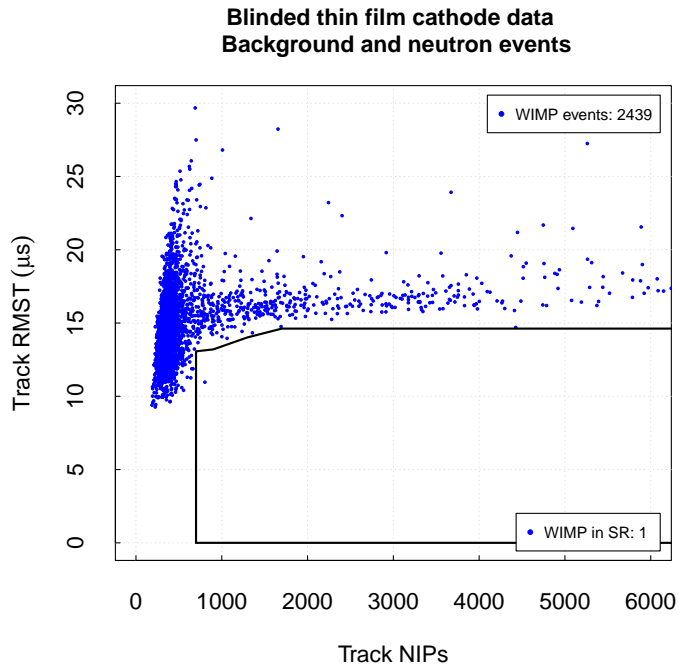


FIGURE 7.17: Opening up the blind dataset containing 53.07 days livetime with a target of 30-10 Torr  $\text{CS}_2\text{-CF}_4$  with the thin film cathode installed. The data reveals a single event in the signal region with a NIPs value of 803 and an RMST of  $10.97 \mu\text{s}$ .

This event, shown in Figure 7.18, appears to be a legitimate event and has no features to distinguish it from neutron events in the same region. Although up to 1.5 events are predicted in the signal region from the cathode originating backgrounds, the position of the event in the NIPs vs. RMST plane shows that it is unlikely to be a part of the cathode background populations. It is potentially leakage from the gamma-ray population that dominate below 700 NIPs.

Despite the observation, in the 11.68 days of non-blind data, of a single anomalous event with a NIPs value of 1450 NIPs and RMST of  $13.24 \mu\text{s}$  (Section 7.3.1), it is noted here that there are no further events in this region of the RMST vs. NIPs plane. This suggests the event is not a new background population introduced by the central cathode. Investigation continues within the collaboration on the origin of this spurious event, and the single low NIPs event that fell in the signal region of the blind dataset.

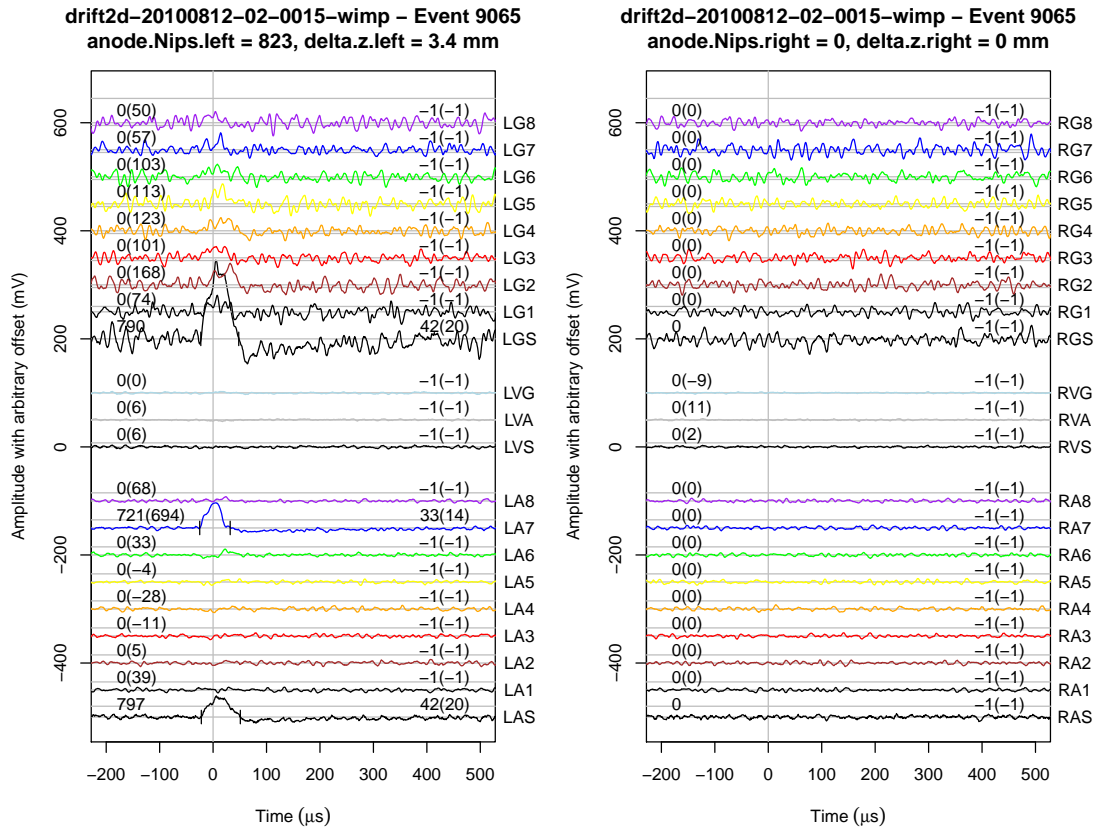


FIGURE 7.18: The single candidate WIMP interaction from 53.07 days of WIMP-search data.

### 7.3.4 Spin-dependent WIMP-proton limit plot from a blind analysis

Given that one event is detected in the acceptance box with an expected background of  $\sim 1.5$  events, it is 90% probable that the box would, on average, contain less than 2.91 events [154]. This provides the upper limit on experimentally observed WIMP interactions in the 53.07 days of livetime. The procedure detailed in Section 7.2 is repeated to determine the efficiency for detecting WIMPs of various masses with the new thin film cathode signal region. The experimentally determined upper limit on the WIMP interaction event rate is then compared to the theoretical efficiency for WIMP detection, as described in Section 7.2.2, resulting in upper limits on the WIMP-proton cross-sections. The resulting limit plot, with a minimum of 0.93 pb for a 100 GeV WIMP, is shown in Figure 7.19.

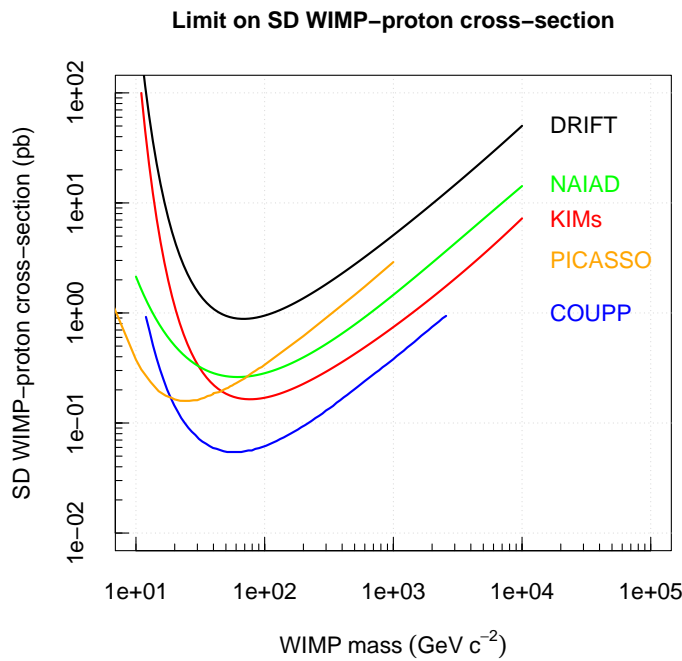


FIGURE 7.19: Upper limits on SD WIMP-proton cross-sections from a blind analysis of the thin film cathode data. Upper limits from leading experiments are also plotted and are discussed in Section 7.2.2. Despite the longer run time, the upper limits from this analysis are slightly higher than those presented in Figure 7.8. This is due to the blind nature of the analysis resulting in a slightly lower WIMP detection efficiency and a single event in the signal region. The limit has a minimum of 0.93 pb for a 100 GeV WIMP.

## 7.4 Conclusions

In this chapter the discipline of blinded analysis has been brought to bear on DRIFT data for the first time. The exercise has been successful, with the blind analysis box containing a well controlled set of events when opened. The resulting limits are competitive with high density targets having no directional potential, and better than rival gaseous detectors by orders of magnitude. The DRIFT event file simulator is shown to be limited by its treatment of signal response in the MWPC — a deficiency that will be rectified in future versions of the simulation code produced by the collaboration. In this analysis, however, corrections have been made to compensate for the deficiencies in this code, rendering the existing simulation useable for producing meaningful upper limits. The blind analysis of 53.07 days of data with a 30-10 Torr  $\text{CS}_2\text{-CF}_4$  gas mixture results in an upper limit on spin-dependent WIMP-proton cross-sections with a minimum of 0.93 pb for a 100 GeV WIMP at 90% confidence.

## Chapter 8

# Conclusions

The evidence for a Universe dominated by non-baryonic dark matter is formidable. The nature of the dark matter, however, remains one of the biggest questions in astrophysics and cosmology today. Weakly interacting massive particles are a favoured candidate, but neither indirect, nor direct dark matter detection techniques have conclusive evidence for their existence. Recently, a number of experiments have hinted at detection of WIMP interactions, but the magnitude of the dark matter question is such that a definitive and unambiguous proof will be demanded before acceptance of such a discovery. The unambiguous signal in the directionality of the ‘WIMP wind’ has the potential to be this definitive proof and, for the past decade, the DRIFT collaboration has pioneered development of a directionally sensitive dark matter detector.

Previous work has demonstrated the directional sensitivity of the DRIFT-II dark matter detector. While development of the directional sensitivity of DRIFT is ongoing, this thesis has described work focussing on using DRIFT to explore new regions of spin-dependent interaction phase space. The work presented in this thesis contributes to this entire process, starting with the first tests of  $\text{CS}_2\text{-CF}_4$  gas mixtures in a full-scale  $1\text{ m}^3$  DRIFT detector. Following this, the design, construction and commissioning of a gas mixing system required for operation of DRIFT with spin-dependent sensitive gas mixtures has been presented. This work not only results in SD sensitivity in the DRIFT-II detector for the first time, but demonstrates the flexibility of the DRIFT detector to operate with different target materials. The system, developed for the  $\text{CS}_2\text{-CF}_4$  mixtures, has put in place hardware that will allow future operation with a range of potentially interesting target gases.

Aside from this, a new class of event was identified that sheds light on signal production mechanisms within the DRIFT MWPC readout planes. The study of these events suggests additional effects that should be included in future versions of the DRIFT detector

simulation to improve realism. The identified effects, in addition, may have consequences for future development of three-dimensional track reconstruction. The possibility of in situ drift velocity measurements using these spark-like events was demonstrated by calculating the mobility from existing WIMP-search datasets. The measurements highlight uncertainties in the DRIFT detector systematics. Future detector upgrades, particularly a residual gas analyser for constant monitoring of gas contamination, are hoped to improve understanding of the observed effects.

This thesis presents the first long-term study of backgrounds in DRIFT with a consistent and systematic analysis of data from the underground DRIFT-II<sub>d</sub> experiment, spanning a period of over three years. This work, through careful selection of cuts, revealed previously unknown sub-populations in the limiting backgrounds in the DRIFT detector and identified their sources. These findings are crucial for the future development and background reduction strategies of DRIFT.

While future efforts should be in eliminating these backgrounds, methods of discriminating the present background events from potentially WIMP-induced nuclear recoils have been developed. The cuts and parameterisation of the existing DRIFT analyses were redeveloped producing a background-free signal region with increased sensitivity to WIMP interactions. The improvements result in a dramatic increase in the total detection efficiency for  $^{252}\text{Cf}$  neutron-induced nuclear recoils, by a factor of 2.4.

An accurate full simulation of the DRIFT detector offers many advantages for investigating directional capabilities, response to backgrounds, and detection efficiency of the DRIFT detector. Simulated nuclear recoil data from an existing DRIFT simulation was analysed and compared to real neutron data over the full analysis chain resulting in the highlighting of some limitations of the simulation, to be rectified in future code development. Despite the existing limitations, methods for correction of simulated data were developed allowing the simulation to be used to deduce meaningful upper limits from spin-dependent sensitive operation of the DRIFT detector.

The culmination of the work presented in this thesis are limits from the DRIFT-II<sub>d</sub> detector underground at the Boulby Underground Laboratory that are competitive with leading dark matter detectors using liquid and solid targets with no directional potential. Limits from a non-blind analysis result in upper limits on the WIMP-proton spin-dependent cross-section with a minimum of 0.75 pb for a 100 GeV WIMP at 90% C.L.

In addition, for the first time, the discipline of a blind analysis was applied to DRIFT. Methods of modelling existing background populations were used to form a signal region in which 1.5 events were predicted in a blinded dataset of 53.07 days of blind data.

Opening the box reveals a single event demonstrating the stability of the detector and the analysis procedure developed in this thesis. The blind analysis results in a limit on the spin-dependent WIMP-proton interaction cross-section with a minimum at 0.93 pb for a 100 GeV WIMP.

It is likely that exploration of WIMP-nucleon cross-sections many orders of magnitude below current limits will be required to determine whether WIMPs are the elusive dark matter. This requires much larger detectors with improved sensitivity. The XENON collaboration, who currently set the most stringent limits on spin-independent WIMP-nucleon cross-sections with the 48 kg fiducial mass XENON100 experiment, are currently working towards XENON1T. This scales the detector to a 1000 kg fiducial mass, with background reduced by two orders of magnitude. XENON1T, set for completion in 2015, expects to probe WIMP-nucleon cross-sections below  $10^{-46} \text{ cm}^2$ . The COUPP collaboration, who currently provide the most stringent limits on WIMP-proton interaction cross-sections, are planning an upgrade that scales the existing detector technology from a mass of 2 kg fiducial to 60 kg. It is estimated that the so-called COUPP-60 experiment will improve their present limits by two orders of magnitude to  $\sim 10^{-39} \text{ cm}^2$ .

The ultimate proof of WIMP dark matter is likely to come from the unambiguous directional signal of the WIMP wind via an array of DRIFT-like dark matter detectors consisting of 100s of cubic metres of fiducial volume. Current efforts in the DRIFT collaboration are towards the next generation DRIFT-IIe detector, in preparation for scale-up to a  $24 \text{ m}^3$  DRIFT-III detector.



# Appendix A

## Background reduction operations

Over the course of DRIFT-II operation a number of actions have been taken to address the likely sources of the background discussed in Section 6.1. These actions, summarised in Section 6.3, are described here.

### A.1 Cathode etching

An operation to clean the central cathode of radioactive contamination was undertaken in February 2008. This used an acid etching technique in which the central cathode was removed from the detector and soaked in dilute nitric acid.

The central cathode was placed into a transportation box that had been lined with several layers of isopropanol-cleaned plastic sheeting as shown in Figure A.1. 180 L of 3 molar nitric acid was produced from a mixture of 34 L of 70% (15.8 molar) nitric acid and 146 L of deionised water. To ensure that the surface tension of the dilute nitric acid did not create excessive force on the 20  $\mu\text{m}$  wires the cathode box was placed at a slight slope and the dilute nitric acid was slowly added to the box until it covered all of the wires of the central cathode. Similarly, after soaking, the dilute nitric acid was slowly drained from the box using a hand pump. The cathode was then transferred to a second plastic-lined box, which was filled with 180 L of pure deionised water and left for 48 hours. After this time the deionised water was removed in the same way. Despite the precautions taken the water tension pulled the 20  $\mu\text{m}$  wires together causing them to become stuck together along a large fraction of their length. As the cathode dried out most of the wires separated themselves but a few remained stuck. These wires were separated by hand using a short piece of 100  $\mu\text{m}$  wire to ensure that no excessive force was put on the cathode wires, minimising the risk of breakage.

After reassembling the detector and replacing it in the vacuum vessel it failed to reach operating voltage. On dismantling the detector it became clear that the central cathode had not had enough time to dry thoroughly after the acid bath and dampness between the layers of the acrylic glass frame had led to sparking in the detector. Also it was evident that the acid had corroded the electrical contact between the central cathode and the field cages. This was replaced and the frame of the cathode was separated to allow all contacts to be thoroughly cleaned and dried before reassembling the detector.

The detector was allowed the usual three days of outgassing before calibration data was taken using both the  $^{55}\text{Fe}$  source and the  $^{252}\text{Cf}$  neutron source. The event rates in each case were initially considerably lower than usual, but then rose over the next few days to levels such that the detector was inoperable. This is suspected to be due to the plastic frame of the detector requiring a much longer outgassing period than usual owing to having been soaked in nitric acid and water for a number of days. The detector was allowed to outgas under vacuum for a further two weeks before more calibration and background runs demonstrated that the detector was running normally.



FIGURE A.1: Photograph taken during the cathode cleaning operation.

## A.2 MWPC etching

In July 2008 a similar nitric acid etch operation was performed on the two MWPC readout planes.

Preliminary tests showed that the 3 molar nitric acid might have adverse effects on the PCB grouping boards and electrical contacts that are present on the MWPCs. It

was thus decided that a less aggressive cleaning process would be used. The procedure adapted consisted of five separate immersions:

1. 1 hour in 180 L of 0.5 molar nitric acid.
2. 1 hour in 180 L of deionised water.
3. 1 hour in 0.5 molar nitric acid (reusing the acid from stage 1).
4. 1 hour in deionised water reused from stage 2.
5. 2 days in fresh deionised water.

The two stage acid bathing was to ensure that if any bubbles formed on the wires during the first acid bath and any parts of the wire were not cleaned, then they would be in the second bath.

### **A.3 Thin film cathode**

The WIMP-like background originating from the central cathode is suspected to be a result of unstable nuclei on the surface of the central cathode wires decaying by alpha emission. Such an event only produces a WIMP-like recoil in the event that the tell-tale alpha becomes embedded in the central cathode wire, and is thus undetectable. One way of reducing this background is therefore to make the central cathode more transparent to alphas so that fewer alpha particles get lost in the central cathode.

Stainless steel wires can be obtained in smaller diameter, but the wires require a given tension in order to reduce the effects of electrostatic repulsion. The tension required is 90% of the breaking limit of the current stainless steel wires, so it is not feasible to use stainless steel wires of a smaller radius.

A number of potential cathode replacements were considered, including quartz fibres and evaporation coated mylar sheet. Mylar sheet of  $0.9\ \mu\text{m}$  thickness, evaporation coated with aluminium, was found to be a suitable solution, in which the range of alphas and the geometry meant that only  $\sim 1\%$  of decays on the surface would result in WIMP-mimicking nuclear recoil events compared to  $37\%$  of decays on the surface of the  $20\ \mu\text{m}$  wires of the current central cathode. This suggests a potential reduction in background of a factor  $\sim 40$ .

A  $1\ \text{m}^2$  cathode constructed from  $0.9\ \mu\text{m}$  mylar sheet was tested at Occidental College on DRIFT-IIc and was shown not to have adverse effects on detector operation or stability.

It was subsequently installed on the DRIFT-II detector underground at the Boulby mine in March 2010 and the detector has been operating stably since the installation.

## Appendix B

### Dataset run details

This table, spanning two pages, contains the run details all of the datasets used in Section 6.3.

dataset no	CS <sub>2</sub> -CF <sub>4</sub> (Torr)	L/R/c	Livetime (days)	Start date	Days since 1 Jan '05
03	40-00	8/4/w	6.413	2007/02/12	772
			0.109 (n)	2007/02/20	780
03b	40-00	8/4/w	2.149	2007/07/21	931
04	40-00	8/4/w	0.749	2008/02/01	1126
			0.03 (n)	2008/02/01	1126
05	40-00	8/4/w(c)	10.112	2008/03/05	1159
			0.034 (n)	2008/03/05	1159
06	40-00	8/4/w(c)	11.441	2008/04/04	1189
07	41-00	8/4/w(c)	6.078	2008/04/18	1203
08	41-00	8/4/w(c)	9.567	2008/04/30	1215
			0.034 (n)	2008/04/30	1215
09	41-00	8/4/w(c)	8.661	2008/05/14	1229
			0.017 (n)	2008/05/14	1229
10	42-00	8(c)/4(c)/w(c)	4.687	2008/09/25	1363
			0.028 (n)	2008/09/25	1363
11	42-00	8(c)/4(c)/w(c)	4.843	2008/10/07	1375
			0.561 (n)	2008/10/06	1374
12	42-00	8(c)/4(c)/w(c)	16.096	2009/01/23	1483
			0.11 (n)	2009/02/11	1502
13	30-10	8(c)/6/w(c)	3.207	2009/06/21	1632
	30-10		0.478 (n)	2009/06/25	1636

14	30-10	8(c)/6/w(c)	9.722	2009/12/03	1797
	30-10		0.428 (n)	2009/12/02	1796
15	30-10	8(c)/6/w(c)	27.115	2009/12/16	1810
	30-10		0.592 (n)	2010/01/26	1851
16	30-10	8(c)/6/w(c)	10.52	2010/02/03	1859
	30-10		0.819 (n)	2010/02/16	1872
17	30-10	8(c)/4(c)/f	2.219	2010/03/20	1904
	30-10		0.587 (n)	2010/03/23	1907
18_U	30-10	8(c)/4(c)/f	6.827	2010/03/26	1910
			0.812 (n)	2010/04/13	1928
18_B	30-10	8(c)/4(c)/f	28.648	2010/04/06	1921
18b_U	30-10	8(c)/4(c)/f	0.452	2010/06/22	1998
18b_B	30-10	8(c)/4(c)/f	4.034	2010/06/22	1998
19	40-00	8(c)/4(c)/f	2.558	2010/07/06	2012
19b_U	30-10	8(c)/4(c)/f	0.882	2010/07/22	2028
19b_B	30-10	8(c)/4(c)/f	7.886	2010/07/22	2028
20_U	30-10	8(c)/4(c)/f	0.282	2010/08/03	2040
20_B	30-10	8(c)/4(c)/f	2.909	2010/08/03	2040
21_U	30-10	8(c)/4(c)/f	0.879	2010/08/12	2049
			0.205 (n)	2010/08/25	2062
21_B	30-10	8(c)/4(c)/f	8.405	2010/08/12	2049
22_U	30-10	8(c)/4(c)/f	0.142	2010/08/27	2064
22_B	30-10	8(c)/4(c)/f	1.332	2010/08/27	2064

TABLE B.1: Descriptions of datasets used for long-term study of backgrounds. Column three contains identification of left MWPC, right MWPC and central cathode respectively, with (c) indicating it has been cleaned in nitric acid, w=wire cathode and f=thin film cathode. Column four is livetime in days with (n) indicating a neutron run. The five dashed horizontal lines correspond to the five actions as detailed in Section 6.1.5.

# Bibliography

- [1] N. Jarosik, C. L. Bennett *et al.* Seven-year Wilkinson Microwave Anisotropy Probe (WMAP) observations: Sky maps, systematic errors, and basic results. *The Astrophysical Journal Supplement Series*, 192:14, 2011.
- [2] A. Friedman. On the curvature of space. *General Relativity and Gravitation*, 31: 1991–2000, 1999.
- [3] G. Lemaître. Expansion of the universe, a homogeneous universe of constant mass and increasing radius accounting for the radial velocity of extra-galactic nebulae. *Monthly Notices of the Royal Astronomical Society*, 91:483–490, 1931.
- [4] E. Hubble. A relation between distance and radial velocity among extra-galactic nebulae. *Proceedings of the national academy of sciences*, 15:168–173, 1929.
- [5] A. G. Riess, A. V. Filippenko *et al.* Observational evidence from supernovae for an accelerating universe and a cosmological constant. *The Astronomical Journal*, 116(3):1009, 1998.
- [6] P. J. Peebles and B. Ratra. The cosmological constant and dark energy. *Reviews of Modern Physics*, 75:559–606, 2003.
- [7] R. A. Alpher and R. C. Herman. Remarks on the evolution of the expanding universe. *Physical Review*, 75(7):1089–1095, 1949.
- [8] A. A. Penzias and R. W. Wilson. A measurement of excess antenna temperature at 4080 Mc/s. *Astrophysical Journal*, 142:419–421, 1965.
- [9] R. H. Dicke, P. J. E. Peebles *et al.* Cosmic black-body radiation. *Astrophysical Journal*, 142:414–419, 1965.
- [10] J. C. Mather, E. S. Cheng *et al.* Measurement of the cosmic microwave background spectrum by the COBE FIRAS instrument. *Astrophysical Journal*, 420:439–444, 1994.

- 
- [11] E. L. Wright, S. S. Meyer *et al.* Interpretation of the cosmic microwave background radiation anisotropy detected by the COBE differential microwave radiometer. *Astrophysical Journal Letters*, 396:13–18, 1992.
- [12] G. J. Mathews. Big bang cosmology. *AIP Conference Proceedings*, 1016(1):7–14, 2008.
- [13] K. Nakamura *et al.* 2011 review of particle physics. *Journal of Physics G*, 37(075021), 2010.
- [14] The ALEPH Collaboration *et al.* Precision electroweak measurements on the  $z$  resonance. *Physics Reports*, 427(5-6):257–454, 2006.
- [15] K. A. Olive and E. D. Skillman. A realistic determination of the error on the primordial helium abundance: Steps toward nonparametric nebular helium abundances. *The Astrophysical Journal*, 617(1):29, 2004.
- [16] R. H. Cyburt, B. D. Fields, and K. A. Olive. An update on the big bang nucleosynthesis prediction for  $7\text{ Li}$ : the problem worsens. *Journal of Cosmology and Astroparticle Physics*, 2008(11):012, 2008.
- [17] L. Searle and R. Zinn. Compositions of halo clusters and the formation of the galactic halo. *Astrophysical Journal*, 225:357–379, 1978.
- [18] V. Springel, S. D. M. White *et al.* Simulations of the formation, evolution and clustering of galaxies and quasars. *Nature*, 435(7042):629–636, 2005.
- [19] P. Bett, V. Eke *et al.* The spin and shape of dark matter haloes in the Millennium simulation of a  $\lambda$  cold dark matter universe. *Monthly Notices of the Royal Astronomical Society*, 376(1):215–232, 2007.
- [20] M. Boylan-Kolchin, V. Springel *et al.* Resolving cosmic structure formation with the Millennium-II simulation. *Monthly Notices of the Royal Astronomical Society*, 398(3):1150–1164, 2009.
- [21] F. Zwicky. Die rotverschiebung von extragalaktischen nebeln. *Helvetica Physica Acta*, 6:110–127, 1933.
- [22] F. Zwicky. Republication of: The redshift of extragalactic nebulae. *General Relativity and Gravitation*, 41:207–224, 2009.
- [23] M. Colless and A. M. Dunn. Structure and dynamics of the Coma Cluster. *Astrophysical Journal*, 458:435, 1996.
- [24] F. Zwicky. On the masses of nebulae and of clusters of nebulae. *Astrophysical Journal*, 86:217–246, 1937.

- [25] E. L. Lokas and G. A. Mamon. Dark matter distribution in the coma cluster from galaxy kinematics: breaking the mass–anisotropy degeneracy. *Monthly Notices of the Royal Astronomical Society*, 343(2):401–412, 2003.
- [26] R. G. Carlberg, H. K. C. Yee *et al.* Galaxy cluster virial masses and  $\omega$ . *Astrophysical Journal*, 462:32, 1996.
- [27] V. C. Rubin and W. K. Ford, Jr. Rotation of the Andromeda nebula from a spectroscopic survey of emission regions. *Astrophysical Journal*, 159:379, 1970.
- [28] M. S. Roberts and R. N. Whitehurst. The rotation curve and geometry of M31 at large galactocentric distances. *Astrophysical Journal*, 201:327–346, 1975.
- [29] B. Fuchs. The amount of dark matter in spiral galaxies. In H. V. Klapdor-Kleingrothaus, editor, *Dark Matter in Astro- and Particle Physics*, page 25, 2001.
- [30] M. G. Walker, S. S. McGaugh *et al.* Comparing the dark matter halos of spiral, low surface brightness, and dwarf spheroidal galaxies. *The Astrophysical Journal Letters*, 717(2):87, 2010.
- [31] A. Einstein. Die grundlage der allgemeinen relativitätstheorie. *Annalen der Physik*, 354(7):769–822, 1916.
- [32] L. King, N. Jackson *et al.* A complete infrared Einstein ring in the gravitational lens system B1938 + 666. *Monthly Notices of the Royal Astronomical Society*, 295(2):41–44, 1998.
- [33] L. V. E. Koopmans, T. Treu *et al.* The Sloan Lens ACS Survey. III. The structure and formation of early-type galaxies and their evolution since  $z \approx 1$ . *The Astrophysical Journal*, 649(2):599, 2006.
- [34] Hubblesite, 2011. URL <http://hubblesite.org/>.
- [35] R. Gavazzi, T. Treu *et al.* The Sloan Lens ACS Survey. IV. The mass density profile of early-type galaxies out to 100 effective radii. *The Astrophysical Journal*, 667(1):176, 2007.
- [36] D. Clowe, M. Bradač *et al.* A direct empirical proof of the existence of dark matter. *The Astrophysical Journal Letters*, 648(2):109, 2006.
- [37] C. S. Kochanek, M. White *et al.* Clusters of galaxies in the local universe. *The Astrophysical Journal*, 585(1):161, 2003.
- [38] C. Mastropietro and A. Burkert. Simulating the bullet cluster. *Monthly Notices of the Royal Astronomical Society*, 389(2):967–988, 2008.

- [39] C.-J. Ma, H. Ebeling *et al.* The impact of a major cluster merger on galaxy evolution in MACS J0025.4-1225. *Monthly Notices of the Royal Astronomical Society*, 406(1):121–136, 2010.
- [40] M. J. Jee, H. C. Ford *et al.* Discovery of a ringlike dark matter structure in the core of the galaxy cluster Cl 0024+17. *The Astrophysical Journal*, 661(2):728, 2007.
- [41] G. Bertone, D. Hooper, and J. Silk. Particle dark matter: evidence, candidates and constraints. *Physics Reports*, 405(5-6):279–390, 2005.
- [42] L. Bergström. Dark matter candidates. *New Journal of Physics*, 11(10):105006, 2009.
- [43] G. Jungman, M. Kamionkowski, and K. Griest. Supersymmetric dark matter. *Physics Reports*, 267(5-6):195–373, 1996.
- [44] H.-C. Cheng, J. L. Feng, and K. T. Matchev. Kaluza-klein dark matter. *Physical Review Letters*, 89(21):211301, 2002.
- [45] M. Schmaltz and D. Tucker-Smith. Little Higgs review. *Annual Review of Nuclear and Particle Science*, 55:229–270, 2005.
- [46] A. Birkedal-Hansen and J. G. Wacker. Scalar dark matter from theory space. *Physical Review D*, 69(6):065022, 2004.
- [47] A. K. Drukier, K. Freese, and D. N. Spergel. Detecting cold dark-matter candidates. *Physical Review D*, 33(12):3495–3508, 1986.
- [48] K. M. Cudworth. Further observations of the planetary nebula in the globular cluster M22. *Astronomical Journal*, 99:1863–1866, 1990.
- [49] J. D. Lewin and P. F. Smith. Review of mathematics, numerical factors, and corrections for dark matter experiments based on elastic nuclear recoil. *Astroparticle Physics*, 6(1):87–112, 1996.
- [50] E. I. Gates, G. Gyuk, and M. S. Turner. The local halo density. *The Astrophysical Journal Letters*, 449(2):L123, 1995.
- [51] S. Desai *et al.* Search for dark matter WIMPs using upward through-going muons in Super-Kamiokande. *Physical Review D*, 70:083523, 2004.
- [52] O. Adriani *et al.* An anomalous positron abundance in cosmic rays with energies 1.5–100 GeV. *Nature*, 458:607–609, 2009.

- [53] J. Chang, J. H. Adams *et al.* An excess of cosmic ray electrons at energies of 300–800 GeV. *Nature*, 456(7220):362–365, 2008.
- [54] A. A. Abdo, M. Ackermann *et al.* Measurement of the cosmic ray  $e^+ + e^-$  spectrum from 20 GeV to 1 TeV with the Fermi Large Area Telescope. *Physical Review Letters*, 102(18):181101, 2009.
- [55] F. Aharonian, A. G. Akhperjanian *et al.* Energy spectrum of cosmic-ray electrons at TeV energies. *Physical Review Letters*, 101(26):261104, 2008.
- [56] D. Hooper. Dark matter: Many birds, one stone. *Nature Physics*, 5(3):176–177, 2009.
- [57] D. Akimov, G. Alner *et al.* The ZEPLIN-III dark matter detector: Instrument design, manufacture and commissioning. *Astroparticle Physics*, 27(1):46–60, 2007.
- [58] E. Aprile, K. Arisaka *et al.* First dark matter results from the XENON100 experiment. *Physical Review Letters*, 105(13):131302, 2010.
- [59] Z. Ahmed *et al.* Dark matter search results from the CDMS II experiment. *Science*, 327:1619–1621, 2010.
- [60] EDELWEISS Collaboration, E. Armengaud *et al.* Final results of the EDELWEISS-II WIMP search using a 4-kg array of cryogenic germanium detectors with interleaved electrodes. *ArXiv e-prints*, 2011.
- [61] C. E. Aalseth, P. S. Barbeau *et al.* Search for an annual modulation in a p-type point contact germanium dark matter detector. *ArXiv e-prints*, 2011.
- [62] R. Bernabei, P. Belli *et al.* New results from DAMA/LIBRA. *The European Physical Journal C - Particles and Fields*, 67:39–49, 2010.
- [63] G. Angloher, M. Bauer *et al.* Results from 730 kg days of the CRESST-II Dark Matter Search. *ArXiv e-prints*, 2011.
- [64] M. T. Frandsen, F. Kahlhoefer *et al.* On the DAMA and CoGeNT modulations. *ArXiv e-prints*, 2011.
- [65] S. Chang, G. D. Kribs *et al.* Inelastic dark matter in light of DAMA/LIBRA. *Physical Review D*, 79:043513, 2009.
- [66] B. Morgan, A. M. Green, and N. J. C. Spooner. Directional statistics for realistic weakly interacting massive particle direct detection experiments. *Physical Review D*, 71(10):103507, 2005.

- [67] D. P. Snowden-Ifft, C. J. Martoff, and J. M. Burwell. Low pressure negative ion time projection chamber for dark matter search. *Physical Review D*, 61(10):101301, 2000.
- [68] G. Fricke, C. Bernhardt *et al.* Nuclear ground state charge radii from electromagnetic interactions. *Atomic Data and Nuclear Data Tables*, 60(2):177–285, 1995.
- [69] J. Engel. Nuclear form factors for the scattering of weakly interacting massive particles. *Physics Letters B*, 264(1-2):114–119, 1991.
- [70] J. Engel and P. Vogel. Spin-dependent cross sections of weakly interacting massive particles on nuclei. *Physical Review D*, 40(9):3132–3135, 1989.
- [71] J. Ellis, A. Ferstl, and K. A. Olive. Re-evaluation of the elastic scattering of supersymmetric dark matter. *Physics Letters B*, 481(2-4):304–314, 2000.
- [72] D. R. Tovey, R. J. Gaitskell *et al.* A new model-independent method for extracting spin-dependent cross section limits from dark matter searches. *Physics Letters B*, 488(1):17–26, 2000.
- [73] G. J. Davies, J. D. Davies *et al.* Liquid xenon as a dark matter detector. prospects for nuclear recoil discrimination by photon timing. *Physics Letters B*, 320(3-4):395–399, 1994.
- [74] V. N. Lebedenko, H. M. Araújo *et al.* Results from the first science run of the ZEPLIN-III dark matter search experiment. *Physical Review D*, 80(5):052010, 2009.
- [75] P. Benetti, R. Acciarri *et al.* First results from a dark matter search with liquid argon at 87K in the Gran Sasso underground laboratory. *Astroparticle Physics*, 28(6):495–507, 2008.
- [76] S. Burgos, J. Forbes *et al.* Studies of neutron detection and backgrounds with the DRIFT-IIa dark matter detector. *Astroparticle Physics*, 28:409–421, 2007.
- [77] D. H. Perkins. *Particle astrophysics*. OUP Oxford, 2003.
- [78] H. Arajo, J. Blockley *et al.* Measurements of neutrons produced by high-energy muons at the Boulby Underground Laboratory. *Astroparticle Physics*, 29(6):471–481, 2008.
- [79] J. Billard, F. Mayet *et al.* Directional detection as a strategy to discover galactic dark matter. *Physics Letters B*, 691(3):156–162, 2010.
- [80] A. M. Green and B. Morgan. Optimizing WIMP directional detectors. *Astroparticle Physics*, 27(2-3):142–149, 2007.

- [81] W. Bragg and R. Kleeman. On the ionization curves of radium. *Philosophical Magazine*, 8:726–738, 1904.
- [82] S. Burgos *et al.* First measurement of the head-tail directional nuclear recoil signature at energies relevant to WIMP dark matter searches. *Astroparticle Physics*, 31(4):261–266, 2009.
- [83] A. M. Green and B. Morgan. Consequences of statistical sense determination for WIMP directional detection. *Physical Review D*, 77:027303, 2008.
- [84] K. Miuchi, H. Nishimura *et al.* First underground results with NEWAGE-0.3a direction-sensitive dark matter detector. *Physics Letters B*, 686(1):11–17, 2010.
- [85] A. Ochi, T. Nagayoshi *et al.* A new design of the gaseous imaging detector: Micro pixel chamber. *Nuclear Instruments and Methods in Physics Research Section A*, 471(1-2):264–267, 2001.
- [86] R. Bouclier, M. Capeans *et al.* The gas electron multiplier (GEM). *Nuclear Science, IEEE Transactions on*, 44(3):646–650, 1997.
- [87] S. Ahlen, J. Battat *et al.* First dark matter search results from a surface run of the 10-L DMTPC directional dark matter detector. *Physics Letters B*, 695(1-4):124–129, 2011.
- [88] J. Billard, F. Mayet *et al.* Directional detection of dark matter with MIMAC: WIMP identification and track reconstruction. *ArXiv e-prints*, 2011.
- [89] I. Giomataris, R. D. Oliveira *et al.* Micromegas in a bulk. *Nuclear Instruments and Methods in Physics Research Section A*, 560(2):405–408, 2006.
- [90] F. J. Iguaz, D. Attié *et al.* Micromegas detector developments for dark matter directional detection with MIMAC. *ArXiv e-prints*, 2011.
- [91] D. Dujmic, J. Battat *et al.* Results from DMTPC 10-liter detector. *Journal of Physics: Conference Series*, 203(1):012029, 2010.
- [92] D. Nygren. The time projection chamber: A new  $4\pi$  detector for charged particles. In *Proceedings of The 1974 PEP Summer Study*, page 58, 1974.
- [93] K. N. Buckland, M. J. Lehner *et al.* Low pressure gaseous detector for particle dark matter. *Physical Review Letters*, 73:1067–1070, 1994.
- [94] T. Ohnuki, D. P. Snowden-Ifft, and C. J. Martoff. Measurement of carbon disulfide anion diffusion in a TPC. *Nuclear Instruments and Methods in Physics Research Section A*, A463:142–148, 2001.

- [95] W. C. Wang and L. C. Lee. Electron attachment rate constants of SO<sub>2</sub> and CS<sub>2</sub> in Ar, N<sub>2</sub>, and CH<sub>4</sub> at varied E/N. *Journal of Chemical Physics*, 84:2675–2681, 1986.
- [96] C. J. Martoff, D. P. Snowden-Ifft *et al.* Suppressing drift chamber diffusion without magnetic field. *Nuclear Instruments and Methods in Physics Research Section A*, A440:355–359, 2000.
- [97] G. Alner, H. Araujo *et al.* The DRIFT-II dark matter detector: Design and commissioning. *Nuclear Instruments and Methods in Physics Research Section A*, 555(1-2):173–183, 2005.
- [98] M. Robinson *et al.* Measurements of muon flux at 1070-metres vertical depth in the Boulby underground laboratory. *Nuclear Instruments and Methods in Physics Research Section A*, A511:347–353, 2003.
- [99] P. F. Smith, D. Snowden-Ifft *et al.* Simulation studies of neutron shielding, calibration and veto systems for gaseous dark matter detectors. *Astroparticle Physics*, 22:409–420, 2005.
- [100] E. Tziaferi, M. Carson *et al.* First measurement of low intensity fast neutron background from rock at the Boulby underground laboratory. *Astroparticle Physics*, 27(5):326–338, 2007.
- [101] J. Morales, B. Beltrán *et al.* The canfranc underground laboratory. present and future. In N. J. C. Spooner & V. Kudryavtsev, editor, *The Identification of Dark Matter*, pages 447–452, 2005. doi: 10.1142/9789812701848\_0067.
- [102] C. Ghag. *Simulation, Calibration & Exploitation of the DRIFT-II Directional Dark Matter Detector*. PhD thesis, Department of Physics and Astronomy, University of Edinburgh, 2006.
- [103] D. Snowden-Ifft. Private memo., 2008.
- [104] Cremat CR-111 charge sensitive preamplifier: application guide, 2006. URL <http://www.cremat.com/CR-111.pdf>.
- [105] Cremat CR-200 Gaussian shaping amplifier: application guide, 2008. URL <http://www.cremat.com/CR-200.pdf>.
- [106] Agilent 34970a data acquisition/switch unit family, 2010. URL <http://cp.literature.agilent.com/litweb/pdf/5965-5290EN.pdf>.
- [107] K. Pushkin and D. Snowden-Ifft. Measurements of w-value, mobility and gas gain in electronegative gaseous CS<sub>2</sub> and CS<sub>2</sub> gas mixtures. *Nuclear Instruments and Methods in Physics Research Section A*, 606(3):569–577, 2009.

- [108] A. Hitachi. Bragg-like curve for dark matter searches: Binary gases. *Radiation Physics and Chemistry*, 77(10-12):1311–1317, 2008.
- [109] D. P. Snowden-Ifft, T. Ohnuki *et al.* Neutron recoils in the DRIFT detector. *Nuclear Instruments and Methods in Physics Research Section A*, A498:155–164, 2003.
- [110] M. Berger, J. Coursey *et al.* ESTAR, PSTAR, and ASTAR: Computer programs for calculating stopping-power and range tables for electrons, protons, and helium ions (version 1.2.3), 2005. URL <http://physics.nist.gov/Star>.
- [111] J. F. Ziegler. The stopping and range of ions in matter (SRIM), 2011. URL <http://www.srim.org/>.
- [112] J. Gauvreau. Private memo., 2010.
- [113] S. Burgos *et al.* Track reconstruction and performance of drift directional dark matter detectors using alpha particles. *Nuclear Instruments and Methods in Physics Research Section A*, 584(1):114–128, 2008.
- [114] W. Blum and L. Rolandi. *Particle detection with drift chambers*. Accelerator physics. Springer-Verlag, 1993. ISBN 9780387583228.
- [115] D. Muna. *Three Dimensional Analysis and Track Reconstruction in the DRIFT-II Dark Matter Detector*. PhD thesis, Department of Physics and Astronomy, University of Sheffield, England, 2005.
- [116] F. Sauli. Principles of operation of multiwire proportional and drift chambers. In *Experimental techniques in high energy physics*, page 92, Geneva, 1977. CERN.
- [117] P. Majewski. From nuclear recoil track to MWPC signals end-to-end DRIFT detector simulation, 2007. URL <http://www.hep.shef.ac.uk/conferences/cygnus2007/talks/majewski.pdf>.
- [118] E. Daw, J. R. Fox *et al.* Spin-dependent limits from the DRIFT-II directional dark matter detector. *ArXiv e-prints*, 2010.
- [119] M. Dion, S. Son *et al.* Negative ion drift velocity and longitudinal diffusion in mixtures of carbon disulfide and methane. *Nuclear Instruments and Methods in Physics Research Section A*, 648(1):186–191, 2011.
- [120] XENON100 Collaboration, E. Aprile *et al.* Dark matter results from 100 live days of XENON100 data. *ArXiv e-prints*, 2011.

- [121] O. Buchmueller, R. Cavanaugh *et al.* Implications of initial LHC searches for supersymmetry. *The European Physical Journal C - Particles and Fields*, 71:1–13, 2011.
- [122] V. Barger, W.-Y. Keung, and G. Shaughnessy. Spin dependence of dark matter scattering. *Physical Review D*, 78(5):056007, 2008.
- [123] L. Roszkowski, R. R. de Austri, and R. Trotta. Implications for the Constrained MSSM from a new prediction for  $b \rightarrow s\gamma$ . *Journal of High Energy Physics*, 2007 (07):075, 2007.
- [124] V. A. Bednyakov. Nuclear spin structure in dark matter search: The zero momentum transfer limit. *ArXiv e-prints*, 2004.
- [125] F. Giuliani and T. A. Girard. Exclusion limits on spin dependent WIMP-nucleon couplings from the SIMPLE experiment. *Physics Letters B*, 588(3-4):151–154, 2004.
- [126] E. Behnke, J. Behnke *et al.* Improved limits on spin-dependent WIMP-proton interactions from a two liter  $\text{CF}_3\text{I}$  bubble chamber. *Physical Review Letters*, 106 (2):021303, 2011.
- [127] S. Ahlen, N. Afshordi *et al.* The case for a directional dark matter detector and the status of current experimental efforts. *INTERNATIONAL JOURNAL OF MODERN PHYSICS A*, 25(1):1–51, 2010.
- [128] E. Behnke, J. I. Collar *et al.* Spin-dependent WIMP limits from a bubble chamber. *Science*, 319(5865):933–936, 2008.
- [129] S. Archambault, F. Aubin *et al.* Dark matter spin-dependent limits for WIMP interactions on  $^{19}\text{F}$  by PICASSO. *Physics Letters B*, 682(2):185–192, 2009.
- [130] H. S. Lee, H. C. Bhang *et al.* Limits on interactions between weakly interacting massive particles and nucleons obtained with  $\text{CsI(Tl)}$  crystal detectors. *Physical Review Letters*, 99:091301, 2007.
- [131] R. Abbasi, Y. Abdou *et al.* Limits on a muon flux from neutralino annihilations in the Sun with the IceCube 22-string detector. *Physical Review Letters*, 102:201302, 2009.
- [132] M. Beltran, D. Hooper *et al.* Deducing the nature of dark matter from direct and indirect detection experiments in the absence of collider signatures of new physics. *Physical Review D*, 80:043509, 2009.

- [133] J. Ellis and R. A. Flores. Elastic supersymmetric relic-nucleus scattering revisited. *Physics Letters B*, 263(2):259–266, 1991.
- [134] B. Schmidt and S. Polenz. Electron motion in counting gases – new answers and new questions. *Nuclear Instruments and Methods in Physics Research Section A*, 273(2-3):488–493, 1988.
- [135] M. Avenier, C. Brogini *et al.* Sub MeV particles detection and identification in the MUNU detector. *Nuclear Instruments and Methods in Physics Research Section A*, 482(1-2):408–424, 2002.
- [136] S. Burgos *et al.* Measurement of the range component directional signature in a DRIFT-II detector using  $^{252}\text{Cf}$  neutrons. *Nuclear Instruments and Methods in Physics Research Section A*, 600(2):417–423, 2009.
- [137] MKS type 1479A metal-sealed Mass-Flo controller, 2006. URL <http://www.mksinst.com/docs/UR/1479.pdf>.
- [138] MKS analog 600 series selection guide: Baratron absolute capacitance manometers, 2009. URL <http://www.mksinst.com/docs/UR/1479.pdf>.
- [139] NI low-cost E series multifunction DAQ, 2008. URL <http://www.mksinst.com/docs/UR/1479.pdf>.
- [140] NI-DAQmx Base software, 2011. URL <http://sine.ni.com/nips/cds/view/plang/en/nid/14480>.
- [141] Qt website, 2011. URL <http://qt.nokia.com/products/>.
- [142] M. O. Krause. Atomic radiative and radiationless yields for k and l shells. *Journal of Physical and Chemical Reference Data*, 8(307):21, 1979.
- [143] National institute of standards and technology photon cross section data, 2011. URL <http://physics.nist.gov/PhysRefData/Xcom/html/xcom1.html>.
- [144] J. A. BEARDEN and A. F. BURR. Reevaluation of x-ray atomic energy levels. *Reviews of Modern Physics*, 39(1):125–142, 1967.
- [145] National institute of standards and technology database, 2007. URL <http://srdata.nist.gov/xps/SELEnergyType.aspx>.
- [146] T. Åberg. Unified theory of auger electron emission. *Physica Scripta*, 1992(T41):71, 1992.
- [147] A. Savitzky and M. J. E. Golay. Smoothing and differentiation of data by simplified least squares procedures. *Analytical Chemistry*, 36:1627–1639, 1964.

- [148] S. Burgos, E. Daw *et al.* Low energy electron and nuclear recoil thresholds in the DRIFT-II negative ion TPC for dark matter searches. *Journal of Instrumentation*, 4(04):P04014, 2009.
- [149] D. P. Snowden-Ifft, T. Lawson *et al.* Low energy alphas in the drift detector. *Nuclear Instruments and Methods in Physics Research Section A*, 516(2-3):406–413, 2004.
- [150] international atomic energy agency nuclear data services database, 2011. URL [www-nds.iaea.org](http://www-nds.iaea.org).
- [151] D. Leonard, P. Grinberg *et al.* Systematic study of trace radioactive impurities in candidate construction materials for exo-200. *Nuclear Instruments and Methods in Physics Research Section A*, 591(3):490–509, 2008.
- [152] M. Pipe and the DRIFT collaboration. Background reduction and spin-dependent limits using DRIFT — a directionally sensitive dark matter detector. *Journal of Physics: Conference Series*, 315(1):012017, 2011.
- [153] R. Veenhof. Garfield - simulation of gaseous detectors, 2010. URL <http://garfield.web.cern.ch/garfield/>.
- [154] G. J. Feldman and R. D. Cousins. Unified approach to the classical statistical analysis of small signals. *Physical Review D*, 57:3873–3889, 1998.
- [155] G. Alner, H. Araújo *et al.* Limits on WIMP cross-sections from the NAIAD experiment at the boulby underground laboratory. *Physics Letters B*, 616(1-2):17–24, 2005.
- [156] D. A. Glaser. Some effects of ionizing radiation on the formation of bubbles in liquids. *Phys. Rev.*, 87:665–665, 1952.